Basement Geology, Tectono-stratigraphic and Diagenetic Evolution of the Presalt Succession in the Northern Campos Basin, Brazil



Michael Strugale

Wolfson College

Department of Earth Sciences

University of Oxford

A thesis submitted for the degree of

Doctor of Philosophy

Trinity 2022

This thesis is dedicated to my wife, Andréia,

and my daughters, Julia and Lara, for all of their love,

support and patience whilst completing my studies.

Contents

Acknowledgments v

Abstract ix

1. Introduction and Thesis Structure 1

1.1 Introduction 1
1.2 Research Aims 5
1.3 Dataset and Methods 6
1.4 Thesis Structure 8

2. Geological Context 10

2.1 Introduction 10
2.2 The Precambrian Basement of the Campos Basin 11
2.3 Lithostratigraphy of the Campos Basin 16
2.4 Diagenetic Evolution of the Pre-Salt Reservoirs of the Campos Basin 21
2.5 Campos Basin: Structure and Tectonic Evolution 26
2.6 NW-SE Transverse Zones of Brittle Deformation 30

3. Basement Geology and its Controls on the Nucleation and Growth of Rift Faults in the Northern Campos Basin, Offshore Brazil 33

3.1 Abstract 34
3.2 Introduction 35
3.3 Geological Setting 37
3.3.1 Basement 37
3.3.2 Campos Basin 41
3.4 Data and Methods 44

3.5 Results 47
3.5.1 Seismic stratigraphy 47
3.5.2 Rift faults and structural compartments 48
3.5.3 Interpretation of intra-basement seismic facies and structures 53
3.5.3.1 The NE Cluster 58
3.5.3.2 Integrating rift and basement structures in the NE Cluster 59
3.5.3.3 The SE Cluster 63
3.5.3.4 Integrating rift and basement structures in the SE Cluster 64
3.5.4 Basement samples and geochronological analysis 66
3.6 Discussion 69
3.6.1 Basement geology 69
3.6.2 Rift tectonics and models for basement reactivation 73
3.6.3 Basement reactivations within the NE Cluster 80
3.6.4 Basement reactivations within the SE Cluster 83
3.7 Conclusions 85

4. Tectono-Stratigraphic Evolution of the Rift and Post-Rift Systems in the Northern Campos Basin, Offshore Brazil 87
4.1 Abstract 88
4.2 Introduction 89
4.3 Geological setting 91
4.3.1 Revised age dating of the presalt sequence 95
4.4 Methods 97
4.5 Results 101
4.5.1 Structural framework 101
4.5.2 Seismic-stratigraphic framework 105
4.5.3 The syn-rift supersequence 107
4.5.3.1 Syn-rift I TSS (SRI) 107
4.5.3.2 Syn rift II TSS (SRII) 108
4.5.3.3 Syn rift III TSS (SRIII) 112
4.5.4 The rift transition sequence 114
4.5.5 The post-rift supersequence 116
4.5.5.1 Post-rift I (PRI) TSS 116
4.5.5.2 Post-rift II (PRII) TSS 117

4.6 Tectono-stratigraphic evolution....118
4.6.1 Rift phase 1 (RP1)....121
4.6.2 Rift phase 2 (RP2)....126
4.6.3 The rift transition phase....129
4.6.4 The post-rift phase....131
4.7 Discussion....135
4.7.1 Strain migration during rifting....135
4.7.2 Rift and post-rift tectono-stratigraphic evolution....138
4.7.3 Implications for the age of the presalt sequence....141
4.8 Conclusions....144

5. Diagenetic Products, Settings and Evolution of the Presalt Succession in the Northern Campos Basin, Brazil 147

5.1 Abstract....148
5.2 Introduction....149
5.3 Geological Context....151
5.4 Materials and Methods....154
5.5 Results....158
5.5.1 Petrography....158
5.5.1.1 Host rocks....159
5.5.1.2 Diagenetic products....164
5.5.1.3 Tectonic, compaction and dissolution features....167
5.5.2 QEMSCAN bulk composition....173
5.5.3 Stable isotopes....173
5.5.4 Fluid inclusions....176
5.5.5 U-Pb geochronology and the timing of diagenesis....183
5.5.6 Interwell distribution of hydrothermal diagenesis....190
5.5.6.1 Section DIP A....193
5.5.6.2 Section DIP B....197
5.5.6.3 Strike section....199
5.6 Discussion....202
5.6.1 Diagenetic environments....202
5.6.2 Paragenetic sequence....204
5.6.3 Diagenetic evolution and controls....206
5.6.4 Distribution of hydrothermal diagenesis....211

5.6.5 Depositional, diagenetic and hydrothermal events along the continental margins of the South Atlantic Ocean 216
5.7 Conclusions 221

6. Summary and Discussion **225**
6.1 Introduction 225
6.2 Geologic History 226
6.2.1 Precambrian to Triassic 226
6.2.2 Early Cretaceous 227
6.2.3 Diagenetic history (Early Cretaceous to Recent) 235
6.3 Implications and Some Reflections 239
6.4 Future work 245

7. Conclusions **247**

8. Appendix A **253**

9. Appendix B **257**

10. Appendix C **265**

11. References **279**

Acknowledgments

This work was only possible because industry and academia worked together for the good and progress of science. Besides their individual relevance, development, wealth, and truly cooperative social- and environmentally sustainable growth of any society only comes when these actors work together.

I want to start this long list of acknowledgements celebrating the role of my DPhil supervisor Joe Cartwright. I will never forget his first invite for a DPhil while looking at the rocks of the Somerset shore back in 2010. I always appreciate his particular way of provoking and stimulating our critical thinking using no more than a couple of paper sheets and a pencil, from which he makes the most challenging questions. My family and I have no words to express our gratitude to you.

I am very thankful to my co-supervisor Laurence Robb for his advice and support. After a forced change in the project scope due to the Covid-19 pandemic, Laurence was the right person to guide me through subjects with which I was mostly unfamiliar. Thank you for your patience and dedication.

Many thanks for the members of my examination board, Professor Mike Daly and Dr Ian Davison, for providing several thoughtful suggestions for this thesis and to push me for the best side of the good science during my Viva examination. They showed me that there are no correct or wrong answers in science but indeed good or poorly explained answers.

Professor John Cosgrove and Dr. Luciano Magnavita are thanked for writing recommendation letters to the Department of Earth Sciences as part of my application to this DPhil program. I am also thankful to Professor Renata Schmitt of UFRJ (Brazil) for helping me throughout the world of basement rocks and continental collisions that built the foundations of the Campos Basin.

I acknowledge Petrobras S.A. for sponsoring and supporting my research and living in the United Kingdom during this DPhil project. The corporate program for long-term overseas

study (PDRHE) is a program that allowed employees to study abroad in the last 30 years, including mine. Nevertheless, this thesis would not be possible without the support of several individuals within the company. To begin with, I shall recognise the role of past and present immediate and upper level managers in disputing my nomination internally and supporting during this program, nominally Carlos Henrique Lime Bruhn, Luis Carlos Sousa, Luiz Schmall dos Santos, Ednilson B. Freire, Daniela Apoluceno, and Roberta Alves Mendes.

Several workmates helped me by offering technical advice, support and the chance to discuss my results and thoughts during the course of this research project. My thanks goes to Bruno Carvalho, Bruno Lima, Fabio Lima, Fernando Jardim, Isabela Carmo, João Paulo Gomes, João Olivito, Jorge André, Julio Sanglard, Leonardo Onofre, Leonardo Tedeschi, Livio Fernandes, Mario Neto, Naoki Arima, and Otávio Borges. Anderson Carly, Emanuel Malta, José Marcelo Bueno, Livia Pacheco, Manuel Bonnet, Roberli Silva, and Sirlene Coelho deserve special thanks for helping me collect, organise, and get the permissions and send the samples and thin sections to the UK. Aldo Koehler, Fernando Tavares, and José Mororó are thanked for their support in navigating through the bureaucracy of getting the needed permissions to use and publish the wellbore and seismic data. Finally, I wish to recognise the importance of some of Petrobras' HR personnel, Aldemario Santos, Cristiane Sumeasu, Juliana Girardi, Magda Aranha, and Tielli Fiorini, in providing assistance for my family and I while abroad.

I am very grateful for the high-profile scientific and camaraderie setting of the 3D seismic lab in the Department of Earth Sciences, where DPhil students, Research staff and undergraduates created a friendly and welcoming atmosphere. Alfredo, Benedict, Claudia, Chris, Ethan, Martino, James, Reybi, and Victoria will be forever in my happiest memories.

Several people from the Department of Earth Sciences, from finance to lab staff and reception, contributed to my work in several ways. Assuming the risk of forgetting some people, I wish to thank Cornellius, Chris Day, Claire, David, Gail, James, Jeanette, Martha, May, Owen, and Stephen. Special thanks to Kat Clayton and Matthew Beverley-Smith for, respectively, helping with XRD and SEM imagery and for making dozens of thin sections.

Several faculty members also contributed when I asked for advice and second opinions, on which I list professors and associated researchers Allan Hiseh, Bruce Levell, Jane Berling, Mike Daly, Phil Holdship, and Stuart Robinson. DPhil students Anna, Annika, Brooke,

Chia-Hsin (Wendy), David, Ian, Kirsty, Raphael, Richard, Tzu-Hao (David) are thanked for their support and friendship.

Wolfson College is thanked for the academic support and for providing lovely accommodation for my family, which made our moving and adaptation to a new country smooth. It also allowed us to meet fantastic students and fellows from around the world. Alice, Angela, Aslihan, Chigusa, Cristina, Estela, Felipe, Jonathan, Luiz, Mariana, Marie and Marie, Paulo, Samuel, Rubens, Todd, Vincent, and their children gathered with us to create such lovey family setting of the greater Garford-Linton Rd community.

I also want to recognize and acknowledge the college's porters, the accommodation office, the college day nursery and the catering team for making our arrival smooth and our stay pleasant and memorable.

Finally, I owe a special thanks to my wife Andréia and my daughters Julia and Lara for all of their love and support, and for always encouraging me to do my best. Please receive, with all love of the Universe, my apologies for the several moments in family that I have missed.

Michael Strugale

February 2023

Abstract

The Campos Basin (SE Brazil) hosts significant hydrocarbon accumulations in reservoirs above and below a layer of evaporites. The rift to post-rift lacustrine carbonates that constitutes the Pre-Salt reservoirs have been the object of several studies focused on the depositional and diagenetic characteristics of these Barremian to Aptian carbonates. Nevertheless, the basement geology, tectono-stratigraphic evolution and geochronologic constraints for the hydrothermal diagenesis are yet to be established. This thesis presents a novel integrated geological study of the entire presalt sequence utilizing 2D and 3D seismic surveys and sidewall cores from a hydrocarbon accumulation in the northern Campos Basin. The basement is constituted by anisotropic, high-grade supracrustal rocks in the East and relatively isotropic granitic rocks in the West. Lithologies, structural style and age suggest a correlation with the onshore Cabo Frio Tectonic Domain. The overall rift evolution probably started during the Berriasian with a peak of rift-related faulting from the Hauterivian to Barremian, followed by a rift transition and post-rift stages (Barremian to Aptian). The pre-existing metamorphic fabric was selectively reactivated whenever its orientation was favourable. Petrography and geochemistry show diagenetic phases composed predominantly of quartz, calcite and dolomite to ankerite series, and secondarily pyrite, Sr-barite and svanbergite. Additional studies of stable isotopes, fluid inclusion microthermometry and LA-ICP-MS U-Pb geochronology in the diagenetic minerals provide evidence for three tectono-diagenetic events that occurred under distinct diagenetic settings during the Barremian to Aptian, the Albo-Cenomanian and the Campanian to Maastrichtian stages. The diagenetic conditions were initially hydrothermal and progressively attained geothermal equilibrium under deep-burial conditions towards the Late Cretaceous. These diagenetic episodes were not necessarily coeval with magmatic events were are always coeval with basin-scale tectonic events described previously using balanced cross-sections in the post salt section.

Chapter 1

Introduction and Thesis Structure

1.1. Introduction

The occurrence of networks of interconnected pores in rocks that lack primary porosity is of high importance in several fields amongst the geosciences, from hydrocarbon exploration and production to groundwater exploitation. Consequently, confusing and contradictory terminology is a major barrier to communication regarding geometry and flow in carbonate reservoirs (Worthington et al., 2000). Processes of epigenic and hypogenic speleogenesis in combination with sedimentary, depositional and tectonic proprieties can led to a complex geometry of secondary porosity (e.g. Cantrell et al., 2004; Davies & Smith Jr, 2006; Sharp et al., 2010; Swennen et al., 2012; Parise et al., 2018).

Hypogene speleogenesis is the dissolution of soluble rocks by fluids from depth, regardless the depth of occurrence (Klimchouk, 2009; Palmer, 2011). The term "hydrothermal" refers to waters that are warmer (>5-10°C) than the surrounding environment (White, 1957;

Machel & Lonnee, 2002). Hydrothermal diagenesis is slightly more specific and related to in situ mineral transformations and does not necessarily denote the formation of a network of caves (Packard et al., 2001; Hollis et al., 2017; Rochelle-Bates et al., 2021). This term has been used with respect to the dolomite- and silica-rich reservoirs in the Western Canada (Packard et al., 2001; Machel, 2004; Vandeginste et al., 2005; Davies & Smith Jr, 2006), and has since been applied in distinct geologic contexts (e.g. Sharp et al., 2010; Hirani et al., 2018; Kyne et al., 2019; Lima et al., 2020; Souza et al., 2021). The processes and products of hydrothermal diagenesis exhibit a close relationship with a diversity of tectonic features (e.g. Davies & Smith Jr, 2006). In addition, faults often act as conduits for deep-seated fluids (c.f. Sibson, 1981). Depositional heterogeneities will result in layers with contrasting porosity and permeability that often form a barrier to the upward fluid flow along the fault. Therefore, the result is a rather complex system of vertical and horizontal DZEPs (Discontinuous Zones of Enhanced Permeability, c.f. Cross & Burchette, 2022).

It is important to mention that most previous studies of hydrothermal diagenesis are based on integrated studies, in which the entire sedimentary section, basement, and complete tectonic plus subsidence history is taken into account to unveil the diagenetic paragenesis, phases and evolution. In addition, these studies have in common being based or have a strong support in outcrop studies despite the possible risks in simply transferring outcrop data to the subsurface context (see discussion in Laubach et al., 2019).

The occurrence of secondary porosity in the sub-salt lacustrine carbonate reservoirs is widely recognized as having a fundamental role in the outstanding production performance of the hydrocarbon accumulations of both Campos and Santos basins, East Brazil (Carminatti et al., 2008; Fetter et al., 2018; Lima & De Ros, 2019; Gomes et al., 2020). To

date, scientific knowledge of these reservoirs regarding sedimentary facies and processes, and diagenetic-related products are satisfactorily understood in the Pre-Salt of the Campos Basin (Carvalho & De Ros, 2015; Muniz & Bosence, 2015; Armelenti et al., 2016; Herlinger Jr. et al., 2017; Mizuno et al., 2018; Muniz & Bosence, 2018; Lima & De Ros, 2019; Oliveira et al., 2019; Olivito & Souza, 2020). The occurrence and products of hydrothermal digenesis in these reservoirs were recognised and studied in depth by Lima and De Ros (2019) and Lima et al. (2020). However, the understanding of the structural framework and the syn- to post-depositional tectonic deformation is quite superficial because are based in basin-scale studies (Mohriak et al., 1990; Stanton et al., 2019; Morgan et al., 2020) and semi-regional studies on the shallow water domain of the Central Campos Basin (Guardado et al., 1989b; a; Mohriak et al., 1990; Goldberg et al., 2017). There is no study at reservoir scale that unveils the role of the stratigraphic and structural framework in the hydrothermal diagenesis.

From the above, it has become clear that an integrated study on which the existent petrographic, stratigraphic and geochemical knowledge should be integrated with a yet non-existing, comprehensive tectono-stratigraphic model based on detailed 3D seismic interpretation. The most successful studies on the distribution of hydrothermal diagenesis are based on integrated, multidisciplinary approaches (e.g. Packard et al., 2001; Sharp et al., 2010; Gomez-Rivas et al., 2014; Martín-Martín et al., 2018). In reality, however, such integration is difficult in several aspects, from the inherent sampling gap in sub-surface reservoir studies (Cosentino, 2001) to the often fragmented “by-discipline” reservoir characterisation workflow within oil companies. Therefore, the gaps in the knowledge that might help to build an integrated and predictive model for the occurrence of vertical and

horizontal corridors characterised by enhanced secondary porosity in the Pre-Salt reservoirs of the North of Campos Basin are as follows:

- ✓ Basement geology, including inherited discontinuities and age, has been largely neglected in studies on the presalt sequence.
- ✓ The age of the onset of rifting is based on poorly-constrained Ar-Ar ages obtained in basalts from wells in the Central Campos Basin (Mizusaki et al., 1992).
- ✓ The syn-rift volcanoclastic and siliciclastic sediments of the pre salt sequence in the deep-water domain of the Campos Basin are unknown in terms of constitution and diagenetic history.
- ✓ There is no proposed scheme for the tectono-stratigraphic evolution that could explain satisfactorily the interplay between fault activity and deposition of the carbonatic lacustrine reservoirs, including possible strain migration during the evolution of the rift system.
- ✓ There was no proposal to adapt the existing lithostratigraphic column of the Campos Basin (Winter et al., 2007) to the new age-calibrations for the deposition of the presalt and evaporite rocks (Tedeschi et al., 2017; Pietzsch et al., 2020).
- ✓ Although recognised in the post-salt sequence of the Campos Basin (Fetter, 2009), inversion tectonics is yet to be described in the presalt sequence.
- ✓ Despite being well characterised in terms of diagenetic products and processes (Lima & De Ros, 2019; Lima et al., 2020), hydrothermal diagenesis in the Pre-Salt reservoirs in the North of Campos Basin are not time constrained and there is no predictive model for its occurrence considering the actual structural and stratigraphic frameworks.

1.2. Research Aims

The primary aims of this thesis are:

> **To establish time-constrained relationships between the structural framework, tectonic and diagenetic events. From that, set a predictive model for their spatial distribution in the presalt succession in the North Campos Basin.**

These aims are achieved through:

- ✓ Establishing the geology and the distribution of bounding structural heterogeneities and internal metamorphic anisotropy of the Precambrian basement.
- ✓ Understanding how the basement structures behave under extension tectonics thus influencing the strain distribution and structural styles of the rifting.
- ✓ Interpreting the whole presalt sequence aiming to set a tectono-stratigraphic model that considers not only the changes in the depositional environments but also the strain diachroneity during the rift and post-rift tectonic stages. Also, adjust the tectono-stratigraphic framework to the new age constraints for the presalt deposition.
- ✓ Performing extensive petrographic descriptions, with complimentary geochemical (compositional and stable isotopes), fluid inclusion and geochronologic studies in the sidewall cores from the basement and syn-rift units.

- ✓ Based on the information obtained from the four previous steps, use seismic-geologic sections calibrated with wells and the lithogeochemical wireline logs to build a model for the 3D distribution of the hydrothermal diagenesis.

1.3. Dataset and Methods

Since this thesis is submitted as integrated format, the data and methods are explained for each of the chapters prepared for or published as papers (Chapters 3-5). A brief summary of the dataset used during this research is presented below.

- ✓ Seismic data: commercial 3D depth converted PSDM 10 km depth seismic survey, consisting of a merge of two streamer, depth migrated (Kirchhoff TTI) acquisitions covering an area of *ca.* 1000 km^2. The seismic data are zero-phase and normal polarity with seismic sections presented such that troughs (black reflections) represent a downward increase in acoustic impedance. Inlines and crosslines are, respectively, EW-trending and NS-trending, spaced 12.5 m and 6.25 m. Within the interval of interest, the 3D seismic has a dominant frequency of 15 Hz and an estimated vertical resolution of 90 m for the sub-salt sequence.
- ✓ Seismic data: Eight 2D semi-regional, dip-oriented deep seismic lines recorded from 8 to 12s TWT provided control of the crustal structure and context of the 3D survey with respect to the regional rift structure.
- ✓ Well trajectories and logs: 34 wells and their wireline logs were used to make well correlation and to guide the seismic interpretation. Lithogeochemical logs were also used to scale up the data from sidewall cores to the near- and inter-well domain.

- ✓ Sidewall cores: 68 samples from 18 wells and their thin sections. More diagenetically altered samples were prioritised. In addition, care was taken to ensure that samples were representative of the overall basement and rift-section contexts with a reasonably widespread distribution.

The following analytical and interpretation techniques were used in this research. Details on each are found in the respective chapter:

- ✓ 2D and 3D detailed seismic interpretation.
- ✓ Analyses of strain distribution and evolution based on the map distribution of fault offsets and length x displacement plots.
- ✓ Conventional petrographic description (transmitted and reflected lights).
- ✓ SEM-based automatic mineralogy mapping (QEMSCAN).
- ✓ C-O stable isotopes, on which X-Ray Diffractometer (XRD) and Isotope Ratio Mass Spectrometers (IRMS) were used.
- ✓ Microthermometric studies on fluid inclusions.
- ✓ Laser Ablation Inductively Coupled Plasma Mass Spectrometer (LA-ICP-MS) U-Pb geochronology on zircon and carbonate minerals.
- ✓ Seismic- and wellbore-constrained geological cross sections.

1.4. Thesis Structure

This thesis is presented following the integrated thesis format, where the main chapters consist of published or papers written intending future publication. Since each paper has only a brief geological context relevant to the main aims of each paper, I provide an extended geological context in Chapter 2 in which the current understanding of the Campos Basin is presented in greater detail. The order and gross outline of the following chapters are as follows:

Chapter 3 – The basement: pre-existing heterogeneities and therefore the constitution and age of the basement exerts fundamental controls in the onset and style of rift basins. This chapter was published in the 33rd volume of Basin Research Journal in 2021, entitled as "Basement Geology and its Controls on the Nucleation and Growth of Rift Faults in the Northern Campos Basin, Offshore Brazil" (https://doi.org/10.1111/bre.12540).

Chapter 4 – The rift and post-rift phases: the whole presalt succession was interpreted and establishes a new tectono-stratigraphic framework. A new regional-scale rift structure in the Campos Basin is defined, the Guriri Fault Zone, which comprises high-strain branches that acted diachronously. Post-rift selective reactivation by tectonic inversion also occurs. In addition, the stratigraphic framework was adjusted to fit the new age constraints for the presalt deposition (e.g. Tedeschi et al., 2017) and a new age for the onset of rifting is suggested as being Berriasian. This chapter was published in the 34th volume (2022) of the Basin Research Journal with the title "Tectono-Stratigraphic Evolution of the Rift and Post-rift Systems in the Northern Campos Basin, Offshore Brazil" (https://doi.org/10.1111/bre.12674).

Chapter 5 – Diagenetic products, settings and evolution: The paragenetic sequence is described and the composition and paleo temperature of the fluids are obtained. The main diagenetic phases were dated using U-Pb geochronology. From that, the small-scale data obtained from the samples were integrated to the well logs and then with the tectono-stratigraphic framework obtained in previous chapters.

Chapter 6 – Summary and discussion: This chapter presents a synthesis of the Chapters 4, 5, and 6, aiming to summarise the interpretations presented. It is made through a continuous geologic history backed in the Chapter 3, where each piece of evidence obtained during this research are organised in chronological order. In addition, some topics on which a better discussion or an alternative methodological approach could have been done are assigned, and suggestions for future works are shown.

Chapter 7 – Conclusions

Appendixes. Appendixes A, B and C are supporting information for, respectively, Chapters 3, 4 and 5.

Chapter 2

Geological Context

2.1 Introduction

The study area locates in the North Campos Basin, 70 km offshore from the coastline of the Espírito Santo State, East Brazil. The Campos Basin is located in the Central Segment of the South Atlantic Ocean and is delimited by the Vitória High to the North and the Cabo Frio High in the South (Guardado et al. 1989a) (Figure 2.1). The basement of the Campos Basin comprises metamorphic and intrusive igneous rocks of the Neoproterozoic to Cambrian age Ribeira and Araçuaí belts, which are part of the Mantiqueira Province (c.f. Almeida et al., 1981). Basement geology and structural framework have a fundamental role in controlling the geometry and evolution of rift basins (e.g. Milani & Davison, 1988; Daly et al., 1989). Reactivation of basement structures controls the initial geometry and the locus of later reactivations in rift and passive margin basins (e.g. Withjack et al., 1998; Fazlikhani et al., 2017).

The basin originated from the rifting of the Western Gondwana during the Early Cretaceous under a broadly E-W extension, which eventually formed the South Atlantic Ocean (Rabinowitz & LaBrecque, 1979; Chang et al., 1992; Szatmari & Milani, 2016). The overall structural style of the Campos Basin is detached, with a detachment surface at the base of the Aptian evaporites (Fetter, 2009) (Figure 2.2).

The focus of this study comprises sediments of the rift and post-rift stages of the basin, which represents the so-called "presalt" sequence that includes siliciclastic and (mainly) carbonate sediments deposited from the Hauterivian to the Aptian.

2.2 The Precambrian Basement of the Campos Basin

The geometry of the structural highs and lows of the basin is controlled by the offshore projection of NE-SW and roughly NW-SE basement structures (Chang et al., 1992; Fetter, 2009). Onshore, the NE-SW trend corresponds to predominantly Neoproterozoic metamorphic and magmatic rocks bounded by high strain ductile shear zones of the Mantiqueira Province (Almeida et al., 1981; Ebert & Hasui, 1998; Heilbron et al., 2008). The NW-SE trend consists of swarms of fractures, joints and tholeiitic dykes whose origin and constitution are not yet completely established (e.g. Calegari et al., 2016) (Figure 2.3).

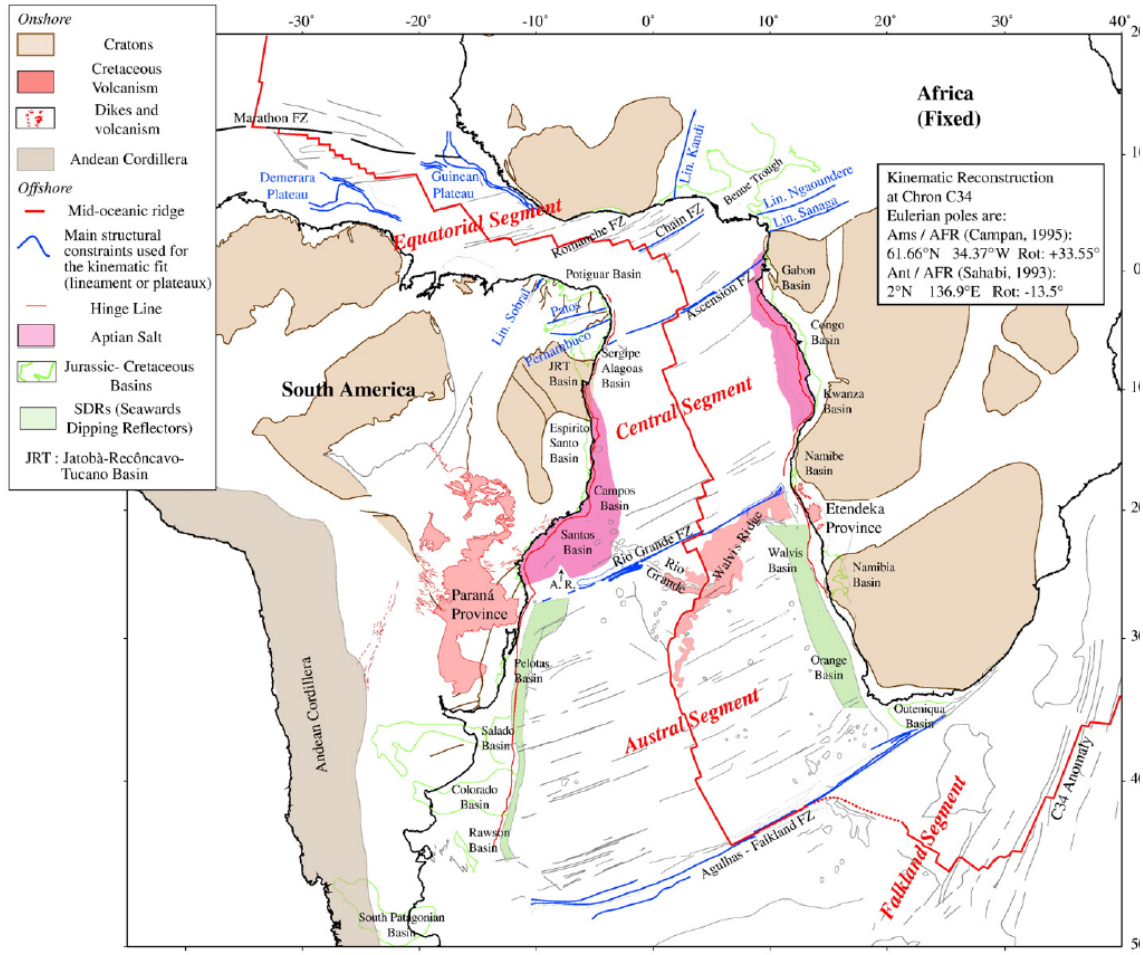


Figure 2.1: General structural and tectonic map of the South Atlantic Ocean and adjacent African and South American continents at Chron 34 (84 Ma) (From Moulin et al., 2010). Location of the Campos Basin is highlighted.

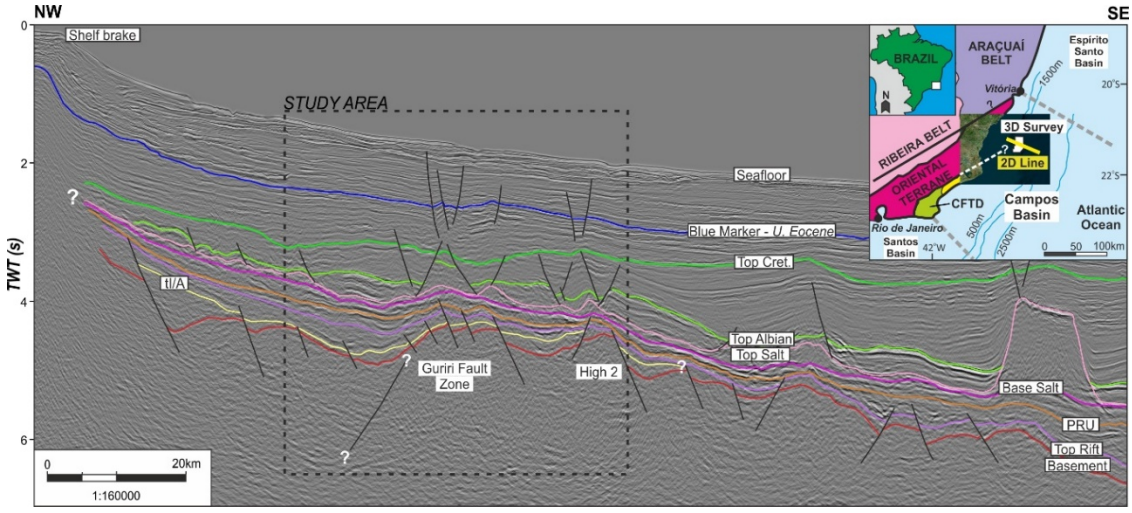


Figure 2.2: Location of the study area and 2D semi-regional dip seismic section of the northern Campos Basin. Geologic map modified from Strugale et al. (2021). CFTD: Cabo Frio Tectonic Domain (c.f. Schmitt et al., 2004).

The Mantiqueira Province, as defined by Almeida et al. (1981), is a NNE-trending orogenic system along the east Brazilian coast that extends from the southern border of the eastern São Francisco craton (16º S) to Uruguay (33º S). The Neoproterozoic to Cambrian Araçuaí and Ribeira belts are the orogens of the central and north domain of the Mantiqueira Province in the SE Brazil (Ebert & Hasui, 1998; Heilbron et al., 2008; Schmitt et al., 2008; Egydio-Silva et al., 2018) (Figure 2.3). The counterpart of the Araçuaí belt on the African conjugate margin is the West Congolian Belt, which is an ENE-verging fold-thrust belt that lies on the west side of Congo craton (Tack et al., 2001). Many authors refer to these orogenic belts as a single tectonic unit, the so-called Araçuaí-West Congo Orogen (e.g. Alkmim et al., 2006; Cavalcante et al., 2019).

The Ribeira (transpressional) and Araçuaí (westward thrust of allochthonous units) Belts have differences in tectonic fabric, *i.e.* NE-SW and N-S oriented, respectively – following the São Francisco Craton boundary. However, both belts exhibit similar pressure and thermal metamorphic regimes (granulite and amphibolite facies), and display structural continuity without a clear boundary between them (Egydio-Silva et al., 2018) (Figure 2.3b). Regarding structural styles, the transition between the two belts is gradual, with a progressive change from NE-trending, subvertical foliation and subhorizontal stretching lineations in the Ribeira Belt, to a gently dipping and less pronounced fabrics in the Araçuaí Belt. Therefore, whether the Araçuaí and the Ribeira belts represent continuous or distinct orogenic belts is a matter of debate.

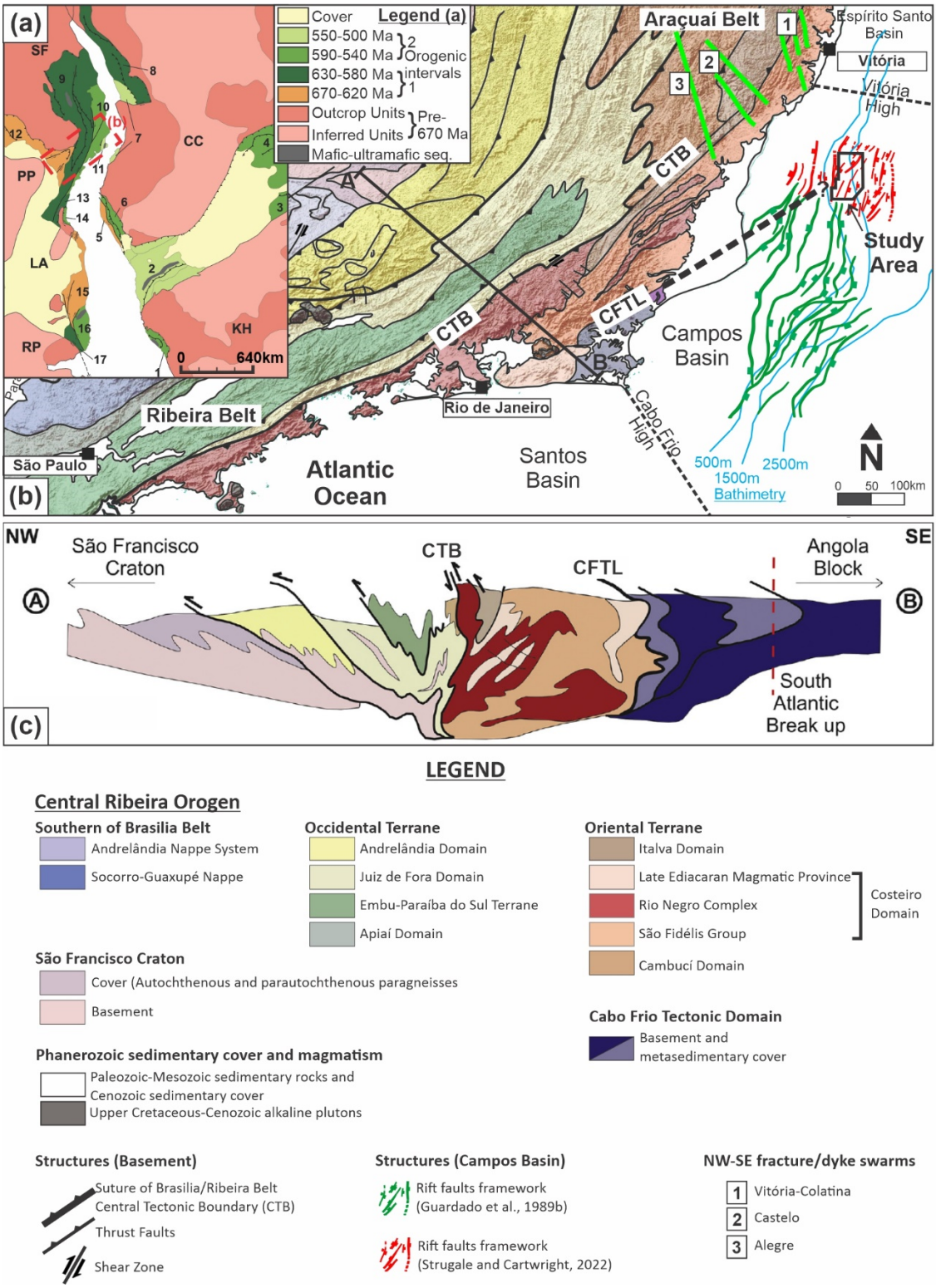


Figure 2.3 (caption on next page)

Figure 2.3: Geotectonic and basement framework of the SE Brazil. a) SW Gondwana reconstructed to ca 500 Ma, with cratons (pre-Gondwana continents) sutured by Brasiliano - Pan African mobile belts, modified from Schmitt et al. (2018). Cratons and cratonic massifs or blocks: CC – Congo; KH – Kalahari; RP – Rio de la Plata; LA – Luis Alves; PP – Paranapanema; SF – São Francisco. Mobile belts: (1) Gariep; (2) Damara; (3) Zambesi; (4) Lufilian; (5) Kaoko (Coastal); (6) Kaoko (Central-East); (7) Angola; (8) West Congo; (9) Araçuaí; (10) Ribeira (Oriental Terrane); (11) Cabo Frio; (12) Brasília; (13) Curitiba Terrane; (14) Paranaguá; (15) Dom Feliciano; (16) Cuchilla Dionísio; (15) Nico Pérez. b) Tectonic map of central Ribeira Orogen, southern Brasília Orogen and southern part of São Francisco (modified from Martins et al., 2021). CTB – Central Tectonic Boundary (c.f. Almeida et al., 1998). CFTL – Cabo Frio Tectonic Limit. The offshore extension of the CFTL is according to Stanton et al. (2019) and Strugale et al. (2021). NW-SE onshore dike swarms are based in Almeida et al. (2013). c) Geological cross section through the Ribeira Orogen modified from Heilbron et al. (2008) and Schmitt et al. (2016).

The projection of the NE-SW main onshore structures towards the Campos Basin implies that the basement comprises the Oriental Terrane of the Ribeira Belt and the quite distinct Cabo Frio Tectonic Domain (CFTD) (Stanton et al., 2019 and references therein) (Figure 2.2). The CFTD represented the latest collision and occurred during the Cambrian (c. 530-510 Ma) and shows a predominantly low-angle NW-SE to N-S structural grain, orthogonal to the adjacent Oriental Terrane (Schmitt et al., 2004). As a response to this compression, the previously amalgamated terranes were overprinted by important NE-SW dextral shear zones that displace the contacts between the terranes and locally reactivated older thrust zones (Heilbron et al., 2008).

Two major Brasiliano structures run roughly parallel to the coastline, the Central Tectonic Boundary (CTB) and the Cabo Frio Tectonic Limit (CFTL) (Figure 2.3b). The CTB is a major tectonic discontinuity that separates the Oriental terrane from the Occidental terrane (Almeida et al., 1998). The CTB is a folded shear zone (Figure 2.3c) which shows a complex long-term structural evolution developed under high-temperature conditions. Mylonitic fabrics and intrusive granite bodies of multiple generations are observed (Heilbron et al., 2008). The CFTL is a low angle tectonic contact folded by mega-scale reclined structure with axis plunging to SW (Schmitt et al., 2016). Its offshore extension

towards NE reaches the vicinity of the studied area. Such extension is based not only by the apparent continuation to NE but also by magnetic maps (Stanton et al., 2019).

The sets and patterns of fracture and tholeiitic dyke swarms in the onshore realm of the Campos and Santos basins and the African counterpart were presented in detail by Almeida et al. (2013); (2021) (Figure 2.3). Most of the tectonic activity along these trends consists of brittle reactivations related to intraplate stress propagation during and after the Early Cretaceous rifting (see Chapter 2.6). However, Cambrian-age dyke emplacement was recently recognised in the Castelo Lineament and correlated with the orogenic collapse of the Araçuaí Belt (Santiago et al., 2020). Therefore, the NW-SE network of brittle structures could record a polycyclic deformation.

2.3 Lithostratigraphy of the Campos Basin

The sedimentary column of the Campos Basin dates from the Early Cretaceous to the recent. It is divided into three tectono-stratigraphic supersequences: rift, post-rift, and drift (Cainelli & Mohriak, 1999; Winter et al., 2007) (Figure 2.4). Rift-related mechanical subsidence started during the Hauterivian and lasted until the Barremian. Bioclastic rudstones (coquinas) were deposited in bioherms stacked onto structural highs (Olivito & Souza, 2020). The post-rift supersequence marks the onset of thermal subsidence, leading to the deposition of mostly abiotic lacustrine carbonates followed by an extensive salt layer during the Aptian (Pietzsch et al., 2020 and references therein). The drift phase is initially characterised by a shallow marine carbonates of Albian age, that gradually changed to deep-water siliciclastic sedimentation (Mohriak et al., 1990). The deposition of the drift stage sediments submitted the evaporites to loading and led to the development of diapirs, salt walls, and intra slope mini-basins in the deep water (e.g. Mohriak et al., 1990).

The current stratigraphic chart of the Campos Basin of Winter et al. (2007) results from accumulated knowledge obtained from the long history of hydrocarbon exploration and production (Figure 2.4). The lithostratigraphy of the presalt succession comprises the Cabiúnas Formation at the bottom, followed by the Lagoa Feia Group, which includes the evaporites. This stratigraphic scheme still works well for lithotypes, and the equivalent seismic-stratigraphic sequences studied here. In this chapter, the main lithological components and the diagenetic by-products of some of these units will be presented. However, a discussion regarding the implications of the new age constraints of the presalt sequence (Tedeschi et al., 2017; Pietzsch et al., 2020) and their implications for the Campos Basin are presented in Chapter 4.

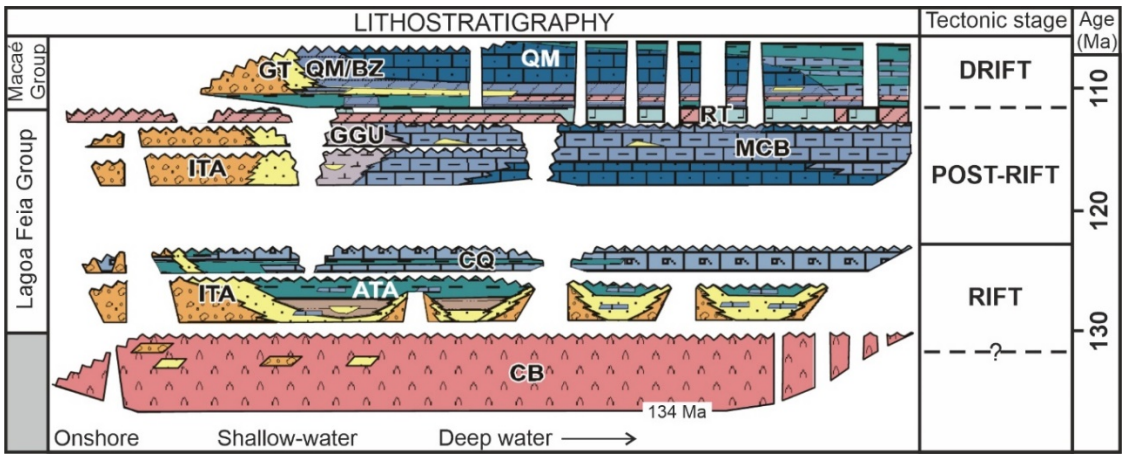


Figure 2.4. Detail of the lithostratigraphic chart of the Campos Basin Formations: CB – Cabiúnas, ITA – Itabapoana, ATA – Atafona, CQ – Coqueiros, GGU – Gargau, MCB – Macabu, RT – Retiro, GT – Goitacás, QM/BZ – Quissamã/Búzios, QM – Quissamã (adapted from Winter et al., 2007).

The Cabiúnas Formation is composed of tholeiitic, sub alkaline, subaerial and subaqueous extrusive and intrusive basalts, often intercalated with continental siliciclastic rocks (Winter et al., 2007). It is contemporaneous to the Paraná-Etendeka LIP (large igneous province) continental basalt floods (Mizusaki et al., 1992) and tholeiitic dike swarms

onshore (Turner et al., 1994; Valente et al., 2007; Almeida et al., 2013; 2021). The Campos Basin also records further magmatic cycles during the Upper Cretaceous to the Paleogene (Winter et al., 2007; Almeida et al., 2021).

Unconformably above the Cabiúnas Formation lies the Lagoa Feia Group, embracing the entire syn- and post-rift supersequences of Campos Basin (Winter et al., 2007). This unit was first described as Lagoa Feia Formation by Schaller (1973) as a sequence of non-marine, fine to coarse clastic and carbonate rocks, and evaporites. It was extensively studied by Bertani and Carozzi (1985a,b) and later subdivided into four distinct depositional sequences bounded by unconformities: Basal Clastic, Talc-Stevensitic, Coquinas, and Clastic-Evaporitic (Dias et al., 1988). More recently, Winter et al. (2007) elevated the Lagoa Feia Formation to a Group, subdivided into six formations: Itabapoana, Atafona, Coqueiros, Macabu and Retiro (Figure 2.4). Apart from the Itabapoana and Atafona Formations, which represents syn-tectonic deposits and are laterally contemporaneous with the other units of the Lagoa Feia Group, the Coqueiros, Macabu and Retiro Formations are vertically stacked in the distal part of the basin.

The Itabapoana and Atafona formations are laterally contiguous and represent the lowermost rocks of the Lagoa Feia Group (Figure 2.4). The Itabapoana Formation presents lithic conglomerates and sandstones deposited by proximal fan deltas associated with the border faults of structural blocks and braided fluvial systems. The formation is up to 5000 m thick in the rift depocenters, adjacent to major faults (Carvalho & De Ros, 2015). The Atafona Formation comprises siltstones, sandstones and lacustrine shales, along with occasional thin carbonates (Winter et al., 2007). With the development of half grabens and concentration of the tectonic activity along the major normal faults, recurrent tectonic events promoted the mixing and gravitational re-deposition of Mg-clay rich, clastic,

volcanoclastic, and bioclastic sediments in deeper, fault-bordered troughs. Therefore, due to syn-rift and mainly to post-rift erosion, the preserved rift section of the Lagoa Feia Group comprises mainly sediments deposited in the central troughs of half-graben structures (Goldberg et al., 2017).

The Coqueiros Formation represents the main hydrocarbon reservoir in the study area (Lima & De Ros, 2019; Olivito & Souza, 2020). Its top bounding surface is the post-rift unconformity (PRU), which is mapped throughout Campos and Santos basins and represents the onset of the post-rift or "sag" stage of Campos Basin (Winter et al., 2007; Muniz & Bosence, 2015) (Figure 2.4). The Coqueiros Formation is mainly composed of bioclastic carbonates and bivalves, informally known as "coquinas", intercalated with shale layers (Baumgarten et al., 1988). These high energy berms are stacked on structural highs, from which lateral gradation to shallow evaporative or shoreface to deep-lacustrine deposits will depend on the balance between subsidence and lake level. Towards the fault-bounded depocenters, gravitational deposits gradually change to hybrid clastic-bioclastic siltstones and shales (Goldberg et al., 2017; Olivito & Souza, 2020). The latter authors also subdivided the Coqueiros Formation into five units, Coq A to E (from base to top), with Coq A positioned in the rift phase and units B to E are interpreted as rift transition phase (Figure 2.5).

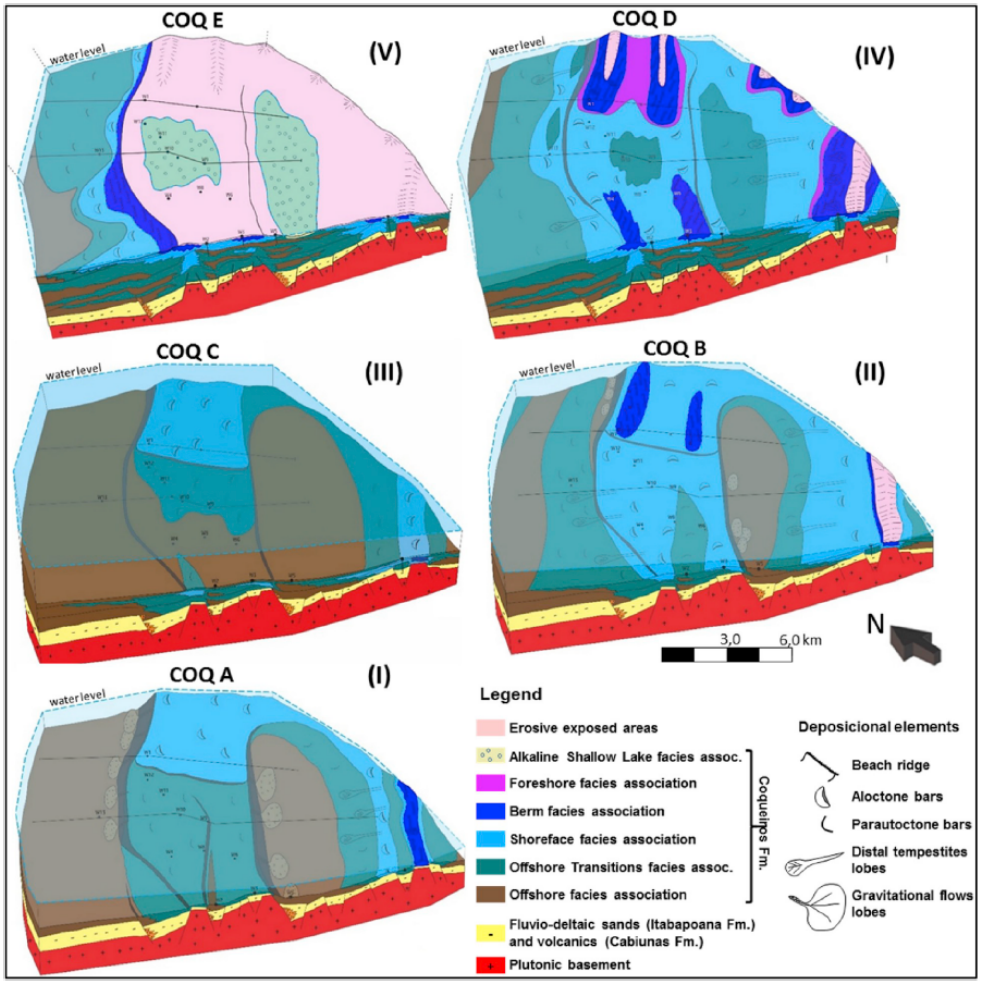


Figure 2.5: Block diagrams showing the predominant facies associations for each seismic-stratigraphic unit, main depositional elements, as well as the paleo-environmental evolution of the Coqueiros Formation (from Olivito & Souza, 2020).

The Macabu Formation was initially described as shallow-marine carbonate facies consisting of nodular diagenetic and laminated stromatolites (Dias et al., 1988). Later, Muniz and Bosence (2015) interpreted the absence of both marine biota and normal freshwater biota and the presence of non-marine ostracods, as evidence of a blackish-water-lacustrine environment. These deposits were reinterpreted as chemical precipitates controlled by the geochemistry of lacustrine lakers (Tosca & Wright, 2015; Wright & Tosca, 2016; Pietzsch et al., 2020). Herlinger Jr. et al. (2017) summarised the Macabu Formation in the North Campos Basin as containing intervals of precipitated fascicular

calcite and spherulitic calcite and spherulitic aggregates interspersed with intraclastic deposits that have been reworked from these precipitates and laminated strata made of syngenetic magnesian (Mg-rich) clay minerals and siliciclastic mud. Although a hybrid biotic/abiotic precipitation probably occurred in the Macabu Formation (Pietzsch et al., 2018), the abiotic chemical precipitation is the dominant control in the precipitation of the majority of its constituents (Lima & De Ros, 2019; Lima et al., 2020).

The upper portion of the post-rift supersequence corresponds to the Retiro Formation, a thick accumulation of evaporites consisting of anhydrite, halite, sylvite, and carnallite (Winter et al., 2007). The evaporites provide a stratigraphic seal for the large hydrocarbon accumulations of the presalt petroleum province in both the Campos and Santos basins (Alves et al., 2017) (Figure 2.4).

Above the evaporites, shallow marine carbonates of the Quissamã Formation were deposited, followed by the marls of the Outeiro Formation (Figure 2.4). The load induced by these units promoted widespread detached thin-skinned salt tectonics with extensional-proximal and compressional-distal domains that was active since the Albian. The related structures are characterised by listric-rollover systems, turtle-back structures, raft tectonics, down building diapirs, salt walls, and compressional salt tongues (Cobbold & Szatmari, 1991; Davison, 2007) (Figure 2.2). In addition, salt tectonics led to raft tectonics of these shallow-water carbonates thus forming seafloor depressions that control turbid currents, which deposited the post-salt turbiditic reservoirs from Maastrichtian to Miocene (Cobbold & Szatmari, 1991; Bruhn & Walker, 1995).

2.4 Diagenetic Evolution of the Pre-Salt Reservoirs of the Campos Basin

Extensive studies of the Coqueiros and Macabu Formations and their correlatives Barra Velha and Itapema Formations in the Santos Basin focused on their petrographic and diagenetic features, and isotopic constitution (Herlinger Jr. et al., 2017; Pietzsch et al., 2018; Lima & De Ros, 2019; Gomes et al., 2020; Lima et al., 2020; Pietzsch et al., 2020). Although covering a significant large paleo-depression with internal highs, these units show a relatively uniform tectono-sedimentary and paleo hydrological pattern. While deep and often isolated lakes characterize the rift-phase, the post-rift ("sag") phase is characterised by an extensive shallow, endorheic lake (Pietzsch et al., 2018). The long, persisting nature of this shallow lake also has correlation with the dynamics of the heat-flow related to the Tristan-Gough plume during the Early Cretaceous. It is interpreted that variations in the thickness of the continental lithosphere and/or lithospheric stretching rates, variations that promote lateral sub-lithospheric flow of plume material below only one arm of the extending rift, that is, the Santos-Campos arm (Morgan et al., 2020).

In the northern of the Campos Basin, recent publications performed petrographic and geochemical studies on the rift and post-rift reservoirs, aiming to characterise the diagenetic evolution and its controls on reservoir quality (Herlinger Jr. et al., 2017; Lima & De Ros, 2019; Lima et al., 2020). Herlinger Jr. et al. (2017) observed that the compositional and porosity evolution of the syn-rift bioclastic rudstone and grainstone reservoirs are controlled by the balance between dissolution and neomorphism of the aragonitic bivalves and gastropods. They also concluded that dolomitisation is an essential process of porosity modification of both rift and sag deposits, showing great diversity of

origins and fabrics. Early dolomitisation relates to the dissolution and replacement of Mg-clays. However, dolomitisation coeval with late fracturing and silicification has locally developed reservoirs with high porosity and permeability.

Many authors have pointed out compelling evidence of hydrothermal activity associated with magmatic events in the Campos Basin (Alvarenga et al., 2016; Lepley et al., 2017; Vieira de Luca et al., 2017), and Santos Basin (Fetter et al., 2018; Souza et al., 2018; Pietzsch et al., 2020). Similar evidence was observed in the Kwanza and Namibe Basins on the African side (Poros et al., 2017; Teboul et al., 2019; Rochelle-Bates et al., 2021). Such evidence comes from the petrography of wellbore and outcrop data, detailed well-tied seismic interpretation, isotope geology and geochronology. Alvarenga et al. (2016) used 2D seismic and well data to tie rift-age volcanic and intrusive rocks to hydrothermal vents and ducts in the central and southern Campos Basin. The ages of episodic magmatism and the resulting hydrothermal diagenesis and forced hydrocarbon maturation were investigated in outcrops of the Namibe Basin in Angola. U-Pb geochronology in dolomites also revealed a previously unknown Paleocene/Eocene (56.8 ± 4.8 Ma) fluid-flow event in the basin (Rochelle-Bates et al., 2021). More recently, U-Pb geochronology in the latest hydrothermal dolomites of the Santos Basin revealed similar ages (59.2 ± 5.3 Ma) (Rochelle-Bates et al., 2022).

Lima and De Ros (2019) summarised the diagenetic and hydrothermal processes in the rift and post-rift reservoirs in the northern Campos Basin, which have undergone a complex and heterogeneous diagenetic evolution (Figures 2.6 & 2.7). Despite the detailed description, Figure 2.7 does not provide a correlation between the intensity of diagenesis with either stratigraphic unit or tectonic structure. Deep-burial alteration (> 2 km) is commonly associated with hydrothermal fluids carried through faults and fracture systems.

Many samples demonstrate dissolution, recrystallization, dolomitisation and/or silicification, ranging from incipient to pervasive, locally resulting in the formation of dolostones and cherts. Typically, the dolomite selectively replaced the interstitial Mg-clay sediments, whereas the calcite spherulitic and fascicular aggregates were only marginally dolomitized. Silicification commonly occurred after dolomitisation. Saddle dolomite, calcite, quartz, chalcedony, svanbergite, Sr-barite, celestine, pyrite, chalcopyrite, galena, sphalerite, zeolite, and bitumen were precipitated by the episodic flows of hydrothermal fluids, replacing pre-existing constituents and filling fractures, and previously created secondary porosity.

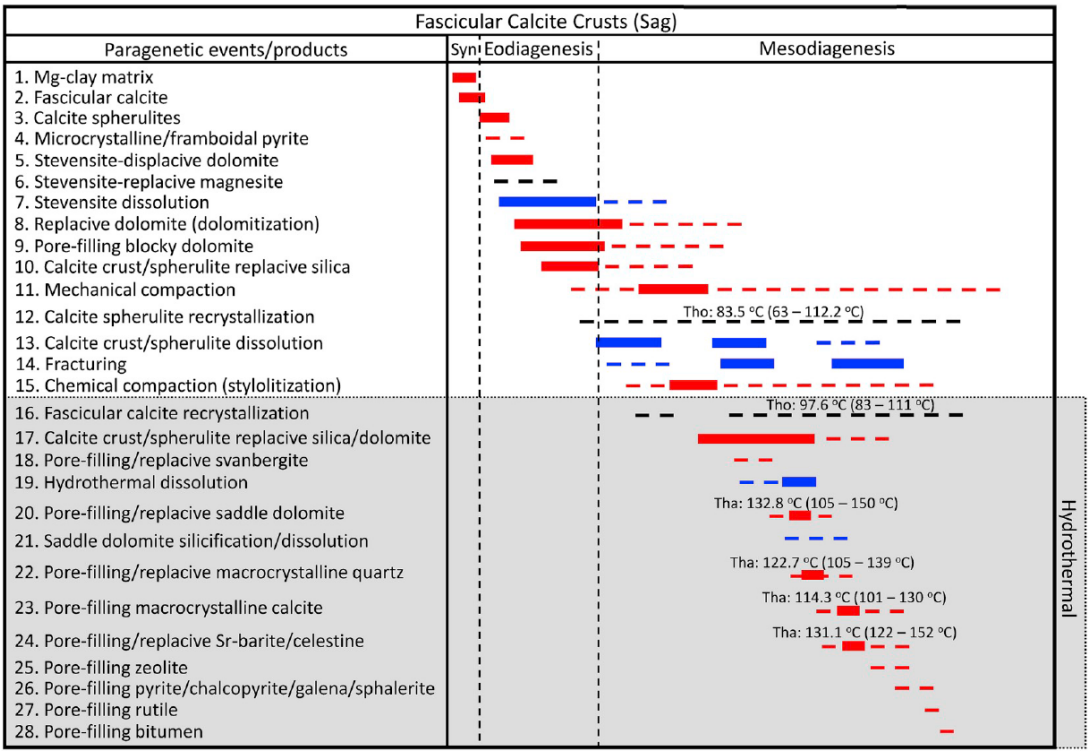


Figure 2.6: Paragenetic sequences interpreted for the sag fascicular calcite crusts from northern Campos Basin, Brazil (from Lima et al., 2020). The paragenetic sequence is divided into syngenetic (Syn), eodiagenetic, mesodiagenetic and hydrothermal phases. The thickness of the lines corresponds to the intensity or abundance of the processes and products. The red lines represent porosity loss and the blue lines porosity increase. Tha and Tho are the mean homogenization temperatures of primary aqueous and oil fluid inclusions, respectively (minimum and maximum limits in brackets).

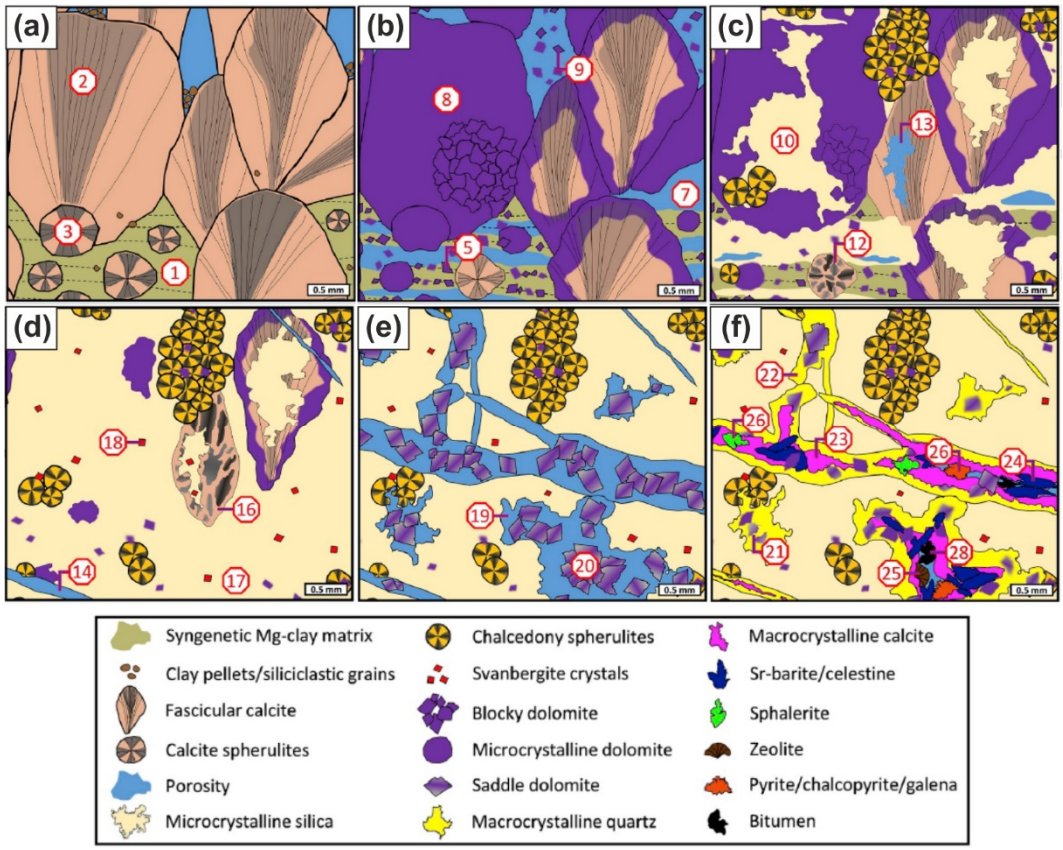


Figure 2.7: Schematic representation of the main syngenetic, diagenetic and hydrothermal processes of formation and alteration of the studied Aptian Presalt deposits, Campos Basin, offshore Brazil (modified from Lima et al., 2020). (A) Syngenetic crust of coalesced fascicular calcite aggregates covering syngenetic Mg-clay matrix partially replaced and displaced by calcite spherulites. B) Microcrystalline and blocky dolomite partially replacing the Mg-clay matrix, calcite spherulites, and fascicular aggregates. Dolomite rhombohedra partially filling inter-aggregate pores. Dissolution of the syngenetic Mg-clay matrix and part of the dolomitized calcite aggregates. C) Microcrystalline quartz and chalcedony spherulites partially to fully replacing preexisting constituents, and filling primary and secondary porosity. D) Silicification of some dolomitized fascicular and spherulitic aggregates. Svanbergite as pseudocubic crystals disseminated in microcrystalline silica or within chalcedony spherulites. Recrystallization of fascicular calcite and initiation of fracturing process. E) Intense silicification, fracturing and dissolution. Saddle dolomite partially filling fracture and vugular pores. F) Macrocrystalline calcite, radiated Sr-barite and celestine, fibro-radiated zeolite, euhedral to subhedral pyrite, chalcopyrite, galena and sphalerite, and massive bitumen filling the secondary pores. The numbering is in accordance with the paragenetic sequence in Figure 2.6.

Eodiagenetic precipitation and dissolution owing to variations in the lake water chemistry followed by episodic flow of hydrothermal fluids under burial conditions controlled the creation, redistribution, and obliteration of porosity in the presalt reservoirs during mesodiagenesis (Figure 2.7) (Lima & De Ros, 2019). Minor hydrothermal alteration occurs

in the sag laminites and the in rift stevensitic ooidal arenites, possibly due to their limited primary porosity. More recently, the hydrothermal diagenesis was further characterised using fluid inclusions, Sr, C and O isotopes and described as have some analogy to carbonate-hosted Pb-Zn Mississippi Valley (MVT) and Irish-type deposits (Figure 2.6). It is interpreted as having occurred between Late Cretaceous and Paleogene and was related to basin-scale magmatic events (Lima et al., 2020). Despite the sophisticated diagenetic history, these authors only proposed a schematic 2D distribution of the diagenesis with respect to stratigraphic units and structures. Therefore, a more refined thus 3D spatial correlation between layers, faults and the distribution of the diagenetic products in terms of mineralogy and intensity is yet to be stablished.

2.5 Campos Basin: Structure and Tectonic Evolution

From the end of the Búzios Orogeny in the Cambrian, a relative tectonically quiescent span of more than 300 Ma followed while the Western Gondwana supercontinent remained intact. The Palaeozoic geological record of South America is characterised by extensive intracratonic sedimentation, exemplified by the Paraná Basin, which also records tectonic disturbances as the consequence of intraplate stress propagation from the Gondwanides in the southern continental fringes of the Gondwana (Milani & De Wit, 2008).

Little information is available for this period in the region represented by the present-day Campos Basin. Leading in to the Early Cretaceous, dyke emplacement and the massive 137-127 Ma Paraná-Ethendeka large igneous province (LIP) occurred in the regions on which the Campos and Santos basins formed (Almeida et al., 2021 and references therein). In the Campos Basin, the Cabiúnas Formation represents this episode and has a close geochemical signature with the Paraná LIP (Mizusaki et al., 1992). Contemporaneously,

the onset of rifting that preceded the Atlantic Ocean was recorded in NE Brazil (e.g. RTJ rift) and Argentina (e.g. Colorado Basin) (Lovecchio et al., 2018; Matos et al., 2021) (Figure 2.1). Initial rifting of the Brazilian continental margin was characterised by both normal and oblique extension leading to a distinctive structural architecture (Cobbold et al., 2001; Moulin et al., 2010).

The South Atlantic Ocean can be divided into four segments: Equatorial, Central, South and Falklands (Torsvik et al., 2009; Moulin et al., 2010) (Figure 2.1). The Campos Basin is located in the Central Segment that lies between Ascension Fracture Zone on the north and by the Rio Grande Fracture Zone to the south. Rifting was diachronous along the East Brazilian margin, as the consequence of Precambrian inheritance and hot spot activity (Morgan et al., 2020; Matos et al., 2021). The width of the stretched, thinned and ultimately hyperextended continental crust, as well as the width of the early oceanic crust between the two continents, increase southward in the Central Segment (Szatmari & Milani, 2016). The rotation of the South American plate during 136-120 Ma has restrained the rifting in the NE Brazil while the oceanic crust was already formed in the Austral segment (Matos, 2021; Matos et al., 2021). Meanwhile, the Santos Basin worked as a kinematic buffer between the Central and Austral segments, accommodating the strain related to an oblique extension in several minor structures thus delaying the linkage of these segments. Consequently, an extensive region of hyperextended continental crust was formed under the Santos Basin. The presence of a thermal anomaly related to the Tristan da Cunha plume worked to decrease the brittleness of the crust and thus explain the hyperextension through the boudinage of the lower crust observed in this stretch of the proto-South Atlantic (Moulin et al., 2010; Morgan et al., 2020) (Figure 2.8).

The Campos Basin has two main structural elements: faults and related structures developed during Early Cretaceous rifting, and the structures related to salt tectonics as a result of sedimentary loading on top of the Aptian evaporites and thermal subsidence. The presalt tectono-sedimentary stages consist of two major phases (rift and post-rift) that are observed in the Campos Basin and elsewhere in the East Brazilian Rift System (EBRIS) (Chang et al., 1992) and in the recently renamed South Atlantic Cretaceous Rift System (SACRS) (Matos et al., 2021). They are characterised by (1) initially localised then strong widespread mechanical subsidence during the Barremian, and (2) thermal subsidence during Aptian-Albian time along with reactivation of some rift faults, immediately following the end of rifting. However, rift evolution is widely understood to be diachronous (Lavier & Manatschal, 2006, Araujo et al., 2022). As a consequence, sedimentary units deposited in a sag-like basin during the post-rift stage in the proximal context of the basin will have their correlative units deposited whilst rifting still persists in a more axial position (Figures 2.2 & 2.8) (Morgan et al., 2020).

In the Campos Basin, major rift tectonics (syn-rift) led to the formation of fault blocks bounded by alternating eastern and western-dipping NNE normal faults, which are laterally continuous for up to 200km and have throws of as much as 2500 m (Guardado et al., 1989). In the study area, the rift framework comprises NNE to NE-striking faults with dips that alternate in polarity in the deep-water domain and have a predominantly westward dip in shallow-water domain (Guardado et al., 1989; Alvarenga et al., 2021).

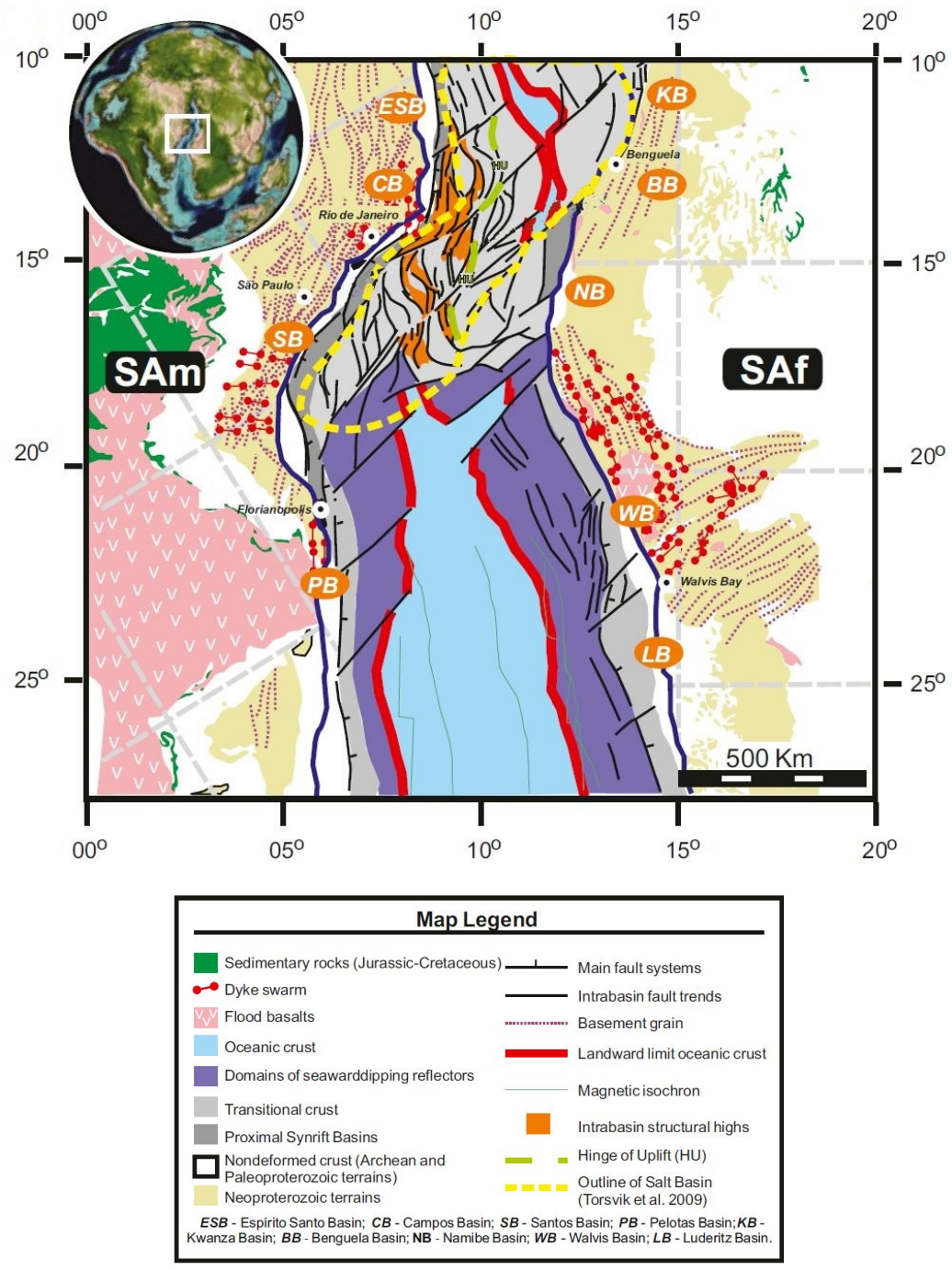


Figure 2.8: Africa (SAf) and South America (SAm) shown in a South Atlantic plate reconstruction for 117 Ma (Heine et al., 2013), with SAf fixed in present-day coordinates (from Morgan et al., 2020). Note the contrast of intrabasin architecture from north to south, with northern compartments defined by sigmoidal intrabasin fault trends that separate structural lows from structural highs. This region coincides with the area occupied by the Aptian Salt basins of Central South Atlantic. Southward around ~17°S, a succession of intrabasin highs and lows terminates abruptly against SDRs. This coincides with the boundary of the region with evidence of long-lived plume influence during rifting. The legend defines map symbols used. Additional data from Torsvik et al. (2009).

The pre-rift basement configuration of the continental crust, along with the Mesozoic magmatism, resulted in different crustal responses to extension, which vary from north to south. It is controlled by a crustal inheritance equivalent to onshore basement terranes (Stanton et al., 2019). In terms of analogues, several authors have shown the control of a layered crust created by low angle thrusts of Caledonian orogeny on the architecture of the North Sea Rift, where these structures were reactivated as rift faults or ramps (Phillips et al., 2016; Fazlikhani et al., 2017). Along the Campos Rifted Margin, the less heterogeneous basement of the northern Campos Basin can be correlated with the post-collisional Cambro-Ordovician magmatic province of the Araçuaí Belt that partially deformed the earlier orogenic structures. The lack of crustal structures localised the strain generating the observed narrow necking zone. Therefore, the Northern Campos basin is characterised by an abrupt crustal architecture, with a narrow and steep crustal necking zone. On the other hand, the highly-extended domain towards offshore is wide and devoid of magmatism and ends at an outer high with a volcanic crustal-oceanic boundary in the Central and South Campos Basin (Stanton et al., 2019).

More recently, Strugale et al. (2021) interpreted the basement of the North of the Campos Basin as being constituted of two geological units, the Cabo Frio Tectonic Domain (CFTD) in the East and the Oriental Terrane of the Ribeira Belt in the West. The NE-SW tectonic limit between these is interpreted to be close to the studied area (Figure 2.2). Although the Oriental Terrane is less homogenous than the Araçuaí Belt, it is still less heterogeneous compared with the supracrustals of the CFTD thus coherent with the interpretation of Stanton et al. (2019). In addition, recent dynamic modelling of the hot material related to the Tristan da Cunha plume suggests that such inherited crustal heterogeneity could have favoured a long residence time of plume material (Morgan et al., 2020). In this case,

heterogeneous thickness in the present-day upper crust points to an early episode of magma emplacement under the present-day shallow water domain of the Campos Basin. With the strain propagation towards the spreading centre, plume material moves towards the offshore while post-rift deposition takes place in the near onshore realm.

Another key element of the central segment of the South Atlantic is the presence of an approximately 1-2 kilometre-thick salt layer (Ponte & Asmus, 1978, Davison, 2007). It is related to the feature associated with the Rio Grande – Walvis Ridge System, a physical barrier which confined the deposition of the thick Aptian evaporite layers to the north (Gamboa & Rabinowitz, 1981; Chang et al., 1992; Szatmari et al., 2021) (Figure 2.1). Offshore rift-related magmatism occurred until the Albian and intraplate magmatic events were observed in the Campos Basin and counterpart onshore basement until the Eocene (Winter et al., 2007; Morgan et al., 2020; Almeida et al., 2021).

2.6 NW-SE Transverse Zones of Brittle Deformation

Post-rift tectonic events have been described in the counterpart onshore basement of the Campos Basin (Chang et al., 1992; Almeida et al., 2013; Lourenço et al., 2016; Santiago et al., 2020). Episodes of brittle reactivations have been described in three main NW-SE to NNW-SSE Lineaments: the Vitória-Colatina, Alegre, Itaoca and Piúma Fracture Zones. The two latter were grouped as the Castelo dyke swarm in Almeida et al. (2013) (Figures 2.3).

The Vitoria-Colatina Lineament was defined as a shear zone of NNW-SSE direction constituted of a swarm of cataclastic fractures projecting into Campos Basin (Chang et al., 1992). It is considered as a long-lived Proterozoic structure and has an important control on the structural highs that controls many of the sub and post-salt oilfields in the basin

(Fetter, 2009). It hosts a dike swarm with ages ranging from 174 Ma (K-Ar) (Almeida et al., 2013) to 133.5 ± 0.4 Ma ($^{39}Ar/^{40}Ar$) (Szatmari & Milani, 2016). The influence of the Vitória-Colatina lineament in the study area is limited compared with the NE rift-related trend, being restricted to controlling depocenter distribution and tips of rift faults as accommodation zones (see Chapter 4).

The Alegre Fault Zone is a set of NNW-SSE oriented fractures formed by extensional tectonics in the Early Cambrian, which were reactivated as normal faults during Cenozoic, probably in the Neogene and Quaternary (Figure 2.3). Basic dikes were found in some related fractures, mostly with NNW-SSE strike. Offshore, the NNW-SSE fault system associated with the Alegre Lineament acted in delimiting the southern limit of the Corvina-Parati Low during the rift phase of the Campos Basin (Calegari et al., 2016). Most of onshore data points to a normal fault regime with minor tension axis at NW-SE direction, compatible with the dextral strike-slip tensor that is thought to have acted during the Pleistocene in SE Brazil (Riccomini, 1989).

The Piúma Lineament is a brittle shear zone characterised by N50W-trending and SW-dipping shear fractures, faults and joints. It records two distinct and kinematically incompatible motions, thereby considering the operation of two tectonic regimes: NNE-SSW extension and E-W transtension. However, these structures were not recognised in 2D seismic lines in the offshore counterpart (Lourenço et al., 2016). Recently, Santiago et al. (2020) recognised two distinct groups of mafic dykes emplaced in the Castelo and the Alegre lineaments. Their interpretation is based on U-Pb geochronology in zircons which yielded ages of 504±6.9 Ma (Cambrian) for alkaline dikes and 141.9±1.9 Ma (Berriasian) for the tholeiitic suite.

Chapter 3

Basement Geology and its Controls on the Nucleation and Growth of Rift Faults in the Northern Campos Basin, Offshore Brazil.

This chapter was published in the 3rd issue of the 33rd volume of Basin Research Journal and was available online on the 14th of February 2021. However, minor modifications were made to follow examiners suggestions, including the Appendix A. The research presented in this chapter is my own work, however, it benefited from collaboration of Renata da Silva Schmitt, who supported the interpretation of metamorphic rocks, geochronological data and proof reading, and Joe Cartwright, who supported with the research strategy, validation, and proof reading.

Strugale, M., Schmitt, R.S. & Cartwright, J. (2021). Basement geology and its controls on the nucleation and growth of rift faults in the northern Campos Basin, offshore Brazil. *Basin Research*. https://doi.org/10.1111/bre.12540.

3.1 Abstract

The rift phase of the Campos Basin developed during the Early Cretaceous on a heterogeneous crust comprising structures inherited from the Brasiliano-Pan African tectonic events, mostly generated during the Neoproterozoic-Cambrian amalgamation of western Gondwana blocks. The main rifting episode took place from the Hauterivian to the Barremian, then was succeeded by the transition and post-rift phases during the Aptian. Rift faults developed as a result of a progressive rotation of extension from E-W to NW-SE. The role of pre-existing intra-basement structures on the style and evolution of the rift faults was investigated using 3D high-resolution seismic data, borehole logs and sidewall samples. Three seismic facies (SF1, SF2, & SF3) and three types of intra-basement structures (Surfaces, Geobodies, and Internal Reflections) were identified and mapped. They represent, respectively, contrasting levels of seismic anisotropy, interpreted as metamorphic foliation, and ductile shear zones that bound rock units with particular seismic facies signatures. Sidewall cores show that banded biotite-gneiss is the predominant rock type in the eastern half of the study area, while more homogeneous granitoid is the dominant lithology on the west. Such a binary division of lithotypes is consistent with the distribution of mapped intra-basement seismic facies and features. The contrasting basement heterogeneity across the study area is the major control in the strain distribution during rifting. Where the basement is highly heterogeneous, the pre-existing fabric was selectively reactivated whenever its orientation was favourable, resulting in faults forming progressively as the extension direction rotates, whilst shallower low to very low angle basement fabric were cross-cut by rift faults. Where the basement is homogeneous, only early formed faults remain active throughout the rifting.

3.2 Introduction

The influence of basement fabric on the structural styles of rift basins based on surface geology and remote sensing has been widely reported in the literature (e.g. Milani & Davison, 1988; Daly et al., 1989). Following the advancement in seismic acquisition and processing in the last 20 years, some authors have used 2D and 3D seismic data to interpret basement heterogeneities, both onshore and offshore. Identifying and mapping basement heterogeneities underneath rift basins using 2D seismic (Withjack et al., 1998; Morley et al., 2004; Bird et al., 2014; Phillips et al., 2016; Fazlikhani et al., 2017) and more recently 3D seismic data (Reeve et al., 2014; Collanega et al., 2019; Lenhart et al., 2019; Osagiede et al., 2020) has revealed close relationships between inherited basement structural anisotropy and the structural style of rifting, agreeing with observations made onshore. However, the geometry and composition of the crystalline basement are still largely neglected or simply considered homogeneous in analogue, numeric and tectonostratigraphic models of rift development (Lenhart et al., 2019).

Studies of the Eo-Cretaceous Pre-Salt reservoirs of Campos Basin have thus far been focused on petrography, diagenetic history and depositional environments of reservoir rocks (Dias et al., 1988; Muniz & Bosence, 2015; Herlinger Jr. et al., 2017; Mizuno et al., 2018; Lima & De Ros, 2019; Lima et al., 2020; Olivito & Souza, 2020). However, only regional scale research into the Precambrian basement and rift structural geology of the basin has been undertaken (Guardado et al., 1989; Chang et al., 1992; Fetter, 2009; Stanton et al., 2019), along with that the basement rocks of Campos Basin have been considered mostly homogeneous in both regional (e.g. Guardado et al., 1989) and local studies (e.g. Lima et al., 2020). Also, the structures that evolved during the rift initiation and

climax are still poorly understood at reservoir scale in the north of the Campos Basin. Finally, correlation of Precambrian units between South America and Africa in the position of the Campos Basin still leads to many open questions, due to the lack of physical continuity and contrasting tectonic and lithological contents between them. In addition, a significant part of the continental crust is submerged under the shelves of South America and Africa (Heilbron et al., 2008; Schmitt et al., 2008; 2016).

We interpreted a 3D high-resolution seismic survey and wellbore data (logs and sidewall cores) to examine the lithological content, structural framework and U-Pb age of the basement. From this data, we explored the relationships between basement heterogeneity and the nucleation, growth, and structural style of the rift faults. Although intra-basement reflectivity has been observed on many deep seismic profiles and from many crustal settings (e.g. Withjack et al., 1998; Stanton et al., 2019), there are few studies that attempt to interpret these reflections systematically (e.g. Phillips et al., 2016; Fazlikhani et al., 2017). In this paper, we map variations in basement structure based on detailed interpretation of seismic facies and discrete intra-basement reflections calibrated for lithotype in wellbore data. From this, basement geology and the character of the interactions between extensional tectonics and pre-existing basement heterogeneities are analysed. In addition, novel data regarding basement composition, structure and age were correlated with the known tectonic units of the basement onshore, thus contributing to enhance the scientific debate on pre-breakup reconstructions of the Western Gondwana and the evolution of the Brazilian continental margin.

3.3 Geological Setting

The study area is located in the northern part of the Campos Basin, 70 km offshore East Brazil (Figure 3.1a). The Campos Basin is part of the Central Segment of the South Atlantic Ocean (Torsvik et al., 2009; Moulin et al., 2010). Its stratigraphy includes Early Cretaceous to recent sediments (Figure 3.2a). The geometry of the internal structural highs and lows of the basin is controlled by the offshore projection of NE-SW & NNW-SSE basement structures (Fetter, 2009). Onshore, the NE-SW trend corresponds to predominantly Neoproterozoic metamorphic and magmatic rocks of the Mantiqueira Province (Almeida et al., 1981). The NNW-SSE trend consists of networks of brittle structures, whose origin and constitution are not yet established (Calegari et al., 2016).

3.3.1 Basement

The study area is located in the offshore extension of the Ribeira/Araçuaí Belts and the Cabo Frio Tectonic Domain (Figure 3.1a - Heilbron et al., 2008; Schmitt et al., 2008; Egydio-Silva et al., 2018). According to Brito Neves et al. (1999) and Schmitt et al. (2018), these belts correspond to high-grade metamorphic and magmatic rocks that resulted from a succession of accretionary and collisional episodes, attributed to the Brasiliano-Pan African tectonic events that were a consequence of Neoproterozoic-Cambrian amalgamation of western Gondwana blocks (the São Francisco and Congo/Angola cratons). Although Araçuaí (Figure 3.1b) and Ribeira (Figure 3.1c) have differences in tectonic fabric (N-S & NE-SW oriented respectively) and strain regimes, they both evolved during the same tectonic events (ca. 0.65-0.5 Ga), and can be considered as two segments of the same orogenic belt (Stanton et al., 2019 and references therein).

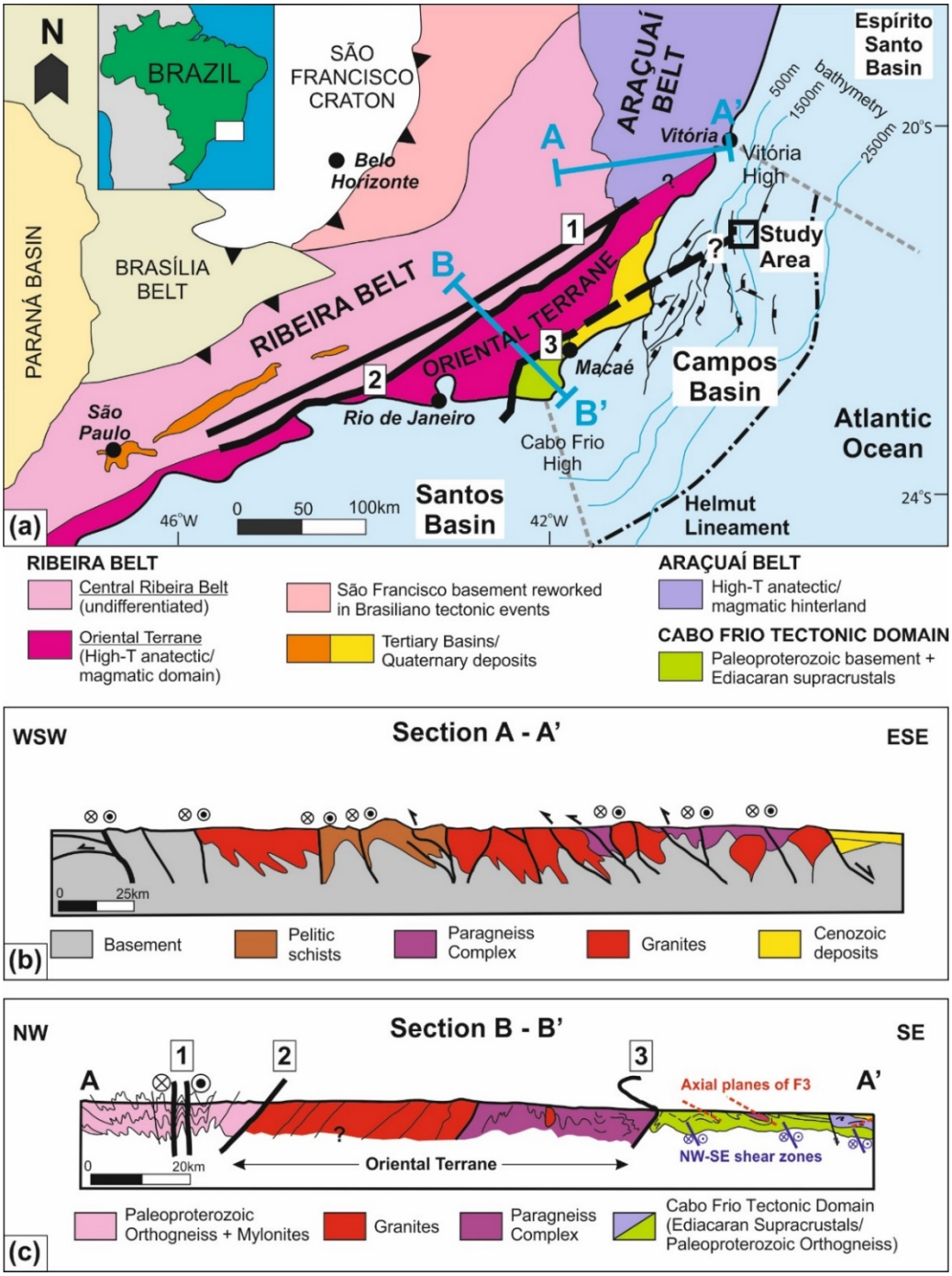


Figure 3.1: (a) Onshore and offshore geological setting of the Campos Basin. Offshore geology modified from Fetter (2009) and Silva et al. (2004); Helmut Lineament according to Dehler et al. (2016). Onshore geology modified from Egydio-Silva et al. (2018) and Schmitt et al. (2016). (b) geologic section A–A' represents the southern part of Araçuaí Belt (adapted from Alkmim et al., 2006). (c) geologic section of the northern sector of Ribeira Belt and the Cabo Frio Tectonic Domain (adapted from Heilbron et al., 2008 and Schmitt et al., 2016). NE-SW Structures: (1) Além Paraíba Shear Zone; (2) Central Tectonic Boundary; (3) Cabo Frio Tectonic Limit (CFTL).

The Oriental Terrane (eastern Ribeira Belt) and the Cabo Frio Tectonic Domain (CFTD) can be extrapolated offshore to the study area, following the trends of their tectonic boundaries (Figure 3.1a – Schmitt et al., 2016; Egydio-Silva et al., 2018). The former is constituted by low P-high T Neoproterozoic para- and ortho-derived gneisses intruded by several magmatic bodies, with NE-SW fabrics that include foliation, folds, and other ductile structures generated during a protracted evolution from ca. 650-500 Ma under a right-lateral transpressional regime (Ebert & Hasui, 1998; Heilbron et al., 2008; Schmitt et al., 2016). Its northwest boundary with the Central Ribeira Belt is defined as a major NE-SW shear zone, the Central Tectonic Boundary (Almeida et al., 1998), parallel to the Além Paraíba Shear Zone (Figure 3.1a & c - Heilbron et al., 2008).

Towards the coast, the Oriental Terrane is in contact with the contrasting Cabo Frio Tectonic Domain (CFTD). This CFTD mainly comprises Paleoproterozoic orthogneisses (2.0 to 1.94 Ga) tectonically interleaved with medium to high P - high T Neoproterozoic para-derived gneisses, both migmatized, denominated Búzios and Palmital successions (Figure 3.1c - Schmitt et al., 2004; 2008; 2016). The metamorphism and coeval ductile structures were developed between 550 & 490 Ma as a result of a plate collisional event referred to as the Búzios Orogeny (Schmitt et al., 2004), confirming a tectonic rejuvenation towards the offshore. The CFTD has a NW-SE to N-S structural grain, orthogonal to the adjacent Oriental Terrane (Schmitt et al., 2004; 2016). Their contact is interpreted as a ductile shear zone folded by F_3/F_4 (CFTL in Figure 3.1a & c). The Neoproterozoic paragneiss preserves S_{1+2} in isoclinal intrafolial structures, refolded by recumbent F_3 folds with a subhorizontal axial plane spaced cleavage. The Paleoproterozoic orthogneiss develops only localized high strain sub-vertical NW-SE zones (Schmitt et al., 2004; 2016). The contrasting rheology of the basement (Paleoproterozoic orthogneisses) and the

supracrustals (Neoproterozoic paragneiss) generates a complex geometry summarized as top to E-SE Km-scale fold nappes in the latter and sub-vertical high strain zones in the former (Figure 3.1c - Schmitt et al., 2008).

The offshore extension of the CFTD along with its geometric/tectonic connections with the Ribeira Belt and their African equivalents are still unclear since a significant part occurs within the submerged continental margins. Egydio-Silva et al. (2018) and Cavalcante et al. (2019) suggest that the CFTD extends northwards to a position of 21°S on the Brazilian margin where it lies beneath the Campos Basin, and reaches as far as the southern part of the West Congo Belt, sharing similar tectonic-metamorphic evolution as ca. 550-500 Ma (Monié et al., 2012; Schmitt et al., 2016). Offshore drilling in the Cabo Frio High (Figure 3.1a) recovered calc-alkaline orthogneiss samples, with igneous zircon cores of 1.98 to 1.96 Ga, & 0.5 Ga thin metamorphic rims compatible with the Paleoproterozoic orthogneiss of the CFTD (Carmo et al., 2017). These ages are also coincident with the basement of the Angola Block in the actual African continental counterpart (Schmitt et al., 2016).

Evidence of basement-related shear zones being reactivated during South Atlantic rifting is documented in the onshore and offshore portions of Campos Basin (Chang et al., 1992; Fetter, 2009; Dehler et al., 2016; Savastano et al., 2017). Stanton et al. (2010) studied magnetic features across the onshore and offshore and showed that syn-rift faults and dikes are parallel to the NE-SW Ribeira Belt shear zones, but are orthogonal to the CFTD structural grain. Later, Stanton et al. (2019) concluded that the presence of heterogeneous (layered) crust of the CFTD or a more homogeneous crust of the Ribeira/Araçuaí belts determined the temporal and spatial distribution of the deformation, and as a consequence, the necking geometry, subsidence and sedimentary evolution of the margin.

3.3.2 Campos Basin

The stratigraphic record of the Campos Basin is divided into three tectonostratigraphic mega-sequences: Non Marine Rift, Transitional Post-Rift, and Marine Drift (Cainelli & Mohriak, 1999; Winter et al., 2007). The presalt sedimentary units here studied belong to the Non-Marine Rift unit and are constituted by four seismic depositional sequences that approximately corresponds to the tectonic stages of the rifting, as defined by Prosser (1993): rift initiation, rift climax, transition and post-rift. These sequences are bounded by regional unconformities named Salt Base Unconformity (SBU), Post-Rift Unconformity (PRU), Top Rift (tRift), Top Basement (tBas), and the Top Itabapoana/Atafona Formations (tI/A) seismic horizon, whose seismic expressions were mapped throughout the studied area (Figure 3.2b).

The rift initiation stage (Hauterivian) is marked by tholeiitic volcanic activity, represented by the Cabiúnas Formation (Mizusaki et al., 1992). The rift climax stage (Early Barremian) is related to the development of an extensive system of half-grabens in which a series of interconnected lake basins persisted, becoming periodically isolated during times of reduced lake-level developing local and regional unconformities (Winter et al., 2007). Sediments deposited during this stage are proximal siliciclastics to continental mudstones of Itabapoana and Atafona formations (Bertani & Carozzi, 1985a; b; Thompson et al., 2015; Mizuno et al., 2018). They are succeeded by bioclastic rudstones and grainstones of the Coqueiros Formation, which was initially part of the rift transition stage (Winter et al., 2007; Mizuno et al., 2018). Later, Olivito and Souza (2020) assigned the basal carbonate section of the Coqueiros Formation to the rift climax stage (Figure 3.2b). The rift transition stage (Late Barremian) is represented by the upper section of the Coqueiros Formation that lies directly over the tRift unconformity (Figure 3.2) and is limited on the top by the

regional Post Rift Unconformity (PRU – sensu Muniz & Bosence, 2015). The Macabu Formation (Aptian) comprises argillaceous and carbonate laminites plus spherulitic carbonate deposits and crusts (Wright & Barnett, 2015; Lima & De Ros, 2019), and represents the post rift (SAG) stage (Figure 3.2). The Macabu and Coqueiros formations constitute the main hydrocarbon reservoirs of the presalt sequence, whose petrophysical properties were strongly impacted by structurally controlled hydrothermal alterations (Lima & De Ros, 2019; Lima et al., 2020).

Systematic fault mapping has only been undertaken to date in the shallow water area of the Campos Basin (Figure 3.1a). The main structural features of the top basement are horsts and grabens delimited by steep normal faults that were active during the Early Cretaceous rifting (Chang et al., 1992). Fault blocks are bounded by alternating eastern and western-dipping NNE normal faults, which are laterally continuous for long distances and have throws of as much as 2500 m (Guardado et al., 1989). According to Heine et al. (2013), the main extension direction of rifting changes from NW-SE during rift initiation to WNW-ESE during rift climax (Barremian). The rotation of extension direction was subsequently endorsed by Savastano et al. (2017) in their study of dyke emplacement and brittle reactivation in outcrops of the CFTD basement rocks in the coastline near the southern limit of Campos Basin.

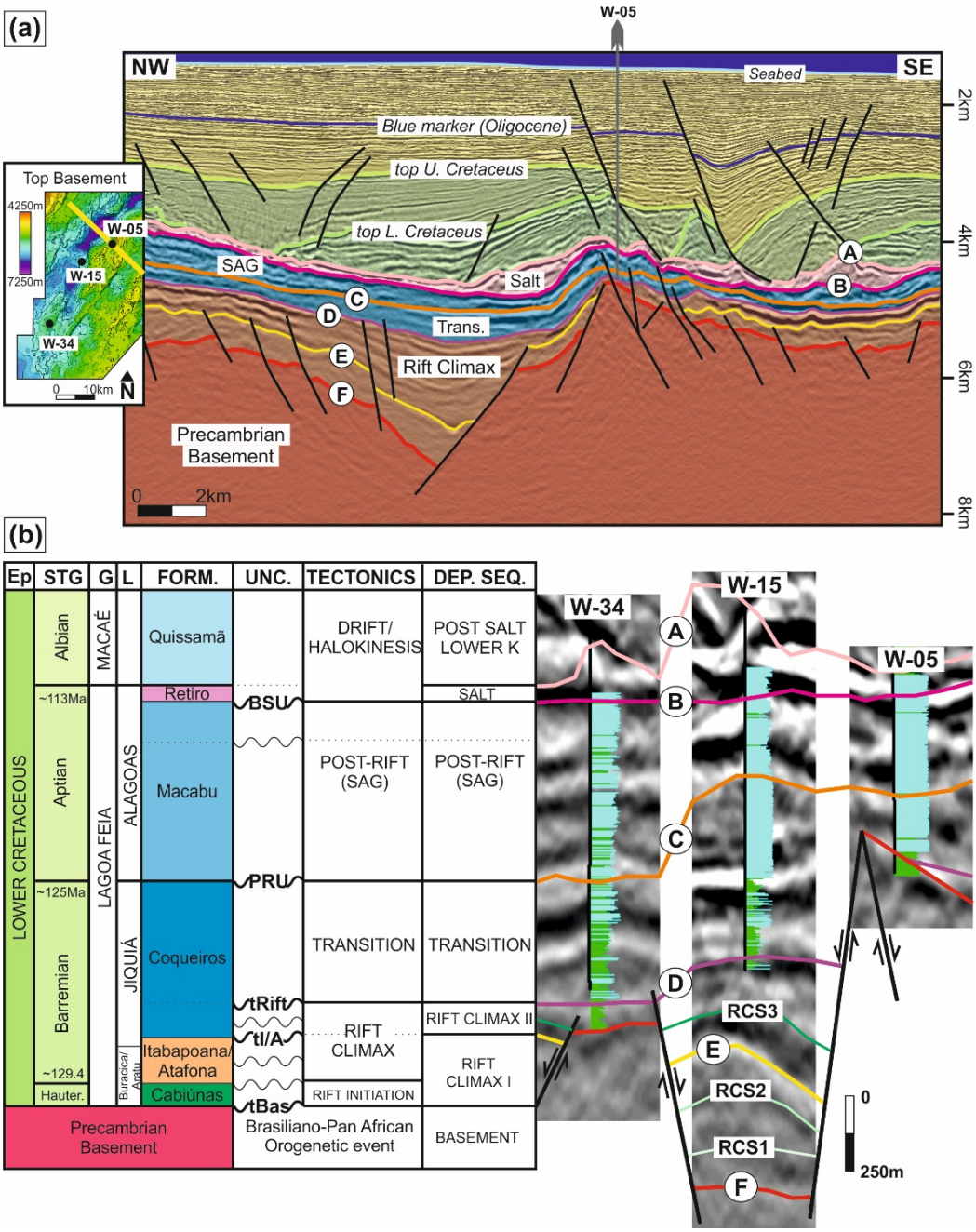


Figure 3.2: (a) NW-SE geologic cross-section of the study area including the main pre- and post-salt structures. Location map shows the position of the cross-section and the wells shown below. (b) stratigraphic and tectonic framework of the Campos Basin in the study area. Lithostratigraphy, ages and tectonics are based on Winter et al. (2007) and Prosser (1993). Wells shows the near-well seismic signature and GR log. Colours coding of the seismic stratigraphic marker horizons and depositional sequences is continued throughout. Mapped seismic horizons: A – tSalt, B – bSalt, C – PRU (Post-Rift Unconformity), D – tRift, E – tI/A (top Itabapoana/Atafona fms.), F – tBas (top basement). Rift Climax Surface (RCS) 1, 2, & 3 are local unconformities within the rift climax sequence. Ep = Epoch, STG = Stage, G = Group, and L = Local stage. GR log scale from zero (blue) to 150 gAPI (green).

3.4 Data and Methods

This work is based on 3D seismic interpretation of a commercial 3D streamer Pre-Stack Depth Migration (PSDM) dataset, which images to 10 km depth. The seismic data covers an area of ca. 1000 km^2 and consists of a merge of two seismic surveys acquired by PGS Geophysical in 2005 and 2010, followed by a depth migration (Kirchhoff TTI) processing sequence. The seismic data are zero-phase processed and the seismic sections are presented with SEG positive standard polarity (downwards increase in acoustic impedance is represented by a positive reflection event (peak) plotted black on a variable density display). Inlines and crosslines of the seismic survey are E-W trending and N-S trending, respectively, spaced at 12.5 m (inlines) and 6.25 m (crosslines). Within the presalt succession, the 3D seismic has a dominant frequency of 15 Hz and an estimated vertical resolution of 90 m, based on a velocity of 5400 m/s. Vertical resolution is obtained following the widely accepted definition of resolution limit that corresponds to Rayleigh's criterion of peak-to-trough separation at $\lambda/4$ (Kallweit & Wood, 1982).

Well logs and geologic markers from 36 hydrocarbon exploration and development wells were used to calibrate the seismic horizons within the sedimentary section. Five wells penetrated basement (Figure 3.3), for which sidewall core samples were described and thin sections extracted. Sidewall core samples from well W-01 were used for geochronological analysis. Zircons were separated from the whole rock by mechanical crushing, milling, heavy-liquid and then magnetic processed. Zircons were collected from less magnetic fractions, then assembled in epoxy-plates and polished to expose the cores, according to procedures suggested by Bühn et al. (2009). These crystals were analysed using an LA-ICP-MS (Laser Ablation Inductively Coupled Plasma Mass Spectrometry) at the

University of Rio Grande do Sul (UFRGS). Data regression analysis was done with Isoplot 3.0 (Ludwig, 2003).

Six main seismic horizons within the players (PRU, tRift, tI/A, & tBas) and the evaporites (tSalt & bSalt) were mapped throughout the 3D seismic survey (Figure 3.2a). Horizon interpretation was firstly made from well markers between seismic-calibrated wells then expanded across the study area, where the truncation of seismic reflections guided the interpretation of the unconformities. Seismic horizons represent the main unconformities within the presalt succession plus the lower and upper limits of the salt layer (Figure 3.2b). The interpreted horizons were used to build structural and isopach maps.

The top basement in the seismic data is usually an interface between two seismic units with contrasting amplitude content and coherence levels. The layered character of the overlying sedimentary rocks is distinguished from the usually transparent to anastomosing reflections of the basement rocks. This boundary is normally expressed on the seismic data as an acoustically harder surface (increasing acoustic impedance downward) concerning the overlying sediments (Figure 3.3).

At least two mapping directions were used for fault interpretation for a better constraint of fault and basement structure. Important to mention that all the basement interpreted were obtained from multi-directional seismic interpretation, that is, the features must have been seen and interpreted in at least two mapping directions. For more complex or uncertain features, arbitrary mapping directions complementary to the lines and traces of the survey were used. Seismic horizons and the structural network of both intra-basement and rift structures were then used to build a 3D structural model. Faults are represented as triangulated surfaces (250 m mesh), from which dip angle and dip direction were

calculated in every node, allowing further construction of equal-area lower-hemisphere stereographic diagrams (stereograms).

Rift faults have their relative age of slip obtained firstly from the observation of syn-kinematic wedges (divergent) sedimentary packages in the hanging wall of the faults, systematically thickening towards the main fault (see Prosser, 1993). Secondly, when syn-kinematic wedges are absent, we assumed that fault nucleation occurred near the horizon on which the fault exhibits its maximum throw (Walsh & Watterson, 1988). Seismic reflectors exhibiting a divergent pattern against a fault plane are the most reliable indication of syn-depositional fault slip and thus a time frame of fault activity since we know the relative age of the sediments (Prosser, 1993), although caveats apply when rift basins are sediment starved (Cartwright, 1991). It is worth noting that no pre-rift sediments have been recorded in the Campos Basin (Winter et al., 2007; Szatmari & Milani, 2016) and the deposits attributed to the rift initiation age in our study area consist of erratically distributed and thin (up to 50 m thick in wells) volcanic layers of the Cabiúnas Formation. To constrain the interpretation of fault age with the creation of accommodation space during fault activity, isopach maps of the Rift Climax I & II seismic-depositional sequences were built and superposed on the fault networks. For descriptive purposes, we refer to "fault nucleation" for both mechanisms of reactivation of pre-existing ductile intra-basement structures/metamorphic foliation or the nucleation of rift faults that cross-cut the pre-existing basement anisotropy. For kinematic analysis purposes, we observed fault heaves and the displacement on tBas and tI/A horizons, initially assuming a pure dip-slip movement in the fault segments, with no later reactivations. Unfortunately, more accurate methods of kinematic analysis could not be used in our dataset. For example, expansion

index, throw-depth and throw-distance plots (e.g. Cartwright et al., 1998; Reeve et al., 2015) could not be applied since the mapped horizons consist of unconformities.

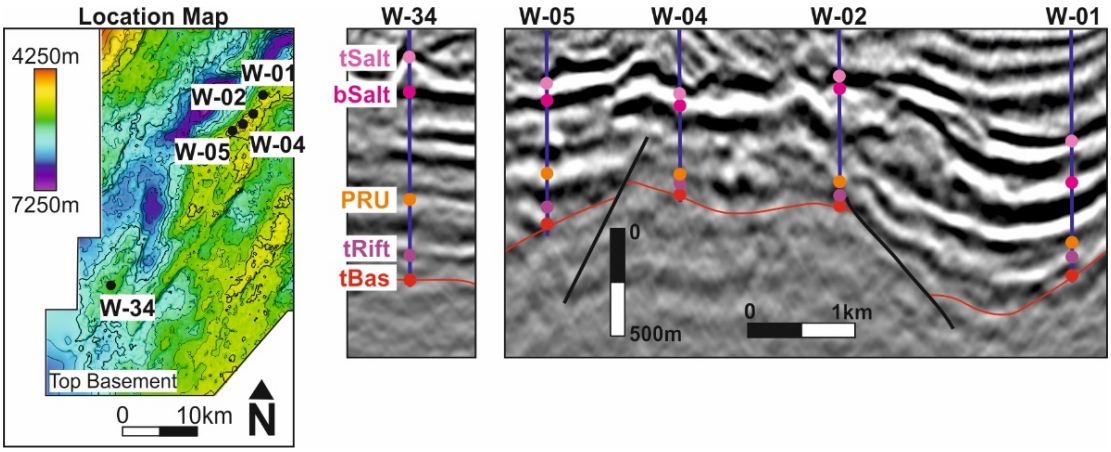


Figure 3.3: Location and seismic signature of wells that reach the basement top. Well markers refer to the main unconformities and mapped horizons as presented in Figure 3.2b.

3.5 Results

3.5.1 Seismic stratigraphy

The presalt sedimentary record was divided in four seismic-depositional sequences that approximately equate with the previously defined lithostratigraphic units and tectonic phases (Figure 3.2): 1) Rift Climax I (RCI), 2) Rift Climax II (RCII), 3) Transition, and 4) Post-Rift. However, the top of the Cabiúnas Formation (i.e. the top of the rift initiation stage) does not have a correlative seismic horizon. For this reason, the tI/A horizon was employed to subdivide the depositional sequences that are equivalent to the rift initiation and climax stages in Rift Climax I & II sequences. Consequently, the RCI sequence includes the volcanoclastic rocks of the rift initiation (Cabiúnas Formation) and the siliciclastic deposits of the early rift climax stage (Itabapoana/Atafona Formations), whilst RCII contains the carbonatic basal section of the Coqueiros Formation (Figure 3.2b), in accordance with Olivito and Souza (2020). The distribution of rift climax sediments is

strongly controlled by the rift-related structural highs and lows (Figure 3.4), which in turn are defined by the major fault zones (Figure 3.5a). The internal unconformities are noticeable within the depositional lows but not in the structural highs. Consequently, wellbore data provides the best evidence for the limit between RCI & RCII (i.e., the tI/A seismic horizon), based on the lithological contrast between siliciclastics of the RCI and the carbonates of RCII in the structural highs.

The two internal unconformities within the RCI sequence (RCS1 & RCS2 – Figures 3.2b & d) only occur within the Low C, which is the only depocentre limited by N-S faults (Figure 3.4b & d). The syn-tectonic character of the RCI is evidenced by the syn-kinematic wedges in the hanging wall of the H3FZ (Figure 3.4d). The RCII sequence is bounded by tI/A and tRift horizons. The tI/A horizon marks an abrupt change in the lithology (siliciclastics to carbonates) and in the position of the depocentres, as the available accommodation space migrates southwards along the strike of the Main Fault Zone (MFZ – Figure 3.5c). Syn-kinematic sedimentation of the RCII is well illustrated in Figure 3.4c, where a wedge-shaped package is observed in the hanging wall of the MFZ. A third internal unconformity (RCS3) is mapped within the RCII sequence. The sedimentary thickness above and below RCS3 reinforces the observed changes in the accommodation space towards the end of the rift climax stage (Figure 3.4b).

3.5.2 Rift faults and structural compartments

Over 100 faults that displaced the top basement horizon (tBas) were mapped within the study area (Figure 3.5a). The faults display a dominantly NE-SW orientation (average of N28E) and primarily dip to the SE, with a subset ranging from N-S to NE-SW, with a

common dip to the west, suggesting that they are a conjugate set to the dominant normal faults (Figure 3.5b).

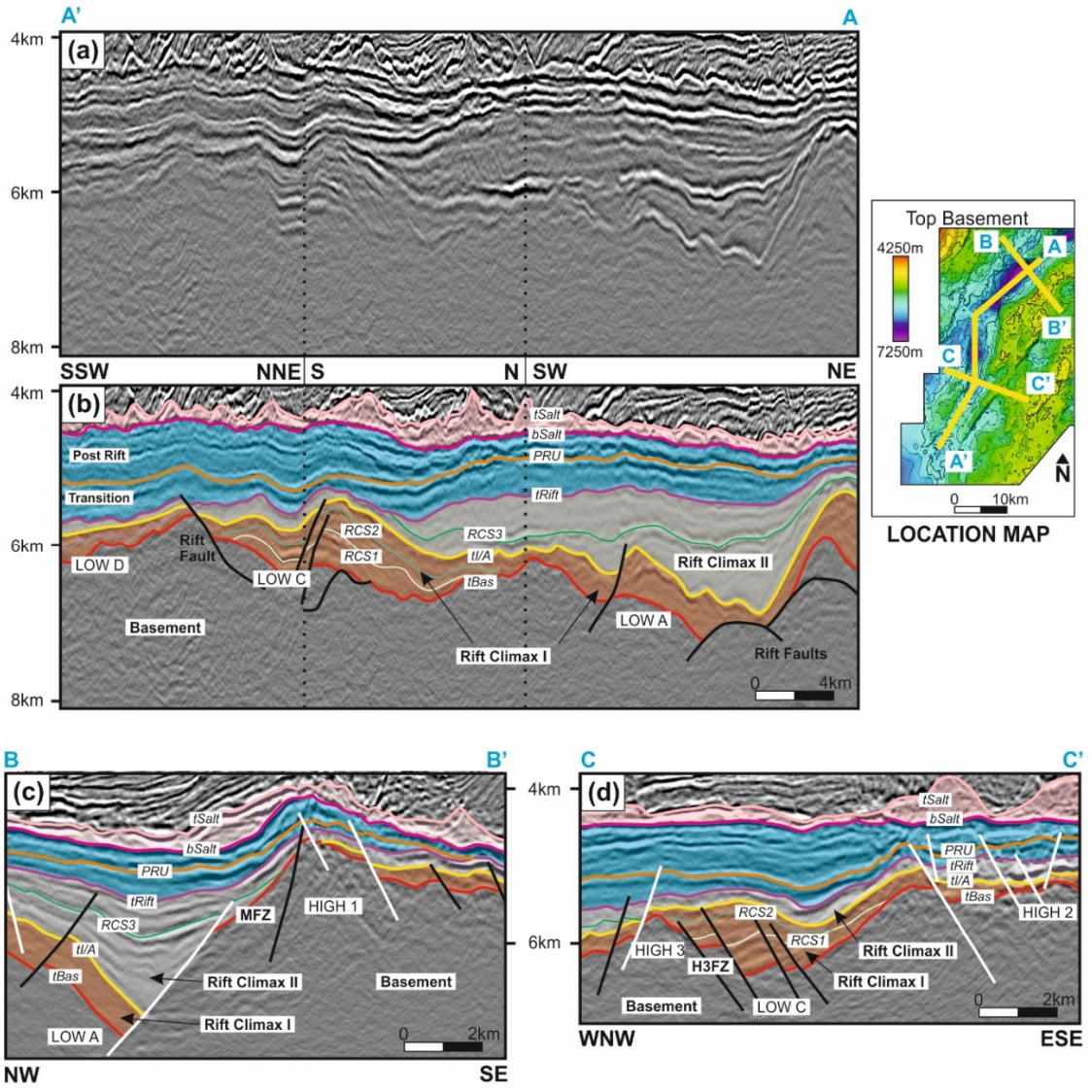


Figure 3.4. Geologic sections showing thickness variations of rift climax packages and their relationship with rift faults. a) Uninterpreted and b) interpreted A-A' kinked seismic section across the Lows A, C & D (Figure 3.5a) presenting the thickness variations of Rift Climax (RC) Strata. Notice the northward depocenter migration from RCI to RCII seismic-depositional sequences. c) Interpreted B-B' dip section across the Low A showing syn-kinematic wedges of RCII against the Main Fault Zone (MFZ). d) C-C' dip section across the Low C presenting syn-kinematic wedge of RCI sediments against the High 3 Fault Zone (H3FZ). In (c) and (d), fault traces in black represent earlier faults while faults in white correspond to late rift faults (see Figure 3.5 and text for explanation).

Four fault ‘zones’ are here delineated and named where fault traces are clustered as a linear array of structures that, in most cases, define the limits between less deformed structural highs and lows (Figure 3.5c). The fault zones comprise those with the highest throws and greatest length. The term fault zone is widely used to describe related fault segments restricted to a relatively narrow zone (Peacock et al., 2000 and references therein, Childs et al., 2009), but here we use this term more generally to encompass a network of related seismically observable faults that form noticeable ‘corridors’ in map view. The fault zones Main Fault Zone (MFZ), Central Fault Zone (CFZ), and High 3 Fault Zone (H3FZ) demarcate the structural highs and lows and comprise hard-linked structures. In contrast, the High 2 Fault Zone (H2FZ) constitutes the High 2 and show most of its segments as soft linked faults, with smaller throws compared to other fault zones. In terms of internal geometry in map view, the fault zones exhibit an anastomosing pattern, except for CFZ and its mostly collinear segments (Figure 3.5c).

The majority of mapped faults are interpreted as having their main activity phase during RCI (Hauterivian to Barremian). Estimation of the relative age of faulting is based on syn-kinematic wedges of RCI or having their highest throws between the tBas and the tI/A horizons. Faults of this age are widely distributed within the study area (Figure 3.5d). Coeval hanging wall depocentres (> 500 m thick) to these faults are isolated and occur in the downthrown blocks of N-S and NE-SW fault segments of, respectively, H3FZ and MFZ. However, the most significant syn-kinematic wedges are observed in the hanging wall of the H3FZ and comprise nearly 1000 m of RCI sediments (Figure 3.4d). The remaining mapped faults are dated as having their main activity phase during RCII (Barremian), based on the same criteria used for RCI faults. These faults mostly occur within the eastern half of the mapped area. Related depocentres comprise up to 1400 m

thick sedimentary intervals that are contiguous along the hanging wall of the MFZ and extend further to the SW and W (Figure 3.5e). Well-developed syn-kinematic wedges of RCII occur against the MFZ (Figure 3.4c). Importantly, although there is no difference in the average strike direction between faults of RCI & RCII, this is not true for faults with syn-kinematic wedges, of which RCI faults strike NNE-SSW and RCII faults strike at NE-SW (Figure 3.5d & e).

Structural High 1 is the most prominent, characterised by a horst complex with synthetic and antithetic secondary faults that gently slope eastward (Figure 3.5a). It is separated westwards from the Low A by a NW-dipping master fault named Main Fault Zone (MFZ). The MFZ consists of a segmented, hard-linked fault array (Figures 3.4c & 3.5c), with frequent dip-linkage in profile, with up to 2000 m cumulative displacement and a relatively low dip angle (mean of 30^{o}). In contrast, the southern tip of the MFZ shows N-S soft linked faults with steeper planes (65^{o} avg.), which defines the boundary with the Low C along with the H3FZ. The eastwards limit of Structural High 1 is defined by the Central Fault Zone (CFZ).

Structural High 2 is an NNE-SSW elongated horst bounded by non-collinear faults that is evident in a staircase geometry of the tBas horizon in profile view. Structural High 3 is a small basement feature in the SW part of the mapped area (Figure 3.5a). It is limited eastwards by a pair of low angle (30^{o}) normal faults in which strike direction changes from NNE to N-S towards the North, and westwards by a ramp with minor antithetic faults that merges with the H3FZ (Figures 3.4d & 3.5c).

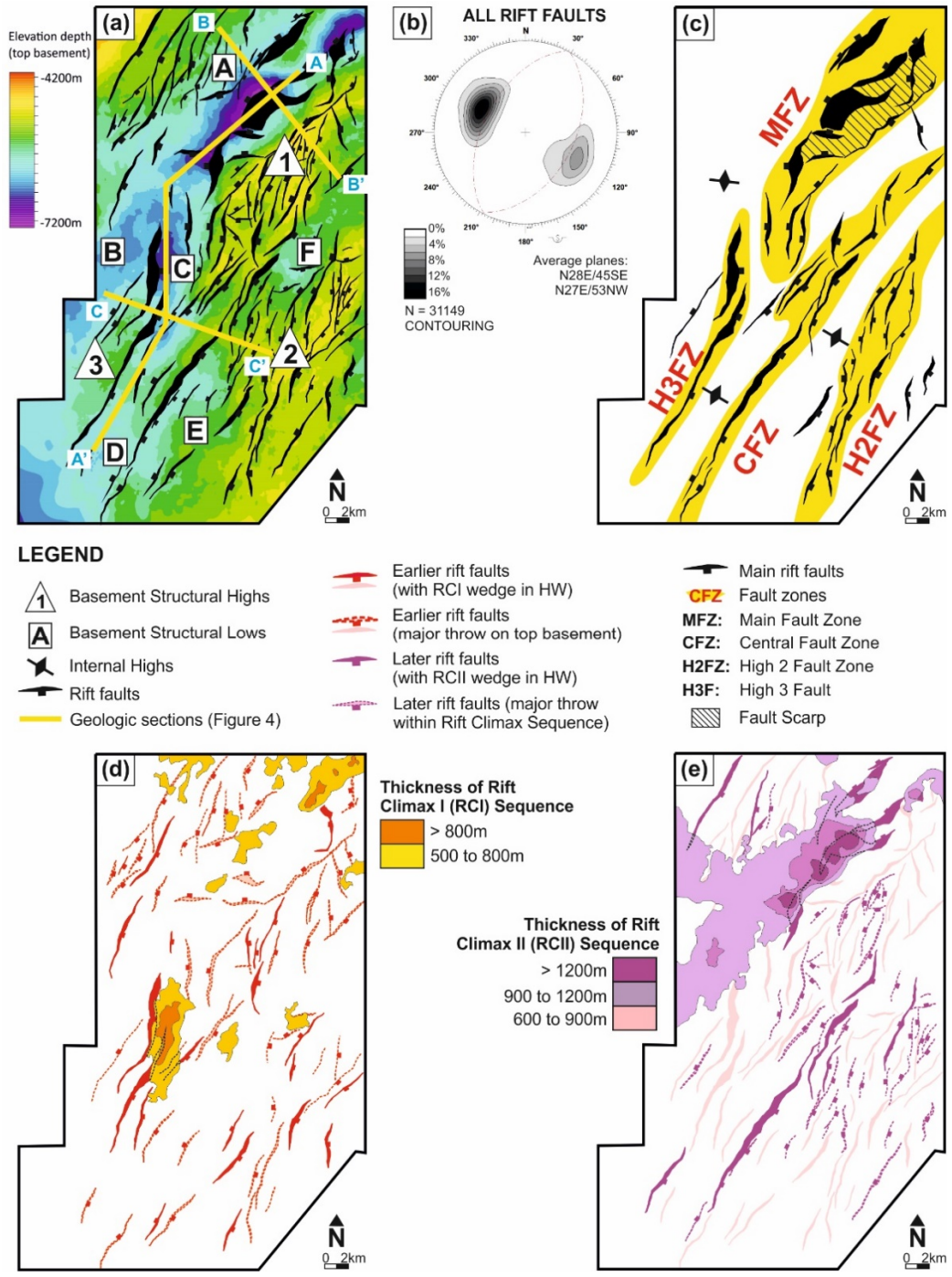


Figure 3.5: Maps of structural framework, top basement compartmentalization, and relative age of rift-related faults. (a) top basement contour map and rift faults showing the structural compartments with respect to basement highs (letters) and lows (numbers); (b) stereographic projection of rift-related faults; (c) rift fault zones and internal highs; (d) rift faults nucleated during Rift Climax I and (e) Rift Climax II sequence, including the main depocentres of both sequences. Rift faults from (d) are shown dimmed in map (e), so these two fault populations in (e) are the set of rift faults shown on (a). The width of fault segments is the fault heave at the top basement horizon.

The structural lows are characterized by half-graben geometries with dominantly NNE-SSW striking axes, except for Low C which strikes N-S (Figure 3.5a). Low A is the most pronounced depression at the level of the tBas horizon. Interestingly, it is the only low for which the faulted border is to the East, given by the MFZ master fault. The westwards ramp of Low A displays antithetic faults to the MFZ striking NE-SW and NNE-SSW. Fault slip in the MFZ and the coeval creation of accommodation space extend up to the base of the post-rift strata (Figure 3.4b & c). Low B is only partially represented in the study area and its faulted limit to the west is interpreted to be similar as on the lows C, D, E, & F. Their faulted limits are given by the H3FZ for lows C and D, and by the CFZ for lows E and F (Figure 3.5a).

3.5.3 Interpretation of intra-basement seismic facies and structures

We mapped and classified the intra-basement seismic response into three distinctive 'seismic basement' facies by adapting the classical seismic facies interpretation methods outlined in workflows for seismic stratigraphic interpretation (Mitchum Jr et al., 1977). The aim is to represent contrasting degrees of amplitude content and organization of internal reflections. We also identified and mapped planar and volumetric features that might represent geologically meaningfully boundaries and internal heterogeneities and hence quantify how they are spatially organized.

Previous studies have classified basement reflections below rift basins based on (1) binary contrasting reflectivity based on amplitude signatures (Reeve et al., 2014; Phillips et al., 2016), (2) seismic facies (Fazlikhani et al., 2017; Lenhart et al., 2019) and packages (Bird et al., 2014) correlated to main basement units supported by onshore geology, and (3) types of basement structures based on their 2D geometry (Collanega et al., 2019; Osagiede et al.,

2020). Except for Collanega et al. (2019), these studies are all of the North Sea Rift. The classification scheme adopted herein (Tables 1 & 2) aims to combine these already existing methodologies. This approach was required due to lack of direct connection between onshore and offshore geology in the Campos Basin (Figure 3.1a), in contrast to the slightly less unpredictable offshore basement geology based on onshore of the North Sea Rift.

Seismic Facies 1 (SF1) represents the least heterogeneous of the facies, SF2 is moderately heterogeneous, and SF3 represents the most heterogeneous basement with respect to seismic reflectivity (Table 1). These seismic facies are limited by or contain correlative surfaces, here called Basement Features (Table 2). Specific criteria were established to interpret the basement features, for which a single surface must appear consistently within a range of at least 100 lines and/or traces. The mapped intra-basement surfaces were categorized in three main features (Table 2): (1) planar discontinuities (Surfaces), (2) 3D volumes that are bounded by surfaces (Geobodies), and (3) planes within Geobodies (Internal Reflection). These internal reflections within the geobodies potentially represent internal heterogeneities but that are not necessarily conformable with the external boundaries.

Table 1: Seismic facies for basement seismic response

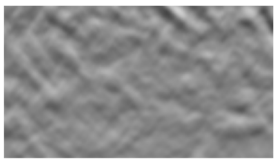
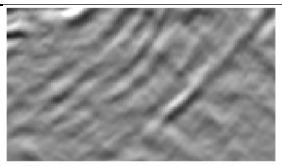
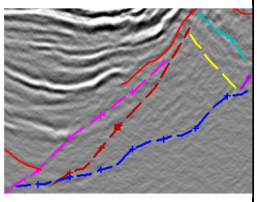
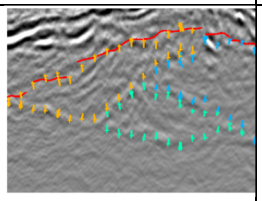
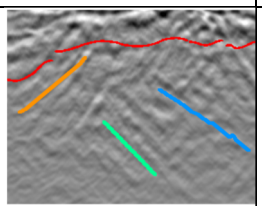
FACIES	NAME	SEISMIC SIGNATURE	DESCRIPTION
SF1	HOMOGENEOUS		Low amplitude (transparent), moderate to high frequency, chaotic to anastomosed reflections.
SF2	MODERATELY HETEROGENEOUS		Moderate to high amplitude, low to moderate frequency, anastomosed to sub-parallel reflections, with some internal coherency.
SF3	HIGHLY HETEROGENEOUS		High to Moderate amplitude and frequency, parallel to sub-parallel reflections, highly anisotropic.

Table 2: Description of intra-basement features. The continuous red line is Top Basement horizon.

FEATURE	MAPPED AS	SEISMIC EXPRESSION	DESCRIPTION	INTERPRETATION
SURFACE	FAULT		Interfaces of contrasting internal reflections (angle, dip direction). Usually, but not always, coincides with geobody's boundary.	Narrow to broad ductile shear zones
GEOBODY	MULTI-Z INTERP.		Geobodies with contrasting internal dip angles/direction that can be mapped in more than one direction.	Tectonic lenses with remnant self- organized heterogeneities bounded by shear zones
INTERNAL REFLECTION	HORIZON		Consistent and trackable internal reflections, usually enclosed by geobodies.	Internal heterogeneities (tectonic foliation?).

The workflow adopted is described using a seismic section as an example (Figure 3.6). In a blank section (Figures 3.6a, A2), we interpreted the tBas horizon and the intra-basement surfaces and geobodies (Figure 3.6b). Such 2D interpretation is then extended and validated in the 3D space. For every surface-bounded geobody of basement structures, we attribute a seismic facies following Table 1. The network of interpreted surfaces that resulted from the interpretation of intra-basement surfaces is tentatively shown in a map view on Figure 3.6c. Notice the absence of structures in the western half of the studied area, in contrast with the highly structured basement in the east. Between these East and West Domains, a roughly N-S boundary is drawn on Figure 3.6c. Such binary division is also backed in the lithologies described in the rock samples (see Item 4.4).

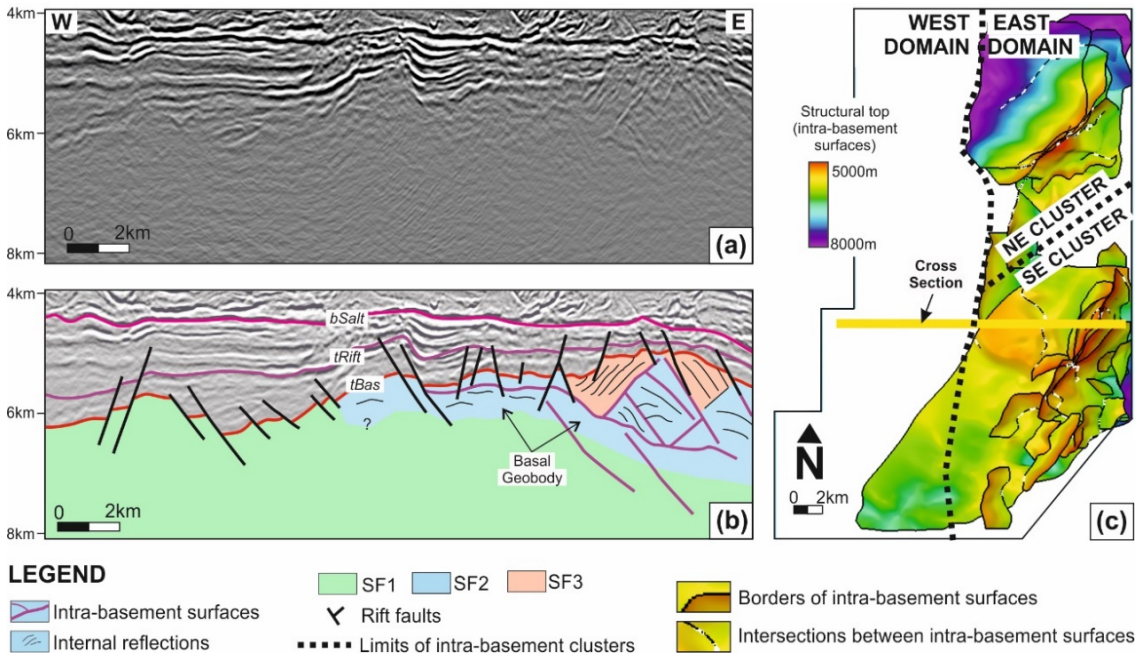


Figure 3.6: The interpretation workflow for intra-basement seismic structure. On (a) uninterpreted and on (b) interpreted seismic section, showing seismic facies (Table 1) and intra-basement features (Table 2). On (c) the 3D network of intra-basement surfaces is tentatively shown in a map view. For larger version of "a" please see Figure A2.

The self-arrangement of intra-basement surfaces on the East Domain allowed them to be grouped into two distinctive areas, here named Clusters NE and SE (Figure 3.6c). When dividing the intra-basement structures into two clusters, we considered the quantity and the distinct main strike direction of the intra-basement features, and the contrasting modes of interactions between basement heterogeneities and rift faults. Also, the lack of a clear physical connection across a NE-SW imaginary line that divides the clusters suggests the presence of a geological boundary (Figure 3.6c). Among the similarities, the NE & SE Cluster of intra-basement structures consist of a low angle (<20^{o}) basal geobody over which discontinuities of higher angle are juxtaposed (up to 45^{o}).

Seismic facies 1 (SF1) is characterised by a chaotic network of low amplitude, moderate to high-frequency seismic response. It dominates the basement seismic response in the West Domain (Figure 3.6b & c) and in depths higher than 7 km in the East Domain (Figure 3.6b). Although the SF1 can be simply interpreted as a consequence of the attenuation of the seismic signal below a certain depth, it can be observed both below the tBas horizon and the heterogeneous SF2 and SF3 seismic facies. SF1 is interpreted as being indicative of a basement that is more isotropic (granitoids or ortho-derived gneiss), which is supported by rock samples (see Section 4.4).

Seismic Facies 2 (SF2) and Seismic Facies 3 (SF3), along with intra-basement surfaces, largely occur in the East Domain (Figure 3.6). SF2 consists of moderately organized, anastomosing to sub-parallel reflections. Its higher amplitude character distinguishes SF2 from SF1. SF3 has been identified only within geobodies bound by intra-basement surfaces and the tBas horizon. It is characterised by high amplitude, highly anisotropic parallel reflections. Although showing contrasting seismic anisotropies, SF2 and SF3 are interpreted as being comprised of heterogeneous, layered basement rocks units such as

foliated metamorphic rocks (e.g. schists and gneisses). The samples obtained in the drilled wells (Figure 3.3) provided the control that these highly reflective seismic domains are metamorphic and not sedimentary formations.

The three intra-basement features defined in Table 2 represent both internal fabrics and major structural boundaries within the basement rocks units. We interpreted surfaces as ductile shear zones that delimit less deformed geobodies. Below heterogeneous SF2/SF3 a low to very-low dip angle (< 25^{o}) tabular basal geobody of SF2 is often observed in both NE and SE clusters (Figure 3.6b). This Basal Geobody is often bounded by surfaces that are conformable with the internal reflections.

3.5.3.1 The NE Cluster

This group of intra-basement heterogeneities lies under Structural High 1 and in the northern part of Low A (Figure 3.7), including a master fault represented by the Main Fault Zone (MFZ). The intra-basement surfaces mapped within this cluster have a mean attitude of N43E/21NW and secondarily N49E/30NE (Figure 3.7f), although their low angle character implies in a highly scattered dip angle pattern. For this reason, a stereogram excluding the surfaces that define the Basal Geobody unit is also shown (Figure 3.7g).

The overall geometry of NE Cluster can be described as a low angle, NW dipping Basal Geobody, enclosed by an asymmetric antiformal structure (Figure 3.7d). The base and the eastern flank of the antiform are made of SF2, while the steeper western limb is marked by SF3. The Basal Geobody becomes increasingly shallower towards the East, eventually merging with the eastern flank of the antiform and thus reaching the Top Basement horizon (Figure 3.7e). The interpretation of these structures suggests that the Basal Geobody has functioned as a ductile detachment for the antiformal structure above (Figure 3.7d & e).

This geometry may represent a fault-bend fold or a detachment fold with respect to the Basal Geobody with a suggested vergence to NW.

3.5.3.2 Integrating rift and basement structures in the NE Cluster

The rift faults that overlie the NE Cluster have a main trend of N28E dipping to both NW and SE, sub-parallel (circa 15°) in strike with respect to the basement structures (Figure 3.7c, g & h). The rift faults show scattered strike and dips, ranging from N-S to E-W and 25° to 70°, respectively (Figure 3.7h). Fault segments dipping to the NW represent MFZ segments while faults dipping to the SE are secondary structures on the footwall and hanging wall blocks of the MFZ.

The interplay between reactivation of basement structures and the MFZ is evidenced by the sub-parallelism between fault segments and the basement fabric (Figure 3.7c-e), and the coeval deposition of syn-kinematic wedges of RCII sediments on the hanging wall of the MFZ (Figure 3.4c). Fault segments on the southern tip of the MFZ and in the northern tip of the H3FZ are N15E oriented (Figure 3.8b) and thus define the limits of the Low C, on which the thicker strata of RCI Sequence are deposited (Figures 3.4d & 3.5d), implying that these fault segments are probably the oldest in the studied area. Syn-kinematic wedges of RCI sediments occur against the H3FZ (Figure 3.4d) while the same geometry is observed in sediments of RCII age in the hanging wall of the MFZ (Figure 3.4c). Consequently, fault segments of MFZ are younger northwards, as suggested by the diachronous thicknesses distribution of rift climax sediments along the H3FZ and the MFZ (Figures 3.4b, 3.5d & e).

During the northward propagation of the MFZ, the newly formed segments became progressively oriented from N30E to N60E (Figure 3.8b), following the basement fabric

(Figure 3.7d & e). Moreover, dip angles decrease northwards, from 60º on southern segments to less than 30º on the northern segments (Figure 3.8a). Apparently, the ultimately lower angle of basement fabric leads to fault segmentation in the hanging wall of the northernmost segments of the MFZ and inhibited the deposition of thicker sediments of RCII when compared to the central segments of the MFZ (compare Figures 3.4c & 3.7e). Also, the obliquity between intra-basement structures and the MFZ segments slightly increases towards the top (compare Figures 3.8b and 3.8c).

On the eastern sector of the NE cluster, rift faults occur as small antithetic (to MFZ) faults dipping SE over the ramp that constitutes the footwall block of the MFZ (Section 7d). In this area, intra-basement structures and the metamorphic foliation occur at an acute angle with respect to the tBas surface, leading to localised reactivation of basement structures during the rifting (Figure 3.7e). Nonetheless, when moving eastwards along the footwall ramp (see SE sector of Figure 3.7d), the heterogeneous basement becomes progressively thinner above the homogeneous SF1 and oriented with a high angle to rift faults. Consequently, rift fault tends to nucleate in a geometrical configuration that cross-cuts the metamorphic foliation rather than one paralleling the foliation *i.e.* in an exploitative geometry.

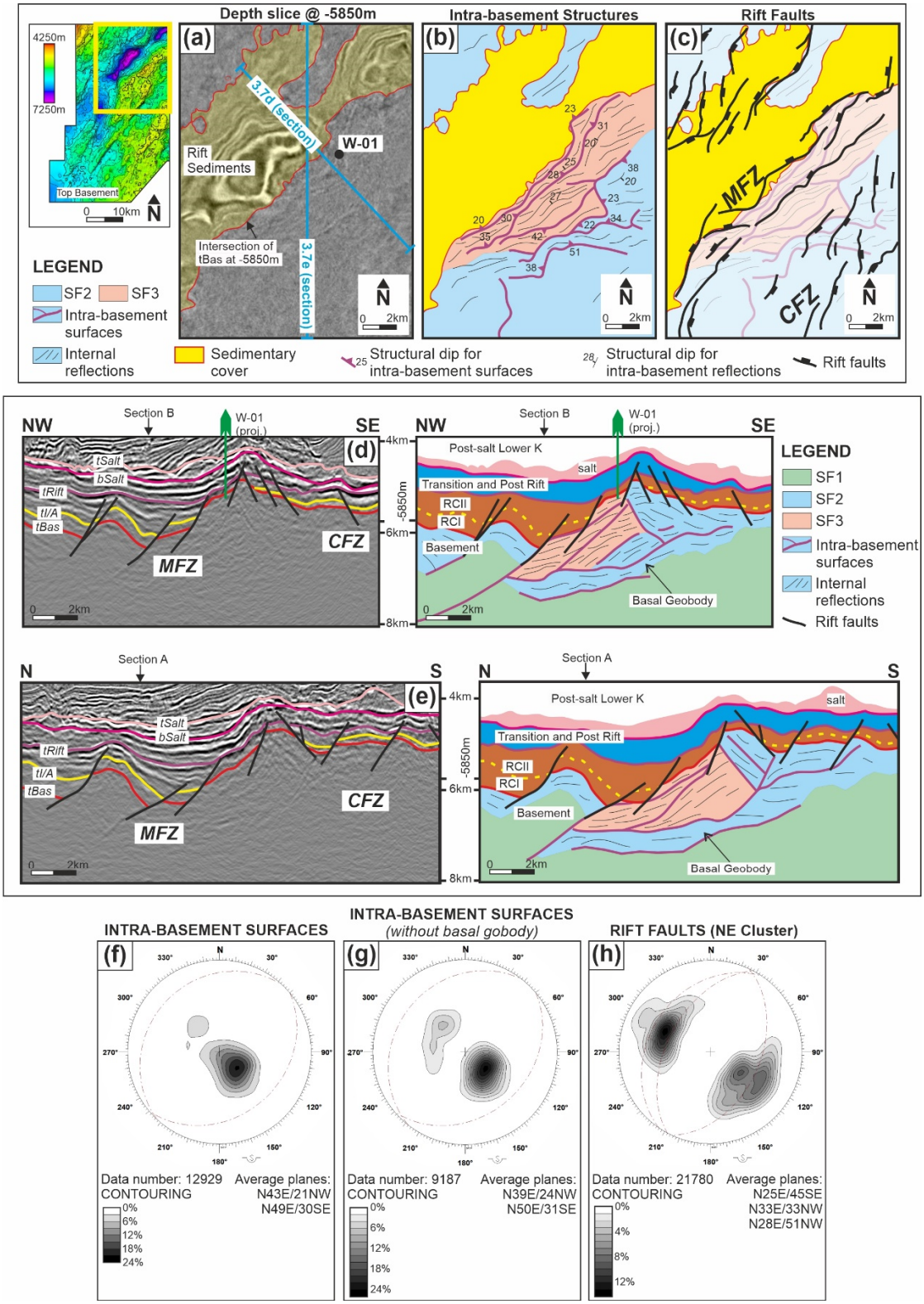


Figure 3.7 (caption on next page)

Figure 3.7: Depth Slice, geological sections and stereograms for intra-basement structures and rift faults of the NE Cluster. Depth slice at -5850 m shows (a) the seismic amplitude signal, the boundaries of sedimentary cover and the location of geologic sections, (b) dip directions and angles extracted from 3D surfaces representing the intra-basement structures and internal reflections, and (c) basement structures overlapped by the intersections of -5850 m-surface with rift faults. Sections (d - dip) and (e - strike) displays the framework of basement seismic facies and structures. Well W-01, used for petrographic and geochronological analysis, is also shown. MFZ & CFZ are two of rift related fault zones. On the bottom, stereograms of all intra-basement surfaces (f), intra-basement surfaces except basal geobody (g), and rift faults over the NE Cluster (h) are shown. For uninterpreted seismic data of d-e please see Figure A1.

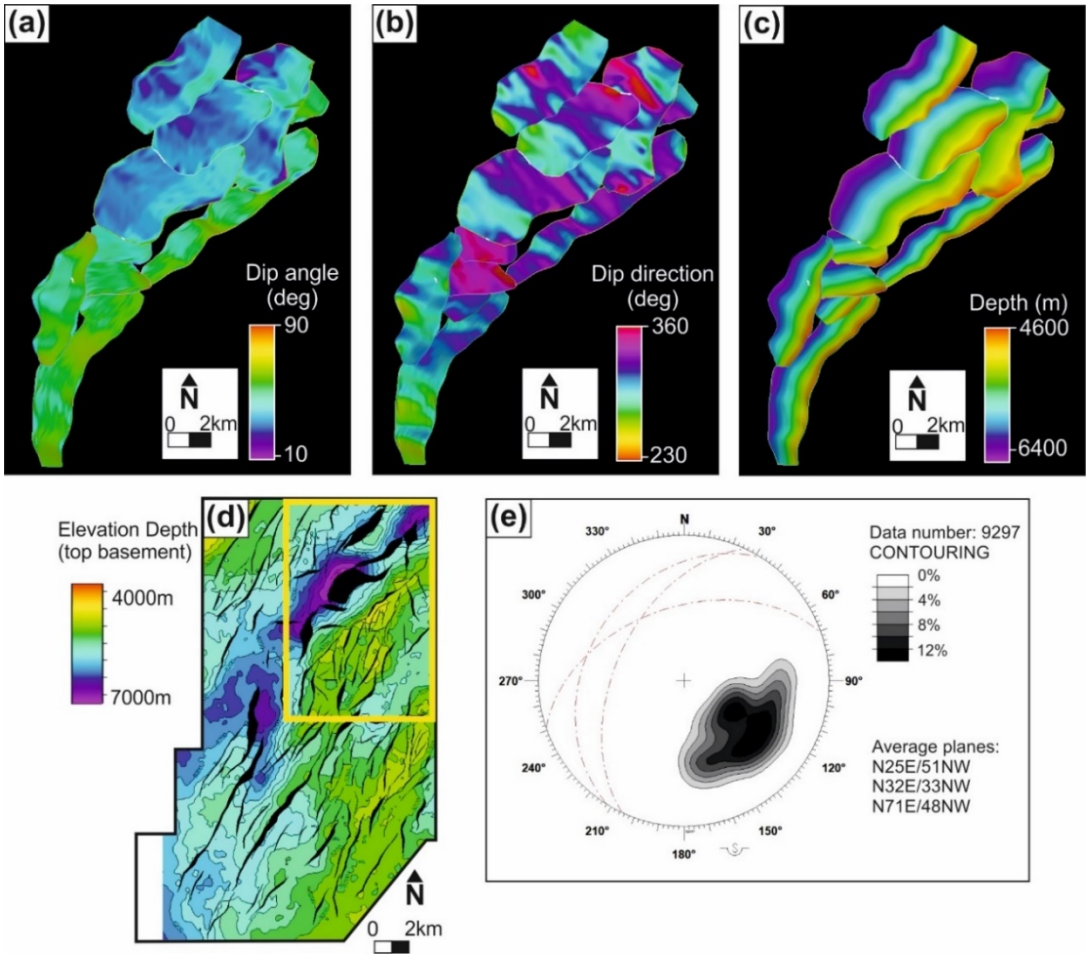


Figure 3.8: Geometric analysis of fault segments within the Main Fault Zone (MFZ). (a) to (c) show top views of fault segments within the yellow window shown on (d), presenting, respectively, dip angle, dip direction and depth of fault segments. (e) presents the stereographic projection of MFZ fault segments and the main clusters of data. Notice from (a) and (b) the shift on both dip and dip direction northwards along strike.

3.5.3.3 The SE Cluster

This group of basement structures underlies Structural High 2, Low F, and the High 2 Fault Zone (H2FZ). It is delimited on the west by the Central Fault Zone (Figure 3.9). The SE Cluster consists of 24 mapped intra-basement surfaces (Figure 3.6c). It shows similarities with the NE Cluster in the form of a pair of laterally extensive, low angle surfaces (Basal Geobody) over which most of the remaining structures overlie, including an antiformal structure on the northern sector of SE cluster (Figure 3.9d).

The geometric attributes of structures within the SE Cluster are presented as a stereographic projection on Figures 3.9e & 3.9g, exhibiting a N22E main trend. However, in the central region, a group of WNW-ESE (N dipping) basement structures is observed, dividing the SE Cluster into two areas of contrasting structural styles, referred here as the northern and southern sub-domains (Figure 3.9b). The northern sub-domain shows a predominance of highly anisotropic basement seismic facies (SF2/SF3) when compared to the southern domain, where SF2 is largely predominant. Apart from the clear contrasts in the structural style observed in the dip sections, the geologic section of Figure 3.9h shows no boundary but a gradual transition from the northern to the southern sub-domains.

The basement structural grain in the SE Cluster is predominantly low angle with boundaries of lenticular shape defined by intra-basement surfaces (Figure 3.9h) that are generally SE dipping (Figures 3.9d & 3.9f). The Basal Geobody is observed in both sub-domains, similarly to what is observed on the NE Cluster except for the dip direction to SE (compare Figures 3.7d & 3.9d). The Basal Geobody is shallower westwards and southwards, where it constitutes basement heterogeneities that have a notably low dip angle (Figures 3.9d & 3.9f).

Basement surfaces of the northern sub-domain often exhibit higher dip angles than the southern sub-domain, and the surfaces dip both to the SE and NW, expressed as an overall slightly asymmetric antiformal geometry (Figure 3.9d). This interpreted fold has a NNE-SSW axial plane dipping SE, indicating a possible NW-vergence, similar to the antiform in the NE Cluster (compare figures 3.7d & 3.9d). In contrast, the southern sub-domain shows exclusively SE dipping basement surfaces, which are less continuous in extent when compared to northern sub-domain. The overlapping geometry of these surfaces which lies with an acute angle over the Basal Geobody is suggestive of a contractional duplex that detaches over the base (Figure 3.9f).

3.5.3.4 Integrating rift and basement structures in the SE Cluster

The collection of faults over the SE Cluster consists of a pair of N26E fault populations, mostly dipping to SE (46°) and secondarily to NW (51°), where the intersection line gently plunges towards the SW (Figure 3.9g). Most of the rift faults belong to the High 2 Fault Zone (H2FZ), which is distinctive from the remaining fault zones since its fault planes and displacements are generally shorter and smaller, respectively. Thus, their fault segments dip to both directions, defining the main geometry of the High 2, in contrast to the single dip direction observed in the other fault zones (Figure 3.5c).

The average strike direction of rift faults on SE Cluster is the same as that exhibited by the intra-basement structures (Figure 3.9e), in contrast with the sub-parallelism observed on the NE Cluster. The parallelism between the rift faults and the shallowest sectors of basement surfaces is prominent in map view and can be also observed in both dip and strike cross-sections of Figure 3.9.

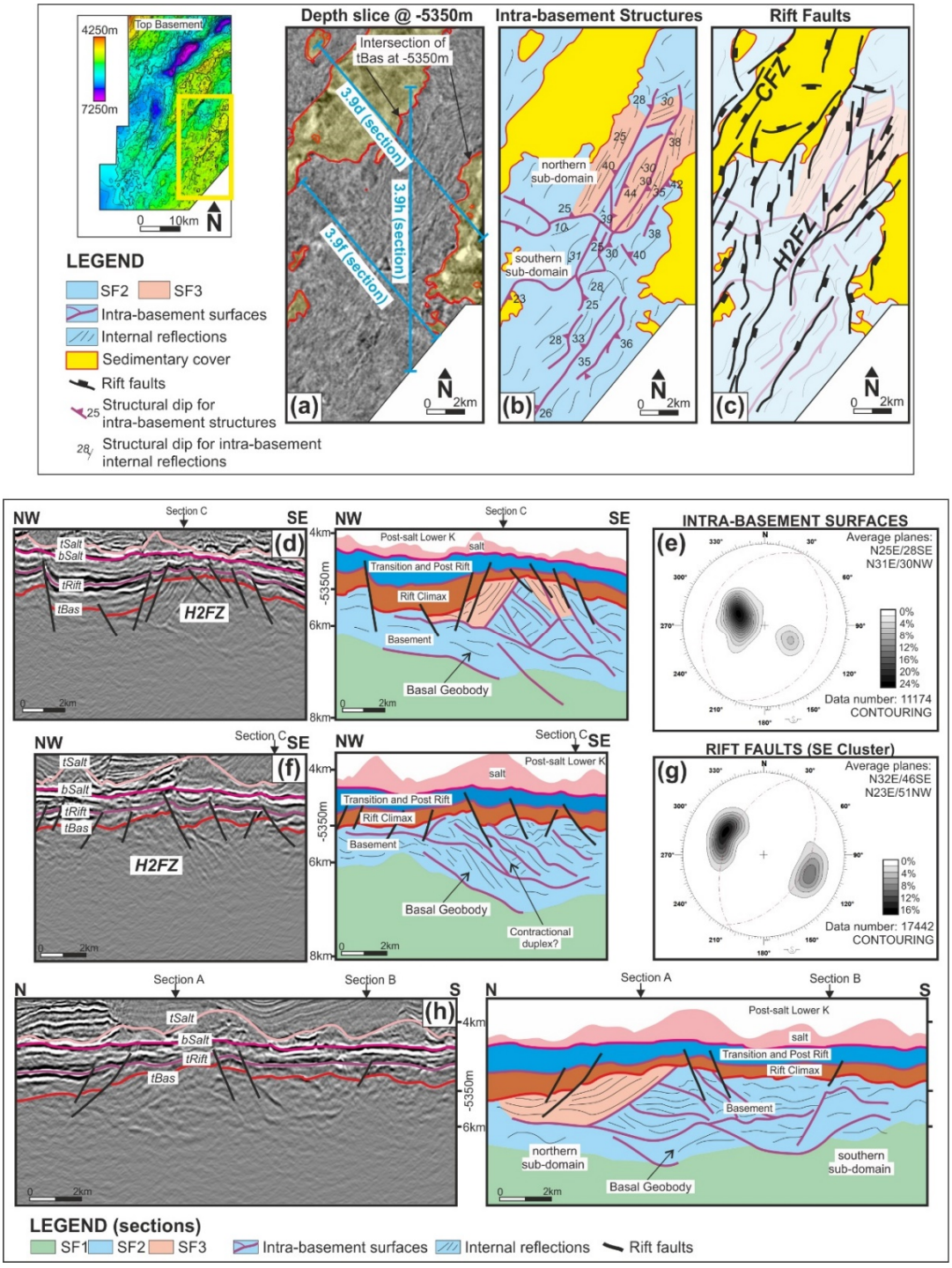


Figure 3.9: Depth slice at -5350 m and geologic cross sections showing the intra-basement structures of the SE Cluster. In (a) is presented the seismic amplitude signal, the boundaries of sedimentary cover and the location of geologic sections. (b) shows dip directions and angles extracted from 3D surfaces representing the intra-basement structures and internal reflections. (c) shows intersection planes of rift faults on -5350 m depth slice over the interpretation of basement structures. Below, three geological sections (d, f, & h), shows on left the uninterpreted seismic section with rift-phase faults and horizons, and on right a geological interpretation of basement structures and sedimentary filling. Stereogram (e) presents the intra-basement surfaces, except the Basal Geobody. Stereogram (g) presents the rift faults over the SE cluster.

The observations above are valid for the sectors of SE Cluster where the basement heterogeneities occur up to a certain depth, typically 2 km and at least 1 km below the tBas surface. The cross-sections of Figure 3.9 shows that SF2, SF3 and basement features are typically identified to depths up to 2 km below tBas, except in portions of the western sides of Figures 3.9d & 3.9f, where the Basal Geobody occurs directly below the tBas. In these areas, the basement structural grain shows a low to very low dip angle (< 15^{o}) and was crosscut by rift-related faults.

3.5.4 Basement samples and geochronological analysis

Five wells recovered basement samples (Figures 3.3 & 3.10a-f). Biotite gneiss is the predominant lithology, and all samples show a tectonic foliation marked mostly by phyllosilicates. Veins of coarse-grained quartz and feldspar intergrowth surrounded by mafic rich flakes suggest in situ partial melting and generation of leucosome (veins), therefore migmatitic domains (Figure 3.10c, 3.10d, & 3.10e). This feature also indicates a subhorizontal compositional banding, related to both the protolith and the subsequent metamorphic event, observed in a single well through 50 meters of drilling (Figure 3.10c). Gneiss samples more enriched in biotite, some with garnet, might be derived from sedimentary protoliths, representing paragneisses. Other gneiss samples show a granitic homogeneous composition that might represent igneous protoliths but could be also leucosome (Figures 3.10d & 3.10e).

In general, samples from wells W-01, 02, 04, & 05 (Figure 3.10a-d) represent a much heterogeneous set of lithologies in contrast with samples from W-34 well (Figure 3.10e). These samples could be equivalent to the outcrops of Búzios and Palmital successions shown in Figure 3.10i,j. In contrast, the westernmost W-34 is more isotropic and might

correspond to homogeneous granitoids, without anisotropy related to gneiss banding and foliation marked by phyllosilicates. The outcrop of Figure 3.10g could be interpreted as being similar in terms of lithology and metamorphic anisotropy. This contrast in lithologies and structures is coherent with the basement seismic features in the East and West domains, described previously (Figure 3.6c).

A sidewall core sample from the basement on W01 (Figure 3.10a) provided enough material to produce thin sections and to extract zircon crystals for U-Pb geochronology studies (Figure 3.10f). This biotite gneiss, with a general granitic composition, is mainly constituted by oligoclase and quartz, and secondarily by muscovite, biotite, microcline and zircon. The abundance of phyllosilicates might suggest that this gneiss could have either a sedimentary or an igneous protolith. The granolepidoblastic texture in thin sections implies that this is a medium to a high-grade metamorphic unit with a tectonic foliation (Figure 3.10f). The projection of the well to the seismic section on Figure 3.7d indicates that this sample would correspond to the western limb of an antiformal structure, Seismic Facies 3 (SF3), within the NE Cluster. Nine spots plotted in the Concordia providing an upper intercept of 533 ± 15 Ma, not forced to zero with a Mean Squared Weighted Deviation (MSWD) of 1.7 (Figure 3.10f). The interpretation of this age is complex because there are no original cathodoluminescence images of the zircons. Though it is most probable that this is a metamorphic age, considering the onshore data from the basement tectonic domains.

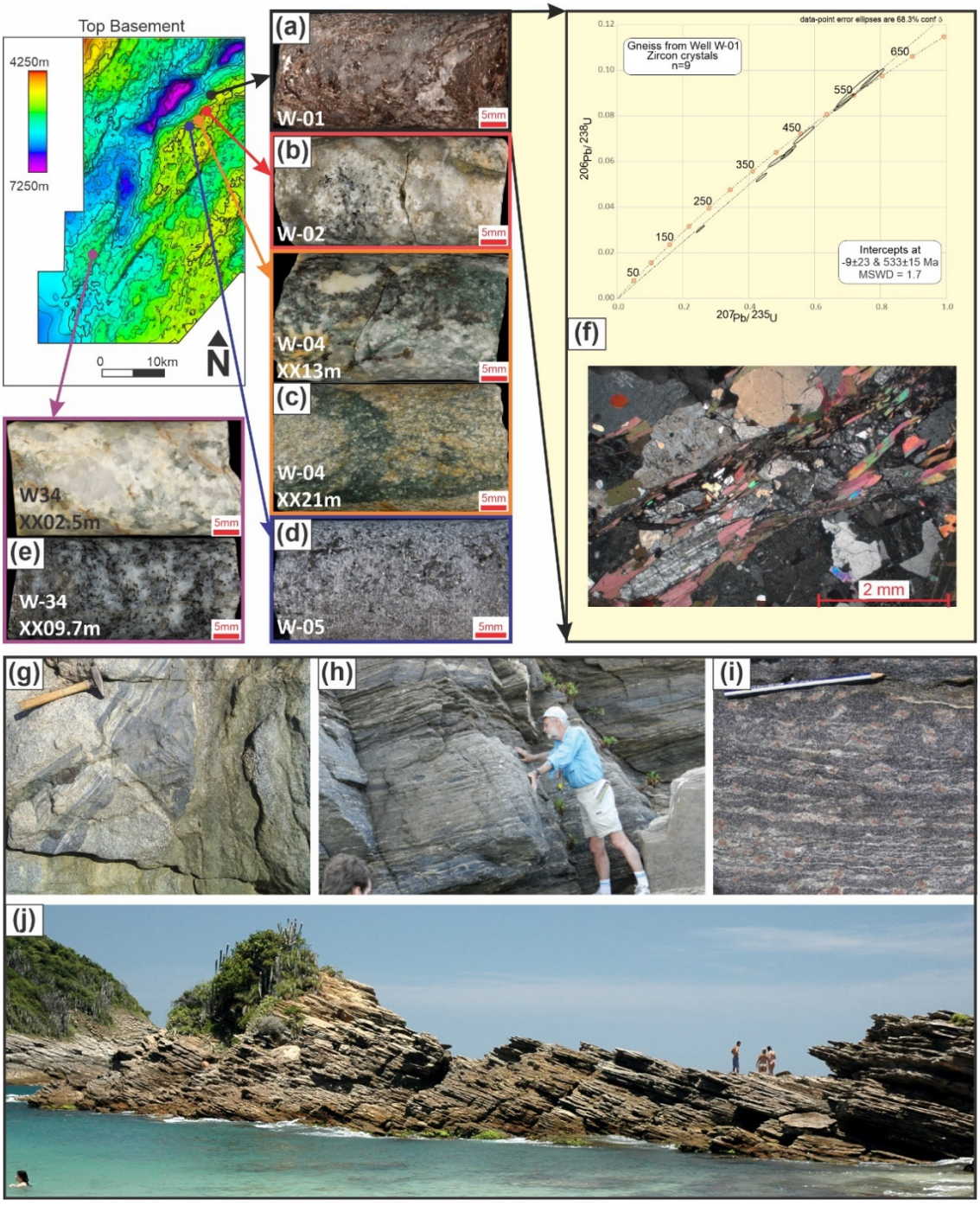


Figure 3.10 (Caption on next page)

Figure 3.10: a-f) Images from basement rocks recovered of five wells in studied area. (a) biotite gneiss, used for geochronological analysis. (b) a leucocratic granitic biotite gneiss from W-02. (c) two images from well W-04 shows a probable migmatitic texture with leucossome and restite rich in biotite and garnet. (d) well W-05 shows a more homogeneous biotite gneiss. The southern/westernmost drill W-34 (e) reached a biotite coarse grained granitoid/gneiss with a discrete foliation and granitic composition. (f) shows the dated sample on top and thin section on bottom shows biotite gneiss with well-preserved granolepidoblastic texture from the northernmost well (W-01). g-j) Photographs of outcrops in the Búzios region that are similar to the samples from the wells (g-i from Schmitt et al., 2016, j taken by the author). g) 1.97 Ga coarse-grained granite with dioritic enclaves, probably coeval and related to magma mingling. h) Tectonic contact between the Paleoproterozoic basement (below) and the Búzios succession, indicated by the hand of J. Bradshaw. i) Kinematic indicators (sigma and S-C foliation) showing top to E movement in the metasedimentary sequence of Palmital Succession as the contact with the Paleoproterozoic basement. j) garnet-sillimanite-rich migmatitic paragneiss of the Búzios succession at Ferradurinha beach evidencing the low angle tectonic foliation of the CFTD.

3.6 Discussion

3.6.1 Basement geology

The basement occurring immediately below the tBas horizon is divided into two lithological and structural domains: homogeneous (West) and heterogeneous (East) (Figure 3.11a). However, when observing the basement units in cross-section (Figure 3.11c), it is noticeable that the homogeneous SF1 that constitutes the West Domain extents under an up to 4 km thick pile of heterogeneous SF2/SF3 basement rocks of the East Domain. This heterogeneous package shows an internal organization consisting of upper SF2/SF3 highly heterogeneous basement over a tabular Basal Geobody of SF2 facies (Figure 3.11c). Therefore, heterogeneous basement in the East Domain is divided into two sub domains in depth, more and less heterogeneous, where the more heterogeneous domain is characterized by a complex network of folds and shear zones and the less heterogeneous is constituted by the tabular Basal Geobody (Figure 3.11c).

Our interpretation is that SF1 on the West Domain represents a more homogeneous set of basement rocks (Figure 3.11a), characterized by granitoids, equivalent to the drill core from W-34 obtained in this sector (Figure 3.10e). Based on the observation of the regional

geologic map and the offshore projection of the Cabo Frio Tectonic Limit (CFTL) (Figure 3.1a), two interpretations are possible for the West Domain. In the first, these rocks may represent the Oriental Terrane (Ribeira Belt), which is characterized by the abundance of syn-tectonic magmatic suites (Heilbron et al., 2008; Schmitt et al., 2016; Egydio-Silva et al., 2018). This interpretation means that the CFTL could coincide with the MFZ, although the fact that the CFTL is a low angle tectonic limit in the outcrops puts limits in this interpretation. Alternatively, the West Domain may correspond to the low strain domains of the Paleoproterozoic orthogneisses that constitute the basement in the context of the Cabo Frio Tectonic Domain (CFTD). It is still not clear if the rocks from the West Domain that extend beneath the East Domain represent the same basement unit. For this reason, we kept both interpretations for West Domain basement (CFTD Paleoproterozoic orthogneiss or the Oriental Terrane of the Ribeira Belt) in Figure 3.11.

This contrast between a highly heterogeneous basement in the eastern part of the study area and a more homogeneous unit to the west is taken to suggest a roughly N-S contact between two distinct geological domains that includes the MFZ (Figure 3.11a). Our interpretation is that the highly reflective SF2/SF3 facies could represent the CFTD Neoproterozoic paragneiss of the Palmital and Búzios successions and the SF2 facies of the Basal Geobody is equivalent to the migmatites that occur in tectonic contacts between these supracrustals and the underlying Paleoproterozoic basement (Figure 3.11c). Such comprehensive structural/tectonic style was observed in the CFTD onshore (Figure 3.1c - Heilbron et al., 2008; Schmitt et al., 2008). Internally, this heterogeneous SF2/SF3 facies exhibits asymmetric folds with vergence to NW and a contractional duplex with a possible tectonic transport to NW (Figure 3.11c). The tectonic transport agrees with kinematic indicators observed onshore in the northern contact zone between the Cabo Frio Tectonic Domain

and Oriental Terrane, but not with the indicators from the central and south part of the Domain that verge to E-SE (Schmitt et al., 2016). Furthermore, the outcrops show in Figure 3.10h-j show a remarkable low angle metamorphic foliation and tectonic contact between the basement and overlying supracrustals and are thus considered similar to the SF2+SF3 facies in the east domain.

The basement samples obtained from wells on the eastern portion of the area (Figure 3.10a-d) are better correlated with supracrustals units of the CFTD. Lithologically, these predominant biotite gneisses could represent paragneiss from both tectonic domains, since the Oriental Terrane also have high-T paragneisses (Figure 3.1). The distinction between these paragneisses is given by the contrasting pressure and age during metamorphic peak (c. 12 Kbar and 520 Ma for CFTD and c. 5 Kbar and 580 Ma for Oriental Terrane (Heilbron et al., 2008; Schmitt et al., 2016; Egydio-Silva et al., 2018; Schmitt et al., 2018). The geochronological data obtained from the well W-01 (533 ± 15 Ma) reinforces that this biotite gneiss is better correlated with the Neoproterozoic supracrustal unit of the CFTD. The structural style of this terrane, with exhumed nappes and duplexes of supracrustals unit on top of a homogeneous Paleoproterozoic continental crust (Figure 3.1c – Schmitt et al., 2016), is also coherent with the overall structural style of the basement in the East Domain, as gentle antiforms of heterogeneous SF3/SF2 over a moderately heterogeneous tabular SF2 (Basal Geobody) and then an homogeneous SF1 basement (Figure 3.11c). The age is coincident with the metamorphic peak obtained in the Cabo Frio Tectonic Domain (Schmitt et al., 2004; 2016) and also in the Pan African belt in the Angola coast (Monié et al., 2012). In addition, the offshore projection of the Cabo Frio Tectonic Limit (CFTL) is positioned by Egydio-Silva et al. (2018) and Stanton et al. (2019) near the study area following the trend with observed structures onshore (Figure 3.1a).

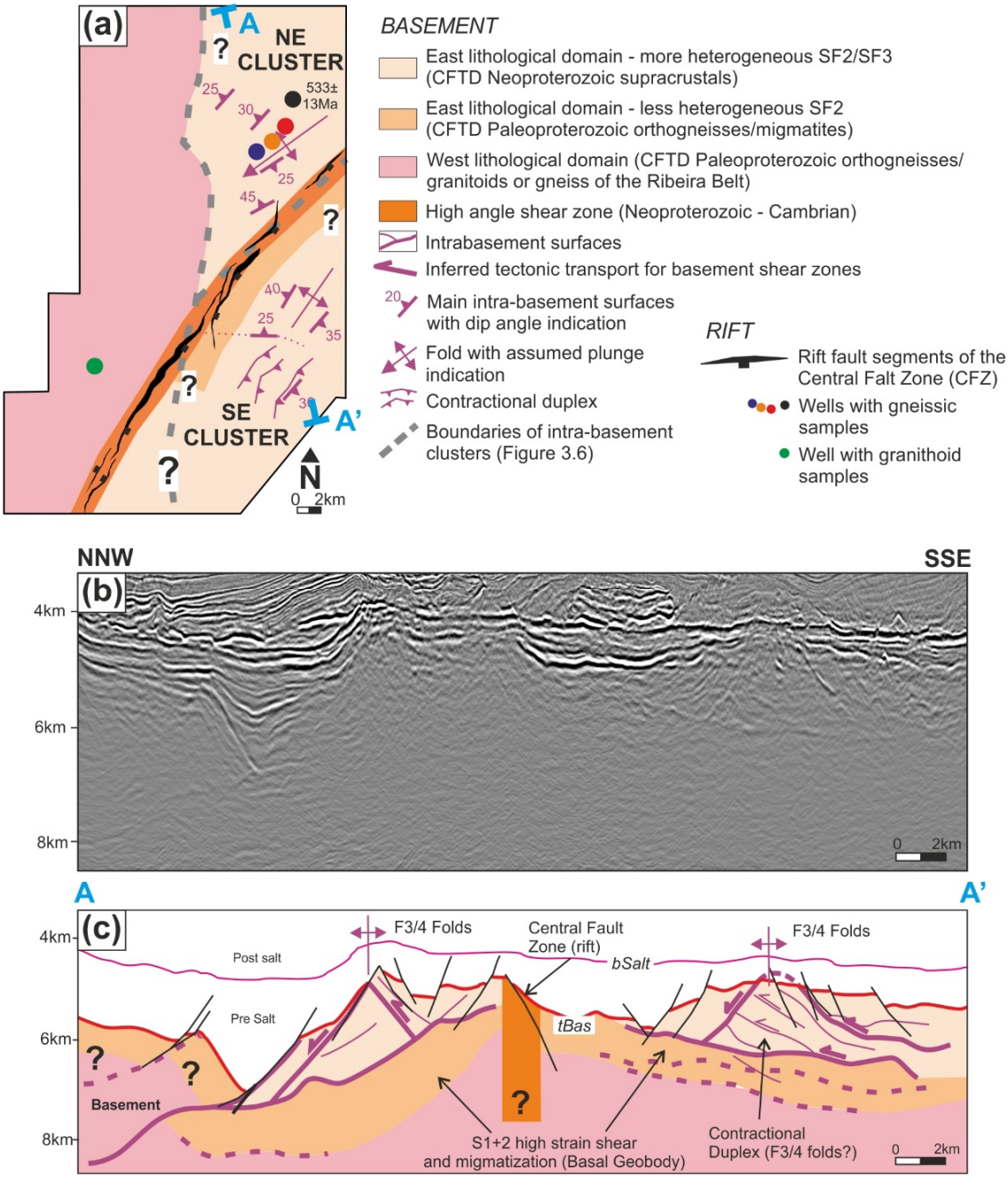


Figure 3.11: Basement geology and tectonic subdivision based on wellbore data and seismic interpretation of intra-basement facies and features. (a) map showing the synthetized basement geology, including structures and the East and West lithological domains at the level of the tBas horizon. (b) uninterpreted A-A' seismic section, from which a (c) A-A' geologic cross-section with the interpretation of the lithologic and tectonic subdivisions of the basement is shown. For an expanded version of "b" please refer to Figure A2.

We also infer the presence of a high strain, sub-vertical shear zone that coincides approximately with the limit between NE and SE Clusters of intra-basement structures (Figure 3.11a). Along with the lack of continuity of structures between the clusters (Figure 3.6c), this limit points divergent dip directions of the basal geobodies, to NW on NE Cluster and to SE in the SE Cluster (Figure 3.11c). It also coincides with the Central Fault Zone (CFZ) of the rift faults. The segments of the CFZ shows a remarkable straight geometry compared with the others whose anastomosing pattern are predominant. Such geometry is consistent with control given by a single, sub-vertical basement structure. Considering the sub-vertical nature of this shear zone, we are not able to map it in the seismic data. Therefore, this structure might be a subsidiary NE-SW structure, similarly to the shear zones observed in the Oriental Terrane of the Ribeira Belt, parallel to its contact with the CFTD (Figure 3.1a). Further pre-breakup reconstructions might shed some light in this subject.

3.6.2 Rift tectonics and models for basement reactivation

The style of rift faults that nucleated from and/or as a result of reactivation of basement shear zones has been discussed in recent studies. While some authors considered the basement shear zones as discrete discontinuities for both analogue models and case studies (e.g. Deng et al., 2018; Vasconcelos et al., 2019 , respectively), others take into account not only the geometry but also the 3D shape of shear zones (Fazlikhani et al., 2017; Collanega et al., 2019; Osagiede et al., 2020). Collanega et al. (2019) concluded for the Taranaki Basin (New Zealand) that broader shear zones lead to *en-échelon* normal fault arrays while narrow shear zones result in continuous faults within the sedimentary cover. It is essential to mention that the Taranaki Basin experienced only an initial rifting

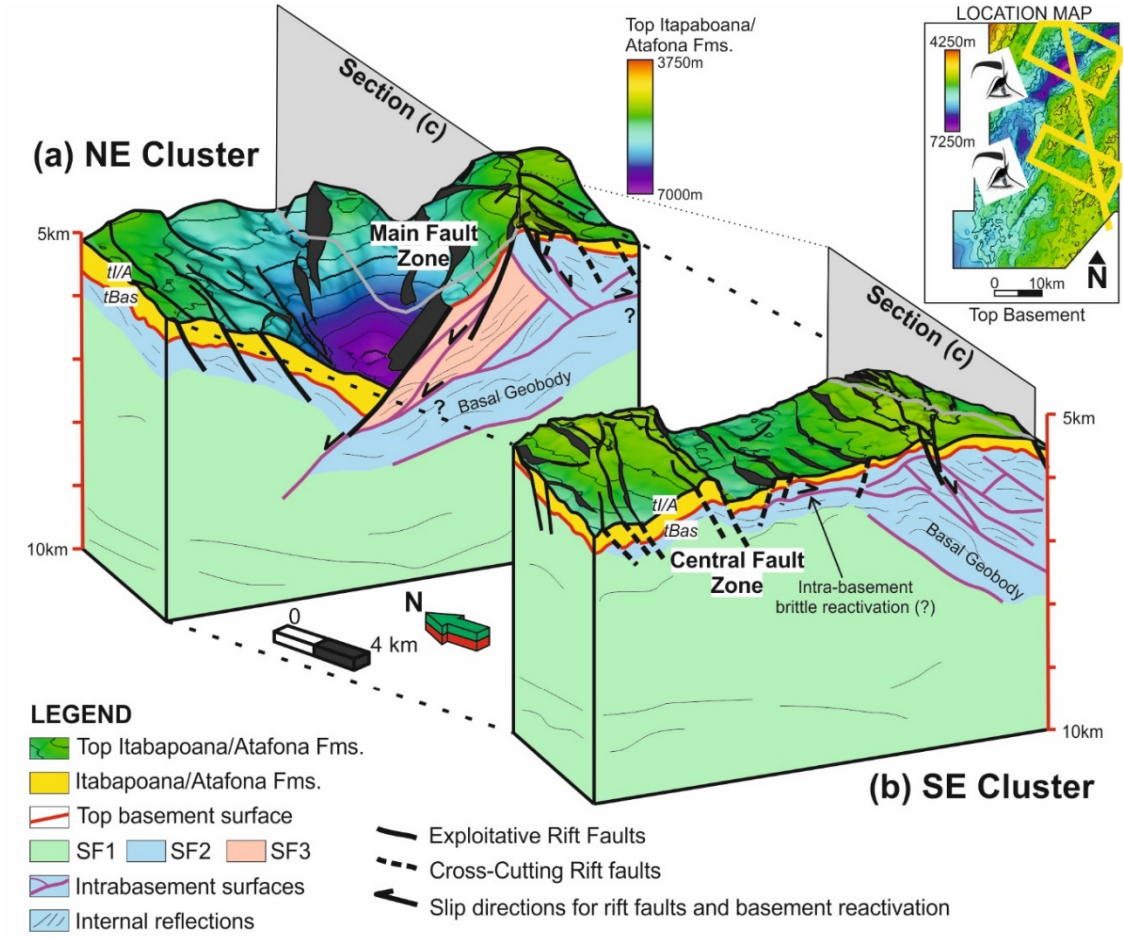
deformation and shows a stratigraphically simple and thick (up to 1800 m) sedimentary filling.

In this study, we used models of basement/rift faults interactions through brittle reactivation proposed to the North Sea Rift by Phillips et al. (2016) and Fazlikhani et al. (2017) as a starting point for the discussion. Both papers considered the angle between basement shear zones and rift-related faults in a profile view as classification criteria, which is a consequence of the angle between the pre-existing intra-basement structures and the extension direction during rifting. Three main schematic models are proposed to explain the interactions between shear zones and rift-related faults, named Merging, Exploitative and Cross-cutting faults (see Figure 3.14 in Phillips et al., 2016). Exploitative rift faults reactivate shear zones parallel to their internal foliation while merging faults became parallel to the shear zones at depth.

Our seismic interpretation identified examples of these three major types of interactions between intra-basement structures and rift-related faults (Phillips et al., 2016). Exploitative and Merging faults are more abundant than Cross-cutting faults as a consequence of the relatively well oriented (roughly orthogonal) basement grain with respect to the average WNW-ESE extension direction of rift tectonics (Figure 3.12). The classification used by Phillips et al. (2016) was designed for the wide and discrete Caledonian shear zones bounded by less heterogeneous basement. However, when investigating a more complex basement structure observed in the Neoproterozoic supracrustals of the Cabo Frio Tectonic Domain, some considerations were necessary. Although we have observed a few examples of the Exploitative type in the SE Cluster (Figure 3.9d), it was not practical to separate the Merging and Exploitative types of interaction. The main reason is the relatively thin sedimentary cover (below the salt) when compared to the area where this classification

was initially proposed (Phillips et al., 2016). Thus, both mechanisms mean that to some extent, the exploitation of pre-existing discontinuities occurs through brittle reactivation. For this reason, we classified the interactions of the basement rift faults as Exploitative and Cross-cutting (Figure 3.12).

It is evident that the attitudes of rift faults in this study (Figure 3.5b) might be taken to suggest a persistent WNW-ESE extension direction if we simply consider that the structures are a conjugate set of normal faults with pure dip-slip motion. This extension direction is compatible with the regional extension directions of the Campos Basin (Heine et al., 2013; Savastano et al., 2017). However, under closer scrutiny, by comparing the relative age of fault activity and the syn-kinematic depocentres of Rift Climax (RC) I and RCII sequences (Figures 3.4c, 3.4d, 3.5d, & 3.5e), it is considered more probable that not one, but two distinct extension directions can be interpreted (Figure 3.13).



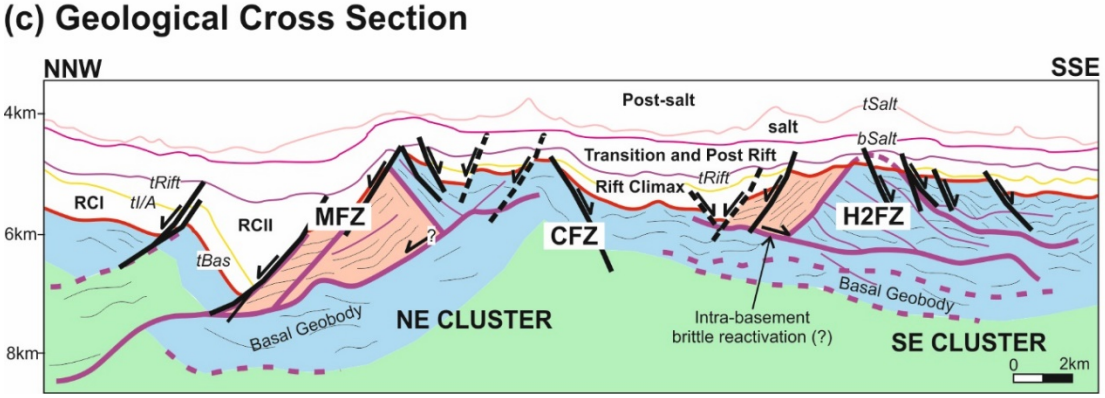


Figure 3.12: Modes of interaction between intra-basement structures and rift faults in the study area. On the top, (a) and (b) shows a 3D perspective of these interactions for NE and SE intra-basement clusters, respectively. Below, a synthetic geological cross-section (c) across both domains showing the contrasting styles of reactivation between NE and SE clusters. Uninterpreted seismic data is shown on Figure 3.11b. Slip motions of rift faults and within basement during rifting are shown. MFZ, CFZ, & H2FZ are rift fault zones.

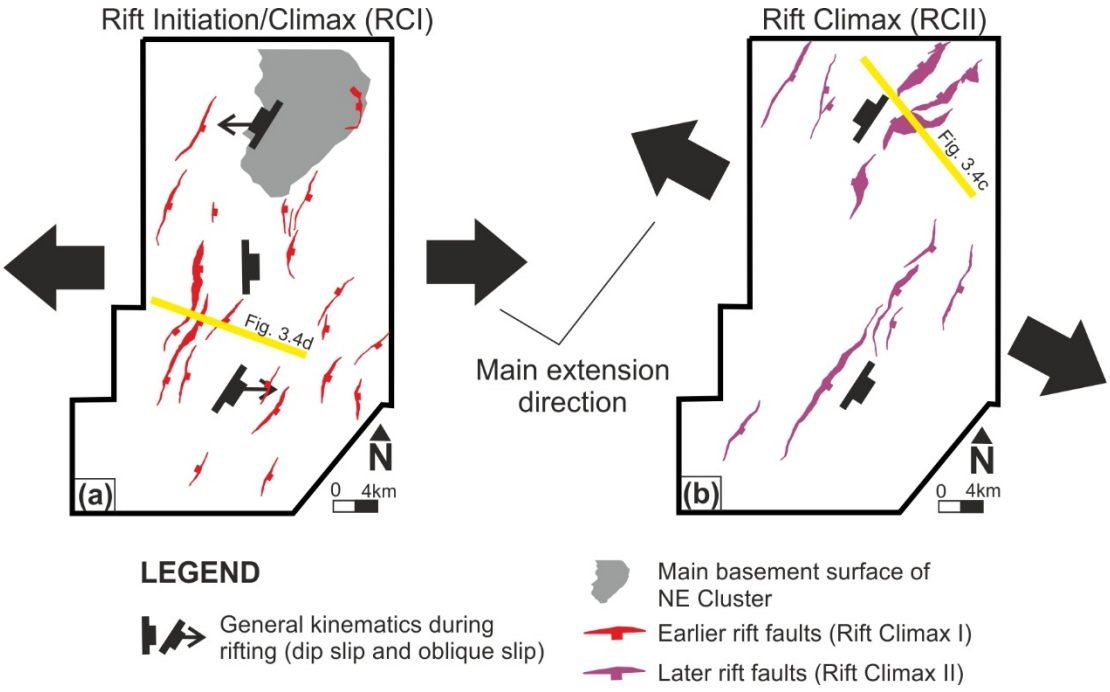


Figure 3.13: Interpreted extension directions during the rift initiation and climax tectonic phases, which are equivalent in time with the sediments of the RCI & RCII, respectively. (a) and (b) presents the fault traces that show syn-kinematic wedges (divergent) seismic reflections of, respectively, RCI & RCII sediments in the hanging wall of faults of each age group. Dip direction of normal faults combined with the position of the syn-kinematic depocentres (Figure 3.5d & e) were used to infer the extension directions for Rift Climax I (a) sequence and Rift Climax II (b) sequence.

This alternative interpretation of two distinct extension directions should be taken with three further caveats, however. Firstly, some of the faults without syn-kinematic divergent wedges are assigned relative ages of initial activity (propagation to surface) based on the assumption that the fault initiation is marked at the maximum throw horizon. There may be exceptions to this widely used criterion (Walsh & Watterson, 1988), for example, where a basin is substantially underfilled during fault-controlled subsidence (Cartwright, 1991), particularly in structural highs. Secondly, the presence of basement heterogeneities can potentially induce stress perturbations that could lead to faults nucleating oblique to the regional stress field (Deng et al., 2018; Collanega et al., 2019; Osagiede et al., 2020). In fact, this case of sub-parallelism between intra-basement and rift structures is observed in

the NE Cluster (compare Figures 3.7f & h) but not in the SE Cluster (compare figure 3.9e & g), where basement and rift structures show the same strike direction. Finally, there are uncertainties in the actual propagation histories of faults that might root at depth into crustal shear zones. For example, the tendency for rift bounding normal faults observed onshore and offshore of Thailand to exhibit low angles shows their ability to reactivate despite being severely miss-oriented with respect to regional stresses (Morley, 2014). This could be the case of the deeper basement fabric where the MFZ nucleated (Figure 3.12c). Although these considerations are valid for the East Domain, faults that nucleated in the homogeneous basement of the West Domain (Figure 3.11a) are unlikely to have been influenced directly in their strike during propagation by basement heterogeneity and thus allow us to make a case for two distinct extension directions based on relative dating.

The relative age of syn-kinematic wedges for faults with contrasting orientation therefore leads us to propose that there was an E-W extension direction operative during the deposition of the RCI sequence that then progressively rotated to a NW-SE direction during RCII. Faults with RCI syn-kinematic wedges show average strike at NNE-SSW while faults with RCII wedges are NE-SW oriented (Figure 3.13). The spatial distribution of the earlier faults (RCI age), shown in Figure 3.5d, is uniform within the studied area and, with the exception of the H3FZ, does not include the fault zones of Figure 3.5c.

Earlier faults can be considered as rift initiation faults, with strain uniformly distributed through growth of generally small-scale faults despite the abundance of intra-basement heterogeneities in the East Domain. Although significant deposition of RCI is observed in some places, the N-S H3FZ shows the most significant wedge-shaped deposits of this age (Figures 3.4d & 3.5d), suggesting that this structure nucleated orthogonally to the active extension direction. Less significant RCI depocentres are found on the hanging wall of the

Main Fault Zone (MFZ), although it is obliquely oriented to the E-W extension along with intra-basement structures exploited during the nucleation of the MFZ. It is not clear if the central and northern segments of the MFZ were active during RCI since no thickening of RCI sediments is observed on the hanging wall and RCI sediments are absent in the footwall as a result of non-deposition or later erosion.

Later rift faults that nucleated during the deposition of the RCII seismic-sequence mostly occupy the East Domain of the study area (Figure 3.5e), roughly coinciding with the position of NE and SE Clusters of intra-basement heterogeneities. In addition, Figure 3.5e shows that most of the fault segments of the MFZ and CFZ, along with significant part of H2FZ, nucleated or have their peak of tectonic activity during the RCII. Faults with syn-kinematic wedges of RCII sediments are NE-SW oriented (Figures 3.4c & 3.13b) sustains the interpretation of a NW-SE extension direction during RCII. The strain localization along the fault zones developed during RCII is in accordance with Walsh et al. (1991), where is concluded that as faults grow, many small faults will no longer be required and will become inactive. Later faults are concentrated in the heterogeneous basement in the East Domain, while only a few occurring in the more homogeneous West Domain. From our results, is suggested that such strain localization could be controlled by intra-basement structures, which could explain the abundance of RCII faults over the East Domain, especially in the SE Cluster (Figures 3.5e & 3.13b). Although Walsh et al. (1991) predict that the strain tends to concentrate in few structures during the late rift climax, the abundance of intra-basement structures that were well oriented to the active extension direction does not follow such a strain evolutionary path.

A supplementary control of the strike and dip direction of basement structures on the mode and style of basement reactivations is given by the thickness of heterogeneous basement,

expressed by seismic facies (SF2 & SF3) underneath the tBas horizon (Figure 3.12b & c). Whereas in the North Sea, basement structures are interpreted to occur up to 10 km below the Base Rift horizon (Fazlikhani et al., 2017), in the study area this deeper limit ranges from 4 km below the Top Basement horizon (i.e. up to 8 km depth) to zero (Figures 3.6b & 3.12b). This shallower limit of observable basement reflectivity could be simply related to frequency attenuation with depth. However, the transparent seismic response suggests that SF1 below the Basal Geobody in the NE and SE clusters probably represents similar basement geology as in the West Domain. Also, the SF1 occurs at similar depths in the West Domain to that in which SF2/SF3 are observed in the East Domain, refuting the hypothesis of frequency attenuation. When SF2/SF3 thickness is less than 500 m, Cross-cutting interaction type tends to dominate (Figure 3.12b). Coincidentally, basement fabric in the thinner portions of SF2 tends to show a low angle character (the Basal Geobody – Figure 3.12c), parallel to the predicted extension direction (Figure 3.13), so a Cross-cutting interaction is more likely to have occurred.

3.6.3 Basement reactivations within the NE Cluster

We observed that central and northern segments of the Main Fault Zone (MFZ) have an abnormal dip (low angle) and strike attributes (Figure 3.8e) when compared to the remaining mapped rift faults as a whole (Figure 3.5b). The MFZ is deeply rooted, merging with a low angle (<25^{o}) highly heterogeneous basement fabric, mostly constituted of SF3 (Figure 3.12a). The combination of MFZ attributes (Figure 3.8) such as obliquity with respect to the main conjugate pair of rift faults (Figure 3.5b) and the coeval deposition of thick syn-kinematic wedges of RCII sediments (Figure 3.4c) suggests that MFZ nucleates as a consequence of basement reactivation during the rift climax stage. Although is clear

that the peak of MFZ fault activity was during RCII, we cannot distinguish if the fault nucleated during the Rift Initiation (RCI) or RCII stage. For that, a study considering the E-W extension during RCI and the orientation of intra-basement structures beneath the MFZ could potentially test the possibility that the basement fabric would be reactivated under a E-W extension. The NE-SW strike, NW dipping low angle basement shear zones could have been obliquely reactivated during Rift Climax I (RCI) by E-W extension. The extensional component was meaningful, leading to deposition of significant RCI layers in the hanging wall (Figure 3.5d). However, there are no RCI sediments in the footwall of the MFZ and no fault-related syn-kinematic wedges of RCI sediments in the hanging wall. Later, the extension direction progressively rotated clockwise to NW-SE strike, therefore inducing dip-slip kinematics on the MFZ and accumulation of the thickest depocentres of RCII deposits in its hanging wall (Figure 3.5e).

The N-S oriented H3FZ and the southern segments of the MFZ have a slightly different evolution compared to its main sector. We suggest that the nucleation of the N-S structures was not triggered by reactivation of basement structures during rift initiation. The relative absence of basement heterogeneities in the expense of a more isotropic basement on W-34 nearby (Figure 3.10e) means that there are fewer structures upon which strain can localise, so faults nucleated regardless pre-existing discontinuities. From this, two possible interpretations are possible: (1) the nucleation of the H3FZ and southern segments of MFZ was concomitant with the onset of the oblique reactivation of basement structures on the NE-SW main segments of the MFZ during RCI. These segments eventually linked and later the H3FZ and the southern segments of MFZ became inactive while the main branch of MFZ kept evolving during the RCII as a consequence of the progressive clockwise rotation of the extension direction from E-W to NW-SE (Figure 3.13). (2) The H3FZ and

the southern segments of MFZ evolved as an isolated graben during RCI. Then the main NE-SW segments of the MFZ nucleated during RCII and thus linked southwards with the pre-existing N-S faults of the H3FZ and the southern tip of the MFZ. Either hypothesis explains the diachronous sedimentation of RCI & RCII sequences along the hanging wall of the MFZ (Figure 3.4b). A definitive answer would require detailed tectonostratigraphic and kinematic analysis, which is beyond the scope of this paper.

Recently, high-resolution Discrete Element Modelling (DEM) have been used to simulate the effects of pre-existing basement discontinuities on the onset and geometry of rift-related faults. Deng et al. (2018) built a DEM including a pre-existing basement discontinuity with constant area and dip angle, overlain by a 6 km thick sedimentary column, but changing its strike direction in order to create four scenarios of obliquity between basement structure and extension direction. Apart from the oversimplified basement heterogeneities and thicker sedimentary section compared to our study area, the resultant geometry from the model using a 60^{o} angle between the maximum extension direction and the orientation of pre-existing basement weaknesses is similar to the MFZ. Here we observed an average obliquity of 15^{o} (i.e. 75^{o} relative to the assumed main extension) with respect to the main strike of the normal faults. This finding reinforces the development of non-collinear rift faults as a consequence of stress-field perturbations induced by broad basement shear zones, such as the results obtained from 3D seismic data by Osagiede et al. (2020). Our interpretation is that the subtle oblique character of the shallower segments compared to the deepest sectors of MFZ along with the overall sub-parallelism between intra-basement and rift structures in the NE cluster (Figures 3.7f & g, respectively) are the consequence of stress-field perturbations propagated upwards through the sedimentary column during RCII.

A more localised, selective reactivation of basement structures is observed on the footwall block of the MFZ. The basement here comprises the eastern limb of the antiform, which merges with the basal geobody towards the east (Figures 3.7d & 12c). We suggest that rift faults in this position have shorter lengths and smaller displacements because of a combination of three factors: (1) the MFZ focused the strain in this region, in accordance with Walsh et al. (1991); (2) basement heterogeneities are less continuous and do not exhibit a persistent orientation when compared to the basement fabric near the MFZ; (3) heterogeneous basement (SF2/SF3) is progressively shallower eastwards and its internal anisotropies (Basal Geobody) are usually oriented at a high angle to rift faults (east of Figure 3.12a). This leads to cross-cutting fault-basement relationships rather than exploitative relationships (Phillips et al., 2016).

3.6.4 Basement reactivations within the SE Cluster

Reactivations of basement shear zones during rifting in the SE Cluster shows a substantial difference in style and mechanisms when compared to the NE Cluster (Figure 3.12). In the NE Cluster, the MFZ localised most of the strain, whereas in the SE Cluster faulting is distributed along several small displacement faults (Figures 3.5 & 3.12). Our interpretation for the contrasting styles of basement reactivations within the SE Cluster is that basement structures within this area are more abundant and is consisted of smaller intra-basement structures in terms of length/area than those in the NE cluster (compare Figure 3.7b & 3.9b, Figure 3.12c). This means a more diffuse strain distribution, where many intra-basement surfaces were continuously reactivated during both the Rift Climax I & II stages thus accommodating minor displacements. On the contrary, few basement structures being reactivated during the evolution of the MFZ (NE Cluster) but accommodating larger

displacements. Strain hardening of the fault planes in early rift faults combined with the number of pre-existing intra-basement structures well oriented to the rift extension that are prone to be reactivated are the most likely explanation for strain distribution in the SE Cluster. This interpretation is supported by noticeable parallelism in strike between intra-basement structures and rift faults, observed both in stereograms (Figures 3.9e & g) and time-slice interpretations (Figures 3.9b & c). In addition, the lower dip angle of basement surfaces combined with the parallelism in strike with rift faults agrees with fault-merge and fault exploiting mechanisms (Phillips et al., 2016) as the predominant basement-rift faults interactions (Figure 3.12b). A similar exploitation mechanism is suggested where the intra-basement structure exhibits an antiform geometry, thus controlling rift faults with dips conformable to the fold limbs (Figure 3.12c). Finally, the Cross-Cut basement-rift faults interaction type predominates where basement heterogeneities are thinner underneath the tBas (basal geobody) and exhibit a predominantly high angle with the rift faults (Figure 3.12b & c). This geometric relationship makes it very difficult for basement structures to be reactivated during the extension such that rift faults nucleates at a high angle with respect to basement anisotropy.

A potential additional mechanism of strain distribution throughout basement heterogeneities during rifting is low angle shear zone reactivation, similar to the outcomes of Fossen et al. (2017). They used macro and micro-structural analysis in outcrops supported by geochronological data to evidence brittle reactivations as shear fractures along low to very low-angle (*c.* 5^{o}) Caledonian basal thrust or décollements on onshore Norway. This type of movement is exclusively intra-basement reactivation and therefore not obvious on seismic data due to the lack of seismic kinematic markers within the basement. An example of such mechanism is observed on the transition between the NE

and SE clusters in Figure 3.12c. Heterogeneous SF3 and merging rift faults interact with a shallow Basal Geobody at a right angle, on which top we assume low angle reactivation. A similar mechanism might also be present within the basement adjacent to the MFZ (Figure 3.12).

3.7 Conclusions

1. 3D seismic facies interpretation of intra-basement reflections leads to the identification of two contrasting basement domains. The East Domain is heterogeneous and is equivalent to the supracrustals of the Cabo Frio Tectonic Domain (CFTD). The West Domain is homogenous and could represent either the Paleoproterozoic basement of the CFTD or the Oriental Terrane of the Ribeira Belt.
2. The rift faults developed from Hauterivian to Barremian as a result of a progressive rotation of extension from E-W to NW-SE, resulting in two fault sets with distinct episodes of deposition of syn-kinematic wedges. Such episodes are approximately equivalent to the rift initiation and rift climax tectonic stages.
3. The rift tectonics took advantage of a basement structure, roughly orthogonal to the extension direction, resulting in a dominance of exploitative brittle reactivation of basement structures during rifting.
4. Contrasting basement heterogeneity between the East and West Domains controlled the strain distribution during rift-related faulting. In the heterogeneous East Domain, the pre-existing fabric was selectively reactivated whenever the orientation was favourable, resulting in faults forming progressively as the extension direction rotates. Where the basement is homogeneous (West Domain), early formed faults tend to dominate throughout the rifting.

Statement of Authorship for joint/multi-authored papers for PGR thesis

To appear at the end of each thesis chapter submitted as an article/paper

The statement shall describe the candidate s and co-authors independent research contributions in the thesis publications. For each publication there should exist a complete statement that is to be filled out and signed by the candidate and supervisor **(only required where there isn't already a statement of contribution within the paper itself).**

Title of Paper	Basement geology and its controls on the nucleation and growth of rift faults in the northern Campos Basin, offshore Brazil.
Publication Status	X Published □ Accepted for Publication □Submitted for Publication □Unpublished and unsubmitted work written in a manuscript style
Publication Details	Strugale, M., Schmitt, R.S. & Cartwright, J. (2021). Basement geology and its controls on the nucleation and growth of rift faults in the northern Campos Basin, offshore Brazil. Basin Research, 33, 1906-1933. https://doi.org/10.1111/bre.12540

Student Confirmation

Student Name:	Michael Strugale		
Contribution to the Paper	I have performed all the seismic interpretation, established the investigation lines, set up hypotheses, correlated the results of the seismic interpretation with wellbore data and compared with case studies elsewhere. Structural mapping and analyses, figures and writing were also performed by myself. Co-author 1 is a specialist in the Precambrian basement in the counterpart onshore and helped with the interpretation and significance of geochronologic data, and reviewing the manuscript. Co-author 2 supervised the research and reviewed the manuscript.		
Signature	Michael Strugale	Date	28 OCT 2022

Supervisor Confirmation

By signing the Statement of Authorship, you are certifying that the candidate made a substantial contribution to the publication, and that the description described above is accurate.

Supervisor name and title:	PROFESSOR JOE CARTWRIGHT		
Supervisor comments	I fully concur with the statements above		
Signature		Date	28 OCT 2022

This completed form should be included in the thesis, at the end of the relevant chapter.

Chapter 4

Tectono-Stratigraphic Evolution of the Rift and Post-Rift Systems in the Northern Campos Basin, Offshore Brazil

This chapter was published in the 5th issue of the 34th volume of Basin Research Journal and was available online on the 29th of April 2022. This published chapter has an accompanying *Supporting Information* file that present complimentary geologic information and graphs and can be found in Appendix B. Minor changes were made following examiners suggestions. The research presented in this chapter is my work, however, it benefited from collaboration with Joe Cartwright, who supported with the research strategy, supervision and proof reading, and Luciano P. Magnavita and Romulo C. Stohler, who reviewed the first draft of the manuscript and provided constructive comments.

Strugale, M. & Cartwright, J.A. (2022) Tectono-Stratigraphic Evolution of the Rift and Post-Rift Systems in the Northern Campos Basin, Offshore Brazil. *Basin Research 34, 1655-1687*.https://doi.org/10.1111/bre.12674

4.1 Abstract

The Campos and Santos Basins have been a focus for subsurface studies since the discovery in 2006 of large accumulations of hydrocarbons in the Early Cretaceous rift and post-rift strata below Aptian evaporites. In this study, regional 2D seismic lines, a 3D seismic survey and well data were interpreted to reconstruct the tectono-stratigraphic evolution of the rift and post-rift stages in the northern sector of the Campos Basin. Detailed 3D seismic interpretation and geologic modelling were used to subdivide the presalt sedimentary record. This revealed a diachronous strain distribution along the Guriri Fault System (GFS), a roughly NE-SW striking fault-bounded horst that was a focus of rift-related deformation. The syn-rift succession is interpreted to be the product of two episodes of rifting (RP1 and RP2) with contrasting fault activity patterns and lithostratigraphy. Volcaniclastics and coarse siliciclastics of RP1 were deposited under WNW-ESE transtension that formed discontinuous half-grabens followed by extensive erosion and tectonic inversion. Structurally controlled bioclastic rudstones and hybrid deposits characterise RP2 and were deposited in elongated half-grabens that delimit the GFS horst, which developed under a NW-SE extension. Deposition under increasingly less tectonically active transitional and post-rift stages dominated by thermal subsidence gradually led to healing of the rift-related structural relief. Selective reactivation of rift faults testify active tectonic inversion through compression from immediate post-rift throughout evaporite deposition. These interpretations are put into the context of recent geochronological data of onshore dyke emplacement and the new age constraints for the end of deposition of the presalt sequence. Therefore, we propose an earlier onset of rifting in the Campos Basin, at the Berriasian.

4.2 Introduction

Several studies of rifting of the Campos Basin in the context of break-up of West Gondwana that formed the South Atlantic Ocean during the Early Cretaceous have been made using a combination of regional 2D seismic, well and potential field data (Ponte & Asmus, 1976; Chang et al., 1992; Stanton et al., 2019). However, relatively few studies have been made using high-resolution 3D seismic data at the scale of segments of basin-wide faults that constitutes the rift system (Fetter, 2009; Olivito & Souza, 2020; Alvarenga et al., 2021). Also, systematic structural mapping is only available for the Central sector of the Campos Basin (Guardado et al., 1989a).

Detailed petrographic and geochemical studies characterised the hydrothermal diagenesis in the rift transition to post-rift presalt carbonates in the North of the Campos Basin, with substantial impacts on reservoir quality (Herlinger Jr. et al., 2017; Lima & De Ros, 2019; Lima et al., 2020). These publications assumed that hydrothermal fluids moved upwards along faults developed during the rift phase. Hydrothermal fluid flow via geologic structures is a subject of broad relevance in subsurface resources geology (e.g. Sharp et al., 2010; Walsh et al., 2018) and are controlled by several factors, from constitution and properties of the basement and sedimentary column (Davies & Smith Jr, 2006; Hollis et al., 2017) to the tectonic regime (Sibson, 1992; Wiprut & Zoback, 2000).

However, the spatial organization and temporal constraints of the rift faults thought to work as conduits for hydrothermal fluids in the presalt succession are poorly understood. Also, the age constraints of the end of presalt and onset of evaporite deposition have been recently challenged (e.g. Tedeschi et al., 2017; Pietzsch et al., 2020), demanding new

investigations on the tectono-stratigraphic evolution of the presalt succession and onset age of rifting.

To undertake the first step towards a more comprehensive understanding of tectono-stratigraphic evolution in the North of Campos Basin, it is essential to 1) constrain in detail the strain distribution related to rift faults in the three-dimensional space and their influence on deposition of syn-rift sequences, and 2) describe the depositional architecture and the deformation in the post-rift sequences. Hence, the seismic architecture of syn-rift horizons and successions is interpreted and compared with some classic publications on tectono-stratigraphy of rift basins (Lambiase, 1990; Prosser, 1993; Morley, 2002; Gawthorpe & Leeder, 2008; Martins-Neto & Catuneanu, 2010). Also, studies on the Phanerozoic brittle reactivations and dyke emplacement in the adjacent onshore Precambrian basement (Calegari et al., 2016; Santiago et al., 2020) and magmatism in the Campos Basin (Almeida et al., 2013; Matos, 2021) are considered for a comprehensive understanding of the constraints of basin evolution. Such a comprehensive approach is necessary due to the poor geochronological control for the onset of rifting.

The aims of this paper are to:

(1) Establish the geometry and kinematics of the rift-related fault framework and their later inversion;

(2) Describe the rift and post-rift tectono-stratigraphic framework and

(3) Discuss our interpretations in the face of the new time constraints for the deposition of the presalt succession and evaporites.

4.3 Geological Setting

The Campos Basin is located in the Central Segment of the South Atlantic Ocean, which includes the contiguous Espírito Santo and Santos basins (East Brazil) (Moulin et al., 2010). These basins originated from rifting of West Gondwana during the Early Cretaceous (Rabinowitz & LaBrecque, 1979; Chang et al., 1992) and evolved as an initially magma-poor, then magma-rich breakup stage (Morgan et al., 2020). The Central Segment exhibits some remarkable tectonic features: 1) southward widening of the basin margin and a strong asymmetry of the necking zone and the continent-ocean boundary, 2) the role of the Santos and São Paulo Plateau as a kinematic 'buffer' between Central and the Austral segments (Moulin et al., 2010), and 3) anomalous rifting without the expected magnitude of rift-related subsidence, and which led to the development of a long-lived extensive shallow carbonate platform and the subsequent salt deposits (Karner & Gambôa, 2007; Pietzsch et al., 2018).

The study area is located 70 km offshore, on the continental slope of the northern part of Campos Basin. The structural map of the rift structures of the shallow water domain of the Central Campos Basin shows major faulted blocks bounded by alternating east and west-dipping NNE striking normal faults, which are laterally continuous for long distances (up to 200km) and have throws of as much as 2500 m (Guardado et al., 1989a) (Figure 4.1).

The rift system in the central and northern Campos Basin has its foundations in two distinctive basement units: the Oriental Terrane of the Ribeira Belt and the Cabo Frio Tectonic Domain (CFTD) (Schmitt et al., 2008; Stanton et al., 2019). The former is constituted by low-P high-T Neoproterozoic para- and ortho-derived gneisses intruded by several magmatic bodies, with high-angle NE-SW fabrics generated under a right-lateral

transpressional regime as result of polyphase amalgamation from ca. 650-500 Ma (Ebert & Hasui, 1998). The CFTD mainly comprises Paleoproterozoic orthogneisses (2.0 to 1.94 Ga) tectonically interleaved with medium to high T-P Neoproterozoic para-derived gneisses, both migmatized. The metamorphism and coeval ductile structures developed between 550 and 490 Ma due to a collisional event called the Búzios Orogeny (Schmitt et al., 2004). The CFTD has a predominantly low-angle NW-SE to N-S structural grain, orthogonal to the adjacent Oriental Terrane (Schmitt et al., 2004; 2016).

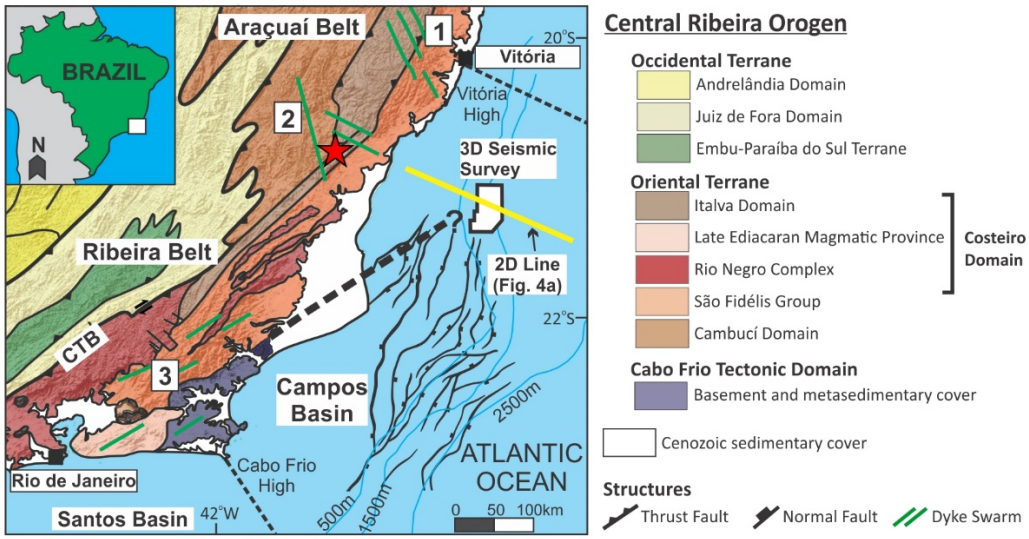


Figure 4.1: Location of the study area (3D seismic survey) and the 2D semi-regional dip seismic section. The geology of the onshore basement is represented as a simplified geological map (modified from Trouw et al., 2013 and Martins et al., 2021). It also shows the NW-SE fracture and Early Cretaceous dyke swarms (1 – Vitória-Colatina Lineament, 2 – Castelo and Alegre, and 3 – Serra do Mar, c.f. Almeida et al., 2021). Red star is the sampling sites of Santiago et al. (2020). CFTD: Cabo Frio Tectonic Domain (c.f. Schmitt et al., 2004). The main rift faults of the Central Campos Basin is also shown (Guardado et al., 1989b).

Two sets of fractures and dyke swarms striking NW to NNW transverse to the basement metamorphic grain in the onshore basement have their offshore projections close to the study area (Almeida et al., 2021): the NNW-SSE Vitória-Colatina lineament (Chang et al., 1992) and the Piúma/Itaoca (Castelo) Lineaments (Lourenço et al., 2016; Santiago et al.,

2020) (Figure 4.1). In common, these structures demonstrate a polyphase evolution, with alkaline dykes being emplaced during the Cambrian, and tholeiitic dykes in the Early Cretaceous age (see age compilation in Pessano et al., 2021). The dykes are interpreted as the result of orogenic collapse of the Araçuaí Belt during the Cambrian and to the opening of the South Atlantic Ocean during Early Cretaceous, respectively. Therefore, they show recurrent episodes of brittle deformation of which precise timing and kinematic relations remain unclear (Calegari et al., 2016; Lourenço et al., 2016; Santiago et al., 2020).

A relative tectonically quiescent period of more than 300 myr followed the Búzios Orogeny. From the Late Jurassic to Early Cretaceous, prior to the South Atlantic Ocean opening, several magmatic events were recorded in the region of Western Gondwana on which the Campos Basin formed. In the present-day onshore basement domain, Early Cretaceous dykes along the Vitória-Colatina lineament yield Ar-Ar ages ranging 136-128 Ma and were emplaced under slightly dextral oblique extension (Almeida et al., 2013). The Castelo dyke swarm reveals U-Pb Concordia age of 141±1.9 Ma (Santiago et al., 2020). Both dyke swarms have geochemical signatures and ages similar to other Upper Jurassic/Lower Cretaceous dyke swarms of the Brazilian coast (Almeida et al., 2013) and to the basalt floods of the Paraná-Etendeka Large Igneous Province (LIP), of which ages ranges from 135 to 131 Ma (Matos, 2021 and references therein).

The rift system formed during the onset of the Campos Basin in Central South Atlantic occurred under an E-W main extension direction, which varies from orthogonal to oblique to the present-day coastal line (Mohriak et al., 1990, Chang et al., 1992). Extension became increasingly oblique southwards and reached its maximum in the ultra-wide rifted margin of the Santos Basin (Araujo et al., 2022). During the early rift phase, magmatism within the Campos Basin was characterised by mafic dike injection onshore and extrusion of

continental flood basalts of the Cabiúnas Formation from the Berriasian to Barremian (Mizusaki et al., 1992; Santiago et al., 2020).

The Campos Basin sedimentary record is traditionally divided into three tectono-stratigraphic supersequences: rift, post-rift, and drift (Cainelli & Mohriak, 1999; Winter et al., 2007). The rift and post-rift supersequences span from Hauterivian to Aptian and represent the presalt succession. It begins with a volcaniclastic unit that represents the Cabiúnas Formation (Figure 4.2). Most relevant data from this unit came from shallow water drilling in the Central sector of the Campos Basin (Mizusaki et al., 1992). These authors demonstrated that Cabiúnas Formation tholeiitic basalts have similar bulk-rock chemistry and ages (K-Ar ranging 134-122 Ma) slightly younger than basalts of the Paraná-Etendeka LIP (135-131 Ma). However, Mizusaki et al. (1992) speculate that such younger ages found in the Cabiúnas Formation could be related to K_2O addition during alteration, affecting the K-Ar ages.

The Lagoa Feia Group is stratigraphically above the Cabiúnas Formation and extends to the top of the evaporites of the Retiro Formation, embracing both rift and post-rift stages (Figure 4.2). It comprises five formations separated by regional and local unconformities, thus representing the primary seismic-stratigraphic markers (Winter et al., 2007) (Figure 4.2). The study area is located in the outer (distal) tectonic-sedimentary domains of the rift section of the Lagoa Feia Group, where isolated grabens were initially filled with siliciclastics to mixed carbonate deposits that evolved to isolated carbonate platforms built over structural highs, continuously in lacustrine conditions (Dias et al., 1988; Muniz & Bosence, 2018).

The lower section of the rift phase is constituted of coarse siliciclastics to shales deposited under strong structural control, formally described as the Itabapoana and Atafona

Formations, respectively. Towards the end of rift stage, this system was replaced by bioclastic rudstones and hybrid laminites representing the Coqueiros Formation (Winter et al., 2007). Recently, its facies associations were reinterpreted in a 3D context and the lower section of the Coqueiros formations was placed in the rift stage, while the upper section was classified as a transition rift stage (Olivito & Souza, 2020).

During the post-rift phase, the onset of thermal subsidence led to the formation of an extensive shallow, highly alkaline evaporative lacustrine system in which the Macabu Formation was deposited (Chang et al., 1992; Pietzsch et al., 2018). This shallow lake was in turn replaced by a highly evaporative shallow marine setting, leading to the deposition of up to 2000 m of evaporites of the Retiro Formation. Traditionally, the age of evaporites is ca. 113 Ma, at the top of Aptian (Winter et al., 2007) (Figure 4.2).

From the Albian, the deposition of the drift supersequence triggered remarkable thin-skinned gravitational gliding of salt and related salt compression in the outer regions of the Campos Basin (Davison, 2007; Szatmari et al., 2021).

4.3.1 Revised age dating of the presalt sequence

The Lagoa Feia Group ranges in age from the Barremian to the Late Aptian (Bertani & Carozzi, 1985b; a; Winter et al., 2007; Thompson et al., 2015). Because of the endemic character of its fauna, it is challenging to make correlations with basins outside the Central Segment of the South Atlantic. Therefore, the depositional age of the presalt sequence had been constrained by radiometric data of underlying basalts of the Cabiúnas Formation (Mizusaki et al., 1992) and at its top by the age of the onset of evaporite deposition of the Retiro Formation (ca. 115 Ma).

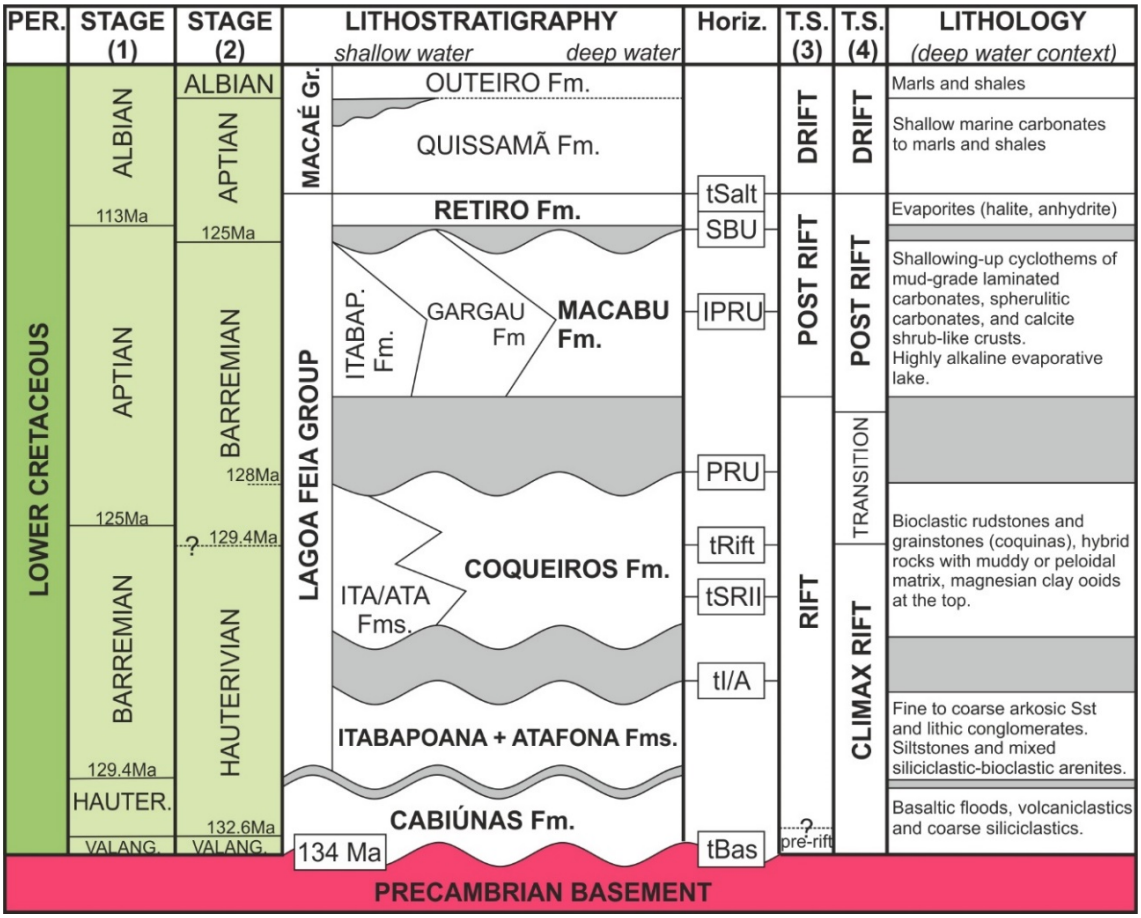


Figure 4.2: Compilation of the stratigraphic framework of the Campos Basin (not to scale). Ages and lithostratigraphy accordingly to Winter et al. (2007) (1). Ages according to Tedeschi et al., 2017; 2019; Pietzsch et al., 2020; Sanjinés et al., 2022 (2), where 128 Ma is the age for the top of the Coqueiros Formation. Horiz.: mapped horizons in this work: tSalt = top salt, SBU = Salt Base Unconformity, IPRU = internal post-rift unconformity, PRU = Post-Rift Unconformity, tRift = top rift, tSRII = top syn-rift II, tI/A = top Itabapoana plus Atafona Formations, tBas = top basement. T.S. (Tectonic Stages) are relative to the whole Campos Basin (Winter et al., 2007) (3) and for the deep water domain of the North Campos Basin (Olivito & Souza, 2020) (4). Lithologies were based on Winter et al. (2007); Lima and De Ros (2019) and Olivito and Souza (2020). The 134 Ma value is the oldest age obtained in the basalts of the Cabiúnas Formation (Mizusaki et al., 1992).

However, the assumption of a late Aptian age for the end of deposition of the Macabu Formation and onset of salt deposition has recently been challenged by several authors (Tedeschi et al., 2017; Lima et al., 2018; Tedeschi et al., 2019; Pietzsch et al., 2020) (Figure 4.2). New high-resolution carbon isotope ($\delta^{13}C$) profiles from shallow- and deep-water drillings in the Eastern Brazilian Margin (Sergipe-Alagoas, Campos and Santos Basins)

were correlated with well calibrated Tethyan sections. These new correlations constrain the end of major evaporite deposition in the South Atlantic to the early Aptian Oceanic Anoxic Event (OAE) 1a interval (124-125 Ma), thus the age of PRU as being 128 Ma (Tedeschi et al., 2019). Also, an increase in atmospheric CO_2, predating the OAE 1a event, resulted in a change in the mode of the carbonate factory, recorded in the last tens of metres of the Barra Velha Formation in the Santos Basin (equivalent to Macabu Formation in the Campos Basin). Hence, it puts further time constraints on the age of deposition of the top of the presalt sequence as not younger than Barremian (Pietzsch et al., 2020). Additional evidence came from new biostratigraphic records from wells drilled in the deep water portion of the Campos Basin, where Aptian sections of up to 800 m thick occur above the salt (Lima et al., 2018; Sanjinés et al., 2022).

However, the new constraints for the age of salt thereof have been challenged by a review paper (Szatmari et al., 2021). Their results kept the age of salt deposition within the usual time frame (i.e. 116-110 Ma), based on ^{39}Ar-^{40}Ar ages from evaporites in the Sergipe-Alagoas basin and a sub-salt volcano in the southern Santos Basin. The main argument of these authors is that the Tethyan section was located in a different realm than the Brazilian margin during Early Cretaceous, thus making the correlation problematic.

4.4 Methods

This study is based on commercial 2D (PSTM) and 3D (PSDM) seismic surveys and well data. Eight 2D semi-regional, dip-oriented deep seismic lines recorded from 8 to 12s TWT provided control of the crustal structure and contextualized the 3D survey. This 3D survey, corresponding to the study area of this work, is a 3D streamer Pre-Stack Depth Migration (PSDM) seismic data consisting of a merge of two seismic surveys (see Strugale et al.,

2021 for details). Well-logs and geological markers from 34 exploration and production wells named W01 to W34 were calibrated with the horizon interpretation in the 3D survey. Sidewall cores from the few wells used to calibrate the rift phase sedimentary units were invaluable in correlating seismic markers with the regional lithostratigraphic framework.

Six seismic horizons (BSU = Base Salt Unconformity, IPRU = Internal Post-Rift Unconformity, PRU = Post-Rift Unconformity , tRift = Top Rift, tI/A = Top Itabapoana plus Atafona Formations, tBas = Top Basement) that crudely correspond to the formal lithostratigraphic units described in Winter et al. (2007) were extensively mapped throughout the 3D survey and represent unconformities or their correlative surfaces in the depocentres (Figure 4.2). They subdivide the presalt sequence into six (seismic) tectono-stratigraphic sequences (TSS) comprising the syn-rift (SRI, SRII, SRIII), rift transition (RTR), and post rift (PRI, PRII) tectonic stages. Local surfaces were also mapped between these horizons to identify changes in the seismic architecture. Faults, fold axes and erosional scarps were also mapped throughout.

The interpreted 3D framework of horizons and faults were converted to a 3D geological model using the Structural Model workflow in Petrel™, based on a 50x50m mesh resolution. Depth, dip and dip direction attributes were extracted from every fault node to construct crossplots and equal-area lower-hemisphere stereographic diagrams (stereograms). True Vertical Thickness (TVT) isopach maps were generated from the model to evaluate thickness variations and evaluate fault-controlled accommodation. Edge effects due to lack of correlation at the margins of the 3D survey were considered during interpretation.

Faults were divided into subpopulations grouped by strike direction and structural domains (Fossen & Rørnes, 1996). Faults were also geographically grouped to represent genetically

related structures and hence fault branches (high strain) and intra-fault zones domains (low strain). The 3D model was used to perform fault length *vs* displacement (LxD) analyses and automatic extraction of horizontal separation (heave) for each modelled horizon.

3D kinematic analysis of more prominent basement faults in rift settings has generally been applied where hanging wall depocentres are thick (typically >2 km), and a large number of syn-rift reflectors occurs (e.g. Duffy et al., 2015; Collanega et al., 2019; Lenhart et al., 2019). Ideally, mapped horizons must not represent erosive or highly condensed/non-depositional events since comparing depositional thickness across the faults is critical for understanding the evolving fault activity. Therefore, underfilled half grabens are challenging to assess since they often exhibit erosion of the footwall crest (McLeod et al., 2000). Also, prominent footwall highs, local and regional unconformities often merge into a few tuned reflectors making correlation challenging.

In the study area, fault scarps, folds, syn-kinematic and prograding wedges, and local structural complexities pose further challenges when using these techniques. Taking account of these limitations, we opted for a more geometrical approach, where the hanging wall and footwall cutoffs of each seismic horizon and their respective seismic-depositional sequence were displayed in map view, resulting in coloured polygons representing the heave for each stratigraphic unit (Figure 4.3a). Heave polygons were analysed for either a single or a combination of horizons, result in tectono-stratigraphic maps on which the gross cumulative strain and spatio-temporal strain variations can be analysed (Figure 4.3b). However, this indeed takes no account of the possibility of underfilling in particular intervals, despite fault scarps occurring only in a handful of fault segments. Hence, for complex faults with significant across-fault correlation uncertainties, the cutoff lines were modified by additional seismic observation, like stratal terminations (onlap, erosional

truncation, and downlap), divergent syn-kinematic reflector and thickness variations, providing better time-constraints of the fault activity (see faults “d” & “e” in Figure 4.3a).

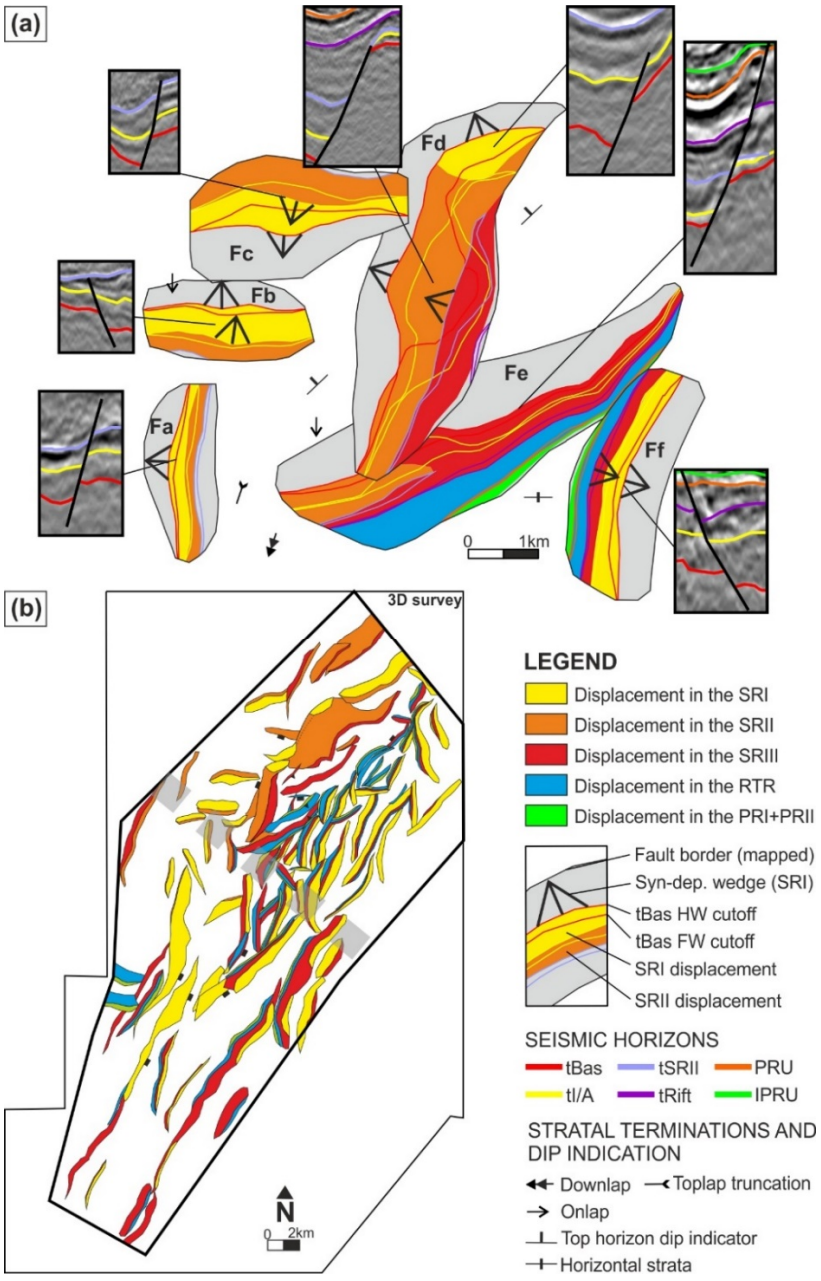


Figure 4.3: (a) Explanatory cartoon using six randomly picked faults (Fa to Ff) to explain the production of the tectono-stratigraphic maps. Seismic profiles across the structures are also shown to present the fault-horizon relationships and across-fault thickness variations. HW/FW cutoff lines were not entirely followed in faults “Fd” and “Fe”. Fd is likely to represent more than one fault segment. In this figure, stratal terminations and dip indicators are merely illustrative. Coloured polygons represents the TSSs (see text for description). (b) strain vs time distribution map according to the methodology shown in “a” for a selected region of the studied area.

4.5 Results

4.5.1 Structural framework

The integration of 2D and 3D seismic structural interpretations from this study were correlated with existing structural maps of the Central Campos Basin (Guardado et al., 1989b; a), to extend the documented structural framework to the northern limit of the basin. In the northern Campos Basin, normal faults striking crudely NNE-SSW, dip both east and west and constitute a similar rift-related fault framework to that mapped towards the south. Therefore, major structural features (i.e. the São João da Barra and Corvina-Parati Lows, and the Badejo high) extend northwards into the study area (Figure 4.4a). In a cross-section perspective, the presalt depocentres are younger towards the offshore, indicating the progressive rejuvenation of the rifting towards the spreading axis (Figure 4.4b). Another notable feature is the shallowing of the seismic Moho below the present-day shelf break where there are thicker rift deposits. This is interpreted as an early stage upper-crustal boudin of an originally thicker upper crust (c.f. Clerc et al., 2018). Also notable is the inverse correlation between the upper crust and presalt sedimentary thicknesses (Figure 4.4b).

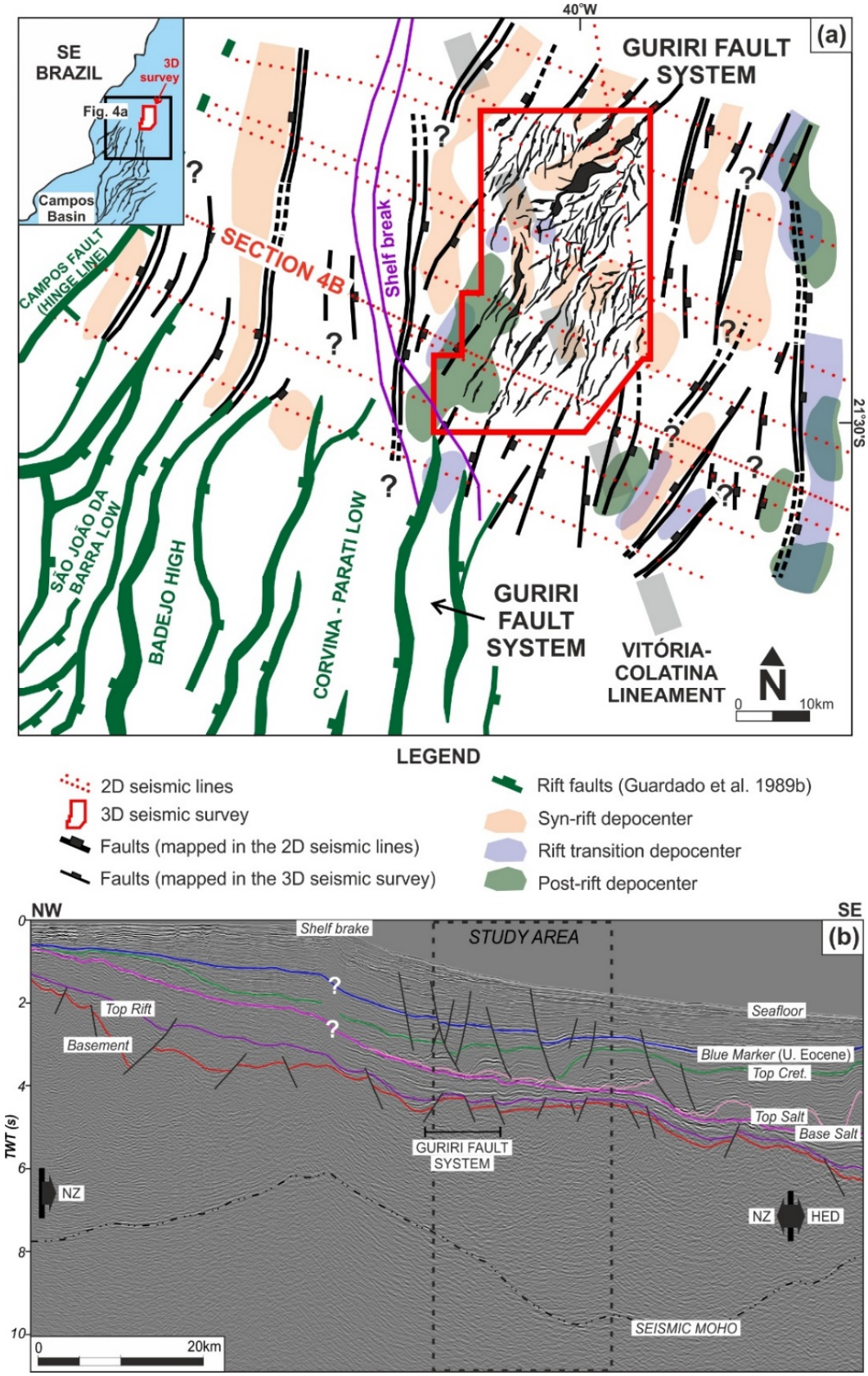
170 normal faults were mapped within the 3D survey. The strike of faults in the 3D survey has an average value of N40 with a significant population at N-S (Figures 4.5a, B2). Dip directions are evenly distributed to E and W, although the faults with major displacements (up to 1250 m) are antithetic to the regional basin dip. Dip angle tends to increase towards the top of the presalt sequence.

Fault distribution and patterns in map view were used to subdivide the area into three major structural domains. These correspond to a central, roughly NE-SW-oriented horst, flanked

by two domains that are structurally lower at the basement level (Figure 4.5a). This horst is 10 km wide and is delimited by the major faults that are the strain loci of the area (Figure 4.4a). The central horst is here named Guriri Fault System (GFS). To the west of GFS, the structural low is denominated the Inner Guriri Low, and to the east is the Outer Guriri Low. These three main structural domains exhibit internal deformation by subsidiary faulting, denoting internal structural highs and lows (Figure 4.5b).

The fault networks that focused the strain, thus acting to delimit the margins of the GFS are subdivided into three fault branches (GFSN, GFSE, & GFSS) (Figure 4.5a). The GFSN and GFSE have fault segments dipping to a single direction (west and east, respectively), while the GFSS exhibits structures dipping to both directions. Elsewhere, a footwall complex (FWC) represents the major positive structural element, flanked to the SSW by a depocentre (Low C). Within the Inner Guriri Low, two internal depocentres are observed (A & B), and the Outer Guriri Low has two internal lows (Low D and Low E) and one internal high (Well 33 High – W33H). LxD_{max} analysis demonstrate that GFS branches focused the strain (Figure B3), and stereographic diagrams show that faults within the GFS branches have a main strike direction (NE-SW) that differs from the average direction of the faults elsewhere (NNE-SSW) (Figure B4).

The structural contours of BSU (base salt) and the isopach map for the presalt sequence are shown in Figures 4.4c & 4.4d, respectively. Interestingly, the latter barely records the rift-related structural framework of Figure 4.5a, attesting the deposition of a significant succession (i.e., the post-rift units) in a different tectonic setting.



(Figure 4.4 - Caption on next page)

Figure 4.4: a) Semi-regional fault framework at top basement level, mapped from 2D and 3D seismic survey (red polygon). Location map is based on Figure 1. The framework is correlated with the fault interpretation of Guardado et al. (1989a). The Vitória-Colatina Lineament is projected from the onshore. b) Interpreted semi-regional two-way time 2D seismic line showing the shallow- to deep-water transition. The crustal domains of the Campos rifted margin (c.f. Stanton et al., 2019) are shown, where NZ is Necking Zone and HED is Distal Highly-extended Domain. The continental-oceanic crustal boundary is aprox. 75 km to the east of the section limit. Note the shallowing Moho and the significant thickness of the presalt section in the shallow water. Depicted in the study area the Guriri Fault zone discussed in this work. For the uninterpreted seismic section, see Figure B1.

The GFSN hosts the major faults in the 3D survey area, with >1000m maximum displacements. The fault pattern in map view is highly segmented with curvilinear fault traces whose strikes range between N-S and NE-SW, and dip systematically to NW. Also, dip angles decrease northwards along the strike, from 45° up to 25°, and splay into two segments towards the north (Figure 4.5a,b). The GFSN has the Low A as the hanging wall block, hosting the thickest depocentre in the area with up to 2.6 km of presalt sediments. Low A consists of three subsidiary hanging wall depocentres which are adjacent to zones of maximum displacement of the main segments of the fault zone (c.f. McLeod et al., 2000). The footwall of the GFSN (i.e. FWC) is internally faulted by NNE-SSW striking, oblique to GFSN and GFSE, mostly E-dipping faults with displacements < 250 m (Figure 4.5b).

The GFSE is the eastward limit of the GFS and constitutes an array of quasi-parallel fault segments that are either hard- (breached relays) or soft-linked (Figure 4.5b). Segments dip systematically to the E with angles ranging from 45° to 70° and maximum displacements of up to 600 m. To the east, the Outer GFS Low has subsidiary depocentres in the hanging wall of the major segments of GFSE (Lows D & E) and an internal high (W33H), which has the thinnest presalt of the 3D survey (Figure 4.5d). Faults within Outer GFS Low have

maximum displacements ranging from 200 to 400 m and are organized as a conjugate set whose intersection branch line is N25 oriented.

The GFSS is an apparent direct south-westward continuation of the GFSN branch but has a contrasting polarity of its main constituent faults, dipping predominantly SE. The east-dipping faults strike N-S to NNE and represent the structures with the largest maximum displacement values, of up to 500 m, that in turn delimit the half-graben of Low C (Figure 4.5a,b). During the course of the rifting, new west-dipping NE-SW striking faults nucleated westwards in an apparent southern extension of the GFSN branch.

We interpret a roughly NW-SE striking transverse structure to the GFS as an accommodation zone (c.f. Morley, 1990) (Figure 4.5a). This interpretation is based on two main lines of evidence. Firstly, an alignment of a number of breached relays and fault tips (Figure 4.5a,b), and secondly, a demarcation in changes in thickness distribution of the presalt tectono-stratigraphic units.

4.5.2 Seismic-stratigraphic framework

The primary hierarchy of the subdivision of the presalt sequence in the study area is two tectono-stratigraphic supersequences: syn-rift (SR), and post-rift (PR), separated by a rift transition (RTR) sequence. The terminology and interpretational diagnostics leading to this subdivision into supersequences was adapted from previous regional and local scales works (Cainelli & Mohriak, 1999; Olivito & Souza, 2020, respectively). In addition, internal unconformities and their correlative conformities allowed the subdivision of the supersequences into units with their own internal organization and termination patterns of seismic reflectors, lithological content, and thickness distribution. They represent units

which are lower in the stratigraphic hierarchy, and therefore denominated as (seismic) tectono-stratigraphic sequences (TSS) (Figure 4.6).

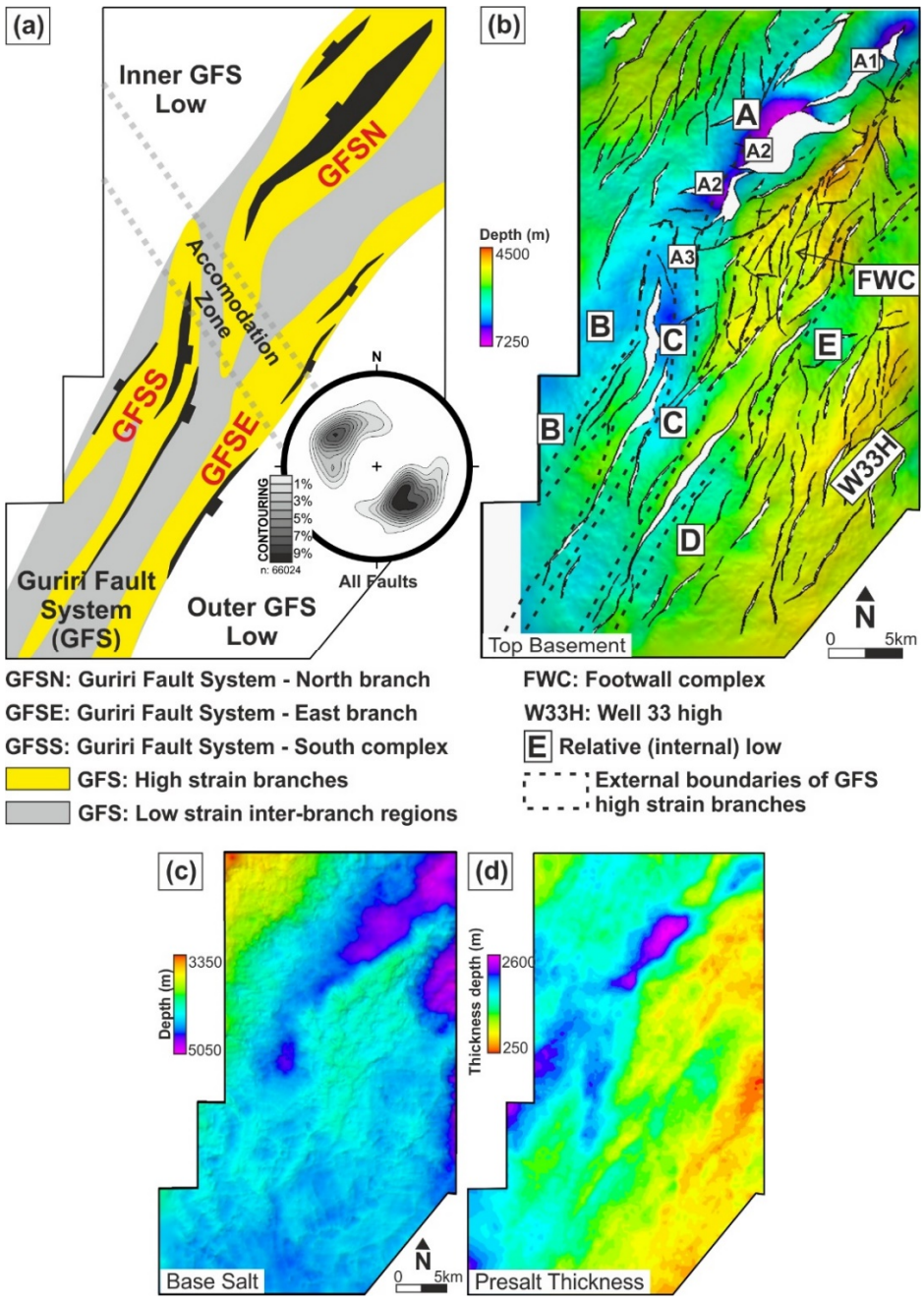


Figure 4.5: (a) Scheme of the major NE-SW trending structural domains showing the GFS (grey), their branches (yellow) and the adjacent structural lows (Inner and Outer GFS Lows). Simplified traces of the major fault segments within the GFS branches (yellow) and stereographic diagram of all the mapped faults are also shown. (b) Top basement (tBas) structural map showing the local structural lows (A to E), their internal subdivisions (A1-3) and highs (FWC, W33H). Dotted lines are the external boundaries of the GFS branches shown in 'a'. (c) Base salt (bSalt) structural map. (d) Thickness map of the presalt sequence.

Six TSSs were recognized; three representing the syn-rift supersequence (syn-rift I, II, & III - SRI, SRII, SRIII), one is equivalent to the rift transition (RTR), and two represent the post-rift supersequence: post-rift I (PRI) and post-rift II (PRII). The syn-rift TSSs show the diachronous distribution of divergent seismic reflectors (wedges) against faults and particular terminations of seismic reflectors (onlaps and truncations) against the delimiting horizons (tI/A, tSRII), justifying this subdivision. Also, the horizon between PRI and PRII sequences (IPRU) shows truncations and contrasting gamma-ray signatures between these TSSs (Herlinger Jr. et al., 2017).

The gross stratigraphy is well-calibrated by well markers and sidewall cores. The following interpretations are based in geological cross-sections and thickness maps (Figures 4.6 & 7, respectively) that evidence the spatio-temporal changes in the distribution and internal organization of each of the TSSs. To illustrate the main lithotypes, side-wall cores from selected wells are displayed in Figure A5.

4.5.3 The syn-rift supersequence

4.5.3.1 Syn-rift I TSS (SRI)

This unit is delimited at its base by a major unconformity (tBas) that separates the Precambrian basement from the sedimentary section. The top surface is also unconformable (tI/A), occurring as an erosive truncation in the structural highs and either as correlative conformity or onlapped surface in the depocentres (Figure 4.6a,c). In Low C, this unit defines classical divergent wedge geometry that are diagnostic of syn-depositional faulting (Figure 4.6c). Elsewhere, SRI commonly occurs as parallel layered internal reflectors, including in the hanging wall of some major GFSN faults (Figure 4.6a). Parallel configurations are commonly inferred as being pre-rift in a rift context, but this is

not considered likely here. Instead, the parallelism is interpreted as low strain syn-rift, where distributed faulting provides the accommodation space, rather than a single major fault leading to pronounced fault block rotation and divergent geometry.

The SRI isopach map shows three NNE-SSE-trending depocentres in the centre of the 3D survey of which Low C is the westernmost and thickest, with >900m of sediments (Figures 4.6c, 4.7a). Interestingly, the map distribution of the SRI thickness shows little correlation with the GFS branches (compare with Figure 4.5a).

Five wells penetrated to the tBas horizon (W01, 2, 4, 5, 34). The recognition and seismic interpretation of the tBas horizon in the study area is not straightforward and was investigated in detail in Chapter 3. Three wells found SRI basalts that sit on top of the basement when it is present (W04, 33, 34). Wells 33 and 34 drilled coarse siliciclastics over basalts, whilst in W04 bioclastic rudstones of the syn-rift III (SRIII) sequence overly SRI basalts. Wells W12, 14, & 25 only reached the top of the SRI and drilled medium to coarse siliciclastics with high feldspar content.

SRI is equivalent to three lithostratigraphic units, Cabiúnas, Itabapoana and Atafona Formations (Figure 4.2). The basalt thicknesses in the wells are below the vertical seismic resolution (~90 m) and, therefore, the top of Cabiúnas Formation was not mapped. Also, the seismic signal of SRI and available well-data made any differentiation between the Itabapoana and Atafona Formations impossible.

4.5.3.2 Syn rift II TSS (SRII)

The syn-rift II (SRII) sequence is delimitated at its base by the tI/A unconformity and at its top by the tSRII horizon. SRII internal reflectors are parallel or onlap onto the tI/A near the active divergent wedges (Figure 4.6a,b), except for a localized truncation over the Low

A1 (Figure 4.6d). The upper section of SRII is often conformable to tSRII in dip sections (Figure 4.6b). However, the strike cross-section shows that tSRII pinches out and is truncated towards the south (Figure 4.6d) and onto the inverted Low C (Figure 4.6f). Deposition of SRII was coeval with substantial footwall erosion in the GFSN, thus constituting a fault scarp that was onlapped during SRIII deposition (Figure 4.6a).

The main characteristic of the thickness distribution of SRII is its occurrence as a sub-basin (Low A) within the Inner GFS Low in the hanging wall of the GFSN (Figure 4.7b). SRII is absent by non-deposition or erosion elsewhere. Up to 1 km of sediments accumulate in this sub-basin and they show remarkable divergent wedges within Low A2 (Figure 4.6a), where the GFSN has its maximum displacement. Within Low 2, a strike cross-section shows that the upper SRII thickens then onlaps onto tI/A horizon towards Low A1 (Figure 4.6d). Elsewhere, parallel to tSRII internal seismic reflectors are predominant (Figure 4.6a,b,d).

There is no well-calibration for the SRII; therefore, its lithology will be interpreted in the context of the following SRIII TSS. The limited areal occurrence of SRII implies that the tI/A and tSRII horizons merge elsewhere as tSRII, consequently representing a significant gap in the sedimentary record (Figure 4.6c,e,f). However, is not clear if the absence of SRII is the consequence of non-deposition, pre-SRIII erosion, or both.

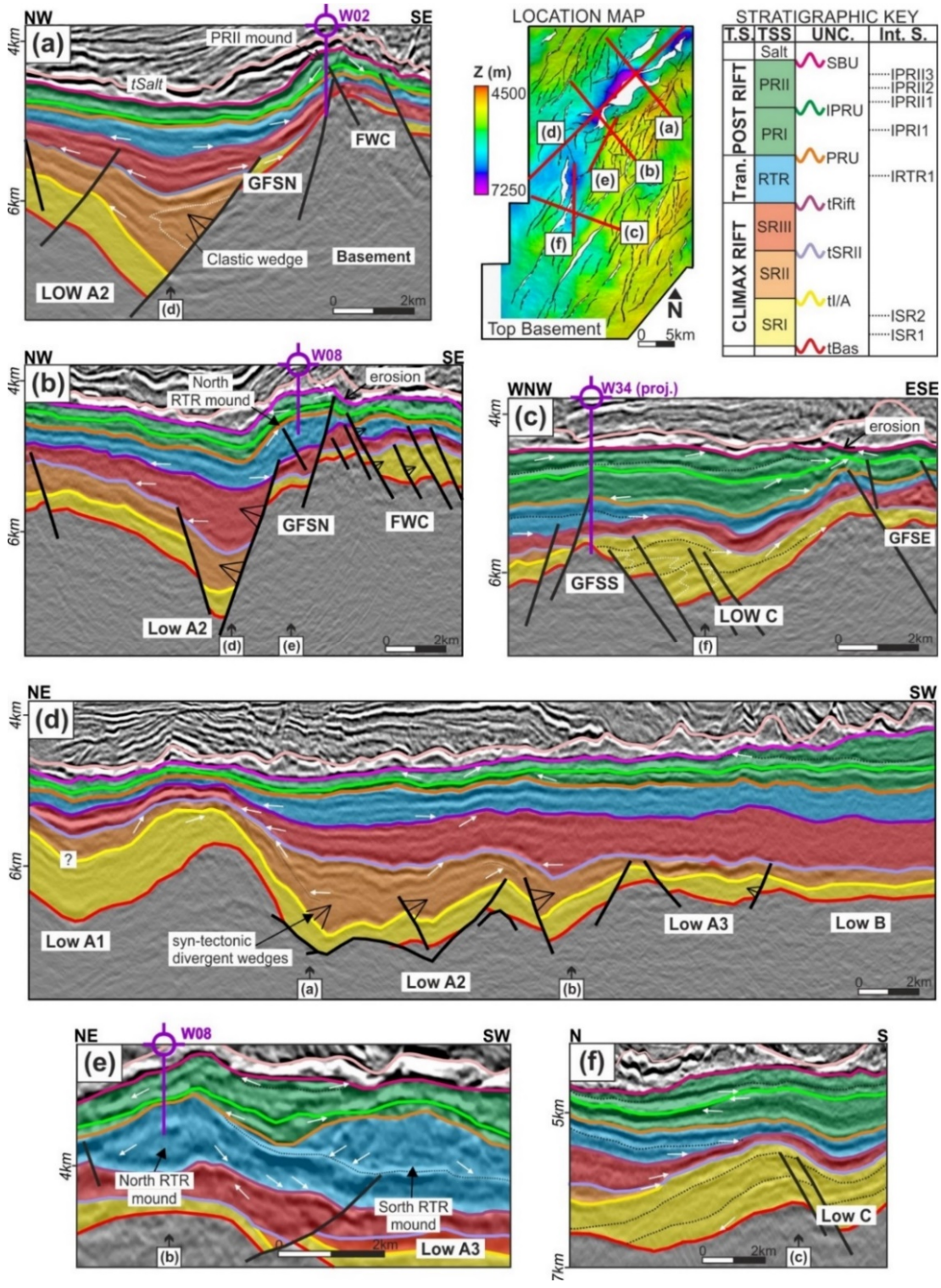


Figure 4.6: Sets of dip (a-c) and strike (d-f) seismic-geologic cross-sections showing selected stratigraphic and structural features. A simplified stratigraphic key is also shown (T.S: tectonic stage of Olivito and Souza (2020); TSS: tectono-stratigraphic sequences; UNC.: unconformities; Int. S.: internal surface. White arrows indicate onlap, toplap, truncation and downlap terminations.

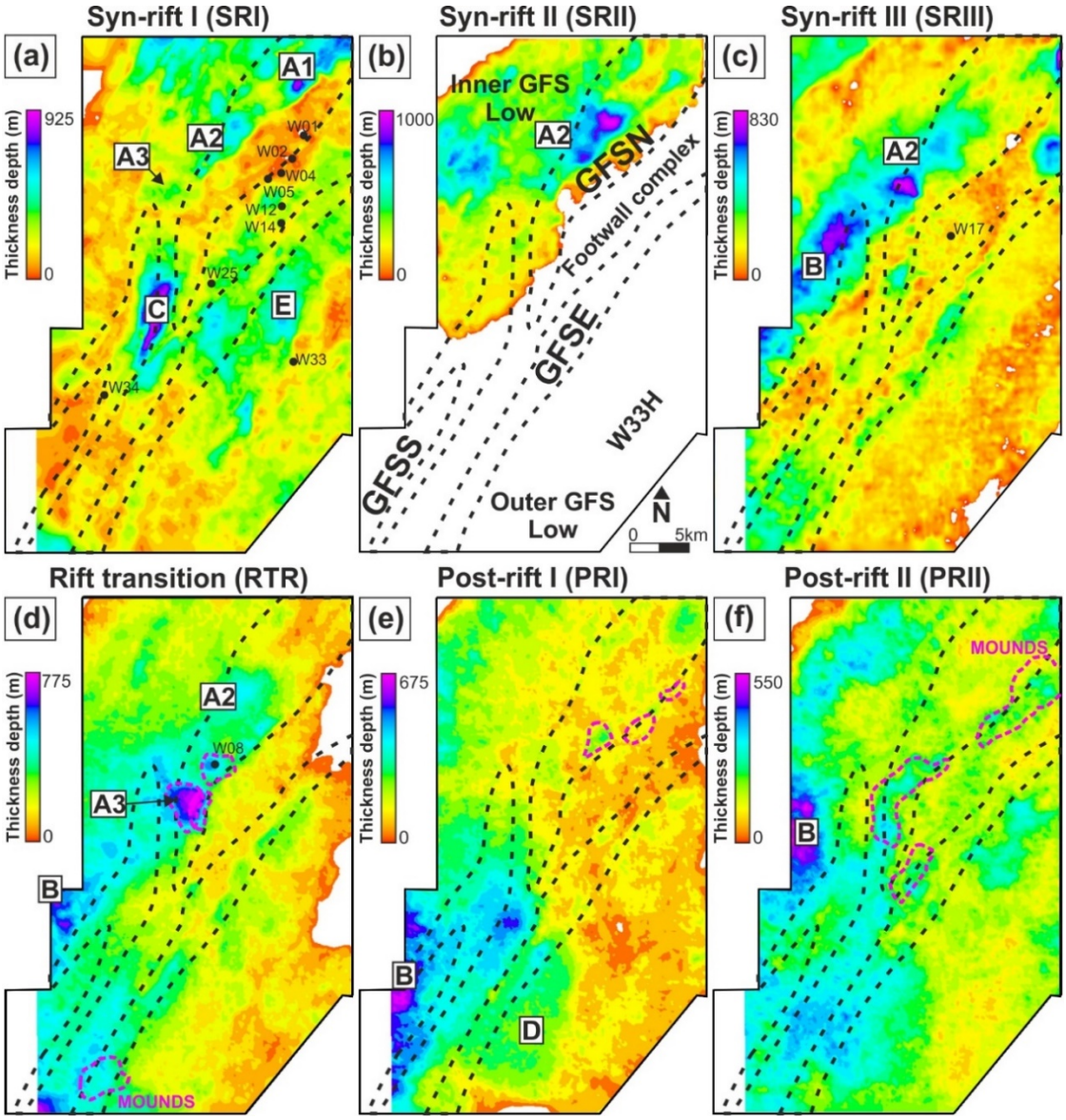


Figure 4.7: Thickness maps of each tectono-stratigraphic sequence (TSS). External boundaries of the branches of the GFS are shown (dotted lines). Structural domains from Figure 4.5a are overlaid in the map in "b". Relevant depocenters for each sequence, according to Figure 4.5b, are shown. Mounds are outlined on the maps of RTR, PRI, & PRII. Wells that drilled tBas, tI/A, and tRift horizons are shown, respectively. The wells that perforated the RTR (except W08) and PR are not shown for clarity.

4.5.3.3 Syn rift III TSS (SRIII)

The syn-rift III (SRIII) sequence is bounded at its base by both tI/A and tSRII surfaces and at its top by the tRift horizon. The tRift is widely distributed in the 3D survey as a mostly conformable surface and rarely shows evidence of erosion (Figure 4.6d). The base of SRIII onlaps the tSRII, onto internal transverse faults in the hanging wall of GFSN (Figure 4.6a,d) and over the tI/A in Low C (Figure 4.6f). SRIII internal reflectors parallel to the base are rare and can be observed locally in strike sections (Figure 4.6d).

The SRIII package resembles the typical pattern of residual relief filling, progressively onlapping onto fault scarps and covering structural highs (Figure 4.6). Therefore, seismic reflectors are often parallel to the top. Syn-tectonic thickening occur related to selected segments of the GFSN (Figure 4.6b) and, more widely, along the GFSE and GFSS branches (Figure 4.7c). Elsewhere, a parallel internal organization is predominant.

The thickness distribution of SRIII follows the main Guriri Fault System (GFS) structural compartments. The isopach map shows the configuration of thicker depocentres on both sides of the GFS horst, ranging from 400 m thick in the outer and up to 800 m thick in the Inner GFS Low. Interestingly, thicker deposits of SRIII in the Outer GFS Low occur near the GFS East (GFSE) branch, while it thins considerably elsewhere (Figure 4.7c). Along the strike of the GFS North (GFSN), thicker depocentres of SRI and SRII are located in the northern and central sectors of the GFSN branch, respectively, while SRIII thickens southwards, following newly nucleated NE-SW striking faults west of GFS South (GFSS) branch (Figures 4.6d, 4.7c). It demonstrates the overall southward strain migration along the strike of the GFSN and subsequently GFSS, thus the overprinting of NE-SW segments over SRI N-S faults that bounds Low C. Consequently, Low B was established and therefore configuring the current horst geometry of the GFS (Figure 4.6c,f, & Figure 4.7c).

Another notable feature is the post-SRII erosion nucleation of subsidiary faults towards the footwall of the GFSN, which are parallel in strike but steeper when compared to the earlier segments of the GFSN. The timing of formation is endorsed by thickening of SRIII (and rift transition - RTR) in the hanging wall block (Figure 4.6a,b). Major rift faults often exhibit erosion in the footwall that are usually related to footwall uplift and the formation of new faults as the consequence of the rotation of the faulted block, in a process known as footwall degradation, where faulting occurs either towards the hanging or the footwall blocks (Hesthammer & Fossen, 1999; Morley et al., 2007).

Wellbore calibration of SRIII is given by the nine penetrations (Figures 4.7c and B5). Bioclastic rudstone (coquinas) is the most common lithotype in the structural highs, while low energy hybrid siltstones occur in the depocentres. The SRIII sequence is therefore correlated to the Coq A unit, the basal unit of the Coqueiros Formation according to Olivito & Souza, (2020).

From the amplitude patterns of the constituent reflectors and similar isopach distribution of SRII (seismic) tectono-sedimentary sequence (TSS) in the Inner GFS Low when compared to the SRIII TSS, it is interpreted that both sequences are part of a single phase of rifting and probably share similar lithological content. The GFSN branch exert a fundamental role in controlling the creation of depositional space for both units (Figure 4.6a). The section equivalent to SRII has been included in the combined Itabapoana and Cabiúnas Formations, while SRIII represents the base of the Coqueiros Formation (Olivito & Souza, 2020). Because of the similarities thereof, SRII plus SRIII are here interpreted as belonging to the basal unit of the Coqueiros Formation and record syn-rift deposits (Figure 4.6b). GFSN activity prevails during the SRII and SRIII deposition, and contrast significantly from the SRI structure (Figure 4.7a-c). In addition, fault scarp formation

during SRII denotes an active sediment-starved graben, which is typical in the early stages of rift filling, followed by generalized fill of the structural relief during SRIII (e.g. Prosser, 1993) (Figure 4.6a).

4.5.4 The rift transition sequence

The rift transition (RTR) TSS is delimited by tRift at the base and PRU (post-rift unconformity) at the top. The tRift is widely recognisable as a conformable surface that is only occasionally onlapped by internal reflectors of RTR. The PRU has an erosive character towards the NE region of the survey that leads to truncation at the top and eventually the complete absence of the RTR in the easternmost portions of the study area (Figure 4.7d). Otherwise, PRU is also a conformable surface (e.g. Figure 4.6d).

Internally, the organization of the seismic reflectors are predominantly parallel except when submitted to erosion related to PRU, where the modest thickness compromised the seismic signal. However, the proximal hanging wall block of the southern sector of GFSN shows a quite distinct pair of mound-shaped reflectors (Figure 4.7d). They have a circular to NE-trending ellipsoidal planform, with 3 to 5 km average length and exhibit downlapping terminations in the base and are onlapped by the post-rift units (Figure 4.6e). They are not contemporaneous because the southern mound downlaps in the internal seismic reflector equivalent to the top of the northern mound (internal surface IRTR1 – Figure 4.6e). However, a dip section shows that the mounds are comprised of wedges that prograde from the footwall complex onto the hanging wall of the GFSN (Figure 4.6b). This figure also shows that the depositional space occupied by the prograding wedge was created by newly formed NNE-SSW to NE-SW striking faults nucleated towards the footwall of the fault zone. These structures are amongst the few that were active during the

RTR and are probably related to the ongoing footwall degradation observed during the SRIII. Finally, the geometry of RTR mounds are similar with the clinoforms observed in deposits in Santos Basin of similar age, except for the absence of syn-depositional tectonics there (Barnett et al., 2021).

The isopach map of the RTR shows an overall thickening to the SW and absence by erosion in the eastern region as major features (Figure 4.7d). It also shows the imprint of the main structural compartments of Figure 4.5a, although the W33H internal high has a thinner RTR than the GFS horst. The two mounds are quite distinctive, hosting the thicker RTR (over 700 m). Tilting to the SW along the GFS exerts the primary control on the first order thickness variations, so the RTR thickens towards the SW despite the GFS and their counterpart structural lows. The southward stepping of the mounds and erosion towards the NE support the interpretation of such widespread tilting to the SW.

Several wells (34) reached or drilled through the RTR sequence, mainly in the footwall complex (Figure B5). The RTR is interpreted as equivalent to the upper section of the Coqueiros Formation, extensively described by Olivito and Souza (2020) as a ramp-margin shallowing-up sequence of bioclastic rudstones deposited in modest water depths. These authors subdivided the upper section of the Coqueiros Formation into four sub-units (Coq B to E) and proposed their inclusion as a transition rift stage. The mounds are interpreted as berm and shoreface facies associations.

The relatively homogeneous isopach distribution and depositional style could be interpreted as resembling a post-rift architecture. However, the role of syn-depositional faulting remain significant in both sides of the GFS horst (Figures 4.6b, 4.7d). Therefore, the RTR is better explained as a transition sequence between clear syn-rift sequences (SRII and SRIII) and clear post-rift sequences (PRI & PRII).

4.5.5 The post-rift supersequence

The post-rift tectono-stratigraphic sequence exhibits aggradational (parallel) to mound-shaped seismic facies and is characterised by a lack of any significant syn-depositional fault activity. It corresponds to the Macabu Formation that extends throughout the Campos and Santos basin, where it is named Barra Velha Formation, both deposited in an extensive sag-like basin geometry (Pietzsch et al., 2018). The Macabu Formation comprises shallowing-up cyclothems of mud-grade laminated carbonates, mm-diameter spherulitic carbonates, and calcite shrub-like crusts, all deposited in a highly alkaline evaporative lake (Wright & Barnett, 2015; Lima & De Ros, 2019). Using well data (logs and cores) as a proxy for depositional facies, clay-content, and therefore water depth, the overall stacking pattern is a deepening (post-rift I - PRI - tectono-stratigraphic sequence - TSS) followed by a shallowing up (post-rift II - PRII - TSS) sequence (Muniz & Bosence, 2015; Herlinger Jr. et al., 2017); the IPRU (Internal Post-Rift unconformity) separates the two TSSs and, according to Herlinger Jr. et al. (2017), is equivalent to a 3rd order sequence boundary.

4.5.5.1 Post-rift I (PRI) TSS

The PRI TSS is delimited at the base by the PRU unconformity and the top by the IPRU (internal post-rift unconformity). The PRU is related to extensive pre-PRI erosion in the NE region of the study area, and similarly to as in the rift transition (RTR), the erosive nature of the PRU and IPRU increase towards the NE. Consequently, PRI discretely onlaps onto the PRU and is truncated by IPRU erosion towards the east (Figure 4.6c-e). Otherwise, these surfaces occur as correlative conformities (see the southern sector of section 4.6d). The PRI filling pattern is dominantly aggradational and therefore shows a parallel internal organization of the seismic reflectors. A few isolated build-ups occur in the crest of the

GFSN (Figure 4.7e) with no clear relation with active faulting, which differs from RTR mounds.

Thickness distribution has two major domains separated by transverse NNW-SSE trace across the centre of the 3D survey (Figure 4.7e), equivalent in position to the accommodation zone shown in Figure 4.5a. To the east, the thickness is typically around 100 m and barely reaches 300 m in the hanging walls of the GFS branches. To the west, the average thickness is around 300 m and reach up to 650 m in the westernmost region. Notice that the main compartments and the sub-compartments of the rift stage are barely recognisable in the isopach map. When observed, thickening in the hanging walls of Guriri Fault System (GFS) branches is probably related to inherited structural relief from RTR, resulting in contrasting accommodation space across the faults.

4.5.5.2 Post-rift II (PRII) TSS

The uppermost unit of the presalt sequence is delimited at the base by the IPRU and at the top by the base-salt unconformity (BSU - Figure 4.6). The PRII internal reflectors are usually parallel to the IPRU, except when it is downlaped by mounds (Figure 4.6a). The BSU is quite distinctive and reveals significant erosion in the hinge of fault propagation folds and footwall blocks (Figure 4.6b,c,e) and within the Inner GFS Low (Figure 4.6d). The internal reflectors of PRII are usually parallel, but often onlapping onto the IPRU as tilting to SW remains active just after the PRI, and are commonly truncated at the top by the BSU. Internal surfaces IPRII1-3 are particularly abundant in the Inner GFS Low and suggest a cut-and-fill geometry (Figure 4.6d,e,f).

Mounded shape packages extensively occur over the up-dip projection of the GFSN branch and are apical to its faults related to footwall degradation (Figures 4.6a, 4.7f). Therefore,

these mounds are symmetrical and prograde onto both footwalls and hanging walls of the fault segment that anchors them.

Apart from differences in terms of average and maximum values, the thickness distribution is similar to that of the PRI, i.e. it is divided into two major domains separated by a NNW-SSE accommodation zone, and does not follow the major structural domains of the rift stage. The main difference between PRI and PRII thicknesses is the lack of broad post-depositional erosion towards the east in the latter. The relatively homogeneous thickness of the PRII shows an increasingly 'sag' depositional geometry in the form of wider depocentres compared to syn-rift and RTR sequences, preceding evaporite deposition (Figure 4.4). However, the present-day configuration of the bSalt, far from being horizontal and undisturbed (Figure 4.5c), points towards significant post-salt tectonism affecting the presalt sequence.

4.6 Tectono-stratigraphic evolution

Having the gross structural and stratigraphic framework established, it is integrated to the tectono-stratigraphic maps (Figure 4.3) for each of the (seismic) tectono-stratigraphic sequences (TSSs - Figure 4.8). These maps focused on an area that includes the Guriri Fault System (GFS) and the near adjacent Inner and Outer GFS Lows. Fault-displacement analysis and fold descriptions provided further input for the kinematic analysis that underpins this summary of the tectono-stratigraphic evolution.

The tectono-stratigraphic maps show that the rift-related subsidence was highly diachronous along the NE-SW striking GFS (Figure 4.8). They also show that the final horst geometry of the GFS had only developed towards the end of rifting. Thickness maps

and the alignment of fault tips and changes in the strike of rift faults suggest the underlying and often cryptic influence of NW-SE transverse structures (Figures 4.3b, 4.5b,d).

Comparison of the three syn-rift TSSs reveals similarities between the maps of SRII and SRIII that make them distinct from SRI. Amongst the differences, we note the lithological contrast (volcanics plus coarse siliciclastics of SRI to carbonates of SRII plus SRIII TSSs – Figure 4.2) and, mostly, the contrasting structural pattern and therefore depocentre distribution (Figure 4.7a-c). Also, the significant time gap related to the tSRII unconformity since it represents the merge of two unconformable surfaces (tI/A & tSRII) in most areas should be considered. Finally, the inversion of the most significant depocentre of SRI (i.e. Low C) clear predates the SRII plus SRIII deposition (Figure 4.6c,f).

It is important here to distinguish between the inversion that predates the SRII plus SRIII, related to stress redistribution during the rift-related extension and best exemplified in the Low C, and the inversion represented by selective reactivation of rift faults during the post-rift stage as result of compressional far-field stress. Interpretation of inversion was based in the occurrence of depocenters in a higher structural position than the neighbour blocks with respect to a newest stratigraphic unit and the observation of displacement variations along a fault, on which normal displacement occurs in the deeper segment and reverse displacement occurs in the shallower segment.

Based on the contrasting strain and depocentre distribution, filling patterns and lithologies, we interpret the syn-rift supersequence as constituted of two distinct rift phases, where the rift phase 1 (RP1) comprises SRI, and rift stage 2 (RP2) comprises SRII combined with SRIII. Our subdivision of RTR, PRI, & PRII closely follows the general classifications of

rift transition and post-rift stages proposed by Olivito and Souza (2020) and Winter et al. (2007), respectively (compare Figures 4.2 & 4.6).

One of the main differences between our interpretation of the rift evolution in the study area from the previous study of Olivito and Souza (2020) is that these authors assigned a climax rift stage to the whole interval below the rift transition, in agreement with most of previous publications (e.g. Winter et al., 2007) (Figure 4.2). Our interpretation is to replace the climax rift stage of Olivito and Souza (2020) to syn-rift supersequence. On the other hand, we agreed with the term rift transition proposed by Olivito and Souza (2020), where the RTR mimics characteristics of both syn-rift and post-rift stages.

By way of summary, we present our interpretation of the tectono-stratigraphic evolution of the presalt sequence in the North of the Campos Basin as a series of evolutionary schematic sections in Figure 4.9. It presents two cross-sections located north and south of the accommodation zone (Figure 4.5a), equivalent in location to the geologic cross sections of Figures 4.6b & 4.6c, respectively. The Figure 4.9 emphasizes the general features of the sediment fill geometries and bounding surfaces. This figure demonstrates that the subsidence is often diachronous and heterogeneous from SRI to PRI, along and across the GFS horst, leading sedimentary thickening to be contemporaneous to aggradational depositional patterns, and subaerial exposure thus erosion in each of the TSSs.

Based on the tectono-stratigraphic maps (Figure 4.8) and the evolutionary schemes of Figure 4.9, the Figure 4.10 summarizes in map view the strain distribution and depocentre creation of each of rift phases (RP1 & RP2) during the deposition of the syn-rift supersequence. The extension directions for each of rift phases were established as been roughly orthogonal to the major active fault segments thus depocentre distribution. Figure 4.10 also shows the effects of the roughly NW-SE structure transverse to the GFS in the

structural style and strain evolution during syn-rift stage. While acting as a WNW-ESE oriented kinematic buffer during RP1, the NW-SE structure is interpreted as an accommodation zone during the RP2 with close spatial relation with the Vitória-Colatina Lineament (Figure 4.4a) (Fetter 2009).

4.6.1 Rift phase 1 (RP1)

Rift phase 1 (RP1) took place over a crustal framework constituted of two distinct Precambrian basement domains (Strugale et al., 2021). In Figure 4.11 a cluster of faults with minor displacements (~200m) can be seen to the east (i.e. the Guriri Fault System East branch - GFSE), in contrast with sparse faults with major displacements (~400m up to 900m) to the west (GFSN-S), reflecting the duality in basement geology, whose implications for rift-related strain are discussed in Strugale et al. (2021).

Most of the early available accommodation space during syn-rift I (SRI) was concentrated in N-S to NNE-SSW elongated half-grabens filled with syn-tectonic sediments (Figure 4.10). Graben asymmetry is given by west-bounding faults, whose fault tips are often to be delimited by WNW-ESE lineaments (Figure 4.8a). Low C best exemplifies these N-S striking half graben, with its divergent fill, two internal truncation surfaces, and footwall erosion (Figures 4.6c & 4.9). Otherwise, most of the SRI internal geometry of seismic reflectors are parallel and therefore do not suggest syn-depositional GFSN faulting (Figure 4.6a,b, & Figure 4.7a).

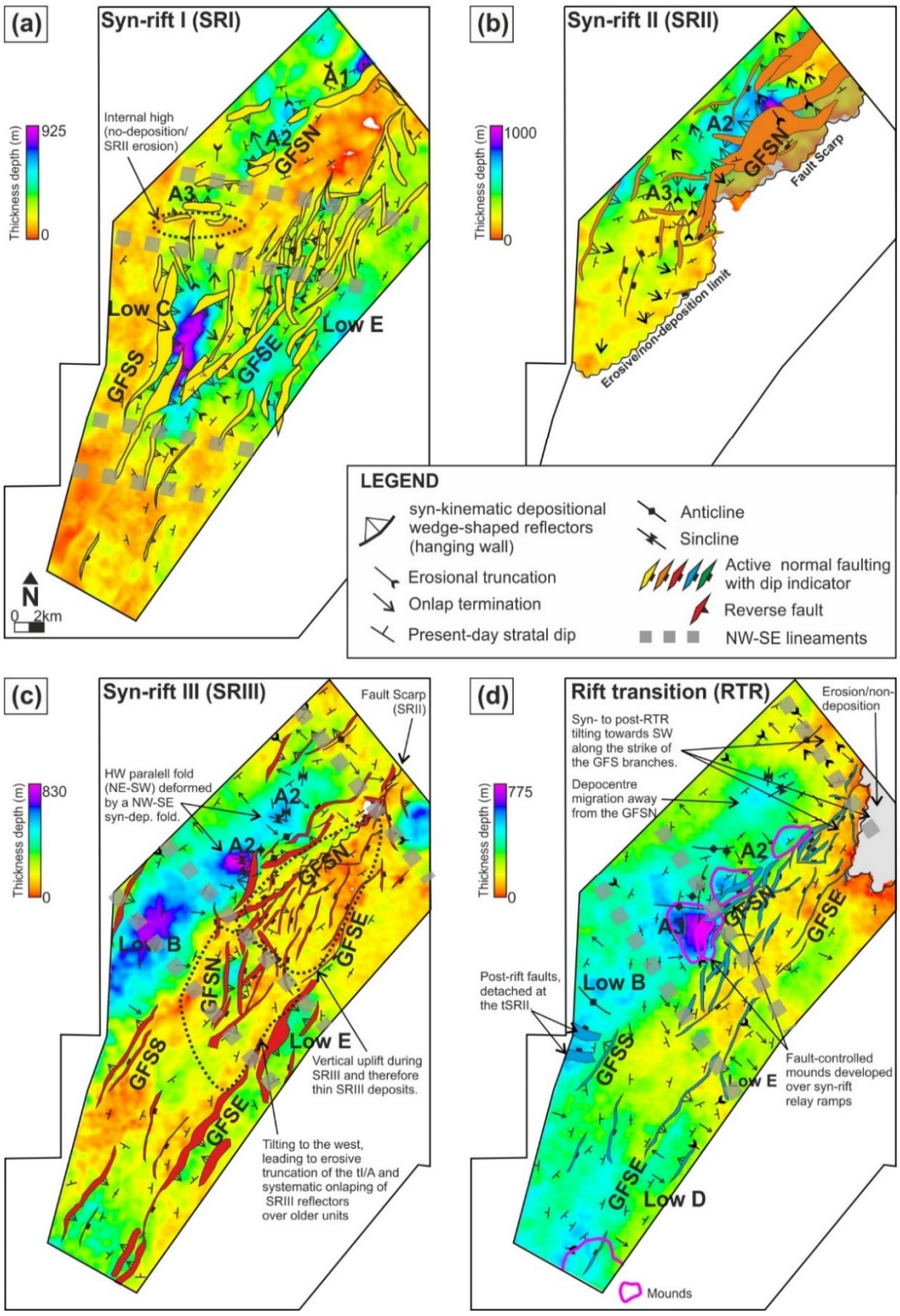


Figure 4.8: tectono-stratigraphic maps of the syn-rift sequences (SRI – a, SRII – b, SRIII – c) and rift transition (RTR – d) built according to Figure 4.3. Polygons represent the active faults for each tectonic stage of which the corresponding thickness map are shown.

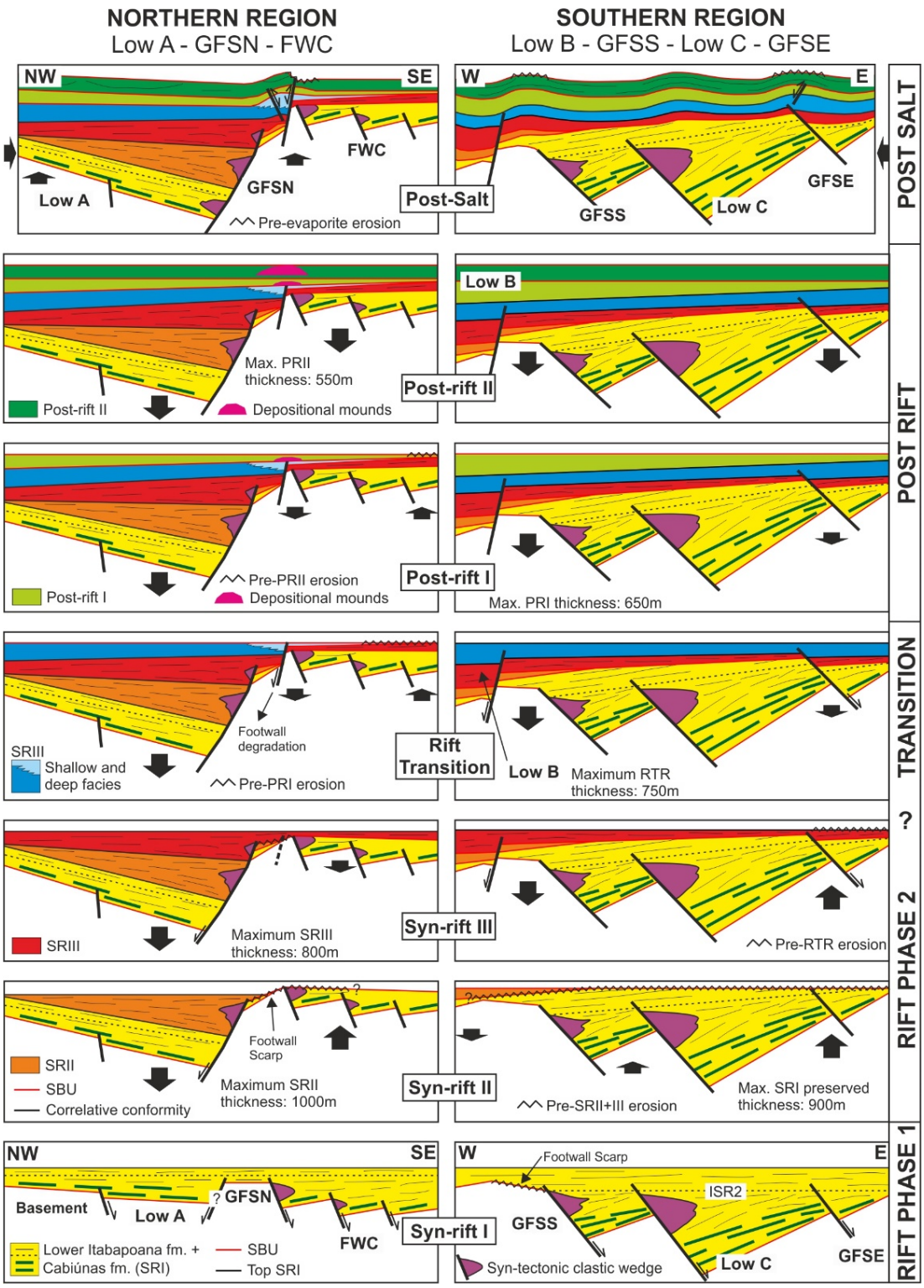


Figure 4.9: Schematic geologic cross sections summarising the tectono-stratigraphic evolution of the presalt sequence in the study area in the north (left) and south (right) of the NW-SE accommodation zone. The column on the right shows the main tectonic stages here interpreted. Black arrows represent local subsidence and uplift based on depositional geometries and thicknesses of each stage. The sections are not to scale and are vertically exaggerated. SBU: subaerial unconformity/exposure. Discussion in the text.

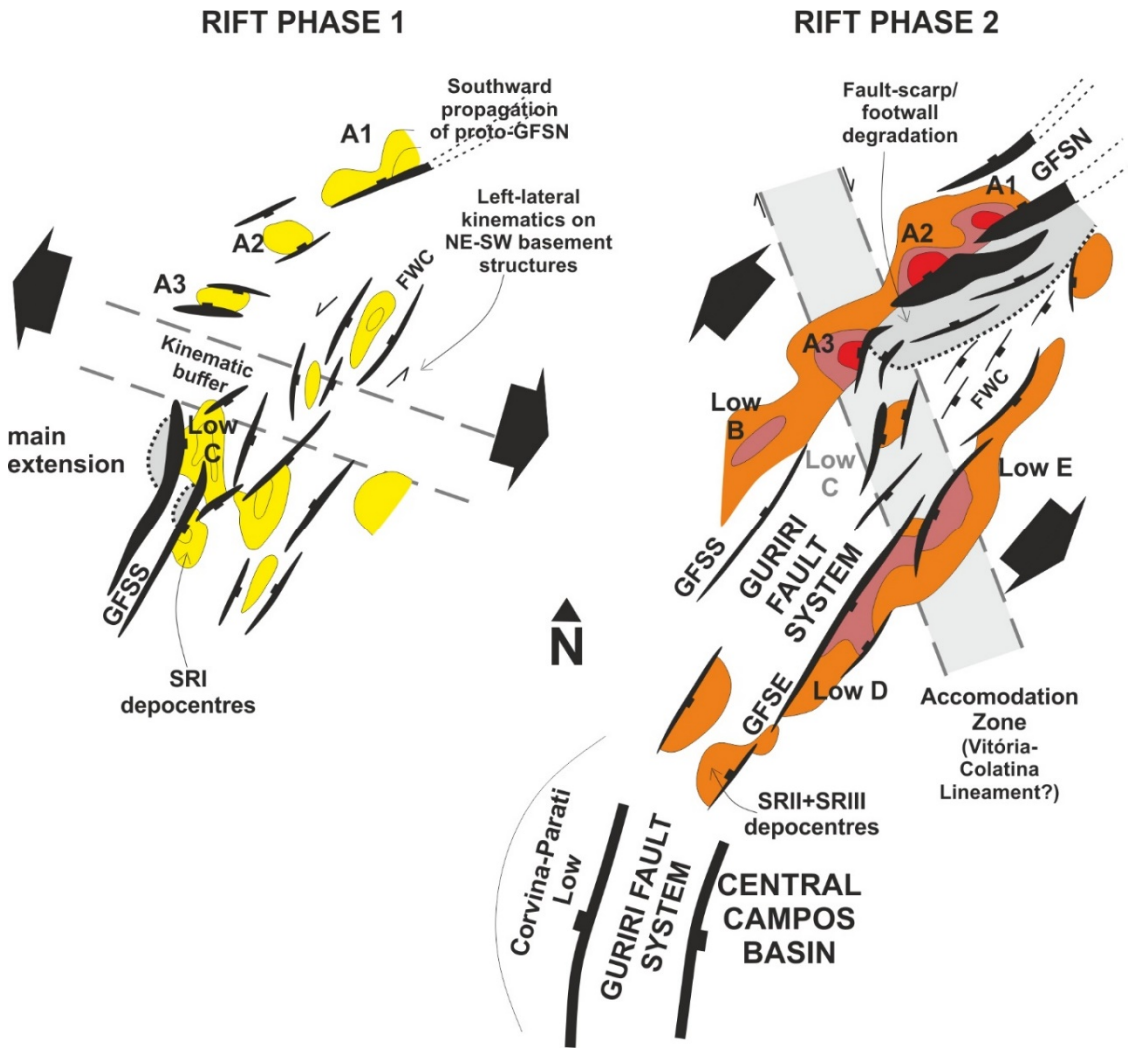


Figure 4.10: Schematic draft showing the strain distribution during the RP1 and RP2 (see text for discussion). Depocentres are coloured according to the age of filling tectono-stratigraphic sequence (yellow – SRI, orange to red – SRII plus SRIII). Notice how the isolated grabens of RP1 are replaced with long and continuous depocentres bounded by the GFS horst. The accommodation zone is suggested to have relation with the Vitória-Colatina lineament based on its location on the map of Figure 4.4a. Not to scale.

Earlier deposition of the SRI is represented by the syn-tectonic volcaniclastic sediments of Cabiúnas Formation. The lack of high amplitude anomalies suggests a low volcanic/clastic ratio for this interval. This contrasts with the thicker Cabiúnas Formation and other correlated magmatic intrusions in the Central and Southern Campos Basin (Stanton et al., 2019). Once the grabens were filled, sedimentation spread more widely resulting in an aggradational filling pattern that tapered even the most prominent footwalls in the GFSS

(Figures 4.6c, 4.9). This pattern suggests that an early phase of sediment-starved grabens was followed by widespread creation of accommodation space and sedimentation. Following the terminology of Prosser (1993), the overall filling pattern of rift phase 1 suggests a cycle of syn-rift to late post-rift half-graben fill, in which the rift initiation system is not recognized. This interpretation, however, should be considered as preliminary due to the low seismic resolution and lack of wellbore calibration in the depocentres.

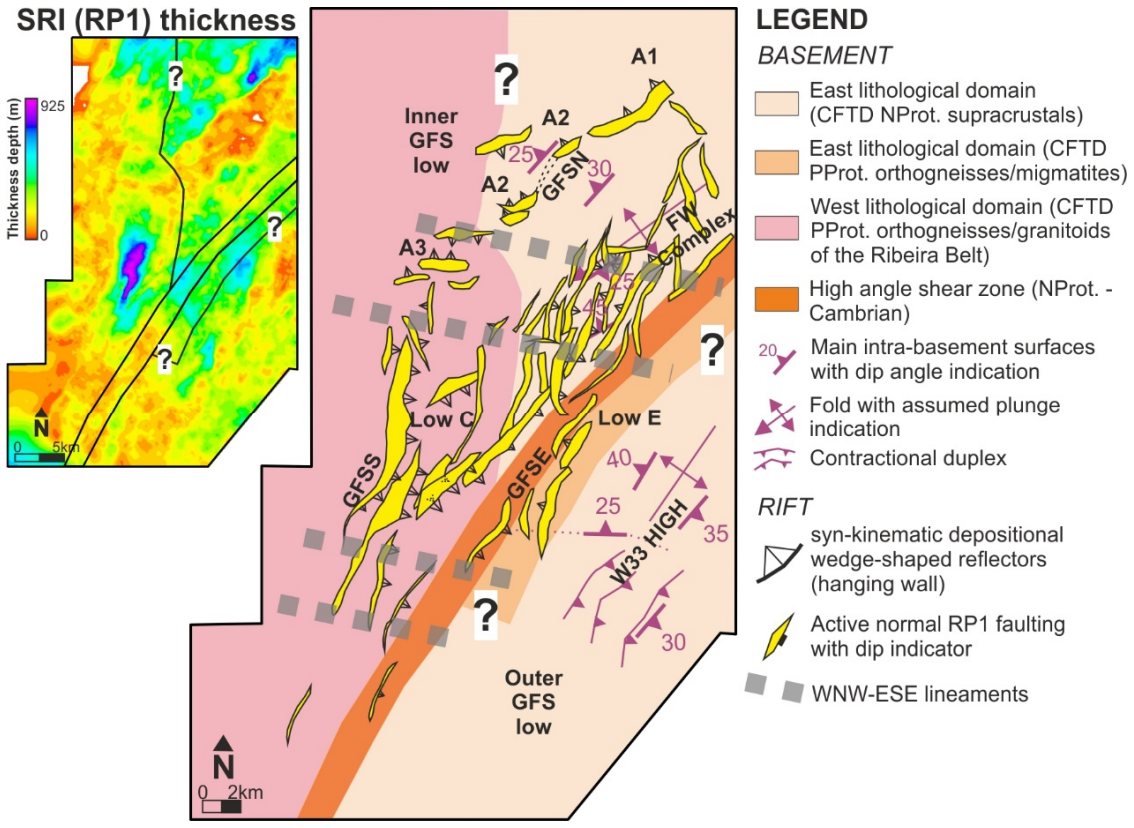


Figure 4.11: Fault framework of early syn-rift (SRI) superposed on the basement geology map (modified from Strugale et al., 2021) comparing the fault distribution and the main basement units. Notice the obliquity between RP1 faults and basement structures in the FWC. The thickness map of SRI sequence is also shown, on the left, along with the main boundaries of basement geology superimposed. CFTD: Cabo Frio Tectonic Domain. PProt: Paleoproterozoic. NProt: Neoproterozoic.

Thickness and paleostress analyses in the SRI are somewhat difficult because the extensive erosion and localized inversions that preceded the RP2. The geometry of N-S to NNE-SSW striking half grabens delimited by WNW-ESE lineaments suggests an WNW-ESE extension (Figure 4.10a) that either reactivated basement structures or nucleated new faults depending on the basement domains (Strugale et al., 2021) (Figure 4.11). In turn, the gentle obliquity between NE-SW basement structure and NNE-SSW rift faults in the FWC could suggest some degree of left-lateral kinematics on basement structures (Figure 4.10). The left-stepping geometry of the depocentres and fault tips suggest that extension was partially accommodated as right-lateral kinematics on the WNW-ESE transverse structure (Figure 4.8a). The contrasting thicknesses across this structure suggest that it acted as a hinge for local subsidence.

4.6.2 Rift phase 2 (RP2)

After a period of relative tectonic quiescence and erosion/non-deposition, another pulse of fault activity occurred, initially restricted to the Guriri Fault System North branch (GFSN), followed by widespread faulting that were either newly formed or reactivated rift phase 1 (RP1) faults. Consequently, the GFSE was fully established, new W-dipping were formed on the GFSS, and major faults developed in the GFSN, resulting in major overprinting of rift phase 2 (RP2) over RP1 structures (Figures 4.8, 4.10).

The first stage of RP2 deposition occurred during the syn-rift II (SRII) sequence in a mini basin (Low A) in the hanging wall block of the GFSN branch. Fault growth and linkage inherited from the previously E-W to NE-SW trending RP1 faults resulted in a fault zone whose main segments were sigmoidal (Figure 4.8b). Towards the syn-rift III (SRIII) sequence, thicker depocentres migrated southwards along the GFSN, from Low A2 to Low

A3, away from the thicker SRI (A1 Low) depocentre (see Figure 4.7a-c). Such southward strain migration kept active during the rift transition sequence (RTR). This along strike strain migration suggests that the GFSN was part of a longer fault zone that extended northwards (out of seismic coverage) on which the strain had been propagating southwards until the rift transition phase (Figure 4.10). Also, the increasingly lower fault dip angles (< 30°) northwards suggests that rotation of fault planes during extension led to the "locking" of the fault (c.f. Reston, 2020) and therefore strain had to migrate southwards.

The filling pattern of the early RP2 (i.e. SRII) is characterised by classic sediment starved/underfilled half-graben accompanied by divergent wedges, footwall uplift and erosion (i.e. fault scarp) in the position of maximum displacement of GFSN (Figure 4.6a). Such a pattern is reminiscent of the rift climax or through-going faulting stages of, respectively, Prosser (1993) and Gawthorpe and Leeder (2008) (Figure 4.9). Rift initiation or pre-rift layers are represented by RP1 deposits (Figure 4.6a,b,d). Discrete onlap of SRII onto tI/A horizon (Figure 4.6a) suggests that fault rotation occurred prior to the onset of deposition, consistent with the unconformable character of the tI/A plus tSRII unconformity (Figure 4.6c,f).

A period of non-deposition within the Inner GFS Low occurred before the onset of SRIII deposition, as evidenced by the onlaps of SRIII onto the tSRII surface (Figure 4.6b,d). Subaerial exposure and erosion occurred elsewhere, tuning the seismic response of the tSRII and tI/A surfaces. These suggest that another episode of tectonic activity that could have rearranged the depositional systems, leading to a long enough period of sediment starvation that allowed the deformation on the substrate that was subsequently onlapped by the SRIII (Figure 4.6d).

The depositional pattern of SRIII tapered of the structural relief of SRII, exemplified by the widespread occurrence of SRIII (Figure 4.7c) and its onlapping onto syn-SRII fault scarps and the footwall complex (FWC - Figure 4.9). Divergent wedges occurring against segments on the south of GFSN, in the GFSE, and west of GFSS (Figure 4.6a,b,c) imply that most of the GFS structures were still active in this interval.

The overall strain distribution during RP2 is relatively homogeneous, defining the present-day rift-related structural compartmentalization of the study area (Figure 4.5a). The tectono-stratigraphic maps of Figure 4.8b,c shows that the two major rift faults, GFSN & GFSE (southern part) are collinear but have opposite dip directions. This change in polarity occurs across the NW-SW accommodation zone (Figure 4.10).

The dominant NE-SW strike of the normal faults with major displacement and length is argued to be the result of a NW-SE to WNW-ESE extension during the rift phase 2 (RP2 - Figure 4.10). Besides this rotation of the extension direction with respect to rift phase 1 (RP1), it was still slightly oblique to the basement structural grain, hence some left-lateral reactivation could still occur. However, a few but remarkable N-S faults were active during the syn-rift III sequence (SRIII) deposition, exemplified in Figure 4.6b and by a N-S graben within the NW-SE accommodation zone (Figure 4.8c). Therefore, we argue for a slight anticlockwise rotation of the extension direction to WNW-ESE during SRIII and a secondary right lateral kinematics along the NW-SE trend (Figure 4.10). The Figure 4.12 exemplifies the potential effects of such change in the extension direction in an area where two non-parallel major segments of the GFSN interact. Notice how the post syn-rift II sequence (SRII) deformation by amplification of hanging wall folding as a consequence of preceding localised shortening and therefore is onlapped by SRIII. This shortening is

also noticeable during rift transition (RTR) sequence, as evidenced by onlap onto folded tRift (Figure 4.12a).

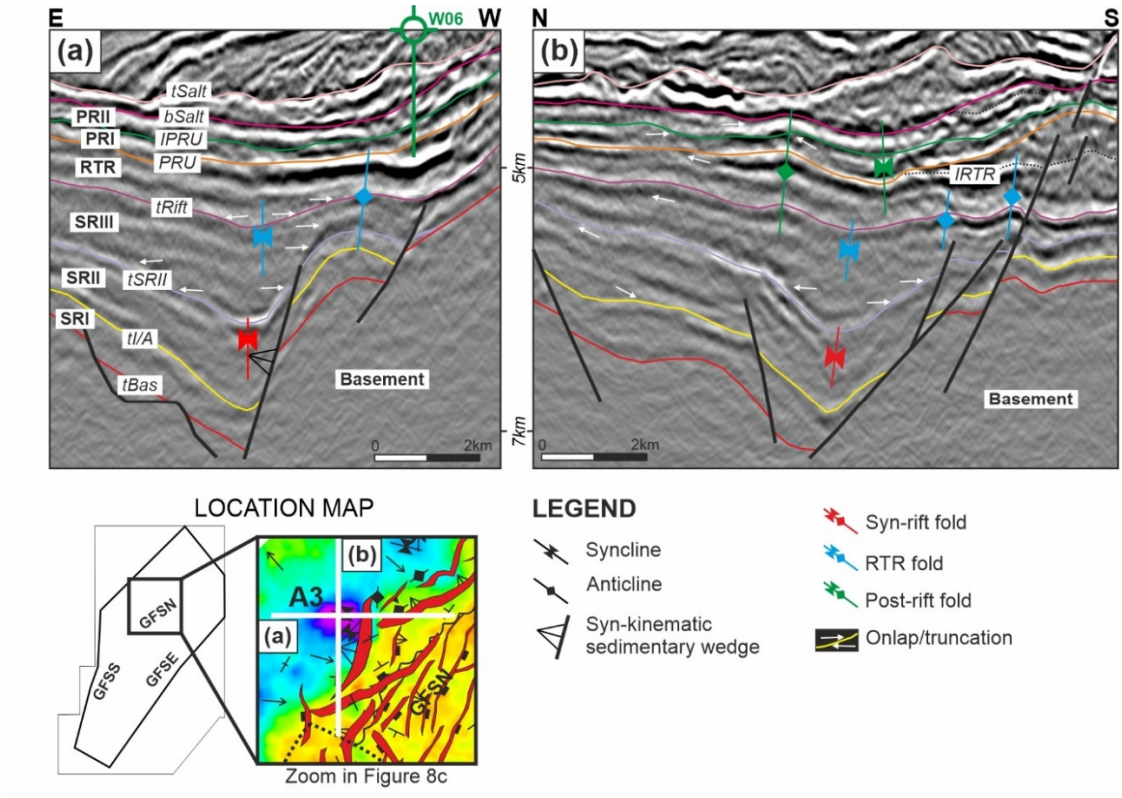


Figure 4.12: Pair of cross-sections showing a complex set of faults, folds, onlaps and truncations related to the interaction of N-S and NE-SW faults in the GFSN branch. Folds of syn-rift age are hanging wall folds related to displacement variations due to segment linkage (see Figure 4.8), amplified by SRIII shortening that also produced RTR folds. Post-rift folds are related to regional tectonic shortening during late post-rift inversion (see discussion in item 4.3.4).

4.6.3 The rift transition phase

The rift transition phase is equivalent to RTR sequence and marks the onset of thermal subsidence coeval with regional tilting to SW and localized faulting related to ongoing displacement of rift phase 2 (RP2) faults. The isopach map demonstrates the interaction of the processes above, leading to the accumulation of remarkable carbonate mounds in the

hanging wall of the Guriri Fault System North (GFSN) branch and an overall thickening of the RTR towards the SW (see Figure 4.8).

Active deformation during the RTR shown in Figure 4.8d is restricted to fault segments located within the GFS branches, most notably in the southern sector of GFSN (Figure 4.12). Strike and dip attributes resemble the later RP2 structures. The onset of SW tilting resulted in localized erosion of later RP2 deposits (i.e. SRIII) in structural highs, mainly in the Well 33 High (W33H) within the Outer GFS Low (Figure 4.7d). The extensive erosion that predates the post-rift deposition suggests increasing tilting during the transition to the post-rift and therefore explains the gentle onlap of both RTR and Post-Rift I (PRI) sequences onto the tRift and Post-rift Unconformity (PRU), respectively, and their overall thickening towards SW (Figures 4.7d, 4.9).

The prominent mounds that developed during RTR are anomalous against its background of uniform sedimentation and gently varying thickness. The geometry and spatial organization of the westward prograding mounded build-ups is the result of 1) southward along strike migration of strain locus in GFSN, that 2) enhance the faulting related to footwall degradation, thus creating depositional space in the hanging wall as demonstrated by prograding wedges (Figure 4.6b) that are 3) fed with sediments as the result of increasing substrate gradient by footwall (FWC) uplift. In the FWC, the deposition occurred in shallow conditions with events of subaerial exposure, thus working as a by-pass zone (Olivito & Souza, 2020) (Figure 4.9).

We interpret that paleostress during the RTR resembles that observed in the latter part of RP2 (i.e. WNW-ESE extension and right-lateral kinematics in the NW-SE lineaments), which explains both NE-SW and N-S normal faulting (Figure 4.8d). Thicker RTR sediments south of the NW-SE trend could suggest a normal fault component with

downthrowing block to South (Figures 4.7d, 4.8d). Finally, the decrease in active faulting and the onset of tilting suggests that thermal subsidence had superseded the rift-related extension (Figure 4.9). The overall thickening to SW observed in RTR and in the post-rift I sequence is part of a wider depocentre that extends towards the Corvina-Parati Low (Figure 4.4a).

4.6.4 The post-rift phase

The post-rift supersequence was deposited under a thermal subsidence regime, leading to an aggradational filling pattern that healed residual relief on the rift-related structures. Subsidence during Post-Rift I (PRI) was asymmetric and thickens westwards, while in the Post-Rift II (PRII) is uniform, followed by subaerial exposure and erosion prior to the evaporite deposition (Figure 4.9).

There was some minor syn-depositional faulting during the PRI, but this was restricted to the segments active during the rift transition phase. The group of carbonate mounds are also anchored over the updip projection of underlying faults, but show no thickness variations across the structures. Towards the top of PRII sequence and throughout evaporite deposition, inversion by selective reactivation of rift-related faults resulted in a set of fault propagation folds (Figure 4.13). We interpret most of the fault propagation folds in the study area as related to the inversion of normal faults through a shortening thought to be orthogonal to the faults. The main evidence is the hanging wall of the previously normal faults being higher than the footwalls (Figure 4.13c,d) (Letouzey et al., 1990; Withjack et al., 2002; Konstantinovskaya et al., 2007).

There were significant changes in intensity of reactivation along the strike of GFSN. In the south, inversion is restricted to the hanging wall (Figures 4.9, 4.13c), while inversion folds

involved both hanging and footwall blocks towards the north, leading to widespread uplift of both GFSN and the adjacent footwall (FWC) (Figure 4.13b). SE dipping normal faults were apparently inverted in the FWC, which suggests the contribution of reactivation of Precambrian metamorphic fabric that resembles the dip and strike direction of the rift faults in this location (Strugale et al., 2021). It also resulted in a monocline structure in the hanging wall block and the formation of up to 500 m of structural relief. The presence of a relict pod of salt in the western side suggests that the structural relief was active during salt tectonics, working as a bulkhead for the eastward salt flow (Figure 4.13b). Notice that the inversion-related folds have no correlation with salt thickness, therefore are not the result of errors during the time-depth conversion due to velocity variations related to variations in the salt thickness.

The interpretation of paleostresses related to tectonic inversion is problematic because of the thin sedimentary cover and strong coupling between basement and the inverted faults. Therefore, newly formed structures may not directly reflect the new stress field but rather the structure that has been reactivated (c.f. Kelly et al., 1999). The orientation of the inversion folds at first suggests a simple NW-SE shortening. However, the framework of fold-axes in the thicker southern half of Figure 4.13a shows two sets of NNE-SSW and NW-SE hinge lines, both deforming the bSalt horizon (Figure 4.13a,e).

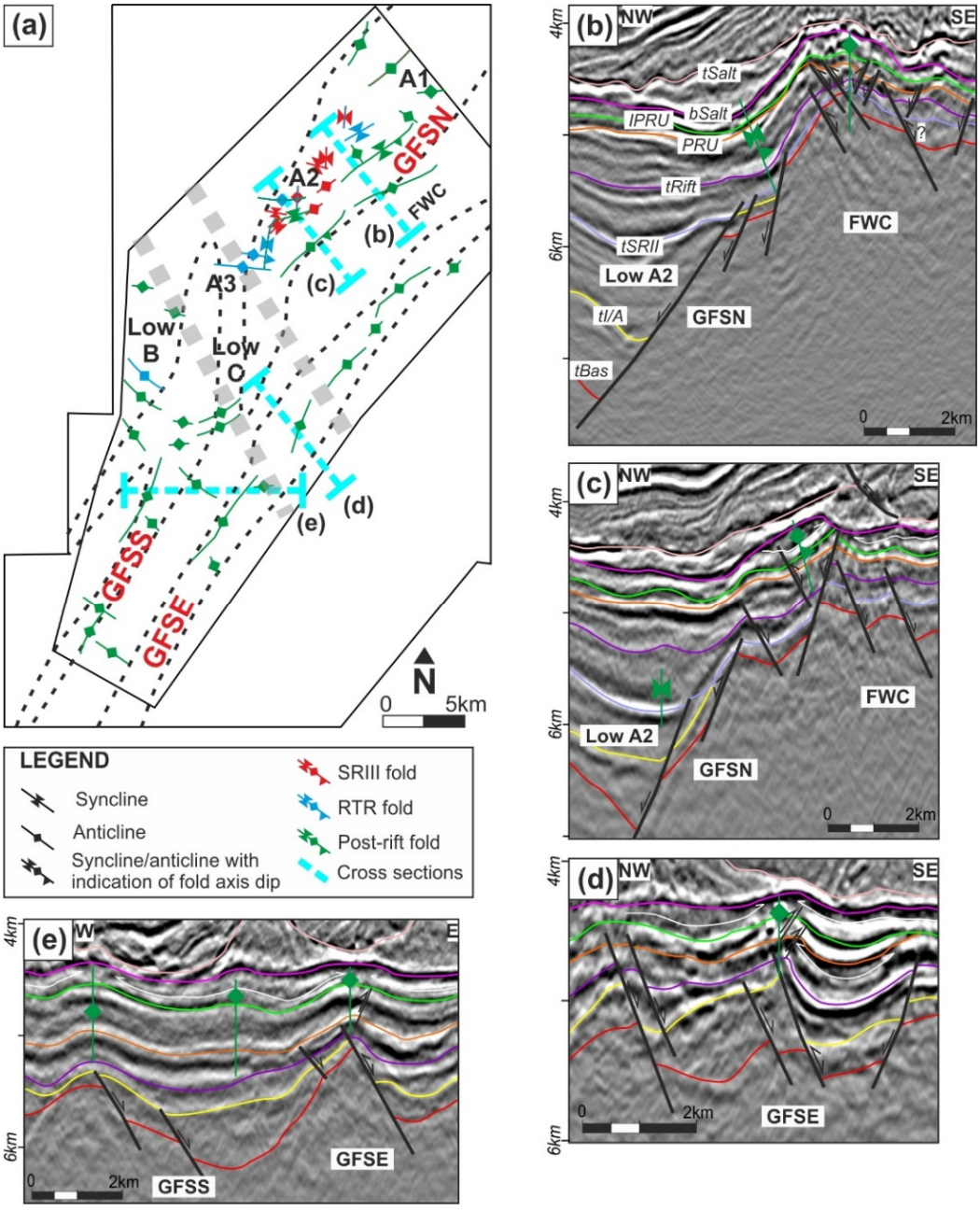


Figure 4.13: (a) Map of folds distribution, showing their geometry and classification according to the age of formation. Dotted black lines represents the GFS branches and dotted grey lines are the accommodation zone (Figure 4.5a). Notice the SRIII hanging wall folds in the lows A1-3 related to displacement variations on the GFSN (c.f. Schlische, 1995). b) GFSN footwall-crest fold with significant proximal hanging wall deformation and possible inversion (double arrowed displacement indicator). Notice the constant thickness of the post-rift across the GFSN, suggesting post-depositional deformation. c) Fault-propagation folding (FPF) in the hanging wall of the GFSN related to reverse kinematics due to inversion, leading to uplift, erosion and scarp development. d) FPF over a fault segment of the GFSE. Notice the erosive truncation in the top of the RTR and within the PRII sequence and inferred reverse faults. e) FPF over a segment of the GFSE, a transverse fold (centre of the section) and a differential compaction fold to the west, probably amplified due to later shortening as evidenced by the deformation of the bSalt horizon.

The erosion in the hinge zones of fault-propagation folds (FPFs) and truncations on the Post-rift II (PRII) sequence by the bSalt horizon is interpreted as the result of significant subaerial exposure of the top of PRII, thus related to the Base-salt Unconformity (BSU). Also, a folded geometry is observed towards the top of the salt in some localities (Figure 4.13c,d), implying that folding was active for a significant time after the onset of evaporite deposition and potentially until the onset of the salt tectonics in the Albian (Cobbold & Szatmari, 1991; Fetter, 2009). In addition, assuming that the inversion leads to localized (e.g. segments of Guriri Fault system East - GFSE) or generalized (GFSN and footwall complex - FWC) uplift, this could have delayed the onset of evaporite deposition over these areas. Consequently, using the basin-scale correlations to estimate the age of the onset of evaporite deposition in the context of the study area could be problematic (Davison, 2007; Kukla et al., 2018; Szatmari et al., 2021). Meanwhile, it is possible that there was significant subaerial epigenetic karstification related to the BSU, resulting in secondary porosity in the upper section of post-rift carbonates. The occurrence of epigenetic karst on top or within carbonate sequences is well known in this type of context (e.g. Saller et al., 1994).

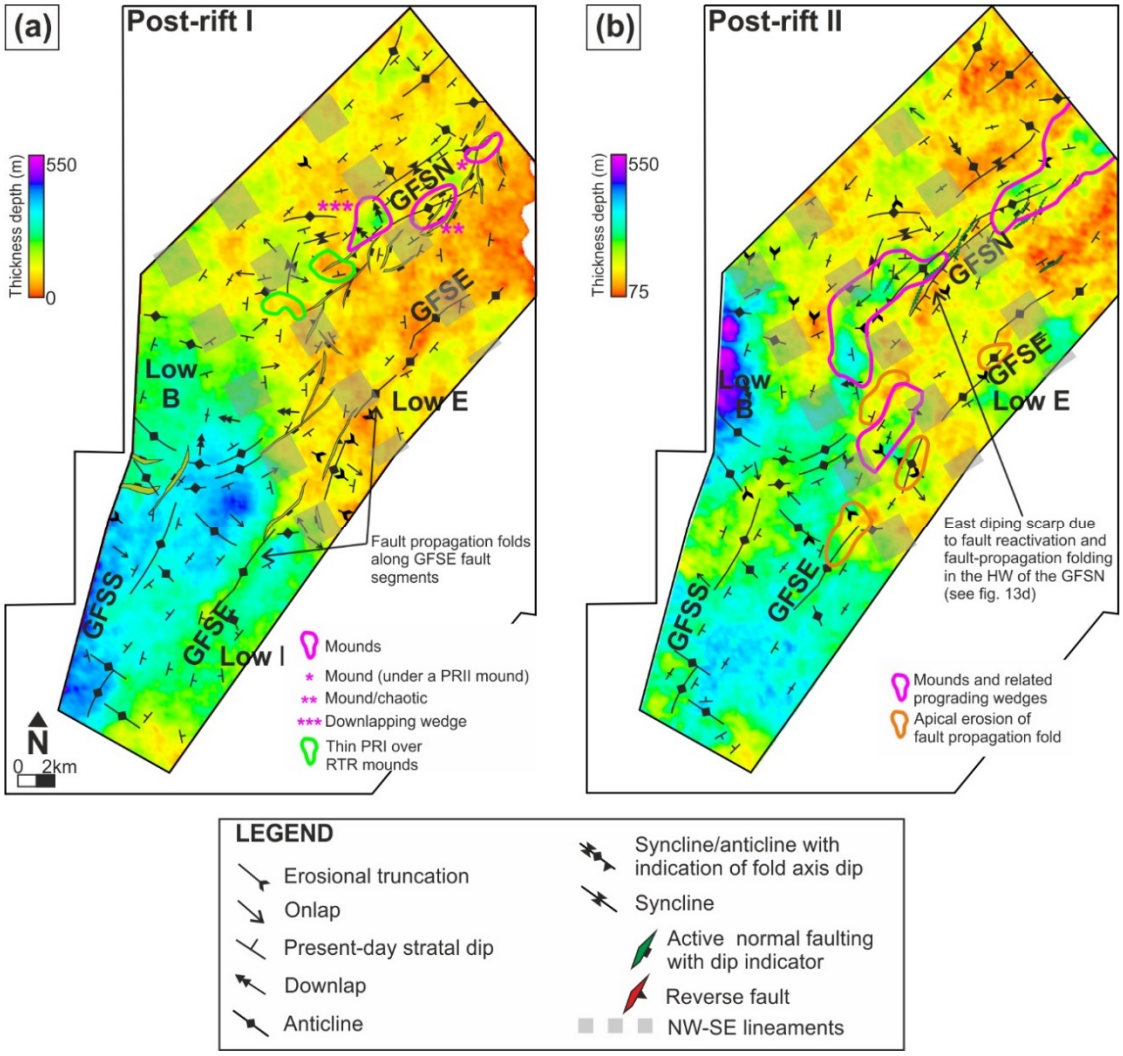


Figure 4.14: Tectono-stratigraphic maps of the post-rift TSSs (PRI – a, and PRII – b). Thickness maps of each phase is superposed by polygons representing the active faults, folds axes, stratal dip and termination geometries extracted from 3D seismic. Mounds and erosive features are also shown. Fault traces of PRII (b) are shown with dotted borders since they do not displace the bSalt horizon.

4.7 Discussion

4.7.1 Strain migration during rifting

The shallowing of the Moho below the present-day shelf-break of the Campos Basin has been observed in several publications (Meisling et al., 2001; Mohriak et al., 2008; Stanton

et al., 2019; Matos et al., 2021). Matos et al. (2021) shown that such uplift correlates with a thicker presalt package, referred by Figure 4.4b. The location of Moho uplifts in the SE Brazilian margin is considered to be related to lateral changes in the lithospheric thickness inherited from Brasiliano orogenic assembly that allowed later along rift-axis flow of plume material (Morgan et al., 2020). The presence of an important basement tectonic limit near the study area (i.e. tectonic limit between the Oriental Terrane of Ribeira belt and the Cabo Frio Tectonic Domain – Figure 4.1) (Stanton et al., 2019; Strugale et al., 2021) could have worked as such a lithospheric limit. Hence, a longer residence of plume material could result in lithospheric thinning and extension thus strain localization, evidenced by the development of major rift faults and thicker depocentres such as the Corvina-Parati and São João da Barra Lows in the shallow waters of the Central and North Campos Basin (Figure 4.4).

Rift basins that evolve to oceanic crust are characterised by strain diachroneity along dip and strike, meaning that strain locus migrates towards the propagation centre (Lavier & Manatschal, 2006). Consequently, rift units in a distal position will correlate to post-rift units towards the onshore (Figure 4.4b). The strain migration is not uniform and will depend, amongst other factors, on crustal heterogeneities. The occurrence of a shallower Moho under thick rift deposits could be interpreted as a proto spreading axis and therefore a strain locus during the rift phase 1 (RP1), located in present-day shallow water domain of the Campos Basin. During the rift phase 2 (RP2), the strain locus moved slightly eastwards (Figures 4.3b, 4.10) before moving rapidly offshore ("jump") as a consequence of a thick boudin of upper crust (c.f. Clerc et al., 2018) formed during RP1 strain localization. This buoyant boudin of upper crust has clear spatial correlations with thinner

RP2 and post-rift deposits and the occurrence of internal unconformities in the eastern half of the study area (Figure 4.4b).

The role of basement-inherited NW-SE brittle fracture and dyke swarms observed in onshore Precambrian basement on the evolution of the rifting in the offshore domain is still a matter of debate. While some publications consider they are fundamental (Fetter, 2009; Alvarez et al., 2021), others do not recognise their expression offshore (Lourenço et al., 2016; Stanton et al., 2019). The regional map shown in Figure 4.4a infers the projection of the Vitória-Colatina lineament transecting the study area. Detailed 3D seismic interpretation identified an active NW-SE accommodation zone from the RP2 onwards near to the position of this regional lineament (Figures 4.8, 4.10, 4.14). Similarly, a WNW-ESE trend worked as a kinematic buffer during RP1, which can be correlated with the Castelo Lineament (c.f. Almeida et al., 2021) (Figure 4.10). Detailed 3D seismic mapping of the presalt sequence (this work) and of the basement (Strugale et al., 2021) did not recognize any discrete NW-SE structure. Therefore, assuming the NW-SE and WNW-ESE lineaments here identified as being correlative to either Vitória-Colatina or Castelo lineaments onshore are still speculative, especially the second.

The inversion structures resulted from selective reactivation of NE-SW rift faults due to orthogonal compression observed towards the end of post-rift supersequence and onwards are best explained by intraplate stress-propagation from oceanic mid-ridge spreading (c.f. Artyushkov, 1973). Such a mechanism had been correlated with Late Cretaceous and Tertiary inversions in the Campos Basin, competing with far-field compression from the Andean Orogen (Fetter, 2009). Considering the estimated onset of oceanic crust generation in the Campos Basin as ca. 117 Ma (Heine et al., 2013), the observed inversion in figures 4.13 and 4.14 could be correlated with the onset of oceanic spreading thus ridge pushing.

4.7.2 Rift and post-rift tectono-stratigraphic evolution

The filling architecture of rift basins in both natural and experimental (physical and numerical) is the subject of numerous publications. Amongst them, 2D and 3D models for tectono-sedimentary evolution of rift basins in general (Prosser, 1993; Gawthorpe & Leeder, 2008), for continental lacustrine environments (Lambiase, 1990; Morley, 2002), and the model for rift sequence stratigraphy of Martins-Neto and Catuneanu (2010) will be compared with our interpretations. In common, these publications point to the difficult task to understand the feedback between tectonic related and purely eustatic-driven sea/lake level changes. This is especially problematic in rift basins where the fault-controlled depocentres form diachronously and the accommodation space in lacustrine settings is subject to local climate constraints, thus disregarding global eustatic curves (Catuneanu, 2006).

Although the references thereof are relevant contributions to understanding the evolution of rift basins they also proposed denominations for the stages and patterns of rift filling that are far to be comparable. The main point is that they mostly rely on the interpretation of regional 2D seismic lines to set up the models. However, our interpretation is founded in a 3D seismic survey, which differs from the models mentioned. Hence, each geologic cross section here presented would fit (or not) in each of the models used as references (Lambiase, 1990; Prosser, 1993; Morley, 2002; Gawthorpe & Leeder, 2008). For example, in the context of the RP2, the syn-rift II sequence (SRII) could represent either the rift climax system (Prosser, 1993), interaction and linkage stage during highstand in a lacustrine or shallow water context (Gawthorpe & Leeder, 2008), and early half-graben stage (Morley, 2002). Our interpretations clearly show that there is no silver bullet in the

literature and therefore is pointless to put effort on trying to fit our results to any individual or a combination of these classifications.

We tentatively compared our findings with the few publications focused on the petrologic-sedimentologic content and the 2D seismic-stratigraphic architecture of a single half-graben in the shallow water domain of the Central Campos Basin (Goldberg et al., 2017; Alvarenga et al., 2021). Three syn-rift system tracts represent the rift tectono-sedimentary record as interpreted by Alvarenga et al. (2021). Their basal unit (Rift Initiation) could potentially be correlated with RP1, and the upper High and uppermost Low Tectonic Activity Systems Tracts could be correlated with, respectively, SRII and syn-rift III (SRIII) (i.e., the RP2). Alternatively, the Low Tectonic Activity System Tract (LTAST) could be correlated with the Rift Transition sequence. However, this latter correlation is problematic because (1) LTAST is wedge-shaped and is similar with either SRII and SRIII, (2) the authors interpret significant LTAST syn-tectonic gravitational deposits (Goldberg et al., 2017), and (3) the lack of data and interpretation in the footwall block does not allow correlations with the graben-fill and a clear understanding of how fault activity evolves towards the end of rifting.

From that, our choice is to use the strain distribution and evolution tied with a well constrained seismic-stratigraphic framework, which is only possible if preceded by high density 3D seismic mapping (e.g.: Figure 4.5). A dense mapping of seismic horizons, faults, and stratal terminations against them, followed by integration with isopach contours to build tectono-stratigraphic maps (Figures 4.3, 4.8, 4.14) were the main criteria to distinguish two phases of rifting (RP1 & RP2) (Figures 4.9, 4.10). The superposing of snapshots of the strain distribution along time was the best strategy to unveil the complex strain evolution. Such an approach could fill the gap originated in the biased sampling by

wellbore data (i.e. wells were drilled only in the structural highs), especially regarding the lack of rock data of gravitational and reworked deposits in the regions where syn-sedimentary tectonism is expected to be high.

Our interpretations reveals that the changes in strain distribution during the rifting are the product of two directions of extension (E-W during RP1 and roughly NW-SE during RP2) (Figure 4.10). PR1 is characterised by small and isolated grabens, with preserved thickness up to 900 m, while RP2 evolves to longer grabens that hosts up to 1800 m thick of sediments controlled by faults that often did not take advantage of RP1 faults (Figure 4.8a-c). In addition, RP1 depocenters were inverted while new faults nucleated or linked from initially isolated RP1 faults (e.g. GFSN), resulting in the final horst geometry of the GFS. Such overall pattern resembles the models of rift basins where they are initially characterised by isolated grabens with small displacements, followed by fault interaction and linkage, leading to the formation of larger grabens (Gupta et al., 1998; Gawthorpe & Leeder, 2008). These models, however, do not necessarily means change in extension directions and do not mention different rift phases.

An addition argument for two phases of rifting is the contrasting lithologies, from volcaniclastics plus coarse siliciclastics (RP1) to carbonates and hybrid siltstones (RP2) (Figure 4.9). Also, the merge of two unconformities (tI/A & tSRII) into a single surface in most of the area is meaningful for a significative gap in the sedimentary record between RP1 and RP2, which is not observed for any other mapped horizon (Figure 4.6).

Superimposed rift phases have been observed in rifts and are related to changes in the stress field during their evolution (Lambiase, 1990; Bosworth, 1994; Morley, 2017). In examples from the North Sea and Sudan, rift phases are directly superimposed or have a “sag” phase in between (McHargue et al., 1992; Phillips et al., 2019). Multiple rift phases are also

recognized in the NE Brazilian margin and within aulacogens in the counterpart Borborema province (Matos et al., 2021). However, the stratigraphic charts of the Campos Basin and the adjacent Santos and Espírito Santo basins (França et al., 2007; Moreira et al., 2007; Winter et al., 2007) only recognize a single rift phase. Therefore, our proposal for two rift phases for the Campos Basin is a significant turning point for the knowledge of the basin. However, we must recognize that such an interpretation is not novel (see Mohriak et al., 2008), but had been neglected in most publications afterwards.

4.7.3 Implications for the age of the presalt sequence

The interpretation of two phases of rifting in the northern Campos Basin here presented shall be confronted with the new age constraints for the end of presalt deposition, the onset of evaporite deposition, and for the post-salt sedimentary column (Tedeschi et al., 2017; Lima et al., 2018; Tedeschi et al., 2019; Pietzsch et al., 2020; Sanjinés et al., 2022). Traditionally, the presalt sequence in the East Brazilian margin is interpreted as a single rift phase plus post-rift succession spanning for 19 myr in total, from Hauterivian (134 Ma) to Late Aptian (ca. 115 Ma) (e.g. Mohriak et al., 1990; Winter et al., 2007). Recently, the age of the end of presalt deposition was interpreted as not younger than Barremian (125 ma) (Pietzsch et al., 2020, Eldrett et al., 2023) and the age of evaporite deposition as being Early Aptian (ca. 124 Ma) (Tedeschi et al., 2017; 2019). Although the age of evaporites is still under debate (see discussion in review paper of Szatmari et al., 2021), the problem remains: how to accommodate two phases of rifting (instead of one), a rift transition and a post-rift stages in an time interval ca. 10 myr shorter than previously assumed.

The first option is to challenge the age of the onset of volcanism assuming it as a proxy for rift-related mechanical subsidence. In the onshore basement counterpart to the northern Campos Basin, tholeiitic dykes emplaced along NW-SE lineaments are dated as been as old as 142 Ma – Berriasian (Santiago et al., 2020) and 136 Ma – Valanginian (Pessano et al., 2021), in close geochemical and temporal relationship with the Paraná-Etendeka LIP and to early manifestations of the break-up of the South Atlantic Ocean (e.g. Matos, 2021). Also, several publications show evidence of Late Jurassic to Valanginian rift-related deposition along the proto Central Segment of the South Atlantic Ocean. For example, the Afro-Brazilian depression in Northeast Brazil (Kuchle et al., 2011; Matos et al., 2021), and Kimmeridgian (L. Jurassic) rift units at the base of the Camboriú Formation in the Santos Basin, equivalent to the Cabiúnas Formation (Alves et al., 2020).

A simple though not definitive solution would be considering the life-span of the presalt envelope as being the previously assumed 19 myr (Winter et al., 2007), and therefore the age of the onset of rifting would be at ca. 144 Ma. In this assumption, we are contesting the oldest ages of the volcanics of the Cabiúnas Formation (i.e. 134 Ma). This assumption is partially supported by the mean age of emplacement of onshore dykes (ca. 142 Ma in the Castelo swarm, Santiago et al., 2020), which is here considered as a possible proxy for the onset of rift-related deformation and perhaps mechanical subsidence. The tholeiitic composition of these onshore dykes is the same of the Cabiúnas volcaniclastics (Mizusaki et al., 1992). However, although this interpretation kept the presalt rift plus post-rift within the average value of the global dataset of life-span of rift basins (ca. 20myr, Woodcock, 2004), the assumption of dyke emplacement and volcanism as proxy to the onset of rifting is problematic, especially in the context of a magma-poor margin (Morgan et al., 2020).

Therefore, an investigation focused on obtaining further radiometric ages in the presalt basalts, especially in the northern Campos Basin, should be considered in future works.

A secondary possibility to adjust the ages of the presalt sequence in face of new age constraints would be to challenge both recently proposed Barremian age for the end of presalt deposition (Tedeschi et al., 2019; Pietzsch et al., 2020) and the Early Aptian age for evaporite deposition (Tedeschi et al., 2019). Both views are contested in the review paper of Szatmari et al. (2021), based on the lack of physical connection between the proto-South Atlantic and the Tethys section used for calibration and problematic radiometric ages for evaporite deposition. Nevertheless, our understanding is that there are good reasons to consider the correctness of the 125 Ma for the end of presalt deposition. Amongst them, the long-termed endorreic character of the pre-salt lake that allowed an equilibrium between lake waters DIC (dissolved inorganic carbon) reservoir and atmospheric CO_2 (Pietzsch et al., 2020). The assumption of an Early Aptian age for the evaporite deposition is reinforced by thick Aptian post-salt sequence described in the Campos Basin (Lima et al., 2018), later studied in detail in the SE Brazilian Margin in Sanjinés et al. (2022), who concluded that the Aptian-Albian border is 10 Ma older than previously assumed (Figure 4.2). If the onset of evaporite deposition occurs between 116-110 Ma as suggested by Szatmari et al. (2021), it means an at least 9 myr gap related to the base salt unconformity. Nevertheless, these authors mention the diachronous character of evaporite deposition in the proto-South Atlantic Ocean (see also Farias et al., 2019). In the northern Campos basin, we observed significant erosion on the top of the Macabu Formation (Figure 4.9). A similar observation was made in the shallow-water domain of the Central Campos Basin (Goldberg et al., 2017; Alvarenga et al., 2021). Such subaerial exposure could imply in the occurrence of epigenetic karstification on the uppermost

section of the presalt sequence, which was never reported in the literature on the Campos and Santos Basins.

4.8 Conclusions

The tectono-stratigraphic record of the presalt of the northern of Campos Basin is subdivided into syn-rift supersequence, rift transition (RTR) sequence, and post-rift supersequence. The syn-rift is composed of three (seismic) tectono-stratigraphic sequences (TSS SRI, II, III), and the post-rift supersequence encompasses two TSSs (PRI, II), with a rift transition sequence (RTR) in between. Subaerial unconformities and their correlative conformities separate them.

The main structural compartments are represented by a NE-SW oriented horst that encompasses high and low strain domains, constituting the Guriri Fault System (GFS). It is constituted by three high strain branches of normal faults named north, south, and east (GFSN, GFSS, and GFSE respectively) and a footwall complex adjacent to GFSN. The GFS horst delimits two relative structural lows, Inner GFS Low to the west and Outer GFS Low to the east.

The syn-rift supersequence records two phases of rifting (RP1 & RP2), where the latter is equivalent to syn-rift II (SRII) combined with syn-rift III sequence (SRIII) and the former with syn-rift I sequence (SRI). Both phases recorded an initial phase of sediment-starved half-grabens followed by widespread deposition that heals the rift-related structural relief. Lithological content and lithostratigraphic units also differ significantly.

Rift phase (RP) 1 was deposited in isolated half grabens typically defined by E-dipping NNE-SSW to N-S faults formed under a roughly WNW-ESE extension. Following the erosion and depocentre inversion of RP1 deposits, rift phase 2 (RP2) sediments deposited

in longer grabens formed by segment linkage of roughly NE-SW fault zones dipping either east or westwards, thus defining an asymmetric horst. This horst comprises a fault system denominated Guriri Fault System (GFS), correlated southwards to a previously unnamed major structural high in the Central Campos Basin. A roughly NW-SE extension was active during early RP2 (SRII) and slightly rotated back to WNW-ESE towards the end of RP2.

The RTR supersequence is related to the onset of asymmetric thermal subsidence coeval with localised syn-depositional faulting. Thermal subsidence dominates throughout the post-rift supersequence. Towards the end of the post-rift stage, NW-SE tectonic shortening promoted selective reverse reactivation of rift faults, resulting in the upward propagation of fault-propagation folds. They were active at least until the onset of salt tectonics during the Albian. The inversion is interpreted as result of intraplate stress propagation triggered by the onset of oceanic spreading in the Campos Basin during Early Albian. Also, erosion of fold hinge zones means that a significant degree of subaerial erosion preceded the onset of evaporite deposition.

Based on ages of dyke emplacement onshore, new age constraints for the end of presalt deposition, and in order not to shorten the traditionally accepted span of the rift plus post-rift stages by a half, we suggest that the onset of PR1 occurred during the Berriasian.

The tectonic shortening and inversion during the post-rift have potential links with the localized syn-sedimentary hydrothermal venting during post-rift deposition and the widespread hydrothermal diagenesis recorded in the presalt succession. In addition, events of subaerial exposure point to potential epigenetic karstification on the top of RTR, PRI and PRII sequences. Hence, these pieces of information should be considered for future investigations and, mostly, for reservoir characterisation and modelling of the Pre-Salt reservoir of the Campos Basin.

Statement of Authorship for joint/multi-authored papers for PGR thesis

To appear at the end of each thesis chapter submitted as an article/paper

The statement shall describe the candidate s and co-authors independent research contributions in the thesis publications. For each publication there should exist a complete statement that is to be filled out and signed by the candidate and supervisor **(only required where there isn't already a statement of contribution within the paper itself).**

Title of Paper	Basement geology and its controls on the nucleation and growth of rift faults in the northern Campos Basin, offshore Brazil.
Publication Status	X Published □ Accepted for Publication □Submitted for Publication □Unpublished and unsubmitted work written in a manuscript style
Publication Details	Strugale, M., Schmitt, R.S. & Cartwright, J. (2021). Basement geology and its controls on the nucleation and growth of rift faults in the northern Campos Basin, offshore Brazil. Basin Research, 33, 1906-1933. https://doi.org/10.1111/bre.12540

Student Confirmation

Student Name:	Michael Strugale		
Contribution to the Paper	I have performed all the seismic interpretation, established the investigation lines, set up hypotheses, correlated the results of the seismic interpretation with wellbore data and compared with case studies elsewhere. Structural mapping and analyses, figures and writing were also performed by myself. Co-author 1 is a specialist in the Precambrian basement in the counterpart onshore and helped with the interpretation and significance of geochronologic data, and reviewing the manuscript. Co-author 2 supervised the research and reviewed the manuscript.		
Signature	Michael Strugale	Date	28 OCT 2022

Supervisor Confirmation

By signing the Statement of Authorship, you are certifying that the candidate made a substantial contribution to the publication, and that the description described above is accurate.

Supervisor name and title:	PROFESSOR JOE CARTWRIGHT		
Supervisor comments	I fully concur with the statements above		
Signature		Date	28 OCT 2022

This completed form should be included in the thesis, at the end of the relevant chapter.

Chapter 5

Diagenetic Products, Settings and Evolution of the Presalt Succession in the Northern Campos Basin, Brazil.

This chapter has been prepared to submit for publication. The research presented in this chapter is my own work, together with several collaborators. Christopher Day, Jenny Omma, Jeremy Rushton, Jon Bouch, and Nick Roberts supported the analyses of, respectively, C-O stable isotopes, QEMSCAN mineral mapping, fluid inclusion microthermometry, cold cathodoluminescence imagery, and LA-ICP-MS U-Pb geochronology. Supervisors, Joe Cartwright and Laurence Robb, contributed to research design, validation and proof reading.

5.1 Abstract

Despite all the effort made towards the comprehension of sedimentary, tectonic, and diagenetic evolution of the presalt sequence in the North Campos Basin (East Brazil), two gaps in the knowledge have yet to be solved: 1) a detailed study of the diagenesis in crystalline basement and rift phases, and 2) the geochronologic framework constraining the diagenetic events that affected the presalt succession. In this study, samples from these geologic units were analysed for mineral composition and paragenetic evolution, fluid temperature and salinity, stable isotope compositions, and LA-ICP-MS U-Pb ages of carbonate phases. This dataset was integrated with lithogeochemical wireline logs and geological cross sections that aim to unravel the geologic controls on the distribution of diagenetic events and the petrophysical proprieties of the sediments. The U-Pb ages of replacive and vein-filling cements reveal three tectono-diagenetic events, named Barremian-Aptian (BADE, 125-117 Ma), Albo-Cenomanian (ACDE, 103-98 Ma), and Campanian-Maastrichtian (CMDE, 83-70 Ma). Each phase presents distinct minerals, formation temperatures, and burial conditions. The hydrothermal qualifier, identified by the temperature contrast between fluid and host rock, was initially high during the BADE, then diminishes over time (through the ACDE) until reaching an equilibrium with the host rocks during the CMDE. Diagenetic events are not always coeval with magmatism but do coincide with regional tectonic events described in the literature and interpreted as the result of increasing intraplate stresses.

5.2 Introduction

Secondary porosity of hydrothermal origin in carbonate rocks is of fundamental relevance in several areas of economic and environmental geology, with relevance to Mississippi Valley Type (MVT) Pb-Zn(Ag) deposits and to the circulation patterns of hydrocarbons and drinking groundwater within reservoirs (Corbella et al., 2004; Loucks et al., 2004; Davies & Smith Jr, 2006; Klimchouk, 2015; Parise et al., 2018). The term "hydrothermal" refers to waters that are warmer (>5-10°C) than the immediate environment (White, 1957; Machel & Lonnee, 2002). Speleogenesis, brecciation, dolomitisation, silicification and "exotic" minerals that include MVT-type Zn-Pb ores are the products of hydrothermal diagenesis (Hesse, 1989; Davies & Smith Jr, 2006; Neilson & Oxtoby, 2008). Therefore, hydrothermal diagenesis can be described as a succession of events of speleogenesis (i.e. generation of secondary porosity by dissolution) and pore-filling which often work selectively within structures and strata of the rock massif during the geological evolution of the rock massif. However, when pore space is low or absent, diffusion takes place in response to changes in burial conditions (Pingitore, 1982). The combination of in-situ transformations, dissolution and precipitation could explain why studies of hydrothermal diagenesis either choose to disregard or not the gross 3D geological framework (faults and strata), as observed in several outcrop studies (e.g. Sharp et al., 2010; Swennen et al., 2012).

The Macabu Formation and the upper part of the Coqueiros Formation constitutes the Pre-Salt reservoirs in the North of Campos Basin (SE Brazil) (Winter et al., 2007; Herlinger Jr. et al., 2017). They represent, respectively, the rift transition (RTR) and post-rift (PR) stages of the basin and were deposited during the Barremian (Tedeschi et al., 2019; Olivito

& Souza, 2020; Pietzsch et al., 2020). These reservoirs were scrutinised and have had their petrographic, depositional, stratigraphic, geochemical and paleo thermometric properties analysed, revealing strong hydrothermal influence during the diagenesis as consequence of magmatic pulses during continuous burial (Herlinger Jr. et al., 2017; Lima & De Ros, 2019; Lima et al., 2020; Olivito & Souza, 2020). Recently, this area was interpreted in terms of basement geology and its influence on the structural style of the faults that affected the overlying rift sediments (Strugale et al., 2021). Furthermore, Strugale and Cartwright (2022) proposed a comprehensive tectono-stratigraphic evolution model for the entire presalt sequence, recognising two episodes of rifting followed by post-rift selective inversion. Also, the formal stratigraphic column of the presalt sequences (c.f. Winter et al., 2007) were constrained to the recently proposed new depositional ages (Tedeschi et al., 2017; Tedeschi et al., 2019; Pietzsch et al., 2020; Sanjinés et al., 2022). Nevertheless, characterisation and diagenetic phases of the basement and the rift phases remain poorly understood and, more importantly, there is no geochronological constraint for the diagenetic events of the entire presalt sequence.

In the studied area, the oil/water contact is locally above the top rift horizon, meaning that the syn-rift III (SRIII) sequence is not only the main hydrocarbon reservoir but also represents a significant part of the aquifer. It is recognized that integrated studies and geological modelling of the whole geologic section is of interest of production design for several reasons (e.g. Packard et al., 2001; Cantrell et al., 2004). Amongst them, to improve the modelling of petrophysical proprieties of the aquifer and to provide geological and time constraints for physical (geomechanical), depositional and diagenetic modelling (Paula Faria et al., 2017; Abarca et al., 2019; Welch et al., 2020). Fracturing and subsequent filling in deep burial contexts are much more continuous in time and have a strong feedback with

rock and fluid chemistry (Laubach et al., 2019). Fortunately, U-Pb geochronology through Laser Ablation Inductively Coupled Plasma Mass Spectrometer (LA-ICP-MS) in carbonates has become widely used in several geologic situations, with especial emphasis on dating diagenetic and brittle deformation events recorded in carbonate cements (Roberts et al., 2020; Rochelle-Bates et al., 2021; Ganade et al., 2022).

The aims of this work are:

- Describe the host rocks, diagenetic products and paragenetic evolution of the syn-rift and rift transition sediments, and the Precambrian basement.
- Characterise the diagenetic mineral phases in terms of constitution, composition, absolute ages, carbon ($\delta^{13}C$) and oxygen ($\delta^{18}O$) stable isotopes, paleo temperatures and fluid salinity.
- Describe the diagenetic environments and build a time-constrained model for the diagenetic evolution, correlating to the tectonic and magmatic events recorded in the Campos Basin.
- Based on geochemical wireline logs, stratigraphic and structural frameworks, propose a predictive model for the distribution of the diagenetic products, to which intensity of variation in secondary porosity might be correlated.

5.3 Geological Context

The study area is located 70 km offshore in the deep water context of the Northern Campos Basin, East Brazil. It is developed over a basement comprising the transition zone between the Cabo Frio Tectonic Terrain (CFTD, c.f. Schmitt et al., 2004) and the Oriental Terrane of the Ribeira Belt, with both units having been involved in the Brasiliano orogenetic tectonic events of Ediacaran to Cambrian age (Schmitt et al., 2016; Stanton et al., 2019;

Strugale et al., 2021) (Figure 5.1a). The Campos Basin formed by rifting of West Gondwana during the Early Cretaceous (Rabinowitz & LaBrecque, 1979; Chang et al., 1992) and evolved as an initially magma poor, then magma-rich breakup stage (Morgan et al., 2020).

Extensional tectonics of rift phase 1 (RP1) probably started during the Berriasian and reached its peak during the rift phase 2 (RP2 – Hauterivian). RP1 resulted in the formation of isolated NNE-SSW-trending, E-W stacked grabens filled with volcaniclastics and coarse arkoses of the Cabiúnas, Itabapoana and Atafona Formations. RP1 faults were reactivated and new faults were nucleated during the RP2, resulting in extensive NE-SW half graben development that fringes a 10 km wide regional horst (the Guriri Fault System – GFS, Figure 4.4). The grabens of RP2 were initially filled with reworked carbonates and hybrid laminites in the depocentres, followed by bioclastic rudstones (coquinas) stacked onto the structural highs and transitioning to lower energy facies towards the depocentres. These units correspond to the lower section (Coq A) of the Coqueiros Formation (Olivito & Souza, 2020; Strugale & Cartwright, 2022) (Figure 5.1b).

The upper section of the Coqueiros Formation is interpreted as a rift transition phase (RTR). Olivito and Souza (2020) subdivided the RTR in three sets of facies associations and organized them into four seismic-stratigraphic units (COQ B to E, Figure 5.1). CoqB to D represent an overall coarsening-up sequence on which bioclastic rudstones and grainstones are the main porous units. On the other hand, CoqE represents a restricted, evaporative environment with higher clay content. The overlying Macabu Formation was deposited during the post-rift stage in a highly evaporative alkaline lacustrine system (Herlinger Jr. et al., 2017; Lima & De Ros, 2019; Tedeschi et al., 2019; Pietzsch et al., 2020). Following a gap whose duration is under debate, extensive deposition of marine-

derived evaporites of the Retiro Formation took place during the Aptian, followed by shallow marine carbonates of the Quissamã Formation (Winter et al., 2007; Sanjinés et al., 2022). The deposition of Quissamã carbonates triggered wide-spread thin-skinned gravitational gliding of salt and related salt compression in the outer regions of the Campos Basin (Davison, 2007; Szatmari et al., 2021).

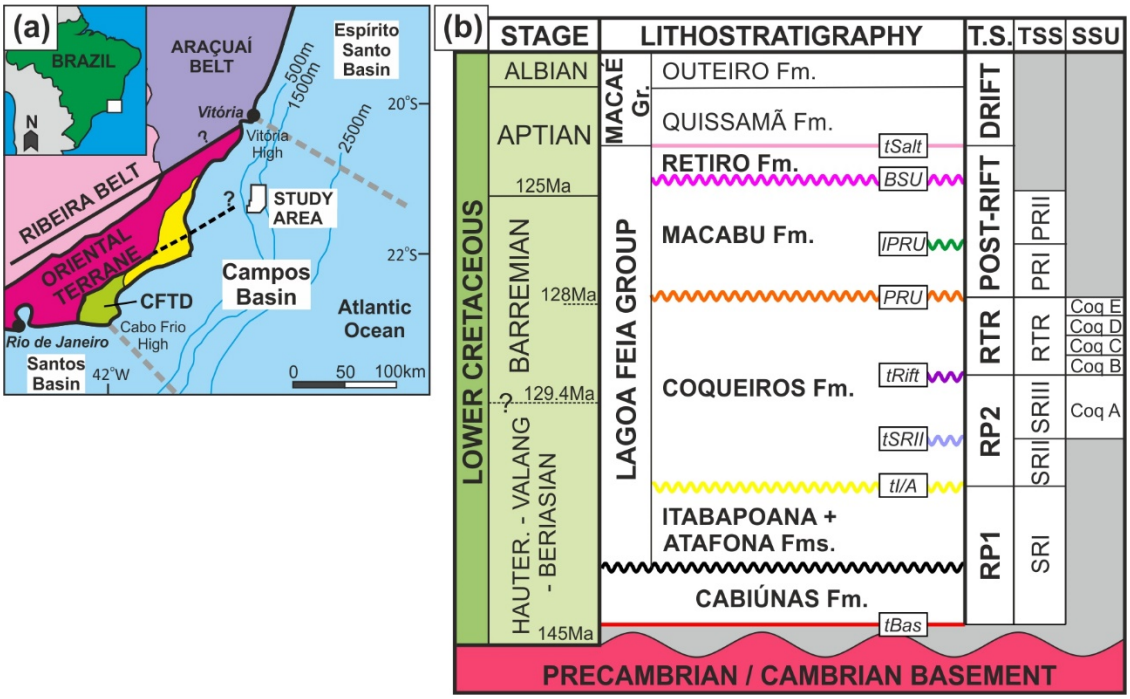


Figure 5.1: a) Location of the studied area and simplified geological map of the onshore basement. CFTD: Cabo Frio Tectonic Domain (c.f. Schmitt et al., 2004). b) Stratigraphic framework of the studied area. Stages are based in Strugale and Cartwright (2022 and references therein). Lithostratigraphy is based in Winter et al. (2007), where the horizons tSalt, BSU and so on are the mapped seismic horizons (see text). Tectonic stages (T.S.) are based in Strugale and Cartwright (2022) and Winter et al. (2007), where RP1 and RP2 are rift-phases 1 and 2, and RTR is rift transition stage. TSS are tectonic-stratigraphic sequences as defined in Strugale and Cartwright (2022), where SRI, SRII, and SRIII are syn-rift I to III sequences, and PRI & PRII are post-rift sequences I & II. SSU are the seismic-stratigraphic subdivisions of the Coqueiros Formation proposed in Olivito and Souza (2020).

The presalt sequence corresponds to the formations of the Lagoa Feia Group, with the exception of the Retiro Formation (evaporites). On the other hand, the Pre-Salt reservoir has been defined as the rift transition to post-rift unit comprising, respectively, the Macabu

and the upper Coqueiros Formations in the Campos Basin. These units are equivalent to, respectively, the Barra Velha and Itapema formations in the Santos Basin (Carminatti et al., 2008; Muniz & Bosence, 2015; Fetter et al., 2018).

5.4 Materials and Methods

This study is based on 67 sidewall cores from 18 wells (Figure 5.2). The strategy for sample selection aimed to represent the more diagenetically altered rocks of RP2 and RTR sequences and also to obtain novel data for RP1 and Precambrian basement. Therefore, they are distinct from those in Lima and De Ros (2019); Lima et al. (2020); and Olivito and Souza (2020), based on high vertical resolution sampling though from fewer wells. Despite low vertical representativeness, our samples came from wells widely distributed in the study area.

At least one standard-thickness polished thin section was extracted from each sample after cleaning using toluene and methanol in a Soxhlet apparatus or ultrasonic bath in Isopropanol. Some thin sections were stained with Alizarin red-S and potassium ferricyanide to differentiate the carbonate minerals as outlined by Dickson (1965). 13 samples were cut and placed in resin pods for automated mineralogical distribution mapping using QEMSCAN (FEI) equipment at Rocktype Ltd laboratory in Oxfordshire (UK).

A total of 16 carbon ($\delta^{13}C$) and oxygen ($\delta^{18}O$) isotopes analyses were performed in the Department of Earth Sciences of the University of Oxford on samples from 10 wells. Powder from selected diagenetic carbonate phases were collected by micro-drilling and subsequently analysed in a PANalytical Empyrean Series 2 powder X-ray diffractometer operating at 40 kV and 40 mA with a Co Kα source. Powder was analysed for oxygen and

carbon stable isotopes in a Thermo Delta V Advantage equipment Isotope Ratio Mass Spectrometers (IRMS), fitted with a Gas Bench II peripheral. All data were reported relative to the Vienna Pee Dee Belemnite (V-PDB) international standard in per mil units (‰). External precision and accuracy were checked in relation to the reference material NBS 19 (TS-Limestone; Coplen et al., 2006), yielding results better than ± 0.03‰ for $\delta^{13}C$ and ± 0.07‰ for $\delta^{18}O$.

Ten thick thin sections (> 100μm) from six wells were selected to obtain U-Pb ages of carbonates from several paragenetic phases. Initially, the samples were imaged through cathodoluminescence (CL) to support the identification of growth phases that will guide the spots for LA-ICP-MS. The cold cathode cathodoluminescence (CC-CL) analysis was performed using a NewTec Scientific Cathodyne® system installed at the Petrography Department of the British Geological Survey (BGS, Nottingham, UK). Frame by frame images were stitched using the imageJ plug-in and methodology of Preibisch et al. (2009). Subsequently, samples were analysed using LA-ICP-MS U-Pb geochronology procedures of Roberts et al. (2017). The analyses were performed in the Geochronology and Tracers facilities at the BGS (Nottingham, UK). A static spot ranging 60-100 μm was used depending on the target size. All quoted ages are lower intercept $^{206}Pb/^{238}U$ dates from Tera-Wasserburg plots, at 2σ, with propagated systematic uncertainties. Regressions are un-anchored as the spread in data permits the accurate assessment of the upper intercept (the initial $^{207}Pb/^{206}Pb$), and goodness of fit is evaluated using mean square of weighted deviates (MSWD). More details on the quality controls are available in Rochelle-Bates et al. (2022).

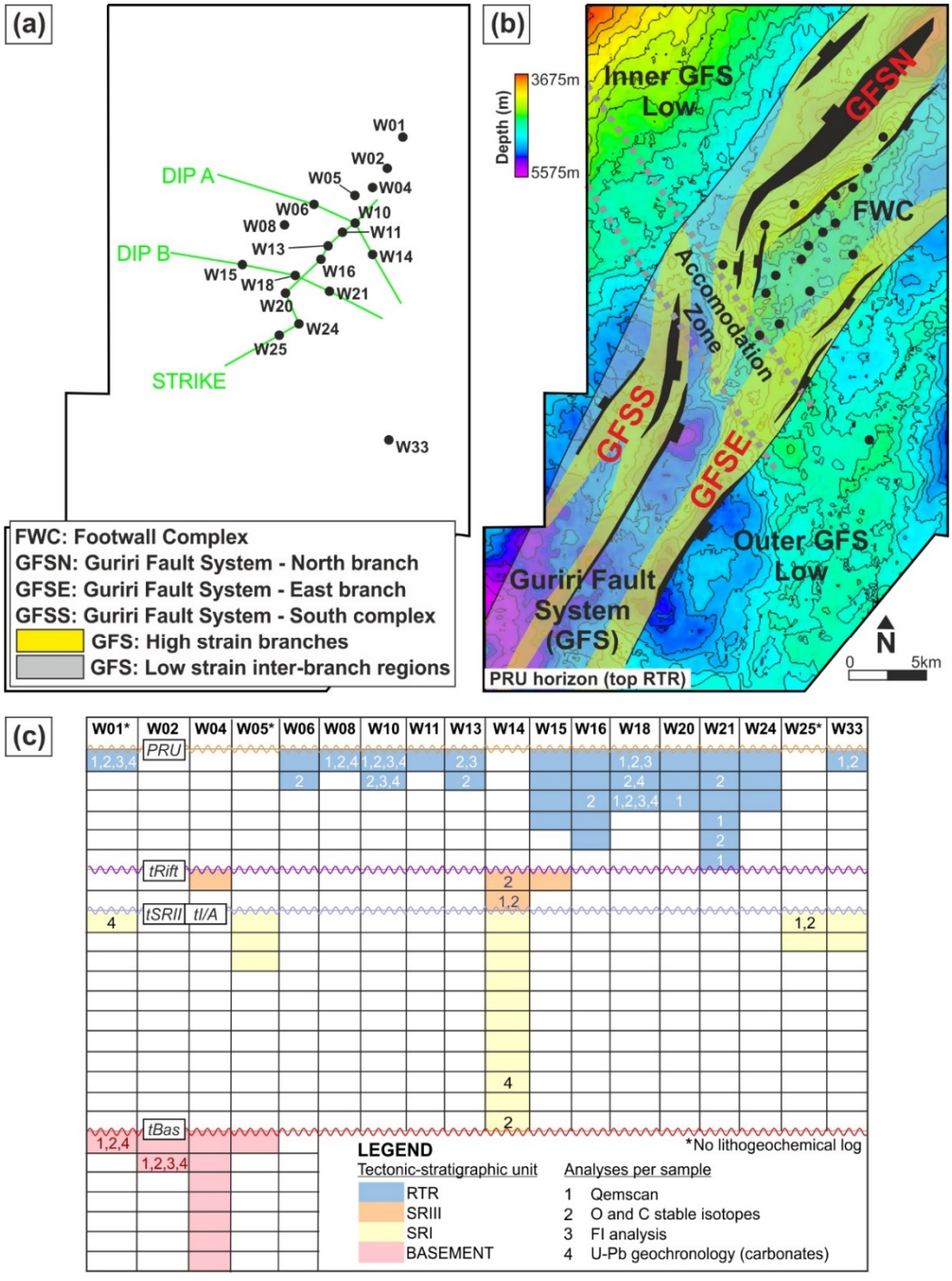


Figure 5.2: a) Index map of the wells used in this study with the location of well section fences. b) Well location overlapped to structural contours of the top of rift transition surface, main structural compartments and simplified fault framework. c) Compilation of the samples used in this study and the respective analyses.

Fluid inclusions (FI) on pore filling saddle dolomite, prismatic and macrocrystalline quartz, and blocky and vein-filling calcite were studied in double-polished rock chips.

Microthermometric measurements of individual fluid inclusions were conducted by the Pore Scale Solutions Ltd using a Linkam TMSG600 heating and freezing stage attached to a Zeiss Axio Imager microscope. FIs where described using the approach of Roedder (1984), where FIs were classified according to genetic type (primary, secondary, and pseudo-secondary) and linked to the paragenetic phase. Groups of genetically-related FIs were considered as a fluid inclusion assemblages ("FIA"). The microthermometric analyses followed the general temperature "cycling" methodology for the study of fluid inclusions in diagenetic cements outlined by Goldstein and Reynolds (1994). Homogenisation temperature determinations (T_h) were made before ice melting determinations. The ice melting data were used to model salinity for aqueous FIs. Homogenisation (T_h), first melting/eutectic (T_{fm}), last ice-melting (T_{ice}) and hydrate melting (T_{hyd}) temperatures were measured with a precision typically of, respectively, ±2 to ±5, ±2 to ±5, ±0.2 and ±0.5°C. The calculation of the salinity of fluid inclusions was undertaken by comparing microthermometric data with the phase relations in experimentally determined salt-water-gas systems under equilibrium conditions for the NaCl-H_2O, $CaCl_2$ -H_2O & NaCl-H_2O-$CaCl_2$ systems (e.g. Oakes et al., 1990). Where paired T_{ice} and T_{hyd} were available, the code *CalcicBrine* (Naden, 1996) was used to calculate salinities in terms of the system NaCl-$CaCl_2$-H_2O. In the absence of T_{hyd} data, salinities were calculated in terms of the system NaCl-H_2O for $T_{ice} \geq$ -21.3°C and by artificially extending the freezing point suppression curve (NaCl-H_2O Binary) for $T_{ice} <$ -21.3°C. No pressure corrections were applied. The samples were also screened using fluorescence to reveal hydrocarbon-bearing inclusions.

The lithogeochemical wireline logs uses element capture spectroscopy that gives the Si, Ca, Mg, Fe, & Mg ratios of the lithologies. Lithogeochemical tools use a standard AmBe

source and a BGO (bismuth germanate) detector to measure relative elemental yields, which are converted to elemental dry weight logs using an oxides closure model calibrated with local lithologies (Zhao et al., 2017). Lithogeochemical data were integrated into the seismic-geological cross sections and cross-plots for elemental values, for instance, Ca x Si, Si x Al, and Mg x Fe weighted by the stratigraphic units, were made.

5.5 Results

This section aims to present the detailed investigations performed in the studied samples, from petrography and geochemistry to geochronology (Figure 5.2b). Initially, samples were described as either host rock or diagenetic facies because it was often not possible to recognise the original rock due to the intensity of diagenesis. From that starting point, focus shifted to diagenetic products (cements, vugs, fractures and veins) which were investigated using QEMSCAN, stable isotopes, fluid inclusion microthermometry and U-Pb geochronology. These data allowed the characterisation of the diagenetic events and their environments and to correlate them with tectonic and magmatic events of the Campos Basin. Finally, lithogeochemical logs overlaid in well section fences constrained interpretations regarding the lateral distribution of more intensively diagenetically altered layers.

5.5.1 Petrography

The rocks described through petrography were initially classified into five lithofacies (crystalline basement, bioclastic grainstones and rudstones, hybrid arenites and siltstones, and arkoses and conglomerates). Considering that our focus is on the diagenetic products, these lithofacies will be briefly described under a group called “host rocks”. Because SRI

conglomerates and arkoses were not yet described by the previous works in the north of Campos Basin, a brief petrographic description is provided. Otherwise, please refer to previous publications on the crystalline basement (Strugale et al., 2021 , Chapter 3) and on the rift transition and post-rift sequences (Herlinger Jr. et al., 2017; Lima & De Ros, 2019; Lima et al., 2020; Olivito & Souza, 2020). Three diagenetic-related facies (dolostones, cherts, and breccias) were recognised and described, which often include tectonic and compaction-related features, such as fractures, veins, and stylolites.

5.5.1.1 Host rocks

Crystalline basement: these samples show granitic compositions with variable quantities of phyllosilicates. Two out of nine basement samples from W01 and W02 exhibit, respectively, widespread brecciation and a discrete network of veins. These fractures are filled by quartz, pyrite and dolomite to ankerite series (Figures 5.3a, 5.5b). The brittle deformation in these samples could be associated to its proximity to the northern branch of the Guriri Fault System (GFSN) branch (Figure 5.2b).

Conglomerates and arkoses: occur in four wells and are constituted of lithic conglomerates and arkoses with fine to granule-size grains, representing the syn-rift I (SRI) sequence (Figure 5.1b). There are also conglomerates related to footwall erosion related to SRII but they are indistinct within the samples analysed. The lithic grains are made of basement and basalt with dimensions up to pebble size. In the conglomerates, the clasts are commonly covered by oxide rim (probably hematite) (Figure 5.3b). In the arkoses, clasts are dominated by equal proportions of feldspars (mostly K-feldspars) and quartz, followed by detrital muscovite, lithic grains, and zircon; the grains are mostly angular and the rocks are poorly sorted (Figure 5.3c). The cement is carbonatic and constituted of Fe-dolomite to

ankerite that often substitutes feldspar grains, leading to an abundance of up to a third of the sample. Feldspar replacement by Al-phyllosilicates is also common. QEMSCAN data, however, suggests that ankerite replaces the feldspar grains and Fe-dolomite to ankerite constitutes the cement (see inset on Figure 5.3c). The constitution and paragenetic phases of SRI are similar with observations made in the equivalent section in the Central Campos Basin (Carvalho & De Ros, 2015).

Conglomeratic rocks occur in all the wells that penetrated the SRI sequence, but coarser and compositionally more heterogeneous specimens occur in W05, located along the trace of the GFSN branch (Figure 5.2). The occurrence of conglomerates with basement and basalt clasts is related to the significant footwall uplift and erosion during SRII stage (Strugale & Cartwright, 2022) (Figure 5.1b). Samples from wells W14, 25, and 33, located away from the Guriri Fault System (GFS) branches, tends to have a more homogeneous composition, that is, minor lithic constitution and better selection (Figure 5.2b).

Bioclastic rudstones and grainstones: The bioclasts are commonly constituted of disaggregated bivalves and ooids replaced by micrite, fine grained blocky dolomite and chalcedony (Figure 5.3d). Matrix is constituted by blocky and prismatic quartz and calcite, where extensive vug-related porosity could occur when not partially or completely obliterated by macrocrystalline calcite (Figure 5.4a). Vugular porosity is common, but many of the analysed samples are completely recrystallised by calcite, quartz and minor dolomite (Figures 5.8a & 5.7b, respectively). Veins are predominantly filled by calcite, sometimes with prismatic quartz lined in fracture walls. One vein in a bioclastic rudstone has a distinct suite of minerals constituted of massive pyrite (Py) with minor nuclei of chalcopyrite (Cpy) and nearby vugs partially filled by Sr-barite (Figure 5.5e).

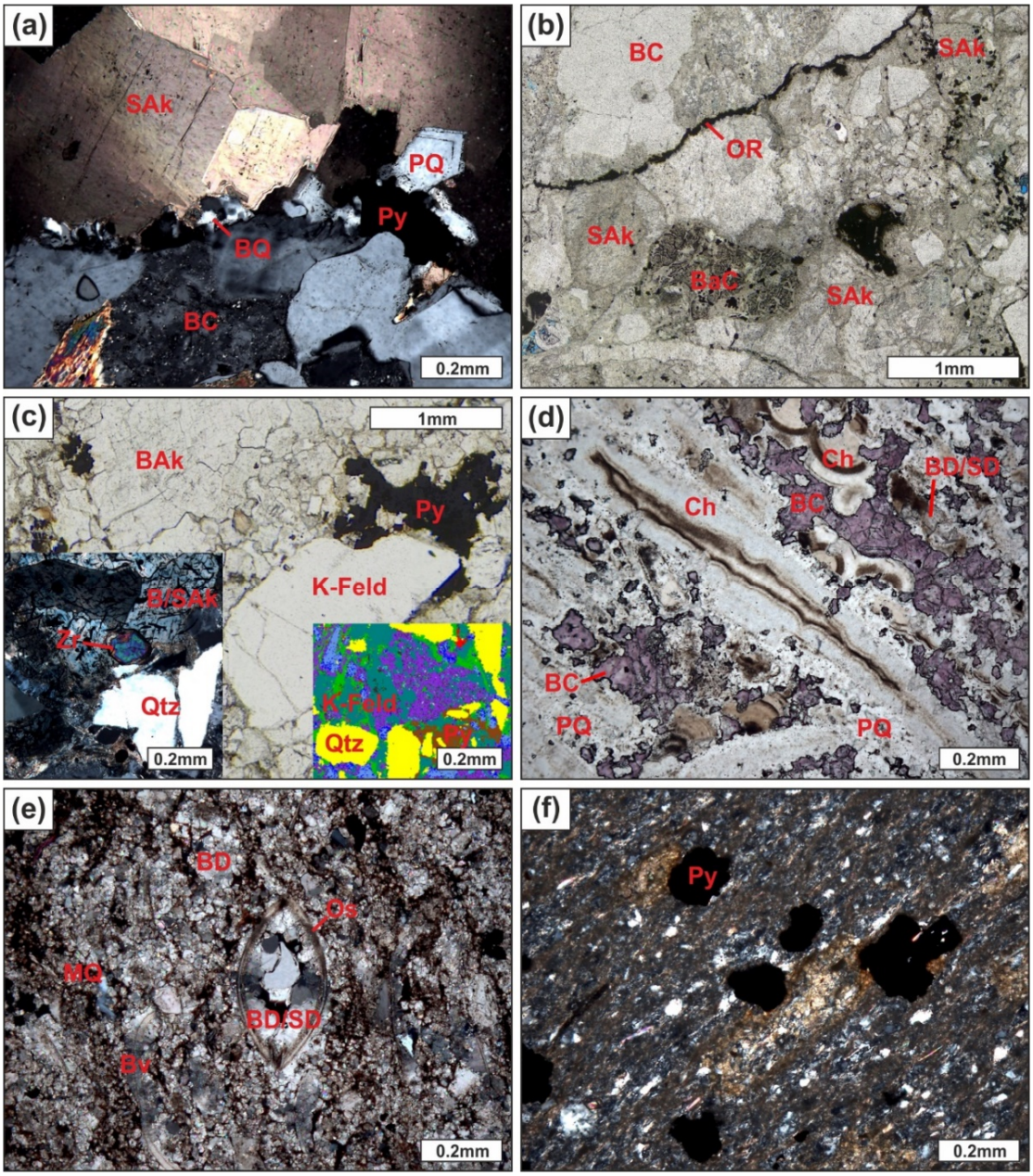


Figure 5.3: a) Brecciated Precambrian basement with post-deformational overgrowth of pyrite (Py), blocky (BQ) and prismatic quartz (PQ), and saddle ankerite (SAk) onto a clast of basement (BC) (XPL). b) Lithic conglomerate constituted of clasts of basement (BC) and basalt clasts (BaC) cemented with saddle ankerite (SAk). Notice the oxide rim (OR) around some of the clasts (PPL). c) Very coarse arkose with K-feldspar (K-Feld) clasts and cement made of pyrite (Py), blocky and saddle ankerite (SAk) (PPL). The small insets show the blue-stained Fe-dolomite cement and zircon grain (Zr) (left) and QEMSCAN imagery showing K-Feld partially replaced by ankerite (purple), Al-phyllosilicates (light green), and ankerite/Fe-dolomite (blue) cement. d) Rudstone made of fragmented bivalve bioclasts replaced by blocky dolomite (BD) with intraparticle space with botryoidal chalcedony (Ch) and blocky calcite (BC) (PPL). e) Bioclastic arenite with ostracod (Os) and fragmented bivalves (Bv) in a matrix of blocky dolomite (BD), microcrystalline quartz (MQ), and Mg-clay (XPL). f) Siltstone with detrital quartz and white mica in Mg-clay matrix and post compaction pyrite nodules (Py) (XPL).

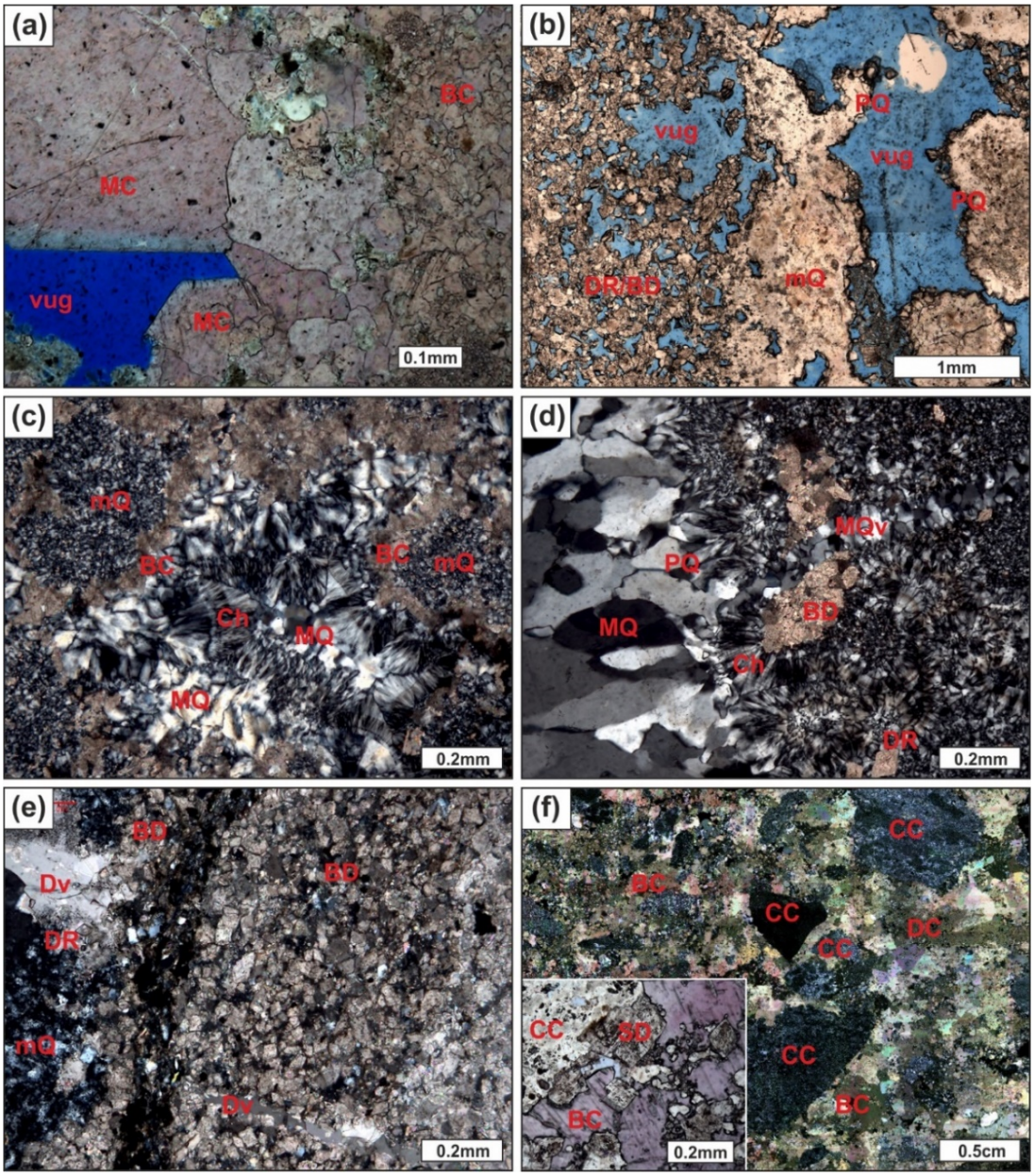


Figure 5.4: Silica and carbonatic diagenetic products. a) Ooids and peloids replaced by blocky calcite and vug partially filled with macrocrystalline calcite (MC) (PPL). b) Extensive vugular porosity in the interface zone between dolostone (left) made of euhedral and blocky dolomite (DR/BD), and chert made of microcrystalline (mQ) and prismatic (PQ) quartz. Vugs in chert have minor Sr-barite crystals (PPL). c) Succession of diagenetic products made of microcrystalline quartz (mQ), blocky calcite (BC), blocky chalcedony (Ch) and macrocrystalline quartz (MQ) (XPL). d) Succession of diagenetic products where early blocky dolomite (BD) is followed by microcrystalline quartz (mQ) and chalcedony (Ch) are finally by quartz as veins (MQv) and vug-filling megacrystals (MQ) (XPL). e) Two generations of dolomite cementation. Extensive early blocky dolomite cement (BD) on the right, with subsidiary dolomite rhombs (DR) in a layer with silica-rich matrix (mQ) on the left, both superimposed by late veins of hyaline dolomite (Dv) (XPL). f) Breccia constituted of chert (CC) and dolostone (DC) clasts in a matrix intensively cemented by hyaline blocky calcite (BC) and saddle dolomite (SD) (XPL). The inset shows the respective stained colours.

The occurrence of bioclastic rudstones and grainstones in the SRIII+RTR with moderate to high shell reworking are interpreted as predominantly shallow lacustrine depositional environment, dominated by storm currents (Olivito & Souza, 2020). These authors also observed an overall coarsening-up and shallowing-up sequence from SRIII to RTR sequences. Wells located in the hanging wall of the GFSN branch (W06, 08, and 15) also have occurrence of high energy lithofacies as RTR prograding mounds onto low energy deposits (Strugale & Cartwright, 2022). These low energy facies constitute the next group of samples to be described.

Hybrid arenites and siltstones: they occur in the seven wells and are characterized by variable proportions of clastic and bioclastic constituents in a notable proportion of magnesian clay (mostly stevensite – see Herlinger Jr. et al., 2017) or organic matter in the matrix. They are composed of detrital quartz and white mica of coarse silt to fine sand grain size, peloids, disarticulated bivalve shells and ostracods (Figure 5.3e); zircon is a common detrital accessory (Figure 5.5d). The samples are sometimes completely replaced dolomite as rhombs and aggregates (Figures 5.4e, 5.6a,d), microcrystalline quartz (chert) and blocky chalcedony as nodules and layers (Figure 5.6b). Pyrite is also abundant and occur as either post-compaction dendritic nodules or subvertical veins that are cross cut by partially filled stratabound fractures (Figure 5.3f). Hyaline dolomite veins occur as fracture fill in chert layers and as vug fill in chert nodules, suggesting that chert may be more brittle than the dolostones (Figure 5.6b,d).

5.5.1.2 Diagenetic products

Dolostones: are predominantly constituted by dolomite rhombs and aggregates of blocky dolomite (BD) in a matrix of Mg-clays, organic matter and some detrital clasts (Figure 5.6a); in some cases, dolomite crystals represents nearly 100% of the sample (see discussion in Warren, 2000). Dolostones commonly occurs as interlaminated with or hosting chert nodules (Figures 5.4d,e, 5.6b). Dolomite rhombs, aggregates and saddle dolomite are also common diagenetic products in bioclastic grain and rudstones, although not particularly abundant in these facies and often preceding calcite cements (Figure 5.3d). Saddle dolomite (SD) has been associated solely with hydrothermal diagenesis since it often occurs as the latest phase of vug filling and reveals high formation temperatures, while blocky dolomite (BD) and dolostones have been interpreted as an eodiagenetic product of in Mg-clay rich lithologies (Lima & De Ros, 2019). However, some low energy deposits have minor dolomite (Figure 5.3f), and dolomite rhombs are sometimes engulfed by saddle dolomite, calcite cements and calcite veins, suggesting a temporal series (Figure 5.4e,f). In addition, dolomite rhombs apparently precede silica cementation (Figure 5.4d). Therefore, dolomitisation is interpreted as one of the earliest diagenetic phases.

Cherts: This term refers to samples or layers that are mostly constituted by siliceous cement that replaced the protolith as microcrystalline, prismatic, and macrocrystalline quartz and chalcedony, often blurring the original rock. Chert cement or constituting entire samples are widely distributed throughout SRIII and RTR sequences. Chalcedony and microcrystalline quartz aggregates commonly exhibits halos of immiscible material thus configuring botryoidal textures (Figures 5.3d, 5.5a). Fracturing and dissolution occur in quartz cements and result in networks of interconnected fractures and vugs with significant

secondary porosity. Vugs and fractures are commonly filled with minerals such as svanbergite, Sr-barite and blocky dolomite (Figures 5.5c,f & 5.6f).

The occurrence of chert interlaminated with dolostone probably relates to the primary sedimentary layering. Dolostones probably reflect a higher abundance of Mg-clay minerals in the host rock. Therefore, cherts formed in less argillaceous facies although the common presence of floating dolomite rhombs in cherts suggest that some clays were present. However, such an interpretation could be problematic because the mechanisms that govern the coexistence of siliceous cement and dolomitisation are not well understood (Hesse, 1989; Packard et al., 2001; Bustillo, 2010). Also, it is often impossible to identify the protolith of cherts and thus assess its primary porosity, making any assumption on the original clay content and primary porosity problematic. On the other hand, dolomitisation of Mg-clays releases orthosilicic acid, which could explain the common occurrence of siliceous cements in dolostones (Lima & De Ros, 2019). Hybrid lithologies contain detrital quartz that could also provide diagenetic silica. However, extensive quartz precipitation in fractured basement suggests that it may constitute an external source of silica (Figure 5.5b). Hence, the abundance of silica cement across the sedimentary section suggests the presence of an external source of silica that could either be represented by the crystalline basement or by the SRI arkoses.

Breccias: they were identified in samples from both basement and sedimentary section, and are solely constituted of intraclasts, which make them distinct from the conglomerates. Breccias occur relatively close (<50m in depth) to unconformities, where samples from wells W01 and W15 are next to tRift unconformity, and W18 sample is close to PRU (Figure 5.2c).

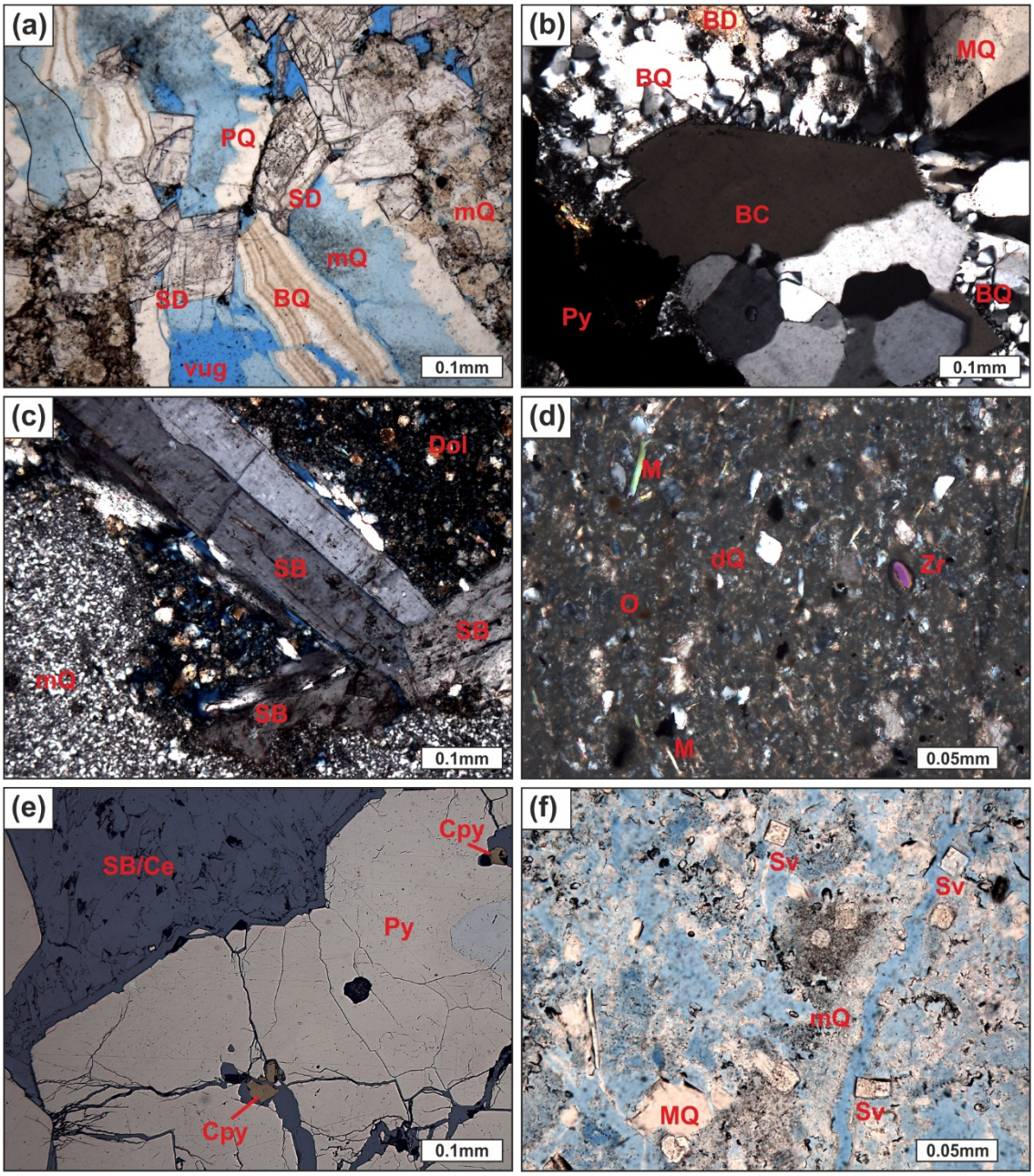


Figure 5.5: Aspects of diagenetic products and accessory detrital and diagenetic minerals. a) Breccia constituted of a microcrystalline quartz as matrix with saddle dolomite (SD), botryoidal quartz (BQ), prismatic quartz (PQ) and late porous microcrystalline quartz (mQ) and open vugs (PPL). b) Shear fracture filled with pyrite (Py). The damage zone is constituted of basement clast (BC) with prismatic (PQ) and macrocrystalline quartz (MQ) onto it (XPL). c) Microcrystalline quartz (mQ) matrix and a vug filled with prismatic Sr-barite (SB) and dolomite (Dol) (XPL). d) Siltstone with abundant organic matter (O) on which is observed detrital quartz (dQ), mica (M), and zircon (Zr) (XPL). e) Sulfide vein constituted of macrocrystalline pyrite (Py), some chalcopyrite (Cpy) and Sr-barite to celestine (SB/Ce) (RL). f) Svanbergite cubes (Sv) in a matrix of partially dissolved microcrystalline quartz (mQ) and some macrocrystalline quartz (MQ) (PPL).

Breccias in basement rocks are exemplified in Figure 5.5b, on which a shear fracture (not shown) exhibits extensive brecciation, resembling a fault plus damage zone system. This breccia is filled with pyrite, quartz and saddle Fe-dolomite. Within the sedimentary succession, several samples show some degree of fracturing that locally has generated brecciated textures (Figures 5.5e & 5.6f) but are best exemplified in Figure 5.4f. These are dilatational, cement-supported breccias comprising up to 1 cm angular clasts of microcrystalline quartz and subsidiary dolostone clasts; both occur in the matrix as finer fractions. Earlier cement is constituted of blocky and saddle dolomite, followed by pervasive blocky to macrocrystalline calcite cement.

The breccia of Figure 5.4f is interpreted as being formed under relatively deep-burial conditions since both chert and dolostone clasts were lithified prior to brecciation, constituting a hydrothermal-related breccia that was later cemented by calcite. Breccias are a common product of hydrothermal diagenesis and occur along faults and below low permeability strata (e.g. Davies & Smith Jr, 2006; Kyne et al., 2019). However, the possibility of this breccia being surficial, related to epigenetic karst, is not excluded, since is relatively close to the PRU unconformity. Matrix-supported breccias are also a common product of epigenetic karst (Loucks, 1999).

5.5.1.3 Tectonic, compaction and dissolution features

Tectonic and compaction features are represented by veins filled with carbonates and quartz, and occasionally sulfides; stylolites and open fractures partially filled with calcite or dolomite also occur. Veins and fractures are either bedding-parallel or orthogonal with respect to the sedimentary layering. Obtaining the orientation of veins in basement and basalt, along with rocks without evident layering, was not possible. Brecciated texture is

commonly associated with fracture sets, especially in cherts. Because the limited field of view of most captions in the main text, mosaics. Further QEMSCAN and CL imagery of selected thin sections with veins are available in the Appendix C1.

Veins are the most abundant amongst the tectonic structures and occur across the basement and sedimentary units (Figure 5.7). Their walls are straight and sharp in more cohesive rocks (basement, basalts and cherts) and wavy to irregular in porous ones (arkoses, rudstones and dolostones). Veins in basement and syn-rift I (SRI) volcanics and arkoses are filled with variable combinations of dolomite, Fe-dolomite and ankerite, with subordinate pyrite (Figure 5.7e-g). In the bioclastic grain and rudstones of syn-rift III and rift transition (SRIII+RTR) sequences, calcite is the predominant vein filling mineral, followed by quartz (e.g. Figure 5.7b). Notice that within these lithologies the vein composition resembles that of the fracture wall (compare Figures 5.6c & 5.7b). On the other hand, dolomite is the principal vein-fill in dolostones, hybrid siltstones and arenites (Figure 5.7d).

Veins in basement and basalt are filled by dolomite to ankerite series, including Fe-dolomites that are either lining the fracture walls (Figure 5.7e-g) or disseminated within the cataclastic matrix (Figure 5.3a, 5.5b). In the first case, the gradation from dolomite to ankerite is clear, starting with rims of blocky dolomite (BD) with pyrite nodules. Following partial dissolution of the BD, saddle Fe-dolomite (Fe-SD) with well-defined growth rims formed, followed by gap deposits (c.f. Laubach et al., 2019) constituted by ankerite (Ak) exhibiting speckled cathodoluminescence (CL). In the second case, cataclastic-related cements are made of speckled Fe-SD and saddle ankerite (SAk) which are associated with early pyrite and rims of prismatic to blocky quartz (Figure 5.3a).

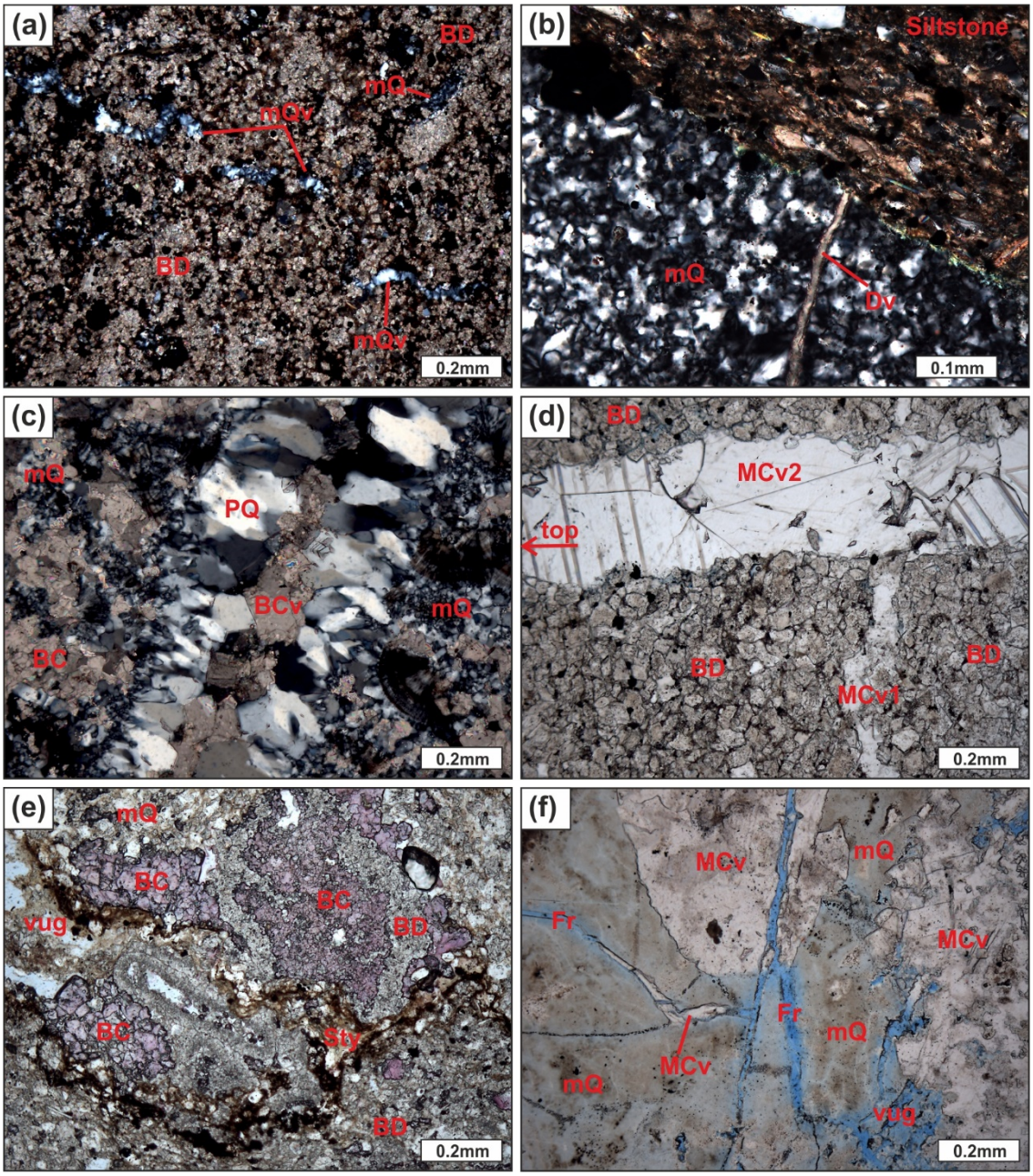


Figure 5.6: Tectonic and compaction features. a) Ptygmatic folding in microcrystalline quartz (mQv) veins in a matrix of blocky dolomite (BD) and microcrystalline quartz cement (mQ) (XPL). b) Contact of dolomitised siltstone and a layer of microcrystalline quartz (mQ) with a dolomite vein (XPL). c) Vein initially filled with lined prismatic quartz (PQ) and later blocky calcite (BCv). The matrix is made of replacive blocky calcite (BC) and microcrystalline quartz (mQ) cement (XPL). c) Dolostone with replacive calcite cement showing an early bed-parallel calcite vein (MCv1) crossed by a vertical macrocrystalline calcite vein (MCv2) (PPL). c) Stained section showing stylolites (Sty) related to vugular porosity in a matrix made of peloids replaced by blocky calcite (BC) and dolomite (BD) (PPL). f) Chert (mQ) showing multiple events of fracturing, brecciation, dissolution and selective filling of macrocrystalline calcite (MCv) (PPL).

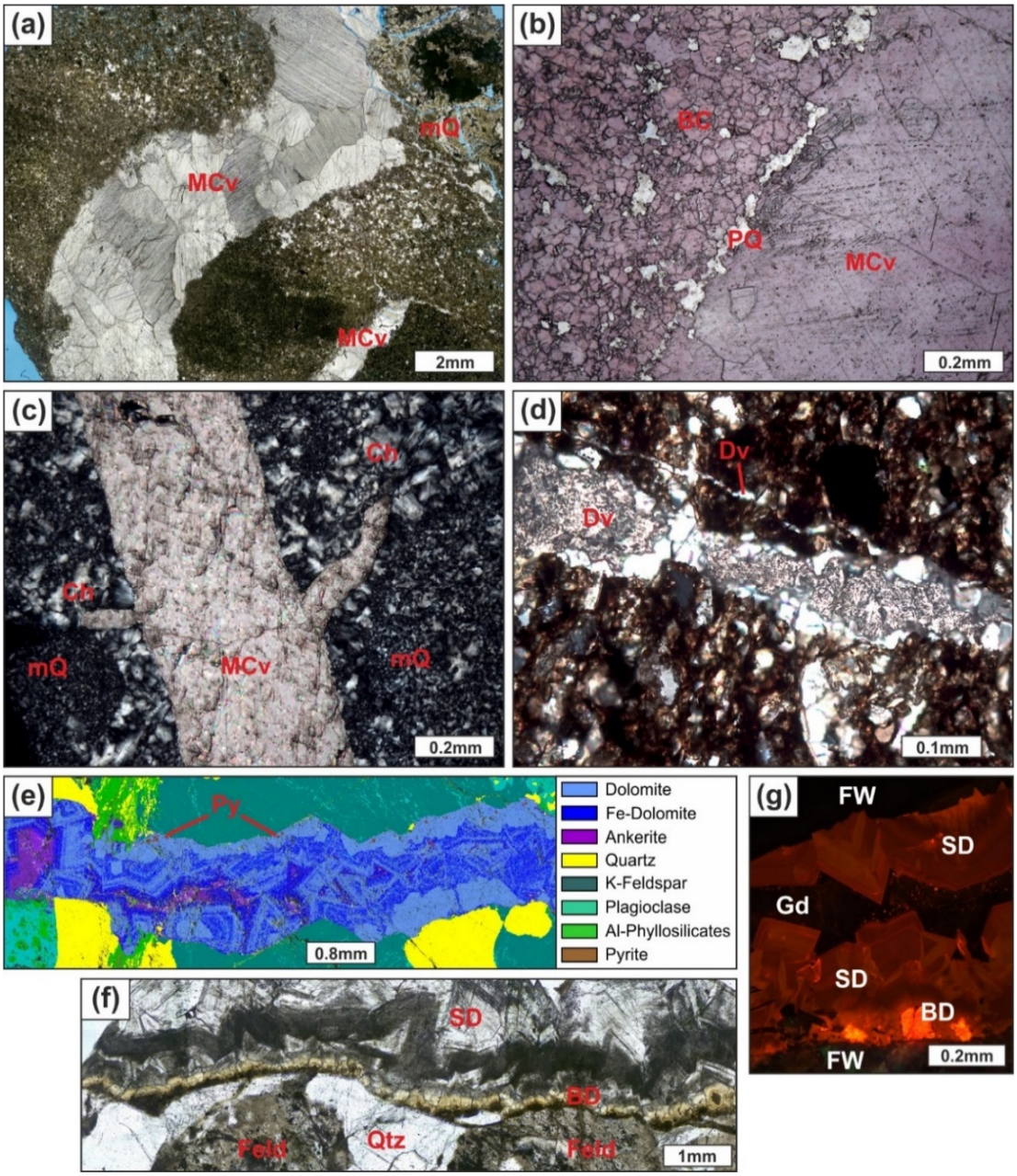


Figure 5.7: Comparison between calcite and dolomite veins. a) Veins of macrocrystalline calcite (MCv) in dolostone with some microcrystalline quartz (mQ) cement (PPL). b) Vein constituted of macrocrystalline calcite (MCv) with a rind of prismatic quartz (PQ) onto a host rock of bioclastic rudstone cemented by blocky calcite (BC) (PPL, stained). c) Sub-vertical macrocrystalline calcite-filled vein (MCv) with subsidiary veins at right angle in a host rock constituted of microcrystalline quartz (mQ) and chalcedony (Ch) (XPL). d) System o sub-vertical dolomite-filled veins (Dv) in a layered hybrid siltstone (XPL). e) High-resolution QEMSCAN and (f) photomosaic of a vein filled by a sequence of blocky dolomite (BD) with pyrite (Py) nodules, and saddle Fe-dolomite (Fe-SD) in basement host rock (PPL). Notice in "e" the compositional gradation/zonation from dolomite, Fe-dolomite than ankerite towards the centre of the vein. g) Cathodoluminescence image of the fracture of "e" and "f" showing bright red-orange colour for the BD, pale orange colour with well-developed growth rims (Fe-SD), and dull brown with speckled orange in the later ankerite gap deposit (Gd) in the centre.

In bioclastic grains and rudstones as well as cherts and some dolostones of SRIII+RTR, veins of macrocrystalline calcite predominate and are chemically homogeneous according to QEMSCAN images (Figure 5.7a-c). Other minerals that occur within calcite veins are dolomite, as floating rhombs, and rims of blocky and prismatic quartz that precede calcite precipitation (Figures 5.6c, 5.7b). An exception is the vein/vug in bioclastic rudstone cemented by replacive and vug-filling calcite and quartz shown in Figure 5.5e. The vein is mainly filled by non-replacive pyrite nodules, some of them exhibiting nuclei of chalcopyrite and sphalerite; pyrite is increasingly fractured towards the margins. These fractures were filled with fibro-radial Sr-barite and anhydrite, which also fills open vugs in nearby host rock, similarly to that observed in Figure 5.8b. Although pyrite is a common diagenetic product in high Mg-clay rocks - as consequence of thermochemical sulfate reduction of organic matter and formation of pyrite nodules (Machel, 2001) - its occurrence as fracture fill in either basement or SRIII rudstones and in Fe-rich dolomites, suggests remobilisation during diagenesis.

Quartz veins are less common and are typically related to quartz-rich lithologies (Figures 5.4d, 5.6c). Due to the difficulty in recognizing sedimentary layering in samples with intense quartz cementation, it is not possible to recognize a preferred orientation. One exception is a subvertical, folded quartz vein in dolostone which suggests an eodiagenetic emplacement of a sand dyke followed by mechanical compaction during burial (Figure 5.6a). In Mg-clay rich lithologies, dolomite veins were identified crossing chert layers interlaminated with siltstones (Figure 5.6b).

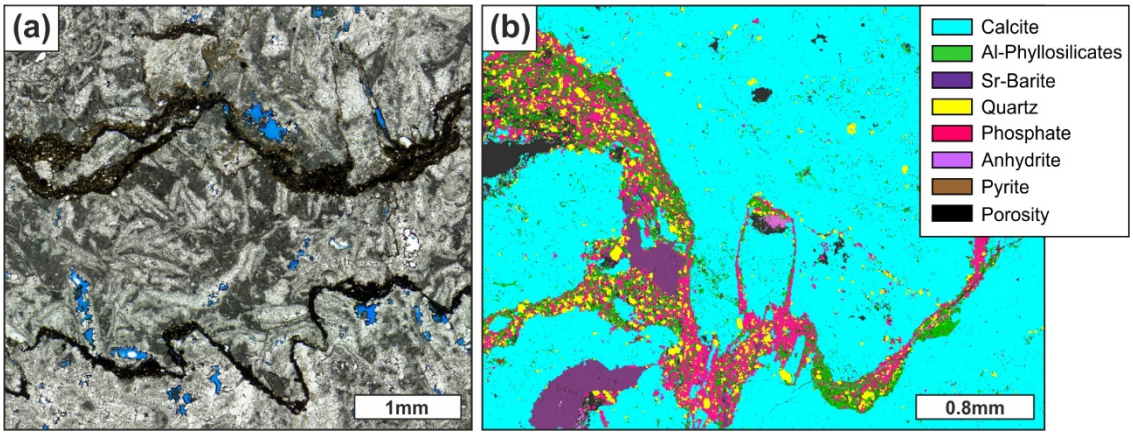


Figure 5.8: Two images of the stylolites observed in a sample of bioclastic rudstone intensively cemented by calcite. a) PPL photomosaic showing two systems of stylolites that cross-cut most of the recrystallised matrix constituents. Notice that minor stylolites are cross-cut by major stylolites. b) High resolution QEMSCAN imagery showing the main mineral constituents of the stylolitic levels. Notice the late vug-fill by Sr-barite and anhydrite.

Stylolites were observed in bioclastic rudstones, hybrid lithofacies and cherts, despite the abundance of clay minerals in the host rock (Figure 5.8a). Petrography and QEMSCAN mapping show that stylolites are characterized by high concentrations of clay minerals (mostly illite), pyrite, barite, anatase (rutile), phosphate, and quartz grains that were involved during the stylolite development (Figure 5.8b). Contact relationships between bioclasts, cements and stylolites shows truncations that suggest multiple events of dissolution and mineral concentration by pressure solution. Well-developed stylolites crosscut thinner ones and most of the cement phases. On the other hand, stylolites in interlaminated hybrid facies tend to occur in the contact zone between chert and dolostone. When occurring in bioclastic rudstones and cherts, stylolites are often accompanied by symmetric porosity enhancement, similar to observations in the Maestrat Basin, Spain (Martín-Martín et al., 2018).

5.5.2 QEMSCAN bulk composition

Bulk compositions of the samples analysed by QEMSCAN (QS50 & QS4) provide the proportions of major and some of the minor elements. Examples of QS4 images are shown in Figure 5.3c, 5.7e, & 5.8b. Appendixes C1 and C2.1 present, respectively, additional images and bulk compositions for QS4 imagery. Table 5.1 reveals quartz and calcite as the most abundant minerals in the carbonate phases, followed by the dolomite group (dolomite to ankerite) and accessory minerals in the form of Al-phyllosilicates, anatase (rutile), phosphates, pyrite, and barite/celestine. In terms of original constituents of the basement rocks, quartz predominates and the proportions of K-feldspar and plagioclase are similar, suggesting a granodioritic composition. The arkose of W25 has a prevalence of K-feldspar and quartz over plagioclase, which could be related to the diagenetic replacement of the latter by ankerite (Figure 5.3c). Overall porosities range from 0.56 to 16.02 % and show no correlation with any particular mineral constituent.

5.5.3 Stable isotopes

The range of $\delta^{13}C$ values are mostly concentrated in an interval between - 1.68 and 1.66‰, with a mean value of 0.85‰ (Table 5.2, Figure 5.9). These results are similar to those described for the diagenetic phases in these rift sediments by Lima et al. (2020) despite the fact that samples from the present study are largely from rift units that were not sampled by these authors. This observation is also valid for mineral phases like Fe-dolomite cement in arkoses and calcite cement in in-situ breccia. The observed ranges for $\delta^{13}C$ are compatible with either marine and freshwater carbonates (Hoefs, 1997) and do not reflect forced hydrocarbon maturation by hydrothermal diagenesis as observed in the counterpart Namibe Basin in Africa (Rochelle-Bates et al., 2021). There is no correlation between $\delta^{13}C$

and $\delta^{18}O$ values, which is also observed by previous works in the Campos, Santos and Kwanza basins (Ceraldi & Green, 2017; Farias et al., 2019; Lima et al., 2020; Pietzsch et al., 2020).

Table 5.1: Bulk composition of the samples analysed by QEMSCAN at 50μm resolution TSS: tectono-stratigraphic sequence (Figure 5.1b).

Depth (m)	Well	TSS	Calcite	Dolomite	FeDolomite	Ankerite	Quartz	KFeldspar	Plagioclase	Al-phyllosilicates/ Illite/Smectite	Anatase	Phosphate	Pyrite	Barite	Anhydrite	Chalcopyrite	Sphalerite	OtherPhases	Porosity
XX58.5	**W01**	**RTR**	0.2	10.7	0.7	0.0	78.3	0.0	0.0	1.8	0.0	0.1	0.2	0.0	0.0	0.0	0.0	0.2	7.7
XX90	**W01**	**BAS**	0.1	2.6	1.1	0.4	29.8	25.5	31.1	7.0	0.0	0.1	0.0	0.0	0.0	0.0	0.0	0.1	2.2
XX93	**W02**	**BAS**	0.1	0.9	2.4	10.7	33.8	17.8	16.0	7.2	0.1	0.1	5.4	0.0	0.0	0.0	0.0	0.3	5.0
XX60	**W08**	**RTR**	1.8	55.0	1.5	0.0	25.3	0.0	0.0	0.0	0.0	0.1	0.0	0.0	0.0	0.0	0.0	0.1	16.0
XX11	**W10**	**RTR**	90.2	0.0	0.0	0.0	1.5	0.0	0.0	1.0	0.0	1.4	0.2	0.1	0.0	0.0	0.0	0.0	5.5
XX80	**W14**	**SRIII**	54.8	0.0	0.0	0.0	24.1	0.0	0.0	0.0	0.0	0.0	9.7	2.2	0.6	0.0	0.0	0.1	8.3
XX42.2	**W18**	**RTR**	29.5	9.0	1.2	0.0	48.2	0.0	0.0	0.9	0.0	0.3	0.0	0.0	0.0	0.0	0.0	0.1	10.9
XX48.5	**W18**	**RTR**	33.8	0.6	0.1	0.0	62.2	0.0	0.0	0.2	0.0	0.0	0.0	0.0	0.0	0.0	0.0	0.0	3.0
XX75	**W20**	**RTR**	22.0	0.9	0.0	0.0	75.7	0.0	0.0	0.4	0.0	0.1	0.0	0.0	0.0	0.0	0.0	0.0	0.8
XX40	**W21**	**RTR**	2.5	19.0	1.0	0.0	46.1	0.3	0.0	17.8	0.2	4.0	1.1	0.0	0.3	0.0	0.0	0.3	7.5
XX48	**W21**	**RTR**	4.0	0.0	0.0	0.0	90.6	0.0	0.0	0.0	0.0	0.0	0.0	0.1	0.0	0.0	0.0	0.0	5.2
XX75	**W25**	**SRI**	0.3	8.6	4.1	9.0	21.0	27.2	0.2	22.7	0.6	0.3	1.1	0.0	0.0	0.0	0.0	0.4	4.4
XX08	**W33**	**RTR**	84.6	0.0	0.0	0.0	0.3	0.0	0.0	0.0	0.0	0.3	0.0	0.0	0.0	0.0	0.0	0.0	14.6

In contrast to the restricted $\delta^{13}C$ values, $\delta^{18}O$ values from the analysed carbonates show a wider variation (from -0.72 to -9.65 ‰ - Figure 5.9). It is observed that coarser, vein filling calcite and dolomite are more depleted in $\delta^{18}O$ than the pore-filling carbonate cements and the replacive carbonates. For example, in Figure 5.7b the BC cement in matrix and the MCv vein fill have $\delta^{18}O$ values of -3.57 and -8.79‰, respectively. Such increasing depletion towards the youngest mineral phases suggests either differences in the temperature of the fluid and/or in their oxygen isotopic composition ($\delta^{18}O_w$). Therefore, the increasing depletion in $\delta^{18}O$ is interpreted as consequence of continuous recycling of carbonate cements during the diagenetic evolution. In other words, veins are the latest

diagenetic phase and therefore will give the most depleted $\delta^{18}O$ values (p. ex. -8.79‰) because the host rock will provide less depleted $\delta^{18}O$ (-3.57‰). These, in turn, are more depleted that the presumably earliest microcrystalline calcite (c.a. -1.00‰, Figure 5.9). Therefore, these steps of isotopic depletion could suggest three episodes of isotope recycling by distinct diagenetic events. Despite the analysed samples being representative of the most diagenetically altered lithofacies, our results in terms of $\delta^{18}O$ still fit within the ranges of both syngenetic and hydrothermal phases in the Campos Basin (Lima et al., 2020).

Table 5.2: $\delta^{13}C$ and $\delta^{18}O$ results of isotopic analyses obtained in several lithofacies and from distinct diagenetic cements. Symbols in the column XRD mineralogy are DOL (dolomite), QTZ (quartz), CAL (calcite), ORT (orthoclase), and ANK (ankerite). It is shown the mean $\delta^{13}C/^{12}C$ and $\delta^{18}O/^{16}O$ and their respective standard deviation (s.d.).

Sampling	Mineral Phase	Well	Depth (m)	XRD mineralogy	$\delta^{13}C$	s.d.	$\delta^{18}O$	s.d.	Sampling Observation
Manual pick	SD	W01	XX90	DOL 98% CAL 2%	-1.68	0.03	-9.65	0.03	Manual picking of vein filling saddle dolomite
Microdrill	BD/SD	W08	XX60	DOL 94% QTZ 6%	-1.04	0.02	-8.43	0.04	Sampled from blocky to saddle cloudy dolomite replacive cement in bioclastic rudstone
Microdrill	BD	W08	XX60	DOL 98% QTZ 2%	0.95	0.05	-0.72	0.04	Sampled from hyaline vug-filling dolomite
Microdrill	BC	W10	XX11	CAL 88% QTZ 12%	0.76	0.02	-0.74	0.02	Sampled blocky calcite replacive cement in bioclastic rudstone
Microdrill	BD	W13	XX16	DOL 75% QTZ 17% CAL 8%	0.23	0.02	-1.36	0.02	Sampled from dolostone (microcrystalline blocky dolomite)
Microdrill	BD	W13	XX68.1	DOL 78% QTZ 20%	1.00	0.02	-1.18	0.04	Sampled from dolostone (microcrystalline blocky dolomite)
Microdrill	BC	W14	XX75	QTZ 56% CAL 44%	1.02	0.05	-0.75	0.03	Bulk sampling from quartz rich (detrital) and replacive blocky calcite cement
Microdrill	BC	W16	XX28.5	CAL 80% QTZ 20%	-3.21	0.03	-1.54	0.03	Bulk sampling from recrystallised hybrid arenite
Microdrill	BC	W18	XX42.2	QTZ 61% CAL 35% DOL 3%	1.36	0.07	-7.01	0.16	Sampled from intraclast macrocrystalline calcite cement in chert-rich breccia
Microdrill	BD	W18	XX43.6	DOL 63% QTZ 37%	1.07	0.04	-2.38	0.04	Sampled from dolostone matrix
Manual pick	BCv	W18	XX43.6	CAL 99% QTZ 1%	1.02	0.02	-8.79	0.03	Manual picking of vein filling macrocrystalline calcite
Microdrill	BC	W18	XX48.5	CAL 96% QTZ 4%	0.61	0.02	-3.57	0.04	Sampled from replacive calcite cement in bioclastic rudstone
Microdrill	BC	W21	XX37	CAL 59% QTZ 41%	1.37	0.04	-5.64	0.04	Sampled from calcite nodule in Mg-clay rich siltstone
Microdrill	BD	W21	XX44	CAL 74% DOL 17% QTZ 9%	-0.62	0.04	-2.68	0.03	Bulk sampling from dolostone intensively recrystallised by replacive calcite
Microdrill	BD	W25	XX75	ORT 78% ANK 12% QTZ 10%	-0.47	0.09	-4.02	0.17	Bulk sampling from arkose cemented by Fe-dolomite
Microdrill	BC	W33	XX08	CAL 100%	1.66	0.03	-1.76	0.03	Bulk sampling from bioclastic rudstone with replacive blocky calcite cement

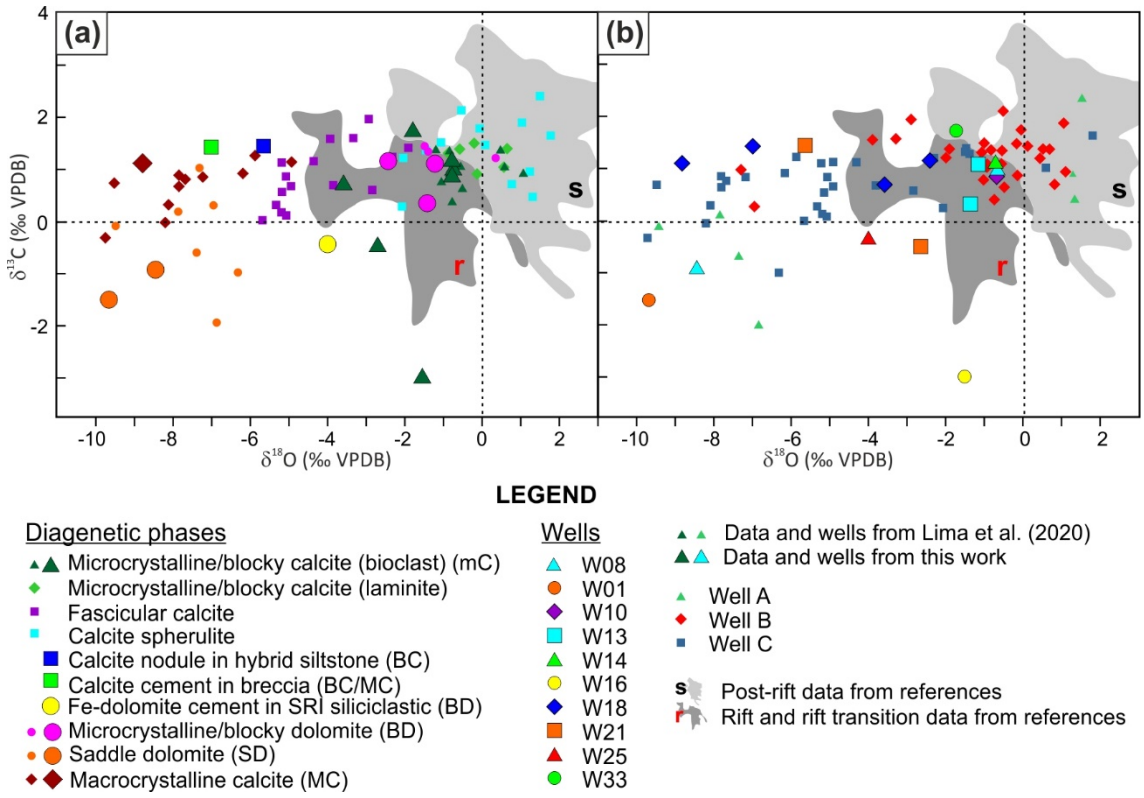


Figure 5.9: O-C stable isotopes composition by diagenetic products (A) and wells (B). In both figures, the results shown in Table 5.2 are represented by bigger symbols superposed onto the data compiled in Lima et al. (2020), represented by smaller symbols and regions that represent data from rift (r) and post-rift (s) units compiled from previous works. Notice that some diagenetic products are missing in previous publications because they were not investigated before or were not observed in this work.

5.5.4 Fluid inclusions

Over 360 L+V fluid inclusions (FIs) were analysed in seven rock wafers representing the major minerals phases (quartz, calcite and dolomites), to observe spatial variations in the homogenisation temperature (T_h) and salinity of within the same mineral phases. Figure 5.10 presents a graphic summary of the results of T_h and salinity (wt% NaCl eq.,) for the mineral phases investigated. The complete dataset of results are shown in Table 5.3, and the description of the results for each sample are available in the Appendix C3.

The majority of FIs are primary and aqueous. There are numerous FIs that could not be classified as either primary or secondary and are therefore classified as pseudo-secondary. Considering such uncertainty, we opt to disregard the morphology of the FIs and classify them as primary plus pseudo-secondary. Only a few hydrocarbon-bearing FIs were described and do not contain a resolvable aqueous phase.

Homogenisation temperatures (T_h) average at 106.1°C (median of 105°C) and increase with depth (Figure 5.11c). T_h in calcites show unimodal distributions with peaks around 95 and 105°C, respectively; macrocrystalline quartz shows two major quartiles, at 100-105 and 120-125°C. The dolomite phases, on the other hand, have more scattered distributions and do not reveal any pattern, despite overall T_h range being similar to calcite and quartz. Despite the values here observed are like those obtained by Lima et al. (2020), the wide range of the T_hs observed could be related to 1) ambiguous behaviour of several FIs that made it hard to determine a precise T_h, and 2) variable fluid temperature during the diagenesis.

Salinities are generally high for all mineral phases, except for saddle dolomite (Figure 5.11b). Average and median of salinities are 21.9 and 22.8 wt% NaCl eq., respectively. Blocky calcite (BC) and macrocrystalline calcite veins have contrasting distributions, respectively, right- and left-skewed. Therefore, BC has the highest average and median values for salinity (22.7 & 23.7 wt% NaCl eq., respectively).

Table 5.3: Statistical summary of the results obtained in aqueous and petroleum inclusions. Fluid inclusions (FIs) are hosted in hydrothermal macrocrystalline quartz (MQ), replacive (MC) and vein-filling (MCv) macrocrystalline calcite, blocky (BD) and saddle (SD) dolomites in basement rocks (Bas.) and also in bioclastic rudstones and silicified bioclastic packstone of the Rift Transition Sequence (RTR). For the fill, L+V means liquid+vapour and L1+L2+V is liquid 1 + liquid 2 + vapour. T_{fm} is the temperature of the first melting; T_{hyd} is the temperature of the hydrate melting; T_{ice} is the temperature of final ice melting; T_h is the temperature of homogenisation, of which the range and average (avg.) of values are presented; Salinity (wt% NaCl eq., and wt% NaCl + $CaCl_2$ eq.): equivalent salinities estimated using the equilibrium conditions predict experimentally for the NaCl-H_2O and NaCl-H_2O-$CaCl_2$ systems, respectively.

Well	Z (m)	Min Phase	Strat unit	Lithofacies	Type	UV colour (HC-bear only)	Fill	T_{fm}	T_{hyd}	T_{ice} (°C) range	T_h (°C) range	T_h (°C) avg. (n)	Salinity (wt% NaCl Eq.)	Salinity (wt% NaCl + $CaCl_2$ Eq.)	Notes
W02	XX93	MQ (inner)	Bas.	Basement	AQ	-	L+V	-	-	-19.5	111	111 (1)	22	-	-
W02	XX93	MQ (outer)	Bas.	Basement	AQ	-	L+V	-	-	-21.5 to 22.6	95-134	108 (6)	23.5 - 24.2	-	-
W02	XX93	MQ	Bas.	Basement	AQ	-	L+V	-	-	-3.5	99-105	102 (2)	5.7	-	Metastable Tice
W02	XX93	MQ (inner)	Bas.	Basement	AQ	-	L+V	-	-	-6.5 to 23	111-123	116.5 (4)	9.9 - 24.5	-	-
W02	XX93	MQ (inner)	Bas.	Basement	AQ	-	L+V	-	-	-	85	85 (1)	-	-	-
W02	XX93	MQ (inner)	Bas.	Basement	AQ	-	L+V	-	-	-18.5	107	107 (1)	21.2	-	-
W10	XX36	MQ	RTR	Bioclastic packstone (silicified)	AQ	-	L+V	-	-	-18.6	157	157 (1)	21.3	-	-
W13	XX68	MQ	RTR	Chert	AQ	-	L+V	-	-	-11.3 to 22.8	112-132	124.5 (6)	15.2 - 24.4	-	-
W13	XX68	MQ	RTR	Chert	AQ	-	L+V	-	-	-	104-123	116 (5)	-	-	-
W13	XX68	MQ	RTR	Chert	HC	Orange	L1+L2+V	-	-	-	89-102	94 (3)	-	-	-
W13	XX68	MQ	RTR	Chert	AQ	-	L+V	-	-	-20.1 to 22.4	118	118 (1)	22.4 - 24.1	-	-
W13	XX68	MQ	RTR	Chert	AQ	-	L+V	-	-	-19.5 to 22.6	122	122 (2)	22.0 - 24.2	-	-
W13	XX68	MQ	RTR	Chert	AQ	-	L+V	-	-	-22.8	121-138	129.5 (2)	24.4	-	-
W18	XX48.3	MQ	RTR	Bioclastic rudstone	HC	Green-white	L+V	-	-	-	57-111	84 (2)	-	-	-
W18	XX48.3	MQ	RTR	Bioclastic rudstone	AQ	-	L+V	-	-	-14.7	132	132 (1)	18.2	-	-

Well	Z (m)	Min Phase	Strat unit	Lithofacies	Type	UV colour (HC-bear only)	Fill	T_{fm}	T_{hyd}	T_{ice} (°C) range	T_h (°C) range	T_h (°C) avg. (n)	Salinity (wt% NaCl Eq.)	Salinity (wt% NaCl + $CaCl_2$ Eq.)	Notes
W18	XX48.3	MQ	RTR	Bioclastic rudstone	AQ	-	L+V	-	-	-16.0	122	122 (1)	19.3	-	-
W18	XX48.3	MQ	RTR	Bioclastic rudstone	AQ	-	L+V	-	-	-15.3 to 16.6	104-129	109.6 (5)	18.7 - 19.7	-	-
W18	XX48.3	MQ	RTR	Bioclastic rudstone	AQ	-	L+V	-	-	-	122-136	129 (2)	-	-	-
W18	XX48.3	MQ	RTR	Bioclastic rudstone	AQ	-	L+V	-	-	-18.2 to 19.2	124-131	127.6 (7)	21 - 21.7	-	-
W10	XX36	MCv	RTR	Bioclastic packstone (silicified)	AQ		L+V	-	-	-19	73-90	81.8 (4)	21.6	-	-
W10	XX36	MCv	RTR	Bioclastic packstone (silicified)	AQ		L+V	-	-	-19 to 20.3	85-132	113.4 (11)	21.6 - 22.6	-	-
W10	XX36	MCv	RTR	Bioclastic packstone (silicified)	AQ		L+V	-52	-22.5 to 22.7	-18.1 to 20.2	114-153	132.7 (11)	20.7 - 22.5	17.5 - 18.2	-
W10	XX36	MCv	RTR	Bioclastic packstone (silicified)	AQ		L+V	-52	22.5	-19.1	139-156	147.5 (2)	21.7	18	-
W10	XX36	MCv	RTR	Bioclastic packstone (silicified)	AQ		L+V	-52	-21.5	-19.3	113	113 (1)	21.8	20.9	Metastable Tice
W10	XX36	MCv	RTR	Bioclastic packstone (silicified)	AQ		L+V	-	-	-	113	113 (1)	-	-	-
W10	XX36	MCv	RTR	Bioclastic packstone (silicified)	AQ		L+V	-52	-23.8	-22.9	107-118	112.5 (2)	24.5	16.8	-
W10	XX36	MCv	RTR	Bioclastic packstone (silicified)	AQ	-	L+V	-52	22.9 to 23.1	-20.2 to 22.8	111-147	122.8 (7)	22.5 - 24.4	17.7 - 19.5	-
W10	XX36	MCv	RTR	Bioclastic packstone (silicified)	AQ	-	L+V	-52	-22.5	-18.5 to 21.5	116-145	124.5 (6)	21.2 - 23.5	19.5	-
W10	XX36	MCv	RTR	Bioclastic packstone (silicified)	AQ	-	L+V	-	-	-19.7	110	110 (1)	22.1	-	Metastable Tice

Well	Z (m)	Min Phase	Strat unit	Lithofacies	Type	UV colour (HC-bear only)	Fill	T_{fm}	T_{hyd}	T_{ice} (°C) range	T_h (°C) range	T_h (°C) avg. (n)	Salinity (wt% NaCl Eq.)	Salinity (wt% NaCl + $CaCl_2$ Eq.)	Notes
W10	XX36	MCv	RTR	Bioclastic packstone (silicified)	AQ	-	L+V	-52	-	-19.5 to 22.4	109-121	112.6 (5)	22.2 - 24.1	-	-
W18	XX48.3	MCv	RTR	Bioclastic rudstone	AQ	-	L+V	-	-	-11.3	83-106	94.3 (3)	15.2	-	-
W18	XX48.3	MCv	RTR	Bioclastic rudstone	AQ	-	L+V	-52	-22.3 to 22.5	-20.3 to 21.3	96-109	104.8 (6)	22.6 - 23.3	18.8 - 19.9	-
W18	XX48.3	MCv	RTR	Bioclastic rudstone	AQ	-	L+V	-	-	-20.8	93	93 (1)	22.9	-	-
W18	XX48.3	MCv	RTR	Bioclastic rudstone	AQ	-	L+V	-52	-	-13.8	93-120	105.3 (3)	22.9 - 24.9	-	-
W18	XX48.3	MCv	RTR	Bioclastic rudstone	AQ	-	L+V	-40 to 52.5	-	-21.4 to 22.2	89-134	107.2 (11)	23.4 - 23.9	-	-
W18	XX48.3	MCv	RTR	Bioclastic rudstone	AQ	-	L+V	-50 to 52	-	-16.5 to 21.7	83-98	90.9 (14)	19.7 - 24.2	-	Some metastable FIs
W10	XX11	BC	RTR	Bioclastic rudstone	AQ	-	L+V	-45 to 52	-13.5 to 22.7	-16.5 to 22.7	65-126	95.9 (32)	19.5 - 24.4	19.4 - 21.2	-
W10	XX11	BC	RTR	Bioclastic rudstone	AQ	-	L+V	-	-	-10.8 to 19.8	103-122	110 (9)	14.7 - 22.2	-	-
W10	XX11	BC	RTR	Bioclastic rudstone	AQ	-	L+V	-	-	-5.0 to 10.7	93	93 (1)	7.9 - 14.6	-	-
W10	XX11	BC	RTR	Bioclastic rudstone	AQ	-	L+V	-	-	-20.5 to 22.6	82-103	95.4 (5)	22.7 - 23.5	-	-
W10	XX11	BC	RTR	Bioclastic rudstone	AQ	-	L+V	-	-	-21.8	63	63 (1)	23.7	-	-
W18	XX42.2	BC	RTR	Bioclastic rudstone	AQ	-	L+V	-35 to 52.0	-10.0 to 12.0	-19.5 to 22.8	78-107	95.2 (17)	22.0 - 24.4	20.6 - 24.8	-
W18	XX42.2	BC	RTR	Bioclastic rudstone	AQ	-	L+V	-40.0	-15.0	-19.8 to 22.1	55-106	87.3 (9)	22.2 - 23.9	-	-
W18	XX42.2	BC	RTR	Bioclastic rudstone	AQ	-	L+V	-35	-	-22.1 to 22.5	99-103	101 (2)	23.9 - 24.2	-	-
W18	XX42.2	BC	RTR	Breccia	AQ	-	L+V	-	-9.0	-19.2 to 22.8	75-123	99.5 (4)	21.8 - 24.4	21.1	-
W18	XX42.2	BC	RTR	Breccia	AQ	-	L+V	-40	-0.5	-21.8	113	113 (1)	23.7	24.2	-
W18	XX42.2	BC	RTR	Breccia	AQ	-	L+V	-52	-9.0 to 16	-22.0 to 22.9	157	157 (1)	23.8 - 24.5	20.4 - 21.7	-
W18	XX42.2	BC	RTR	Breccia	AQ	-	L+V	-	-9.0	-18.5 to 23.5	73-121	92.7 (14)	21.2 - 24.9	21.1	-

Well	Z (m)	Min Phase	Strat unit	Lithofacies	Type	UV colour (HC-bear only)	Fill	T_{fm}	T_{hyd}	T_{ice} (°C) range	T_h (°C) range	T_h (°C) avg. (n)	Salinity (wt% NaCl Eq.)	Salinity (wt% NaCl + $CaCl_2$ Eq.)	Notes
W18	XX42.2	BC	RTR	Breccia	AQ		L+V	-	-15.0 to -17.0	-22.5	87-137	107.6 (8)	24.2	20.5 - 20.8	-
W18	XX42.2	BC	RTR	Breccia	AQ		L+V	-46.0	-13.0 to 15.0	-22.3 to 22.6	88-121	99.5 (10)	24.0 - 24.2	20.9 - 21.2	-
W01	XX58.5	SD	Bas.	Basement	HC	Blueish	L+V	-	-	-	110-146	126.6 (9)	-	-	-
W02	XX93	SD	Bas.	Basement	AQ		L+V	-	-	-10.2 to 13.8	73-113	95.6 (4)	14.5 - 17.4	-	Dolom. 2
W02	XX93	SD	Bas.	Basement	AQ		L+V	-	-	-10.2	88-111	98.4 (5)	14.1	-	Dolom. 2
W02	XX93	SD	Bas.	Basement	AQ		L+V	-	-	-8.0 to 18.5	87-157	121 (5)	11.7 - 21.2	-	Dolom. 2
W02	XX93	SD	Bas.	Basement	AQ		L+V	-	-	-15.0	95-113	101 (3)	18.5	-	Dolom. 2
W02	XX93	BD	Bas.	Basement	AQ	-	L+V	-	-	-22.5	111-112	111.5 (2)	24.2	-	Dolom. 1
W02	XX93	BD	Bas.	Basement	AQ	-	L+V	-	-	-16.5 to 23.8	97-116	109.3 (7)	23.5 - 25.1	12.4	Dolom. 1
W02	XX93	BD	Bas.	Basement	AQ	-	L+V	-	-	-22.0	84-102	96 (3)	18.6 - 23.8	-	Dolom. 1
W02	XX93	BD	Bas.	Basement	AQ	-	L+V	-52	-24.6	-23.9	111	111 (1)	25.2	15.3	Dolom. 1
W18	XX42.2	BD	RTR	Breccia	AQ	-	L+V			-16.5 to 22.5	97-109	104.5 (4)	23.5 – 24.2		

The observation of very low temperatures of first melting (T_{fm}) are indicative of the presence of $CaCl_2$ in the aqueous system. Where it was possible to collect paired T_{ice} and T_{hyd} data (n=35), salinities were modelled in the system NaCl-$CaCl_2$ (Naden, 1996). Salinities modelled in this way tend to be similar to those calculated in the system NaCl-H_2O for 21 FIs (21 – 26wt% NaCl+$CaCl_2$ eq.). However, BC have values above and MCv below 20 wt% NaCl-$CaCl_2$ eq. Calculated NaCl/$CaCl_2$ ratios indicate that Na+ is the dominant cation (NaCl / NaCl-$CaCl_2$ is typically between 0.8-0.9 [by weight]).

Homogenisation temperatures (T_h) were compared with stable isotope data when $\delta^{18}O$ and T_h data are available for same sample or same mineral phase in the same well. The average T_h value for the most abundant carbonate phase were considered. Despite significant dispersion, there is a positive correlation between T_h and depletion in $\delta^{18}O$ (Figure 5.10c).

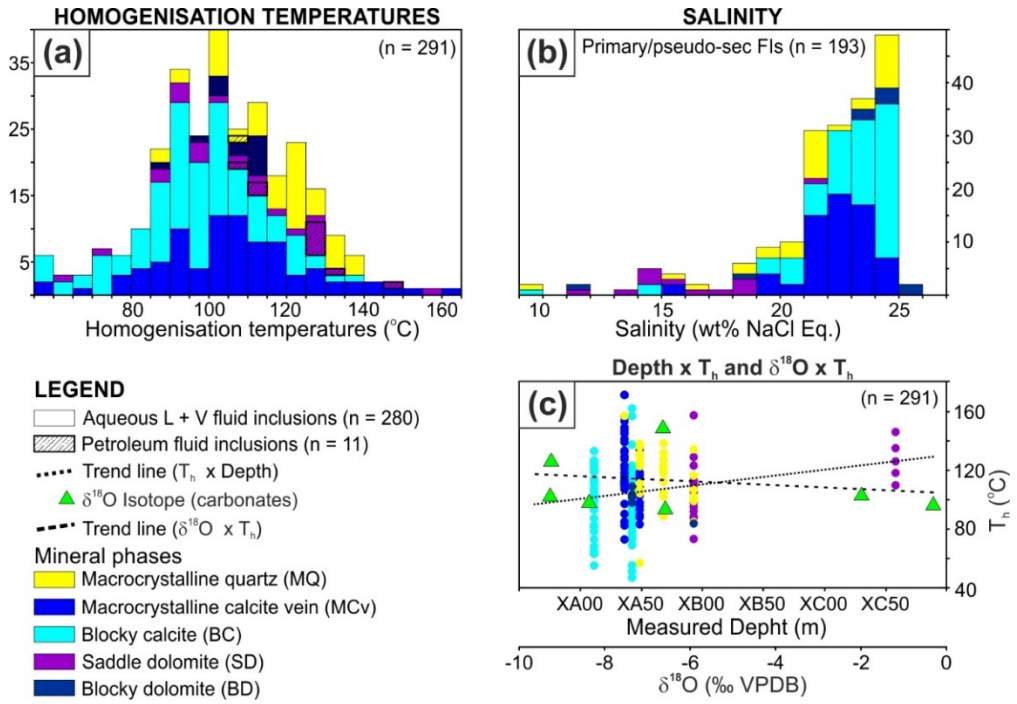


Figure 5.10: a) Homogenisation temperature (°C) histograms of aqueous and petroleum primary and pseudo-secondary fluid inclusions (FIs) hosted in hydrothermal mineral phases. b) Histogram of salinities estimated for aqueous FIs computed using the NaCl-H_2O system. Bars are coloured accordingly to the host mineral. c) Cross plots of Depth x T_h, and $\delta^{18}O$ x T_h with respective trend lines. Points representing the T_h are coloured accordingly to mineral phases. Depth increases to the right.

5.5.5 U-Pb geochronology and the timing of diagenesis

20 Tera-Wasserburg concordia plots were obtained from selected cements in nine samples from seven wellbores. They sampled crack-filled veins, vug-filling, replacive and cements of dolomites and calcite in the crystalline basement, from SRI arkoses and RTR breccias and bioclastic rudstones. Each plot represents one analysis consisted of pooled $^{238}U/^{206}Pb$ versus $^{207}Pb/^{206}Pb$ data from a single mineral phase recognized as it from CL imagery. Six examples of concordia plots are shown in Figure 5.11a-f and are focused on results obtained within the same well; the complete set of results is available in Appendix C4. Analyses were made on different cements of the same sample whenever possible to observe possible age variations within minerals presumably from the same diagenetic phase (Figure 5.11g-j). In reality, besides showing clear differences within the dolomite phases (Figure 5.7e-g), petrography and CL imagery were not able to distinguish calcites formed in different ages. Three of the plots where considered unsuccessful because (1) high common lead content, or (2) samples with analytical uncertainties that preclude a regression.

Figure 5.12 shows a detailed compilation of the samples with geochronologic, C-O stable isotopes and fluid inclusion data. They are presented in a geologic perspective, that is, their position with respect stratigraphic unit and wellbore location. The following Figure 5.13 provides a summary of measured ages, homogenisation temperatures (T_h) from the fluid inclusion study and the subsidence curve with predicted temperatures at burial condition. Chose T_h values were obtained in the same mineral phases whose absolute ages were obtained though U-Pb geochronology. These data are correlated to tectonic and magmatic events and also with the lithostratigraphic column of the Campos Basin (Winter et al., 2007; Fetter, 2009). In Figure 5.13, ages for the minerals that are petrographically similar,

for example, blocky and macrocrystalline calcite, are not grouped to show that they could have been formed during different diagenetic phases (see Figure 5.11h).

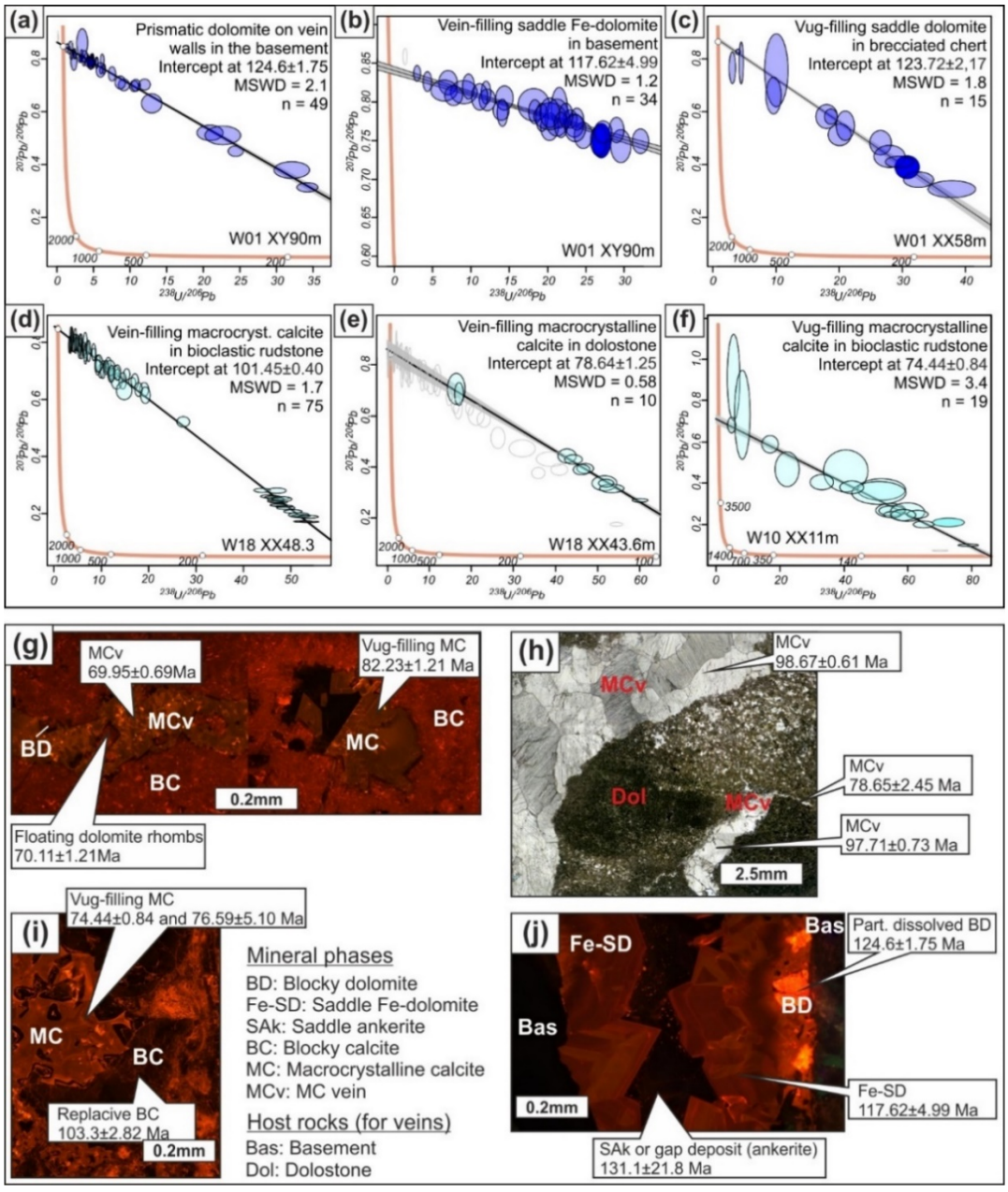


Figure 5.11: a-f) Tera-Wasserburg concordia plots showing pooled $^{238}U/^{206}Pb$ versus $^{207}Pb/^{206}Pb$ data for carbonate phases from samples collect in the lower section of the presalt interval and cements in basement rocks. Quoted age uncertainty includes propagated systematic uncertainties. Data point error ellipses are 2σ, MSWD, mean squared weighted deviates. g-j) Examples of different mineral phases dated in same sample through U-Pb geochronology. a) Bioclastic rudstone with vein and vug-filling calcite (CL imagery). b) Dolostone with two generation of MCv veins resolved by geochronology (PPL mosaic). c) Bioclastic rudstone showing contrasting ages for matrix and vug-filling calcites. d) Dolomite to ankerite vein filling in fractured basement.

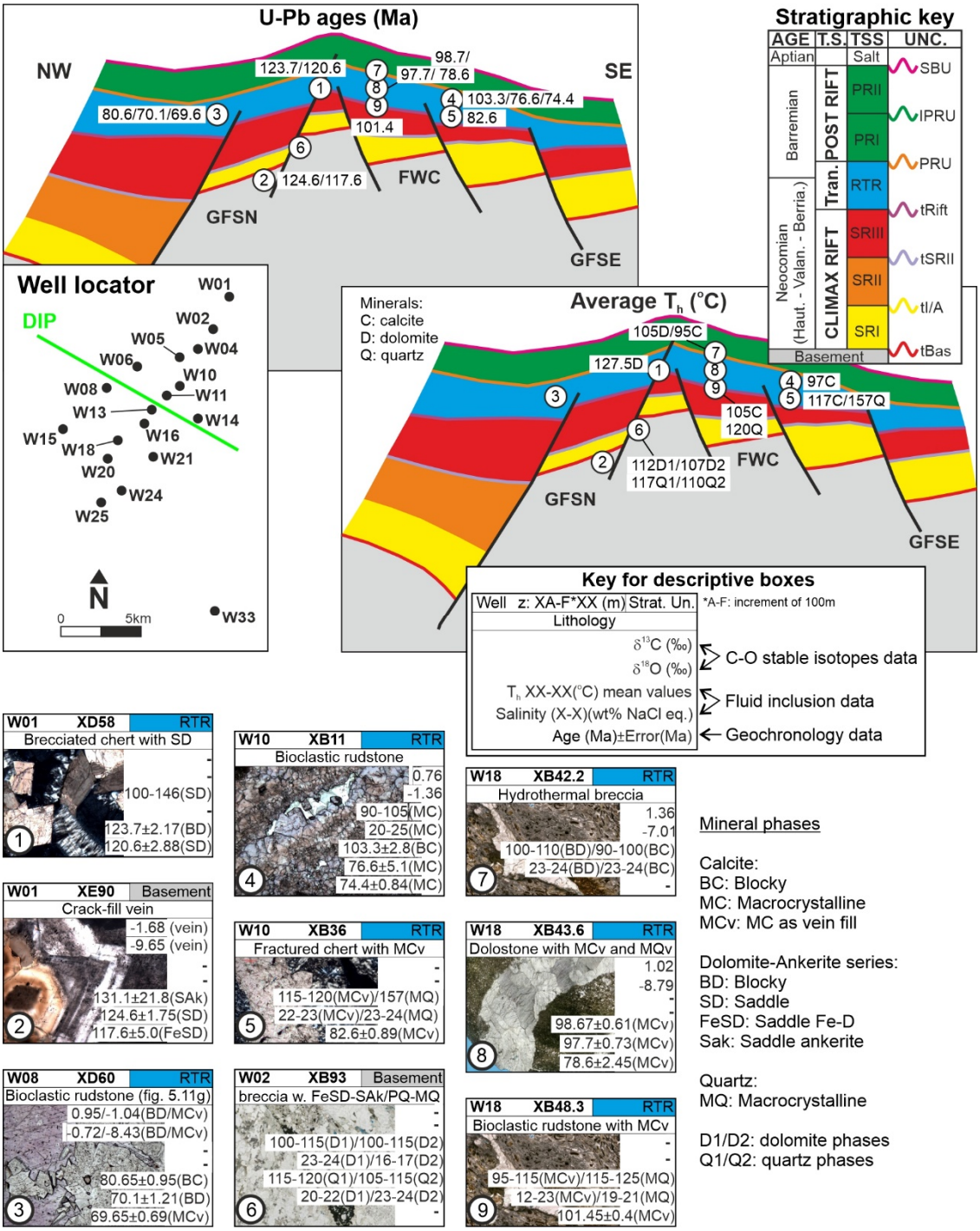


Figure 5.12: On the top, pair of summarised geological cross sections showing simplified U-Pb ages and mean T_h for different diagenetic mineral phases from samples 1 to 9. Detailed dataset are present in the descriptive boxes on the bottom with the numbers respective to the cross sections. Selected samples are those with geochronologic data, except for nr. 7. It is shown doing to its proximity to samples 8 and 9. A crop of Figure 5.2a is shown to contextualise the well location with the approximate position of the cross section. For complete stable isotope and fluid inclusion data please see Tables 5.2 and 5.3, and Annexes C3 and C4.

The absolute ages are clearly clustered into three intervals that coincide with the post-rift inversion (Chapter 4, Strugale & Cartwright, 2022) and with tectonic events described in the post-salt layers of the Campos Basin (Fetter, 2009). These periods are interpreted as episodes of diagenetic mineral formation and recrystallisation. Due to their contemporaneity with tectonic events, they are interpreted as tectono-diagenetic events, named BADE – Barremian to Aptian (125-117 Ma), ACDE - Albo-Cenomanian (103-98 Ma), and CMDE – Campanian to Maastrichtian (83-70 Ma). A Hauterivian age was obtained for a saddle ankerite vein in the basement, but it has over 20 Ma of uncertainty and therefore could be part of the first cluster of ages (Figure 5.11j). Ages for the first cluster were measured in dolomites, while the second and third ages came predominantly from calcites.

BADE ages were obtained in carbonate veins in the basement and in saddle dolomite (SD) crystals from a brecciated chert of the RTR sequence (Figure 5.11a-c). The ages of 124.6 ± 1.75 and 117.62 ± 4.99 Ma were collected from the BD and Fe-SD phases shown in Figure 5.11j; unfortunately, no reliable age was obtained in the ankerite gap deposit and in the breccia-fill saddle ankerite of Figure 5.3a. Also, ages of 123.72 ± 2.17 and 120.56 ± 2.88 Ma were measured in SD and dolomite overgrowths in the matrix of the sample in Figure 5.5a (chert).

The clustered ages of BADE and the Fe-rich character of mineral phases suggest that the same fluid is likely to have percolated across the basement and RTR units, under similar burial conditions. Petroleum fluid inclusion data in SD provide T_h ranging 110-146^{o}C. These temperatures are significantly higher than the estimated value based on the subsidence curve (~70^{o}C, Figure 5.13), thus attesting to the strong hydrothermal qualifier of the BADE in shallow burial conditions (c.f. Machel & Lonnee, 2002).

Even though there is no magmatism of Barremian-Aptian age in the Campos Basin, it is reasonable to assume that the basin was under a high geothermal gradient inherited from the volcanism associated with the syn-rift I sequence. Ages of BADE are in part older than the depositional age of the hosting RTR (Coqueiros Formation) according to the traditional stratigraphic chart of the Campos Basin (Winter et al., 2007) thus suggesting that this unit could be older than it has been interpreted (see discussion in Chapter 4.7.3).

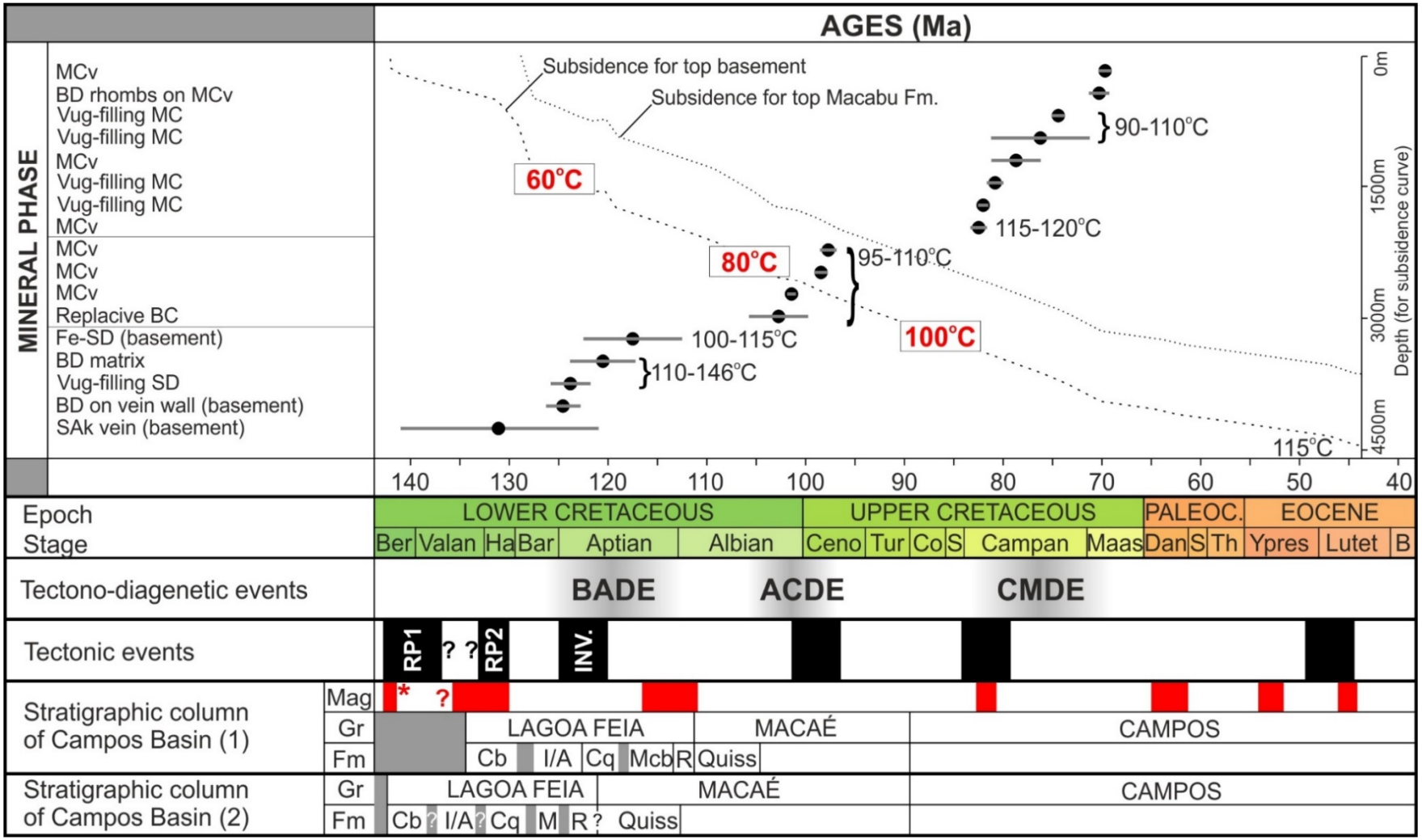
Another characteristic of the BADE is that minerals attest to a fluid enriched in Fe, which is exemplified in Figure 5.11j. From that, it is possible that fracture-fill pyrite observed in some samples of basement and RTR (Figure 5.3a & 5.5e) could have been formed during this time instead during the latest diagenetic phase (Lima et al., 2020). Fe-rich carbonate cements are commonly formed from fluids that percolated basement, basalts and arkoses prior to reaching sites of mineral precipitation (Everett et al., 1999; Dewit et al., 2014).

The ages that defined the ACDE were obtained from two wells where the oldest value (103.3 ± 2.82 Ma) was measured in matrix-replacing blocky calcite. Interestingly, in the same sample, vug-filling macrocrystalline calcites resulted in a younger age of 74.44 ± 0.84 Ma (Figures 5.11f,i), which corresponds to the subsequent CMDE event. Three values within a system of MCv veins of 101.45±0.4 (Figure 5.11d), 98.67 ± 0.61, and 97.71 ± 0.73 Ma (Figure 5.11h) were obtained from different regions. It is pertinent to reinforce that neither conventional petrography, QEMSCAN mapping, nor cold cathodoluminescence (CL) imagery were able to distinguish these different generations. It is possible that individual crystals either formed diachronously or during a prolonged period of time, similar to what was noted by Lander and Laubach (2015) for quartz-filled fractures.

T_h data shows entrapment temperatures higher than those predicted by a subsidence curve of ~85ºC, but not as high as during the BADE (Figure 5.13). Nevertheless, T_h values are still at least 5ºC hotter than the host rock and the diagenetic environment is thus considered hydrothermal (c.f. White, 1957) but at deeper burial conditions than BADE (Figure 5.13). There is no magmatism recorded in the Campos Basin during the Albo-Cenomanian (Winter et al., 2007). Fetter (2009) observed a peak of deformation at this age in restored sections of the post-salt of the Campos Basin.

The youngest cluster of U-Pb ages spans the Campanian and most of the Maastrichtian (83-70 Ma) (Figure 5.13). CMDE ages came from eight pooled datasets obtained from the same samples where the ACDE was measured. With one exception (dolomite in Figure 5.11g), all the data came from vein and vug-filling calcites (Figure 5.11g-i).

The petrographic descriptions shown no clear paragenetic relationship of calcite formation as either matrix replacement or vein filling. The latest matrix-replacing cements were identified on CL imagery as marginal but contrasting ages on the MCv calcites was only possible from the geochronology (Figures 5.11e & 5.11f). Ages from both cements (replacive and vug-fill) and fracture fill (MCv) are indistinguishable, including a sample that contains veins related to both ACDE and CMDE events (Figure 5.11h), although the youngest ages were obtained in veins.



(Figure 5.13 - caption on next page)

Figure 5.13: Ages obtained for mineral phases identified. Temperatures in black are the T_h intervals obtained from fluid inclusions. Ages are superimposed to subsidence curves (stippled and dotted lines) and predicted temperatures (in red) (Lima et al., 2020). Tectonic events RP1, RP2 (rift phases 1 & 2) and INV. (inversion) are according to Strugale and Cartwright (2022), while the three that follows are according to Fetter (2009). Stratigraphic charts according to (1) Winter et al. (2007), including the magmatic events (Mag), where (*) is the age of onshore tholeiitic dykes (Santiago et al., 2020 , Figure 4.1) and (2) according to Figure 5.1. Gr: Group, Fm: Formations: Cb – Cabiúnas, I/A – Itabapoana and Atafona, Cq – Coqueiros, M – Macabu, R – Retiro (evaporites), Quiss – Quissamã.

The time relation between U-Pb clustered ages and tectonic events suggests recurring events of matrix replacement and vug filling, that could not only be attributed to hydrothermal diagenesis but also to brittle deformation related to "structural diagenesis", which is the study of the relationships between deformation or deformational structures and chemical changes to sediments (c.f. Laubach et al., 2010). This interpretation is reinforced by fluid inclusion data, which suggest that diagenesis might have been triggered by a hydrothermal overprint, with T_h ranging 115-120^{o}C in the oldest of the samples (Figure 5.13). However, towards the end of the Campanian, T_h's were essentially the same as predicted by the subsidence curve.

5.5.6 Interwell distribution of hydrothermal diagenesis

In this section all the data presented so far is integrated with lithogeochemical wireline data and tentatively correlated with the seismic framework (horizons and faults). The main aim is to search for geologic controls other than stratigraphy on the distribution of hydrothermal diagenesis. Such correlation is a common challenge within the oil industry because of sampling bias (Cosentino, 2001) and the difficulties in transferring structural data from analogue outcrops to sub-surface settings (see discussion in Laubach et al., 2019).

Based on core description and wireline logs, Olivito and Souza (2020) observed that gamma-ray (GR) curves respond well to facies association and depositional energy of the rift transition (RTR) sequence, equivalent to the upper section of the Coqueiros Formation. However, these authors did not investigate porosity variations and GR alone is not able to resolve the diagenetic imprint. In addition, the intensity of diagenesis varies strongly within several scales of observation, from thin section to seismic-scale (Packard et al., 2001; Cantrell et al., 2004; Sharp et al., 2010). As a consequence of the poor seismic quality and resolution (>90 m vertical), direct correlation between seismic facies and diagenetic imprint is not possible. Therefore, the fact that lithogeochemical logs provide relative elemental abundance for Ca, Mg, Si, Fe, and S allows near and inter-well correlations with diagenetic cements observed in the rock samples (Figure 5.14). In addition, well logs constitute a useful method to fill the gap in the representativeness of the analysed samples. Lithogeochemical logs show Ca & Si as the main constituents, as suggested by thin sections, QEMSCAN and XRD data (Tables 5.1-2), although carbonates are more abundant than quartz. Cross-plots show that minor elements (Fe, Al, Mg, and S) are positively correlated with Si. The Al curve is interpreted as a good proxy for siliciclastic grains within the carbonates, represented by detrital feldspars, micas, and terrigenous and/or authigenic clay minerals. Mg & Al contents are relatively high in post-rift sequences and can be correlated with the extensive occurrence of authigenic Mg-clays in this interval (Herlinger Jr. et al., 2017). In addition, Fe content usually has a positive correlation with Al and thus with clastic and diagenetic sulfides in organic-rich facies. The increase in Fe and Mg do not have correspondence with Al & Ca, respectively. Despite its low mobility under Ph>5.5, APS minerals like svanbergite suggest local remobilisation of Al during

diagenesis. Nevertheless, it is interpreted that the Al content is mostly primary and was not influenced by later diagenesis.

In some situations, peaks in the Si log are not followed by increasing Al and Fe. As noted above, in most cases, Si is positively correlated to Al & Fe, which are proxies for detrital grains or authigenic Mg-clays. Given the abundance of quartz as cement even in carbonatic facies (Figures 5.4d & 5.6c) and the average T_h values higher than carbonate phases (Figure 5.10b), it is interpreted that Si abundance is not depositional but related to hydrothermal diagenesis. Therefore, a proxy for hydrothermal silicification is the increasing Si values when not followed with increasing Al. Consequently, an external source of Si is required for such widespread silicification. Basement rocks are the best candidates for being source of Si for overlying sediments (Figure 5.5b) (Packard et al., 2001; Menezes et al., 2019; Teboul et al., 2019). In addition, the clastic sediments of SRI sequence constitutes another potential source for Si as evidenced by the strong dissolution of feldspars and their replacement by dolomite (Figure 5.3c).

Geochronological data were useful to distinguish diagenetic events though time. However, these data only constitute a secondary source of information for inter-well correlations because of the lack of contrast in cement composition. While the BADE event is marked by dolomites with significant Fe content, ACDE and CMDE in the investigated samples have calcite as major mineral phase (Figure 5.13). Therefore, it is not possible to make assumptions on the distribution of each diagenetic phase but to assume that they probably indistinctly affected the whole section.

The following topics start with one not-to-scale well-section with the complete lithogeochemical and GR wireline log record (Figure 5.14), where interpretation criteria

for the recognition of hydrothermal silicification are established. These criteria are then extended to two seismic-geologic sections on which the occurrence of hydrothermal silicification is interpreted constrained by the stratigraphic and structural frameworks (Figures 5.15, 5.16).

5.5.6.1 Section DIP A

This section is located in the centre of the main structural high and include four of the main structural compartments, namely, the hanging wall block of the GFSN (W06), GFSN, FWC (W10) and GFSE (W14) structural compartments (Figure 2a,b). The internal subdivisions of the Coqueiros Formation (CoqA to E) are based on Olivito and Souza (2020) and will be used throughout. The high Si, Al and Fe values of SRI sequence in well W14 coincides with the siliciclastic lithofacies (arkoses) cemented by Fe-dolomite to ankerite, whereas peaks of high Fe & Mg could be related to dissolution and precipitation of saddle Fe-dolomite (Figures 5.3c, 5.14a). Subordinate Ca peaks that are followed by lower GR values represent intercalations of bioclastic rudstones with a siliciclastic matrix. The transition to SRIII is quite sharp, marked by the tI/A unconformity and an abrupt increase in the Ca content as a consequence of the predominance of bioclastic rudstones cemented by calcite. A sample collected on the tRift surface contains abundant pyrite and Sr-barite, and secondarily chalcopyrite hosted in a bioclastic rudstone (Figures 5.5e, 5.14b).

The well-log signatures of the RTR sequence in well 06 compared with W10 & W14 are quite contrasting. The uppermost 100 meters of the three wells show a box-shaped GR with low Al contents (Figure 5.14c). However, the Si average content is higher in W06 than

W10 & W14, and Si curve is often independent to Al content in the first. Similar behaviour is observed not only in the lower RTR section of W06, despite the serrated GR log and relatively higher Al content (Figure 5.14d), but also in the post-rift sequences. Notably, the Si peaks are irrespective of changes in GR and Al values (Figure 5.14e) and the much higher Si counting in the post-rift interval of W06 than W10. On the other hand, average Si values in the post-rift sequence of W14 are somewhat in between the observed values in wells W06 and W10. Moreover, there are complimentary peaks of S in the post-rift II sequence of W06 (Figure 5.14f), suggesting a similar cement composition of the Figure 5.14b.

In terms of location with respect to the structural compartments, W06 is in the hanging wall block of the GFSN branch, W10 is in the footwall complex (FWC), and W14 is close to the GFSE branch. In the first instance, increasing Si average content in W06 and W14 could be correlated to the proximity from high-strain branches of the Guriri Fault System (GFS), whereas W10 is located in least deformed FWC (Figure 5.2b). Moreover, the fact that the GFSN contains fault segments with much higher displacement than the GFSE could imply a more effective role as pathway for hydrothermal fluids when the accumulated strain is higher.

Considering that the wells are not located in the major faults mapped in the seismic data (Figures 5.15-16) and based on the role of structures as feeders for hydrothermal fluids thus related diagenesis (e.g. Packard et al., 2001, Sharp et al., 2010), the differential enrichment in Si (also in Fe and S) across the studied wells point to an interpretation where faults worked as feeders and the diagenetic fronts spread laterally once the flow reached a porosity interface. The wider the lateral spreading the higher the capacity of the fault to

work as vertical feeder. If considering the fault-valve mechanism of Sibson (1981), more efficient feeders would be the faults subjected to more episodes of displacement. In other words, faults within FWC (as the W14) are less effective feeders so the lateral extend of the diagenesis is reduced or perhaps absent. The interplay between feeders, porosity and permeability of the layers during fault-related diagenesis, and lateral extension of the diagenetic brines or ore-rich plume was described by several publications (Packard et al., 2001; Sharp et al., 2010; Dewit et al., 2014; Walsh et al., 2018).

Since the GFS branches were subjected to selective post-rift reactivation (Strugale & Cartwright, 2022) , then is reasonable to assume that they acted as the loci of hydrothermal diagenesis, enhancing the fault-valve mechanism and allowing percolation of diagenetic fluids across the sedimentary section. From the observation of two diagenetic events after the BADE, is interpreted that some of the faults might have worked as hydrothermal feeders not only during the post-rift phase, but throughout a geologic evolution marked by recurrent tectonic activity.

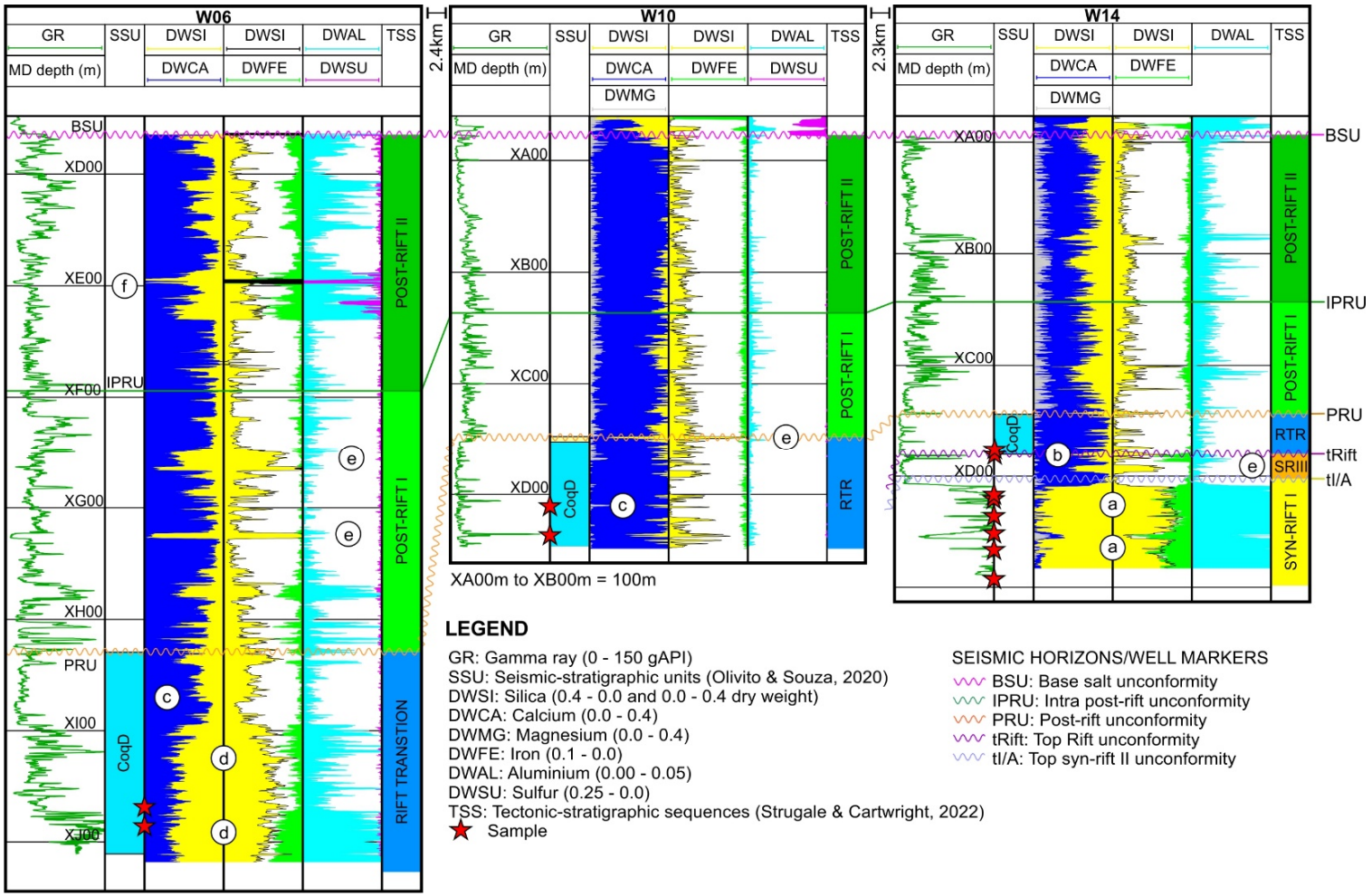


Figure 5.14: Wellbore panel detailing the wireline record, thickness variations, where the elemental ratio from lithogeochemical logs is compared between the wells of the well section DIP B. See text for discussion.

5.5.6.2 Section DIP B

The main criteria to recognise regions more affected by hydrothermal diagenesis are based on Si and Al curves of lithogeochemical well-logs and, potentially, wellbore location with respect to the structural compartments. Hence, this and the next chapter aims to use the stratigraphic and structural frameworks to observe the extent of silicification in the inter-well space. As with Section DIP A, DIP B represents the four main structural compartments of the study area in a southern position (Figure 5.2a,b). However, wells are located in positions slightly distinct from Section DIP A with respect to the main structures. On the hanging wall of GFSN is observed a well-developed CoqD wedge characterized by a box-shape log pattern that progrades onto mudstones of CoqC and hybrid deposits of CoqB (Figure 5.15a,b). CoqB is interpreted as a mound-shaped complex stacked along the footwall crest of GFSN that progrades toward the hanging wall but not as much as CoqD (Figure 5.15c).

The CoqE unit is characterised by low porosity/high clay and Al content and typically occurs in wells within the main structural high. However, notice that the Si weight increase in W21, close to a seismic-scale fault (Figure 5.15d). In addition, the underlying CoqD is silicified in both W18 and W21 wells, despite the lack of high Al contents. Samples collected beneath CoqE show a rather complex diagenetic history, exemplified in the insets of QEMSCAN and photomosaic (Figure 5.15e,f). The low permeability of the CodE layer suggests that it could have acted as an aquitard, increasing the residence time of rising hydrothermal fluids and leading to the formation of hydrothermal breccias and macrocrystalline quartz and calcite (Figure 5.15e). U-Pb ages in calcite veins of the sample

of Figures 5.11h & 5.15e show two contrasting ages, suggesting that the CoqE layer was an aquitard for two diagenetic events near the W18, the ACDE and CMDE (Figure 5.13). The overall Si values in the three wells of Figure 5.15 somewhat resemble the pattern seen in Figure 5.14 with respect to the structural compartments. The W15 and W21 have similar Si values despite the distance from the nearby fault. Assuming the correctness of the criteria thereof, GFSN was more efficient in carrying hot fluids to further lateral distances than the fault near the W21. Interestingly, the fault near W21 is not the GFSE but a major structure internal to the FWC. Also interesting is the fact that the closeness of W18 was irrespective to Si enrichment, suggesting that not only the distance from the fault is important to estimate the intensity of hydrothermal diagenesis, but also the structural position with respect to the fault. Hence, the hanging wall block could be more susceptible than the footwall of the GFSN. Therefore, the W15 could have been affected by an extra source of silica, perhaps related to basin-scale hydrologic patterns. The GFS is the first structural high after a long east-dipping slope in this sector of the Campos Basin (see Figure 4.4, Strugale & Cartwright, 2022). Finally, Si enrichment only in the RTR of W18 is probably a consequence of overlying less-permeable CoqE zone, trapping the rising hydrothermal fluids underneath this zone.

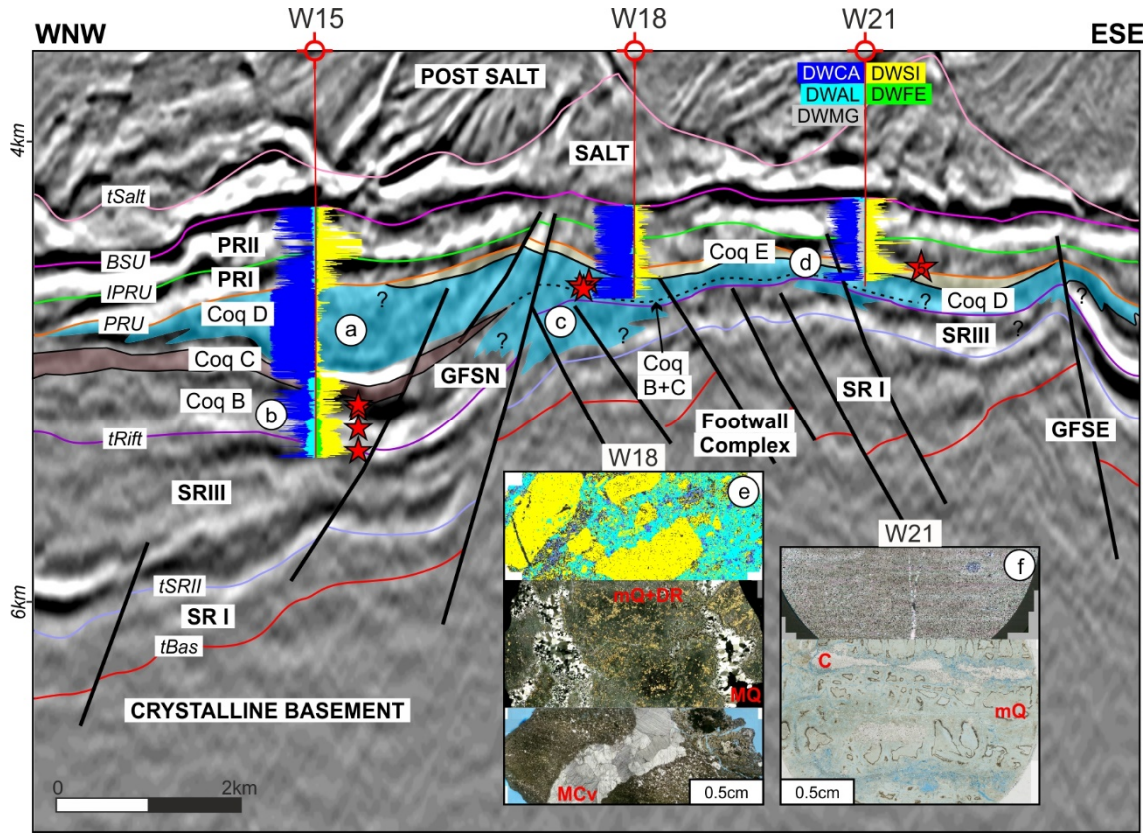


Figure 5.15: Seismic-geologic section located on the southern part of the Footwall Complex (FWC) and Guriri Fault System North (GFSN) and East (GFSE) branches (see Figure 5.2a for location, vertical exaggeration: 2.5x). Seismic horizons and stratigraphic units reflects the stratigraphy shown in Figure 5.1b. Pale blue areas are interpretation of occurrence of bioclastic rudstones based on Al, Ca weights and thin sections. The approximate position of samples are marked by red stars. Parts of the photomosaic and QEMSCAN imagery for selected samples from wells 18 and 21 are also presented. Images and calling points "a" to "f" are described in the text. For description of well log mnemonics, see the legend of Figure 5.14.

5.5.6.3 Strike section

Figure 5.16 shows the strike section that connects seven wells along the main axis of the Footwall Complex (FWC) (Figure 5.2a,b). There is a modest overall trend of Si enrichment towards the south. Log signatures of CoqE (Si & Al rich) remains the same as observed in Figure 5.15. The only exception is the W20, on which CoqE has low Si content despite its thickness (Figure 5.16a). Si enrichment in parts of the post-rift sequence could be explained by the absence of the less permeable CoqE unit in W24 and W20 (Figure 5.16b) and

therefore there was no aquitard to delay the upward fluid migration. However, notice that northernmost well (W10) also has an absent CoqE but no enrichment in Si ratio is seen above it. In addition, W20 also has the highest Si average within the rift transition sequence (RTR) (Figure 5.16c). These observations suggest that the faults near W20 where somewhat more effective in carrying hydrothermal fluids and there was no effective feeder near the W10.

The overall increase in the intensity of diagenesis towards the south is also supported by stable isotope and fluid inclusion data. The $\delta^{18}O$ data show an overall increasing more depleted values towards south, with values of -0.74 and -1.54‰ for W10 and 16, up to -8.79‰ in W18, and -4.02‰ in the SRI arkoses of W25 (Figure 5.9). Fluid inclusion data from wells along the FWC show some variations within the same mineral phase. In general, average T_h for carbonates decreases southward; for quartz and for salinity no significant change in behaviour is observed. Salinities in macrocrystalline calcite veins (MCv) decrease towards the north, from 21-24 (W18) to 17-19 (W10) wt% NaCl+$CaCl_2$ eq. Therefore, these data suggest that a different brine related to a later hydrothermal phase (MCv) is related to a slightly lower average T_h and higher $CaCl_2$ as dissolved salt, have acted more intensely in the southern part of the study area, next to the accommodation zone (Figure 5.2b).

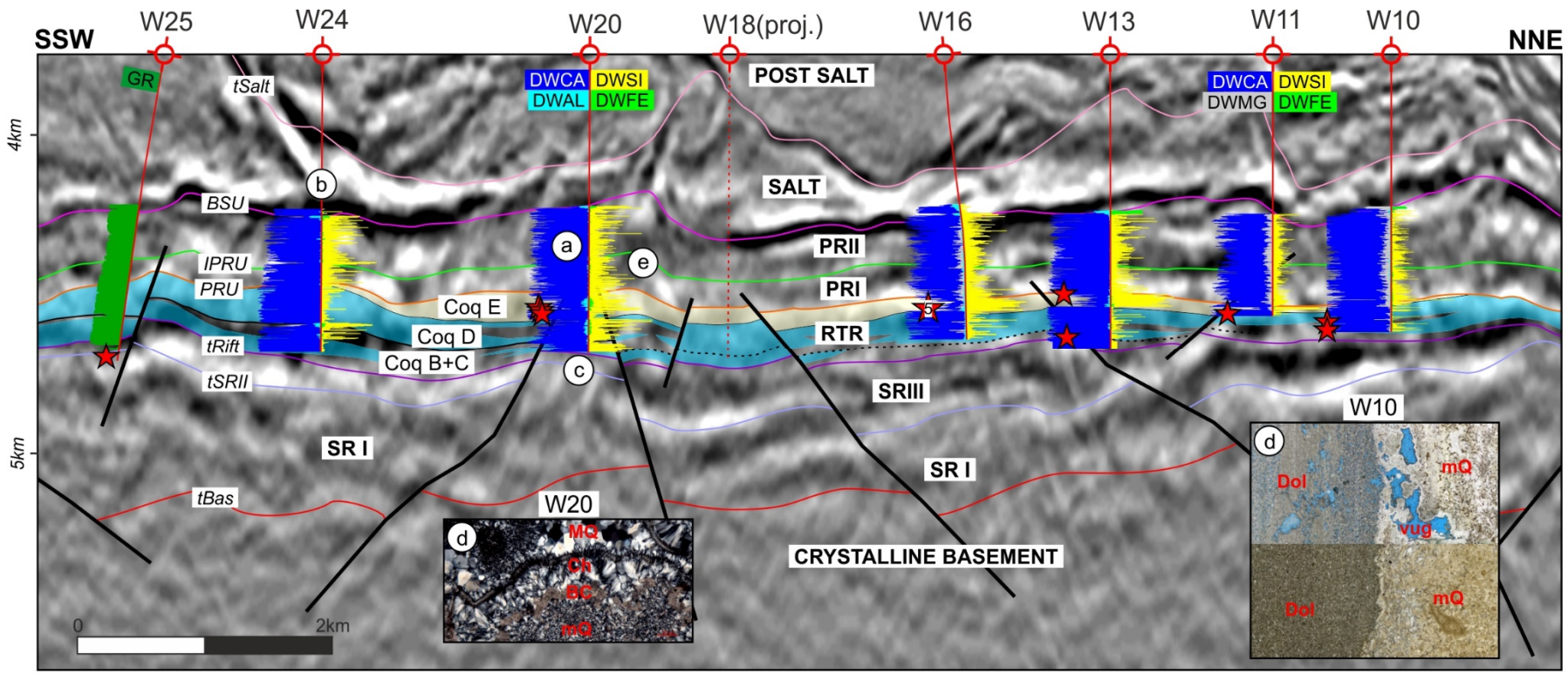


Figure 5.16: Well-section curtain along the footwall complex (FWC). W18 is the linking line with Figure 5.15. Pale blue areas are interpretation of occurrence of bioclastic rudstones based on Al, Ca weights and thin sections; it is highly speculative between W20 and W16. The approximate position of samples is marked by red stars

The question of diagenetic and hydrothermal Si distribution within the RTR along strike is addressed by comparing the samples from CoqD unit in wells 20 and 10 (Figure 5.16d). Both have abundant microcrystalline quartz (mQ) cement but only in W20 are the vugs filled with macrocrystalline quartz, suggesting that later silicification was more efficient in W20 than in W10, preserving open vugs in the latter. If it is assumed that the macrocrystalline quartz (MQ) in W20 was the latest diagenetic event, one could interpret the differences as a consequence of the magnitude of the nearby fault, a feature not observed near the W10. In addition, it is clear that the fault next to W20 developed a fault-propagation fold interpreted as result of post-rift reactivation in the GFS (Strugale & Cartwright, 2022). However, this is apparently also true for some faults within the footwall complex.

5.6 Discussion

5.6.1 Diagenetic environments

Definition and boundary conditions for diagenesis have been subject to confusing terminology, depending on which geological context or discipline within the geosciences the terms were defined (Choquette & James, 1987; Machel, 1999; Morad et al., 2000; Klimchouk, 2012). The deep burial realm (c.f. Machel, 1999) is perhaps the most prolonged, most complex, and arguably the least well understood of all diagenetic realms. A recently published review paper compares terminologies relating to diagenetic environments for marine carbonates (Immenhauser, 2022). In addition, there are classifications based on temperature contrasts between the fluid responsible for mineral formation and ambient or host-rock temperature (Machel & Lonnee, 2002). The terms hydrothermal and geothermal were proposed by these authors, based on the assumption

that a fluid classified as hydrothermal should be >5-10ºC hotter than the host rock (White, 1957).

Most of classification schemes are based on burial depth, in which a steady increase in the temperature is expected as burial depth increases (e.g. Machel, 1999). This model was applied to describe the diagenetic evolution of the Pre-Salt reservoirs in the North of Campos Basin (Herlinger Jr. et al., 2017; Lima & De Ros, 2019; Lima et al., 2020). They interpreted the diagenetic evolution as being related to a steady increase in burial conditions and consequently in temperature during thermal subsidence (Figure 5.13). From the Palaeocene, magmatic events in the basin increased the heat flow in the basement, triggering along-fault flux of hot brines that modified the rocks through extensive hydrothermal diagenesis.

The data collected during this research provided absolute ages and temperature of crystallization of different mineral phases, from which three tectono-diagenetic events were evident: BADE (Barremian-Aptian), ACDE (Albo-Cenomanian), and CMDE (Campanian-Maastrichtian) (Figure 5.13). In addition, T_h measurements collected in dated minerals provide the fluid temperatures at the time of mineral formation, which is compared with predicted temperature based on the subsidence curve. Hence, a novel setting for diagenetic environments and their geologic evolution for the presalt of the North of Campos Basin during the Cretaceous is proposed (Figure 5.17).

The proposed diagenetic evolution is based on classifications of diagenetic environments (or realms) based on burial depth (Machel, 1999) and on the temperature contrast between mineral formation temperature (and the related fluid) and the host rock (Machel & Lonnee, 2002) (Figure 5.17). In general, the diagenetic evolution of the presalt sequence is characterised by a marked temperature contrast during BADE events, that progressively

decrease as sediments are buried and then reach equilibrium during the Campanian. This interpretation differs substantially from previous works (Lima et al., 2020) and also suggests that magmatic events might not have been present during hydrothermal diagenesis, but that recurring active tectonism was occurring.

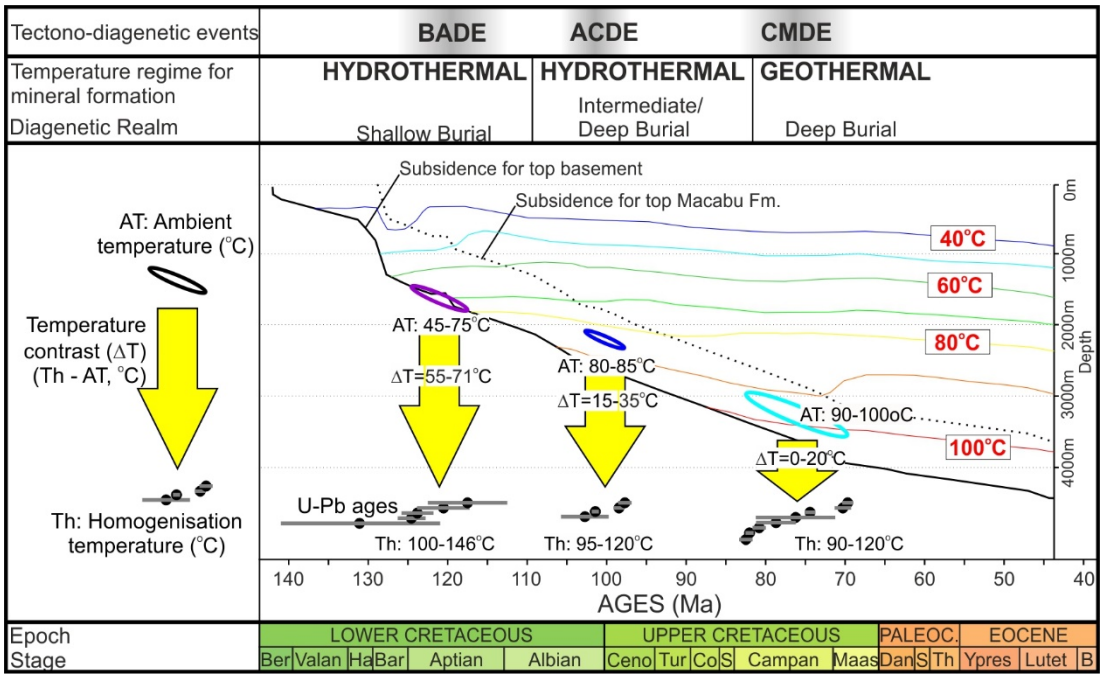


Figure 5.17: Interpretation of the tectono-diagenetic events with respect to diagenetic realms (c.f. Machel, 1999) and the temperature regime for mineral formation, or hydrothermal qualifier (c.f. Machel & Lonnee, 2002). The diagenetic realms are based only on the burial depth at the time of diagenesis. Ambient temperatures (AT) were taken from subsidence and temperature curves with respect to depth (adapted from Lima et al., 2020). Temperature contrast (Th – AT) indicates the intensity of the hydrothermal qualifier.

5.6.2 Paragenetic sequence

The previously published paragenetic sequences were based on the assumption that subsidence leads to progressive burial or mesodiagenesis (Herlinger Jr. et al., 2017; Lima & De Ros, 2019; Lima et al., 2020). The same principle was applied for the section equivalent to the syn-rift I (SRI) sequence in the Central Campos Basin (Carvalho & De

Ros, 2015). Once geochronologic data became available, a better definition of diagenetic environments was possible and it became clear that the paragenetic evolution was not linear but marked by episodes of mineral recrystallisation and formation (Figures 5.13 & 5.17). Hence, a simplified, age constrained paragenetic evolution for the basement and syn-rift I (SRI) sediments is proposed, and for the syn-rift III (SRIII) plus rift transition (RTR) sequences (Figure 5.18). The paragenetic relationships for RTR should be useful for the post-rift Macabu Formation.

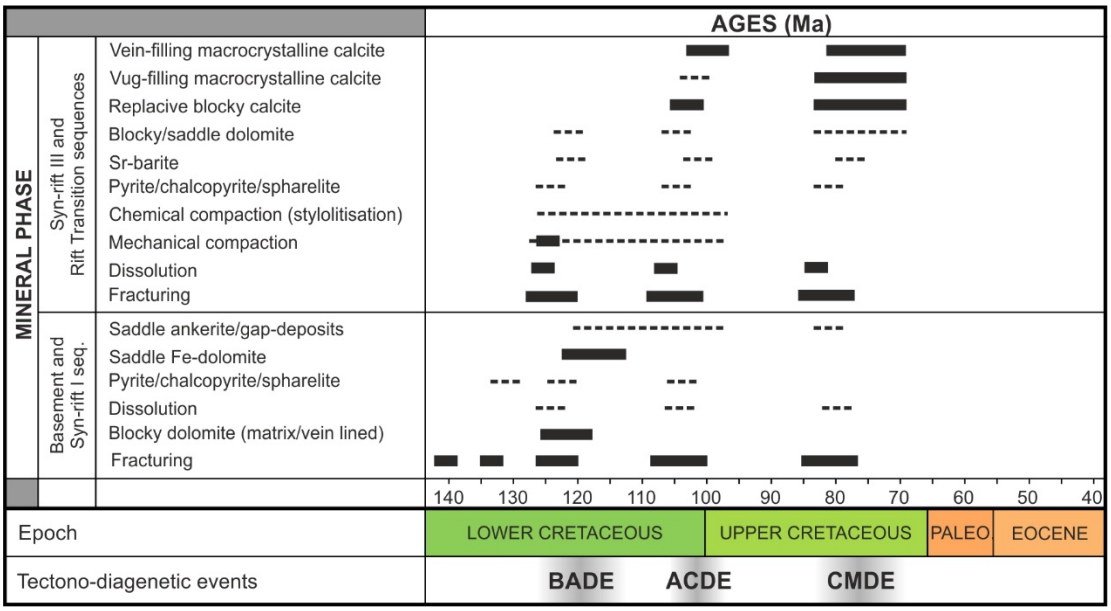


Figure 5.18. Interpretation of the paragenetic evolution of the main mineral phases and processes investigated in this study compared with the tectono-diagenetic events. Mineral phases are subdivided accordingly to the geological unit. Thick bars for carbonate minerals and tectonic deformation reflect the geochronological constraints of Figure 5.13.

Diagenetic phases for each event are preceded by fracturing and dissolution, which is a consequence of the mineral formation being contemporaneous with the deformation events that involve the basement (Fetter, 2009; Strugale et al., 2021). Therefore, it is assumed that the presalt sequence is mechanically coupled to the basement despite any strain partitioning related to contrasts in mechanical proprieties (Turner & Williams, 2004). Consequently,

strain propagated throughout the whole section results in fault reactivation and related fracturing in the fault-related damage zones in both the basement and sedimentary section (Kelly et al., 1999; Walsh et al., 2018). In addition, mechanical coupling suggests that the stress affected the whole sedimentary section, leading to widespread fracturing and consequently mineral precipitation and recrystallisation. Evidence for this is the network of calcite veins formed during two diagenetic events in the same sample (Figure 5.11f).

Despite the relatively well constrained diagenetic evolution presented in Figure 5.18, the age of emplacement of pyrite, chalcopyrite and sphalerite remains unclear and could have happened during either BADE or ACDE events, or both. Therefore, it is recommended that a geochronological study based on the Re-Os system is carried out on both pyrite nodules in clay-rich lithologies and in fracture/vug-filling in basement and carbonates (see Creaser et al., 2002; and Hnatyshin et al., 2020)

5.6.3 Diagenetic evolution and controls

The Barremian-Aptian Diagenetic Event (BADE) has a hydrothermal character (ΔT = 55-70^{o}C) and occurred during or just after deposition of the post-rift sequence (Figure 5.17). It has important implications for the depositional ages of the presalt sequence. According to Winter et al. (2007), the deposition of the Coqueiros Formation occurred at around 122-123 Ma, which is similar to ages obtained in the vug-and vein-filling dolomites of BADE (Figure 5.11j). Also, T_h values from petroleum fluid inclusions in these dolomites are >110^{o}C and consequently are likely to be related to a hitherto unknown burial event which would also have affected the maturation of organic matter. Therefore, BADE ages are interpreted to favour recent publications that consider both the Macabu and Coqueiros

Formations as Barremian in age (Tedeschi et al., 2019; Pietzsch et al., 2020; Strugale & Cartwright, 2022) (Figures 5.1b, 5.13).

Mantle plume-induced thermal anomalism during the early break-up of the South Atlantic Ocean resulted in lithospheric thinning, rifting and in anomalous thermal gradient (Chang et al., 1992; Moulin et al., 2010). The Campos Basin in particular is initially magma poor, but then became magma rich as oceanic crust formed in the Albian (Morgan et al., 2020). Nevertheless, the Cabiúnas volcanics are part of the syn-rift I sequence (Figure 5.1b) and are dated at 136-130 Ma (Mizusaki et al., 1992). It is therefore suggested that there is no magmatic event coeval with BADE. Magmatic events have been considered to be the primary heat source for diagenetic hydrothermal fluids in the Campos Basin (Lima et al., 2020), but despite the persisting cooling that occurred at the end of the Cabiúnas volcanism, heat flow was probably still significant during the BADE event. However, a tectonic event is considered necessary to establish the pathways for hydrothermal fluids from a deep-seated realm to the sedimentary section.

A common pathway for hot fluids is active faults operating through the fault-valve mechanism (c.f. Sibson, 1981; 1992). Strugale and Cartwright (2022) recognized deformation related to selective reactivation of rift faults along the Guriri Fault System during the post-rift phase, which likely lasted until the end of the Albian. Therefore, it is suggested that the BADE event is related to post-rift inversion and, more importantly, that U-Pb ages represent evidence of this inversion since dated minerals were emplaced in fractures and breccias in the basement (Figure 5.13). This also indicates that the basement was involved in post-rift deformation. In addition, it also suggests active near-surface hydrothermal venting formed the fault-controlled mounds identified in the post-rift II sequence (Figures 4.7f & 4.14).

The occurrence of hydrothermal venting coeval with the deposition of the Macabu Formation is conceivable as travertine-like deposits despite basin-scale geochemical data not being conclusive (Pietzsch et al., 2018; Pietzsch et al., 2020). In addition, mantle-derived CO_2 sourced by hydrothermal fluxes is interpreted as the carbon source for hydrothermal diagenesis (Lima et al., 2020) and magmatic-related hydrothermal-venting complexes were identified in the shallow water domain of the Campos Basin (Alvarenga et al., 2016). Finally, based on the analogue of present-day lacustrine carbonates (Bischoff et al., 1993; Dekov et al., 2014), fault-related hydrothermal-venting mounds were interpreted as being common as reservoir-scale geobodies in the Santos Basin (Fetter et al., 2018).

The minerals considered as exotic in carbonate samples are described as pyrite, chalcopyrite, sphalerite, Sr-barite, and svanbergite (Figures 5.5c,e-f, 5.8b). For basement samples, the dolomite-ankerite series and pyrite filling fractures can also be considered "exotic" (Figure 5.7e-g). This mineral suite was initially considered to be the latest diagenetic phase (Herlinger Jr. et al., 2017). Our interpretation is that it could be part of any of the diagenetic events (Figure 5.13) but more likely to the two with hydrothermal character (BADE and/or ACDE, Figure 5.18). Stable isotopes and fluid inclusion studies were used to classify this phase as hydrothermal (Lima & De Ros, 2019; Lima et al., 2020). However, according to Figure 5.13, the CMDE event is mostly of a non-hydrothermal nature. In addition, T_h for Sr-barite ranges between 125-135^oC (Lima et al., 2020), which is compatible with T_h observed during the BADE event. Pyrite is clearly earlier than Sr-barite in carbonates and it the earliest filling stage of basement fractures (Figure 5.5b). Therefore, it is suggested that the "exotic" mineral suite is likely to be coeval with the BADE event and is perhaps the latest mineral forming event. However, temperature and

burial conditions during ACDE and CMDE events do not exclude the possibility of sulfide and sulfate precipitation (Figure 5.18).

During the Albo-Cenomanian diagenetic event (ACDE), another pulse of hydrothermal diagenesis occurred, characterised by lower temperature fluid (Figure 5.17). Like the BADE event, ACDE is not coeval with magmatism but is related to a tectonic event that is observed in the post-salt succession (Fetter, 2009). As seen in the BADE, lack of coeval volcanism suggests that deep-seated fluids of hydrothermal character could have been released during sub-seismic scale reactivation of faults in both basement and presalt section (Sibson, 1981; Eichhubl & Boles, 2000; Bezerra et al., 2021). Although episodes of intrusive and extrusive magmatism occurred during the Late Cretaceous of the Campos Basin (Thomas Filho et al., 2000; Matos, 2021), their effect in the thermal profile of the sedimentary column was apparently restricted in extent.

For CMDE, the latest diagenetic event, the volcanism interpreted as responsible for triggering hydrothermal diagenesis in the presalt of the Campos Basin is validated (Lima et al., 2020). Moreover, CMDE is also coeval with a tectonic event described in the post-salt sequence (Fetter, 2009) (Figure 5.13). However, T_h values show a slightly overall cooling during the Cretaceous, with fluid temperatures within the hydrothermal event observed to be consistent with predicted burial temperature towards the end of CMDE event. Therefore, the CMDE is described as being a geothermal diagenetic event taking place at 3-4 km depth (Figure 5.17). The geothermal classification refers to minerals formed at similar temperature of the host rocks (Machel & Lonnee, 2002). Accordingly the term “geothermal” could be omitted unless special emphasis needs to be placed on the geothermal nature of a particular mineralization event. Therefore, for comparison purposes, CMDE event is referred to as geothermal in the present study. Finally, despite

the coeval magmatism and CMDE diagenetic event, it remains likely that hydrothermal or geothermal diagenetic events in Campos Basin are dependent of tectonic not magmatic events. Magmatism being dependent of tectonic events is a question that remains open.

Replacive and vein-filling cements coeval with fracturing but without a clear input of hydrothermal fluids as suggested from CMDE event are not evident. Compaction of porous in clastic sediment has been viewed as a predominantly mechanical or coupled mechanical-chemical process (Bjørlykke, 1999) during which mineral content and diffusion are fundamental controls on the constitution of the cements (Pingitore, 1982). More recently, Laubach et al. (2010) proposed the term "structural diagenesis" that aims to combine deformation and chemical changes in sediments. This concept was further explored in a review paper in which fracture patterns can be interpreted as chemical transformations in a mechanical context on which fractures could remain open for over 40 Ma (Laubach et al., 2019). Therefore, the contemporaneity of tectonic and diagenetic events combined with extensive replacive and fracture-filling mineralisation despite the lack of coeval basin-scale magmatism (Figures 5.13, 5.17-18) are strong arguments that qualify the diagenesis of presalt sequences in the North of Campos Basin as an example of structural diagenesis. Structural diagenesis also involves chemical reactions that are coeval with deformation. In this study, cements and fracture fill that either mimic, or differ from the host rock mineralogy are common in both ACDE and CMDE events. Calcite is by far the predominant cement and no calcite older than 103 Ma occurs in the sequence (Figure 5.13). On the other hand, vein and vug-filling dolomites are the principal carbonate phases related to the BADE diagenetic event, with both sulfates and sulfides included (Figure 5.18). The continuous increase in the Fe content in dolomites of BADE (Figure 5.7e-g) suggests an increasing Fe enrichment in the fluid that ultimately resulted in spots of pyrite, chalcopyrite

and sphalerite. It was not possible to conclude if such enrichment in Fe was effect of a more efficient hydrothermal flow bringing Fe from basement and SRI arkoses and volcaniclastics or just the proximity of studied samples from these geologic units. As observed in Lima et al. (2020), mineralogy, T_h and salinity are compatible with Mississippi Valley ore deposits (MVT) (Paarlberg & Evans, 1977; Leach et al., 2005), although the close relation with normal faults make this case more similar to the Irish subtype (Hitzman & Beaty, 1996; Wilkinson et al., 2005). MVT-type deposits are notable examples of basinal fluids being transported by fluid-circulation patterns of basin-scale dimension.

5.6.4 Distribution of hydrothermal diagenesis

Interpreting the three-dimensional variations of diagenesis in mesodiagenetic or hydrothermal settings is complex even in outcrop and mining studies (Packard et al., 2001; Vandeginste et al., 2005; Sharp et al., 2010; Swennen et al., 2012; Hirani et al., 2018; Kyne et al., 2019). This is because of the number of parameters that have to be known in advance regarding rock and fluid proprieties that are impacted by episodes of fluid percolation under variable burial and tectonic conditions (Corbella et al., 2004; 2014).

The interpretations presented in the previous sections were integrated to propose a predictive model for the distribution of four main diagenetic products: hydrothermal silicification, Fe-rich dolomitisation, sulfide and sulfate mineral precipitation and hydrothermal breccias (Figure 5.19). Due to the lack of well-log proxies for the occurrence of calcite cement outside the bioclastic grain and rudstones in Figure 5.19, there is no model for its abundance outside these geologic units. Nevertheless, calcite veins occur in lithologies other than bioclastic rudstones, like dolostones and cherts (Figure 5.7a,c). Present day porosity occurs as well connected fracture-vug networks in chert (Figures 5.4b,

5.5f, 5.6f) and as partially filled vugs in calcite rich bioclastic rudstones and grainstones (Figure 5.8).

The existing model for the distribution of hydrothermal diagenesis in the North Campos Basin only represents the gross stratigraphy within a simplified structural model (Lima et al., 2020). There are further works that used rock samples to characterise the hydrothermal diagenesis as being related to silicification in the southernmost Campos Basin (Vieira de Luca et al., 2017; Wennberg et al., 2021) and in the African counterpart Kwanza Basin (Poros et al., 2017; Teboul et al., 2017; Tritlla et al., 2018). In all cases, hydrothermal silicification has been described as a key control in creating and the obliterating porosity since 1) it increases the brittleness of the rock and 2) it has the potential to dissolve previous cements.

Silicification is a common diagenetic process in carbonates when silica is available from siliceous fossils, or is made available by continental runoff (Hesse, 1989; Bustillo, 2010). Active volcanism, epigean weathering of volcanic rocks, and dissolution of Mg-clay minerals are also mentioned and probably represent the main candidates for Si sources in the study area (Lima & De Ros, 2019). Furthermore, felsic basement being percolated by hydrothermal fluids could also represent a source of silica (Vandeginste et al., 2013; Bezerra et al., 2021).

Basement samples with extensive quartz overgrowths (Figures 3a & 5b) testify to silica remobilisation during diagenesis. In addition, thick syn-rift I (SRI) arkoses and conglomerates could also represent a potential source of silica. Clay-rich layers often shows high Si & Al contents in lithogeochemical logs that are interpreted as the result of local-sourced silicification. For this reason, units like CoqC and CoqE were not assigned as being affected by hydrothermal diagenesis in Figure 5.19. Instead, they have probably

acted as aquitards to hot fluids that percolates along faults, increasing fluid residence time and leading to hydrothermal brecciation and intense silicification (Figures 5.15e & 5.16a). In addition, brittle chert layers submitted to deformation could represent fractured, and thus more permeable, units that are prone to dissolution (Packard et al., 2001; Teboul et al., 2017) (Figure 5.6f).

Breccias are a common by-product of hydrothermal diagenesis (Davies & Smith Jr, 2006; López-Horgue et al., 2010) and are related to tectonic faulting combined with volumetric changes related to dolomitisation and hydrothermal dissolution. Amongst the several characteristics thought to be diagnostic of Mississippi Valley Type (MVT) deposits, they are classically carbonate-hosted with mineralisation often occurring close to lithological contrasts and preceded by dissolution-related zones of brecciation that could be interpreted originally hypogenic karst (Corbella et al., 2004; Leach et al., 2005). They are also close-related to tectonic events irrespective of the geotectonic context of the hosting sedimentary basin (Garven et al., 1993; Leach et al., 2001). In the Irish-type MVT Zn-Pb ores, hydrothermal brecciation commonly precedes the mineralization in lithological contacts within carbonatic sequences located in the hanging wall of feeder normal faults (Torremans et al., 2018; Walsh et al., 2018). The occurrence of chalcopyrite, pyrite, sphalerite, and Sr-barite within bioclastic rudstones, in which Sr-barites have T_h of 122-152^{o}C (Lima et al., 2020) (Figures 5.5e & 5.8b) and high fluid salinity (Figure 5.10), have some similarities with MVT deposits, in particular the Irish type occurrences (Hitzman et al., 2002; Leach et al., 2005).

Several publications describe faults as having acted as pathways to transient fluid flow (c.f. Sibson, 1981), feeding diagenetic fluids to sedimentary layers in which laterally extensive fluid-related diagenesis is driven by the porosity at the time of fluid migration

(Davies & Smith Jr, 2006; Sharp et al., 2010; Corbella et al., 2014; Walsh et al., 2018). Once the hydrothermal fluids reach the sedimentary units, the lateral and vertical extension of their effectiveness as a diagenetic inductor will be governed by contemporary porosity and permeability (Sharp et al., 2010; Souza et al., 2021). Figures 5.14-16 show that overall Si content in lithogeochemical logs increase either towards the GFSN and GFSE faulted branches or southwards along the strike of the footwall complex (FWC). The GFSN branch records the most significant post-rift deformation (Figure 5.13, Chapter 4.6.4). From the assumption that the more active (or reactivated) the fault, the higher the chance of the fault being prone to act as a fluid pathway, it is reasonable to suggest that hydrothermal silicification was more intense near the GFSN branch (Figure 5.19d). Similarly in terms of mechanism but less laterally-extensive alteration is observed in the GFSE and related to some major faults within the FWC (Figures 5.16a & 19e), which is explained by the much less strain (displacement) accumulated in these structures.

The steady though modest increasing in the relative proportion of Si in the wells towards the south (Figure 5.16), is interpreted a supplementary effect of tectonic activity along the NNW-SSE accommodation zone in addition to inversion in the GFS branches (Figure 5.2b). It is noticeable that the accommodation zone affects the thickness distribution of the post-rift sequence, suggesting that it was active during this time (Figure 4.14). In addition, the NNW-SSE structural trend in the Campos Basin and in the onshore basement is often interpreted as the loci of tectonic activity from the Early Cretaceous onwards (Fetter, 2009; Calegari et al., 2016). Salinity from fluid inclusion analysis shows a significant decrease towards the south, suggesting the inflow of a less saline brine with respect to $CaCl_2$ only in the southern part of the footwall complex. Fetter (2009) described NNW-SSE lineaments as important tectonic features in distributing the strain related to ridge-push

once the oceanic crust, forms from ca. 117 Ma (Heine et al., 2013). This age also coincides with the end of the BADE diagenetic event. Therefore, the accommodation zone could have worked as a pathway for a brine of different composition during the BADE, but of localised extent.

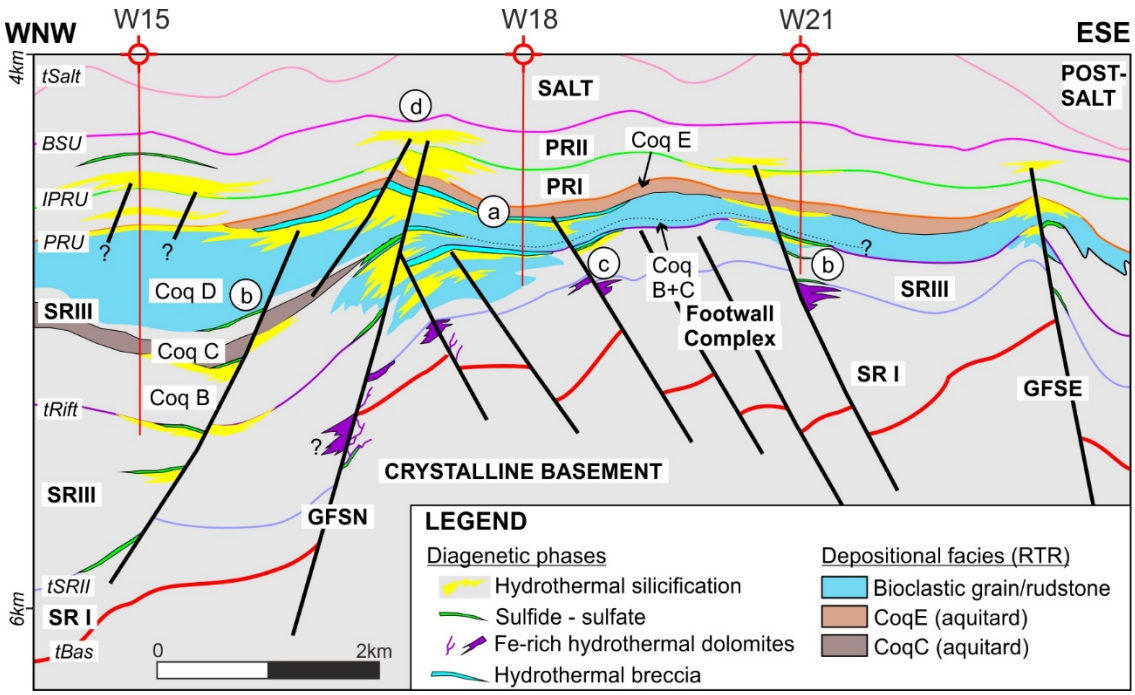


Figure 5.19: Model for distribution of main hydrothermal products (see text) overlaid to the stratigraphic and structural framework of Figure 5.15. This scheme is representative of the BADE and ACDE tectono-diagenetic events. The three wells shown are only reference for the seismic horizons because this model is based on the interpretations on Figures 5.14-16. Structural compartments are also shown (GFS: Guriri Fault System, branches North, South, and East)

Another interpretation that could explain the intense hydrothermal diagenesis evident in the hanging wall of the GFSN is the regional, basin-scale hydrodynamics of the presalt sequence. The gross hydrogeologic system comprise of volcaniclastic and arkosic strata, representing a potential bottom aquifer, overlain by carbonates and correlative low energy deposits in the depocentres. In Figure 4.4, it is evident that the whole basin is tilted towards the deeper water domain. This geometry is also observed along other regional seismic lines

across the Campos Basin (Stanton et al., 2019) and is the result of differential subsidence across the hinge line in post-Albian times (Mohriak et al., 2008).

Not only classic MVT deposits but also hydrothermal dolomitisation and silicification in North America have been attributed to increasing hydraulic head in foreland basins as consequence of evolving thrust-belts in the tectonic active margin of the basin (Clendenin & Duane, 1990; Packard et al., 2001; Leach et al., 2005; Davies & Smith Jr, 2006). In spite of the overall basinal dip to the east, basement highs in the Campos Basin could work as bulkheads to the regional flow, forcing upward migration and subsequent precipitation of fluid related phases. The Guriri Fault System (GFS) constitutes a horst bounded by west-dipping faults with over 1.5 km of displacement. Basement highs are amongst the classic metallotects for MVT deposits (Paarlberg & Evans, 1977; Clendenin & Duane, 1990). The GFS could, therefore, have acted as an abutment to the regional scale basinal flow, focusing and enhancing diagenesis in its hanging wall and footwall crest. The enrichment in Si in the post-salt sequence (W15, Figure 5.15) and the presence of sulfur- and iron-rich intervals in the same sequence in W06 (Figure 5.14f), both located in the hanging wall block of GFSN, provide evidence of hydrothermal diagenesis, as well as similarities to MVT-type ore deposits.

5.6.5 Depositional, diagenetic and hydrothermal events along the continental margins of the South Atlantic Ocean

U-Pb geochronology has been recently used to date carbonate cements and reveal diagenetic, tectonic and magmatic events in different positions along the Atlantic Ocean (Roberts & Walker, 2016; Rochelle-Bates et al., 2021; Ganade et al., 2022). Regarding the Central Segment of the South Atlantic Ocean (c.f. Moulin et al., 2010), the U-Pb ages

presented in this work are novel for the Campos Basin but have been used to study depositional and diagenetic cements in the adjacent Santos Basin (Lawson et al., 2022; Rochelle-Bates et al., 2022) (Figure 5.1a) and also in its African counterpart, the Namibe Basin (Rochelle-Bates et al., 2021). Figure 5.20 presents a geochronologic and geographic frameworks for the ages obtained by the authors thereof compared with the ages and tectono-diagenetic events described in this work.

For the Santos Basin, Lawson et al. (2022) obtained ages interpreted as depositional for the Barra Velha formation (the equivalent to the Macabu Formation in this study) of 115.83 ± 1.65 Ma (TIMS-ID U-Pb dating) and 114.46 ± 4.72 & 109.73 ± 9.26 Ma (LA-ICP-MS). A similar age was obtained in carbonate shrubs and spherulites of Barra Velha Formation, where U-Pb LA-ICP-MS yields a pooled age of 106.9 ± 4.3 Ma (Rochelle-Bates et al., 2022). However, these authors have interpreted these ages as diagenetic, not depositional. Regardless of their interpretation, these ages are somewhat in between the BADE (125-118 Ma) and ACDE (103-98 Ma) diagenetic events (Figure 5.20). Important to mention that these ages were obtained in cements formed under shallow- to intermediate-burial conditions (between 1-2 km) thus clearly diagenetic (Figure 5.17).

Younger hydrothermal cements were found in the pre-salt rocks of both the Santos and Namibe basins (Rochelle-Bates et al., 2021; 2022). They detected an Upper Cretaceous magmatic-related hydrothermal diagenesis, with ages of 82-74 & 90-80 Ma, respectively. These ages are similar to our Campanian-Maastrichtian (CMDE) event (Figure 5.20). Even younger Paleocene ages were obtained in both Santos (59.2 ± 5.3 Ma and 58.0 ± 4.6 Ma) and Namibe (56.8 ± 4.8 Ma) basins (Rochelle-Bates et al., 2021, 2022). Fetter (2009) described a peak of deformation with similar age in post-salt of the Campos Basin usin balanced sections (Figure 5.13). The lack of Paleocene to Eocene diagenetic events in the

North Campos Basin could be related to sampling bias, that may not have sampled the equivalent cement during this research.

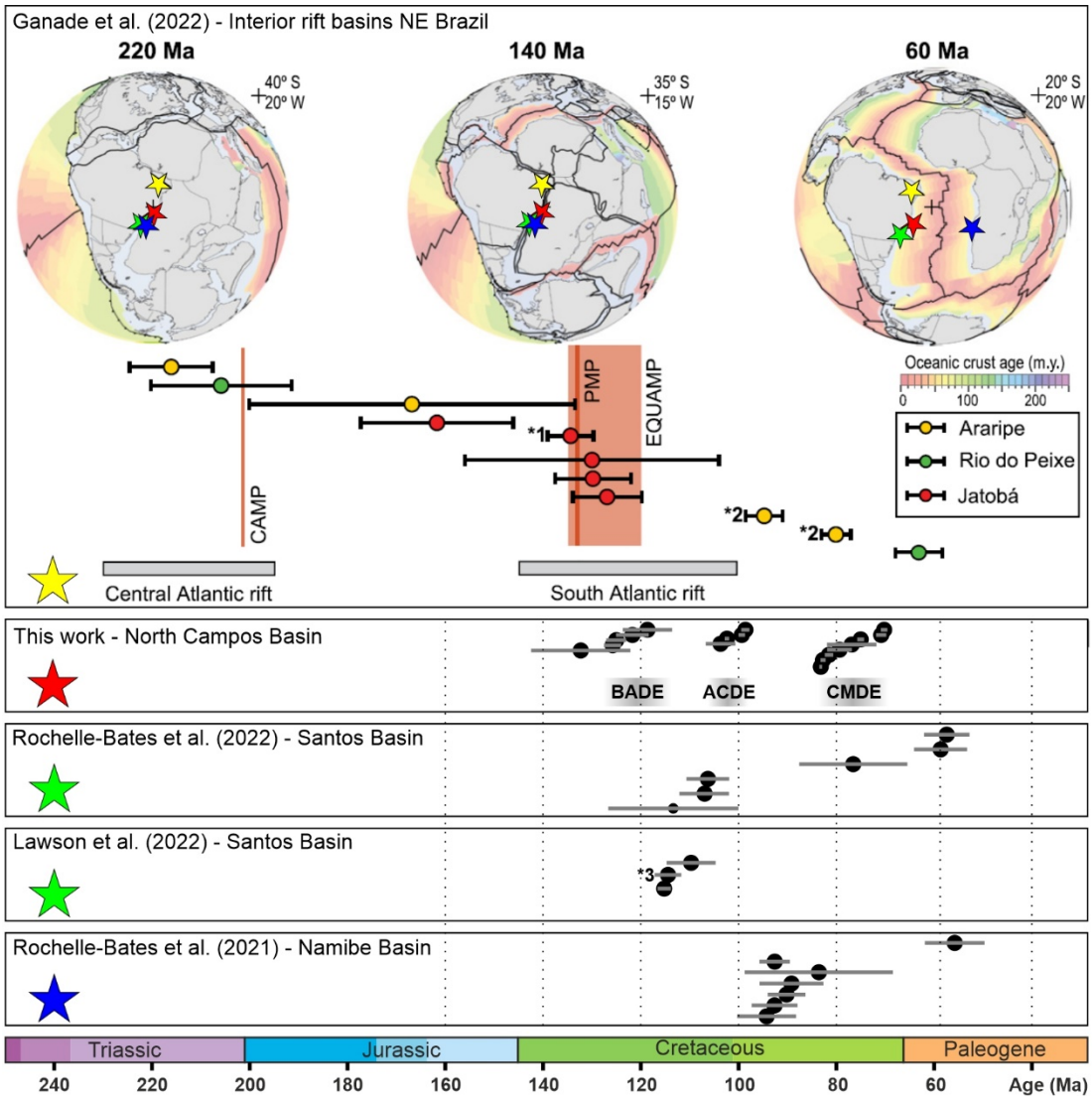


Figure 5.20: Compilation of the geochronologic data from diagenetic carbonate cements available for the Brazilian Margin (Ganade et al., 2022; Lawson et al., 2022; Rochele-Battes et al., 2022) and Namibe Basin (Rochelle-Bates et al., 2021) compared with the results of this work (Figures 5.12-13). On the top is show the plate configuration in three key moments of the Atlantic rifting and ages obtained across the interior rift basins of NE Brazil, named Araripe, Rio do Paixe and Jatobá, by Ganade et al. (2022) and (*1, *2) references therein. Coloured stars are the approximate location of the studied areas during the margin evolution with respect to the South Atlantic opening. CAMP: Central Atlantic magmatic province; PMP: Paraná magmatic province; EQUAMP: Equatorial Atlantic magmatic province. All data were obtained through LA-ICP-MS except *3, obtained by U-Pb isotope dilution.

The observations above can be interpreted as that tectonism, magmatism and enhanced diagenesis could be controlled by regional-scale tectonics, because similar diagenetic ages were observed in both margins of the Central Segment of the South Atlantic Ocean regardless the occurrence of coeval magmatic events. Given the symmetry between the margins, regional tectonic events could be attributed to episodes of increasing oceanic spreading combined or not with changing dynamics in the Andean Orogen. Intraplate tectonics is an important mechanism for the deformation of both intracratonic realm and continental-margin basins in the South American continent during the Phanerozoic (Assumpcao, 1992; Cobbold et al., 2007; Milani & De Wit, 2008; Bezerra et al., 2011). Despite the good temporal correlation between orogenetic pulses in the Andean Orogen from Early Cretaceous to the present with tectonic and magmatic events in the South Atlantic (Cobbold et al., 2007; Mohriak et al., 2008), other authors justify these events based only in pulses of rapid oceanic spreading in the Meso-Atlantic chain (Kukla et al., 2018). Fetter (2009) interpreted three tectonic events that affected the post-salt package in the Central Campos Basin during the Albian, Campanian and Palaeocene, correlated with the clustered ages and tectono-diagenetic events of this research (Figure 5.12-13). However, he did not mention a particular causing mechanism but only general geodynamic processes.

Regarding the clustering of ages obtained from diagenetic cements of Figure 5.20, two behaviours are observed: while Palaeocene ages are well clustered around the interval of 60-50 Ma in Santos, Namibe and Rio de Peixe basins, Early and Late Cretaceous ages are scattered and whatsoever correlated across the ocean. Firstly, the earliest diagenetic cements dated in the Namibe Basin are at least 10 Ma younger than the polled ages obtained in the Santos Basin and around 30 Ma younger than BADE event. On the other

hand, Cretaceous diagenetic ages across Santos and Campos basins are quite similar; ACDE and CMDE are in phase with clustered ages for Santos Basin (Figure 5.20). Regarding the BADE event, although being marginally time-related to the earliest cements of the Santos Basin, it is also marginally correlated (though younger) to clustered 140-125 Ma ages of diagenetic cements dated by LA-ICP-MS in the NE Brazil (Ganade et al., 2022). Ages from these authors are in turn correlated with the 135-120 Ma Equatorial Atlantic Magmatic Province (EQUAMP) (Hollanda et al., 2019) and the 135-134 Ma Paraná-Etendeka Province (Rocha et al., 2020) (Figure 5.20). If we gather all the geochronologic data from diagenetic cements of the Brazilian Margin shown in Figure 5.20, they suggest that earliest diagenetic-related cements are progressively younger southwards and perhaps follows a continent-scale pattern of tectonic events whose loci migrated from north to south during the Mesozoic. Such pattern apparently does not follow the magmatic events in terms of location and ages thus might suggest a southward strain migration.

5.7 Conclusions

The crystalline basement, syn-rift I (SRI) volcanoclastics and arkoses, syn-rift III (SRIII) and rift transition (RTR) sediments are described as host rocks and diagenetic products.

Wellbore samples from the North Campos Basin reveal a complex paragenetic evolution. Basement and SRI show Fe-rich dolomites, pyrite and quartz as diagenetic products. SRIII and RTR have a wide predominance of quartz and calcite. Locally, chalcopyrite, pyrite, sphalerite and Sr-barite constitute a distinct phase that have similarities with Irish Type Mississippi Valley Zn-Pb ore deposits.

Fluid inclusions in quartz, calcite and dolomite cements revealed homogenization temperatures (T_h) in the range 90 to 130ºC and correlated to present-day depth. Fluids are moderately to highly saline (>21wt% NaCl Eq.) and >15wt% NaCl-$CaCl_2$ eq. and stable $\delta^{13}C$ values in carbonate cements are clustered between - 1.68 and 1.66‰ while $\delta^{18}O$ exhibits a greater variation (between 0 to -10‰ VPDB). The most depleted values of $\delta^{18}O$ in carbonates are correlated with higher T_h and latest diagenetic phases (veins and vug-fillings).

The U-Pb ages of replacive and vein-filling cements reveal three tectono-diagenetic events, named Barremian-Aptian (BADE, 125-117 Ma), Albo-Cenomanian (ACDE, 103-98 Ma), and Campanian-Maastrichtian (CMDE, 83-70 Ma). These events were coeval with regional tectonic events related to basin inversion as results of propagation of intraplate stress that affected the crystalline basement and overlain sedimentary section. No direct correlation between magmatic and diagenetic events were observed.

Each of the tectono-diagenetic events occurred under contrasting diagenetic settings. A hydrothermal qualifier complementary to burial depth is needed to describe the

temperature contrast between fluid and host rock at the time of diagenesis. Therefore, BADE is hydrothermal, shallow-burial, ACDE is hydrothermal, intermediate to deep-burial, and CMDE is (geothermal) deep-burial.

The tectonic events lead to fault reactivation and fracturing, allowing hot basinal brines to move upward along faults but also creating fracture networks within the sedimentary layers, enhancing the lateral flow of these brines. Therefore, tectonism is interpreted as the trigger process for the diagenetic episodes. The contemporaneous tectonic and diagenetic events are interpreted as examples of "structural diagenesis" (c.f. Laubach et al., 2010).

The proxy for intensity of the hydrothermal diagenesis is given by the Si abundance in the lithogeochemical logs. Diagenetic calcite and dolomite were not resolvable by the wireline logs. More intense diagenesis occur along the hanging-wall block of the North branch of the Guriri Fault System (GFSN), as a cumulative effect of selective fault reactivation and the abutting effect of the GFS horst on the regional basin hydrodynamics.

Fault reactivation also created transient along-fault permeability during diagenesis along the other branches of GFS and major faults within the footwall complex, but with less intensity compared to GFSN. In addition, layers with high clay content worked as aquitards and delayed the upward fluid migration, leading to formation of hydrothermal breccias underneath, until eventually displaced by fault reactivation.

Secondary porosity is vastly predominant over primary porosity in the main reservoir units and is represented by a network of open to partially filled fractures and vugs. The layers replaced by diagenetic and hydrothermal quartz are especially prone to fracturing due to its high brittleness contrast with carbonate strata when submitted to later tectonic stress.

Interconnected stratabound fractures and vugs, unconformable surfaces and stylolites constitutes an important stratigraphic-controlled high-permeable layers. The role of faults

on the present-day network of secondary porosity could not be evaluated. Nevertheless, the incorporation of these conditioners in geologic and flow-simulation models would increase the confidence in the production forecast for future projects aiming to increase the recovery factor.

U-Pb geochronology has been deployed here as a fundamental tool to recognise tectonic events that affected carbonate sediments, extending the limited number of previous studies world-wide that have used this dating technique in this way. However, despite the geochronological constraint, it is still not possible to distinguish the age of calcite cements based only in conventional techniques such as petrography or geochemical analyses.

Chapter 6

Summary and Discussion

6.1 Introduction

The core of this thesis consists of two papers published in the Basin Research Journal (Chapters 3 and 4 - (Strugale et al., 2021 , and Strugale & Cartwright, 2022) - respectively) and one last chapter that is intended to be submitted either as a full length publication or as a shorter format publication. The first paper describes the Precambrian basement in terms of lithologies, age, structural framework and its effects on the structural style of the rift faults nucleated during the Early Cretaceous. In addition, a correlation with the onshore basement is proposed. The second paper proposes a comprehensive model for the tectonic-stratigraphic evolution of the presalt sequences and propose a new age for the onset of rifting. Finally, Chapter 5 examines in more detail the diagenetic phases, their paragenesis

and ages of the presalt succession. From that, an integrated geologic model for the distribution of hydrothermal diagenesis for the presalt sedimentary section. Such an integrated approach is important to build more predictive geological and simulation models for hydrocarbon production as well as to allow the assessment and the quantification of the most relevant uncertainties.

Presenting the thesis as an integrated format has several advantages but has a disadvantage in lacking a full narrative account of the geological evolution to underpin the main questions addressed by the thesis and set them in a broader context. Hence, this chapter has the goal to summarise the geologic history following the main findings of the previous three chapters, and to explain the evolution as it is, a continuum. It is followed by a discussion on which I made some considerations regarding the implications of the results here obtained. This discussion also includes some personal observations on the difficulties in integrating multidisciplinary information on the processes related to the assurance of production development projects. Finally, some suggestions for future work are presented. These ideas could be tackled by both academia and industry.

6.2 Geologic History

6.2.1 Precambrian to Triassic

The basement of the presalt sequence in the North of Campos Basin is constituted of metamorphic and magmatic rocks that are the result of successive orogenetic events under a right-lateral transpressional regime from ca. 650-500 Ma (Ebert & Hasui, 1998; Heilbron et al., 2008; Schmitt et al., 2008) (Figure 2.3). Sidewall cores shown isotropic granitoid rocks and granoblastic to foliated orthogneiss and biotite gneiss. A minimum metamorphic age of 533 ± 15 Ma was obtained from zircons though LA-ICP-MS U-Pb geochronology

(Figure 3.10). Wellbore calibrated seismic interpretation revealed that the basement can be subdivided into three seismic facies that represent contrasting degrees of heterogeneity. It was observed that the more homogeneous seismic facies are abundant in the west and more heterogeneous are common in the east of the 3D seismic survey (Figure 3.6). In addition, the structural grain in the eastern half is characterised by low dip-angle foliation and transected by possible NE-SW sub-vertical shear zones (Figure 3.11). Previous publications, lithological and geochronological data suggest that the tectonic limit between the Oriental Terrane of the Ribeira Belt with the Cabo Frio Tectonic Domain could be in or close to the study area (Strugale et al., 2021).

From the Cambrian to Triassic, very little information is available about the Campos Basin. During the Palaeozoic, the Gondwana Shield remained relatively stable while being surrounded by active orogenic belts. It resulted in extensive foreland to intracratonic basins (e.g. Paraná-Cape-Karoo Basins) flanked by the Gondwanides, an active accretionary-belt on which four tectonic cycles were recognised (Milani & De Wit, 2008). During the Triassic, however, the first episodes of rifting occurred in both south and northern branches of the present-day South Atlantic Ocean (Lovecchio et al., 2018; Ganade et al., 2022). However, there is still a significant time span between these events and the estimated age for the onset of rifting in the Campos Basin, that is, ca. 134 Ma (Mizusaki et al., 1992; Winter et al., 2007).

6.2.2 Early Cretaceous

The age of onset of rifting is based on the oldest K-Ar ages (134 Ma) obtained in basalts from wells drilled in the shallow water domain of the Central Campos Basin (Figure 4.2). However, the significant dispersion in these ages (134-111 Ma) points towards a

significant risk of the K-Ar system having been affected by alteration (Mizusaki et al., 1992 and references therein). More recently, Santiago et al. (2020) obtained U-Pb ages in zircons of 141.9±1.9 Ma from a couple of NW-SE tholeiitic dykes in the onshore basement (Figure 4.1). Despite being outliers within the age clusters of the magmatic rocks related to the tholeiitic Paraná-Etendeka Large Igneous Province (LIP) (see review in Gomes & Vasconcelos, 2021), geochemical data of these dykes shown several similarities. Though speculative, is proposed here that the onset of the extensional tectonics related to the rifting in the North of Campos Basin occurred during the Berriasian (Strugale & Cartwright, 2022) (Figure 6.1). If this assumption is correct, it would imply in a significant modification in the previously published lithostratigraphic chart of the basin (Winter et al., 2007) because it ages the onset of rifting by c.a. 9myr (Figure 6.1). Important to notice that these authors consider the onset of rifting to be coeval with the onset of volcanism represented by the Cabiunas formation. Furthermore, if the new age constraints for the end of sedimentation of the Coqueiros and Macabu Formations are taken into account (Tedeschi et al., 2019; Pietzsch et al., 2020) and combined with the recently published Aptian ages for the post-salt shallow marine carbonates (Sanjinés et al., 2022), the time span of the presalt interval remains similar to that shown by Winter et al. (2007) (see Chapter 4.7.3 for discussion). In summary, the whole presalt sequence would be 5 to 9 myr older than has been considered in the last decades.

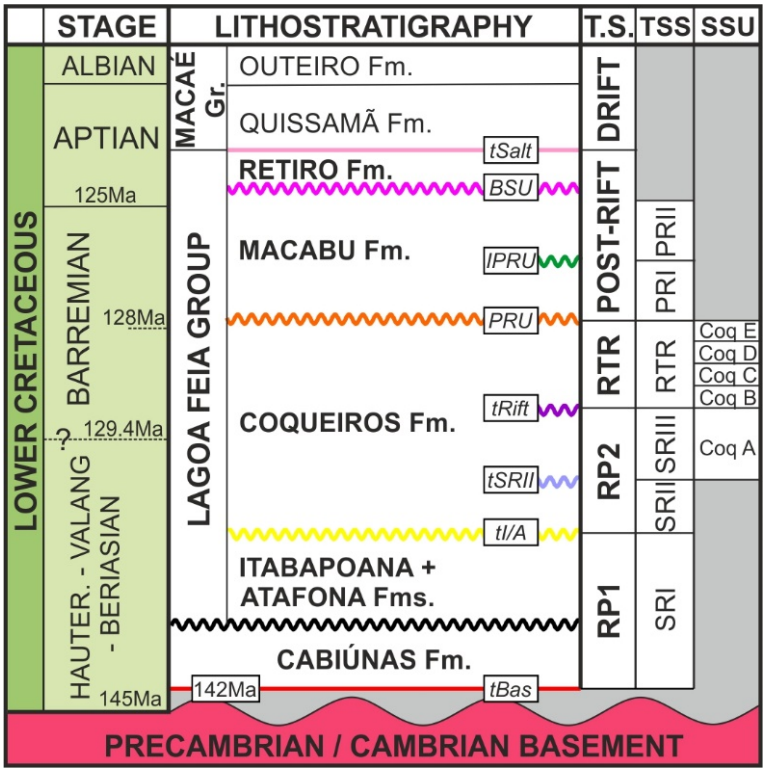


Figure 6.1: Stratigraphic framework of the studied area. Stages are based in Strugale and Cartwright (2022 and references therein). Lithostratigraphy is based in Winter et al. (2007). Interpreted seismic horizons are tSalt, BSU and so on (see text). Tectonic stages (T.S.) are based in Strugale and Cartwright (2022), where RP1 and RP2 are rift-phases 1 and 2, and RTR is rift transition stage. TSS are tectonic-stratigraphic sequences, where SRI, SRII, and SRIII are syn-rift I to III sequences, and PRI and PRII are post-rift sequences I and II. SSU are the seismic-stratigraphic subdivisions of the Coqueiros Formation proposed in Olivito and Souza (2020).

Directly following the formation of the subaerial unconformity at the top of the crystalline basement, subaerial and subaqueous volcanism, volcanoclastics, and intrusive tholeiitic magmatism and related volcaniclastics that characterise the Cabiúnas Formation (Figure 6.1). It became progressively replaced by coarse-grained arkoses (Itabapoana Formation) and fine-grained deposits in the fault-controlled lakes (Atafona Formation). These three units are impossible to differentiate in our seismic dataset because of resolution limitations and therefore were grouped as the syn-rift I (SRI) sequence. WNW-ESE transtension created a series of isolated NNE-SSW-oriented half-grabens bounded by WNW-ESE lineaments (Figure 4.10a). A good correlation of fault geometry and density with the major

compartments and structures of the metamorphic basement is observed and suggests that a number of basement structures were reactivated as rift faults (Figure 4.11, also see Chapter 3). Fault-related sedimentary wedges were interpreted in the hanging wall of the major faults, along with erosion in the footwall crests. Towards the top of SRI, some hybrid deposits occur, represented by bioclastic-rudstones in a matrix of arkose arenites. A summary diagram of the rift to post-rift tectono-stratigraphic evolution of the study area is presented in the Figure 4.9.

The top of the SRI sequence is defined by the tI/A horizon, that marks a significant change in the lithology, from siliciclastic- to carbonate-dominated (Figure A5). The tI/A horizon is an unconformable surface in most of the studied area. It is interpreted in this thesis to precede a change in the extension direction, from WNW-ESE to NW-SE. Such a change resulted in localised depocentre inversion and, more importantly, this new extension direction led to fault nucleation and reactivation of SRI faults. In contrast to NNE-SSW faults of SRI, faults active during SRII+III are NE-SW oriented and of greater extension and displacement. The resulting structure has regional significance, configuring a NE-SW-oriented horst delimited by high-strain branches that encloses a footwall complex (Figure 4.10). This system connects southward to a similar, previously unnamed, faulted system (Guardado et al., 1989) (Figure 4.4) and is denominated Guriri Fault System (GFS) (Figure 4.9). In the study area, the GFS comprises three high-strain branches (north, south and east) that delimits a footwall complex and an internal low (Figure 4.5a-b).

The SRI sequence is interpreted as being a yet unrecognised rift phase (rift phase 1 - RP1) that includes three formal lithostratigraphic units (Figure 6.1). This recognition was based on 1) tI/A horizon is an angular unconformity of great extent, 2) strong lithological

contrast, 3) change in structural style and depocentre inversion, and 4) change in the extension direction (Figures 4.9 and 4.10).

The onset of syn-rift II (SRII) sequence is marked by intense fault activity along the north branch of the Guriri Fault System (GFSN), in whose hangingwall up to 2 km of sediments and clastic wedges were deposited (Figure 4.6). The SRII time is also characterised by significant erosion of the footwall crest of GFSN and the onset of its degradation towards the footwall (c.f. Hesthammer & Fossen, 1999; Morley et al., 2007) (Figures 4.8b & 4.9). Elsewhere, erosion and/or non-deposition is related to the top of SRII (tSRII surface). Consequently, the tSRII and tI/A surfaces merge as the tSRII horizon over most of the study area (Figure 4.9). Unfortunately, no well was drilled though the SRII. Nevertheless, SRII is interpreted as the basal sequence of the Coqueiros Formation, in contrast to the previous interpretation of Olivito and Souza (2020) that correlated SRII with the Itabapoana and Atafona formations.

The syn-rift III (SRIII) sequence has up to 800 m of carbonatic and hybrid (carbonatic plus siliciclastic) sediments that onlap onto the tSRII surface. The SRIII truncates the tSRII in structural highs or is a conformable surface within depocentres (Figure 4.6). The GFSN remained active and show a southward strain migration along the strike. During the SRIII, the gross geometry of the GFS was achieved when the southern and northern branches of GFS and the initially isolated segments of GFSE linked (Figures 4.7c-d & 4.10). Towards the end of SRIII, the residual relief of isolated structural highs were healed.

The rift transition sequence (RTR) was deposited onto the top rift surface (tRift) and is more or less a vertical continuum of the SRIII thus configuring an overall coarsening-up sequence. However, I opt to maintain the terminology of Olivito and Souza (2020) since the RTR is characterized by very localised fault activity (in the south of the GFSN) thus

the thickness map still show the imprint of the GFS (Figure 4.7d). In addition, bioclastic bioherms that prograded westward from the footwall of active fault segments, while SRIII is marked by bioclastic rudstones and grainstones stacked onto structural highs (Figure 2.5). The high energy facies are composed of bioclastic rudstones and grainstones that laterally changes to hybrid siltstones and arenites often rich in Mg-clays, and finally to siltstones rich in organic matter towards the depocentres. Over the footwall complex, the depositional environment evolved into a restricted shallow and evaporative lake. In addition, significant erosion/non-deposition on the eastern sector indicates a regional tilting to the SW, which remained active during the post-rift stage.

The SRIII plus RTR sequences are equivalent to the classic section of the Coqueiros Formation (Hauterivian to Barremian), with the addition of SRII sequence that was originally interpreted as being part of the Itabapoana and Atafona formations by Olivito & Souza (2020) (Figure 6.1). These authors proposed an evolutionary depositional model and subdivided the Coqueiros Formation into five seismic-stratigraphic units (CoqA to E), whose equivalence to the interpretation here described is shown in Figure 6.1 and discussed in Chapter 4.6.

The post-rift unconformity (PRU) horizon marks the onset of the post-rift sequence, which is over 1 km thick and subdivided in PRI and PRIII (Figure 6.1). The post-rift sequence corresponds to the Macabu Formation and was deposited from the Barremian to the beginning of the Aptian (Tedeschi et al., 2017; Pietzsch et al., 2020). For the first time, thickness maps do not have the imprint of the GFS structure. Instead, changes in thickness patterns are governed by a NNW-SSE lineament that crosses the centre of the study area, by regional tilting to SW that remained active during the PRI sequence, and by mounds

rooted in the up-dip projections of rift fault segments during PRII (Figures 4.7e,f). PRII also marks the period when the thermal subsidence prevails (Figure 4.9).

No samples of the post-rift sequence were analysed in this research. However, several works provide the key information needed for a comprehensive understanding of the deposition and diagenetic evolution, not only from the Campos but also from the correlative Barra Velha Formation in the Santos Basin (Muniz & Bosence, 2015; Herlinger Jr. et al., 2017; Pietzsch et al., 2018; Lima & De Ros, 2019; Lima et al., 2020; Pietzsch et al., 2020). In brief, according to these authors, the post-rift sequence consists of shallowing-up cyclothems of mud-grade laminated carbonates, spherulitic carbonates, and calcite shrub-like crusts, deposited in a highly alkaline evaporative lake. After eodiagenesis and throughout mesodiagenesis, these units were submitted to intense hydrothermal diagenesis that changed substantially the primary constituents and porosity of the Macabu Formation (Lima et al., 2020).

A period of subaerial exposure and erosion preceded evaporite deposition and generated the base salt unconformity (BSU, Figures 4.9 & 6.1). The time span of this gap and therefore the age of onset of salt deposition is object of debate (see the review paper of Szatmari et al., 2021). In Chapter 4, it is argued that in the study area the gap was long enough to allow both creation of structural relief through selective reactivation of rift faults and significant erosion (Figure 4.9). Tedeschi et al. (2019) and Szatmari et al. (2021) argued that the onset of evaporite deposition is diachronous across the proto-South Atlantic Ocean, so it is no surprise if it has taken longer to begin over the GFS structural high.

The deposition of the evaporites of the Retiro Formation in the Campos Basin was coeval to the continental-scale evaporite deposition in the Eastern Brazilian Margin and marks a slow intrusion of marine waters from the North Atlantic Ocean (Tedeschi et al., 2019). It

was followed by shallow-marine carbonates of the Quissamã Formation, later covered by the marls of the Outeiro Formation as result of transgression caused by the combination of enhanced thermal subsidence and global eustasy (Winter et al., 2007). The deposition of the Quissamã Formation marks the onset of salt tectonics, which is characterised by thin-skinned gravitational gliding of salt and related salt compression in the outer regions of the Campos Basin (Davison, 2007; Szatmari et al., 2021).

The Quissamã Formation was thought to have been deposited during the Albian, but a recent regional study on the East Brazilian Margin revealed that the planktonic foraminifera in this unit are of Aptian age (Sanjinés et al., 2022). This finding is consistent with the new age interpretations for the deposition of the Coqueiros and Macabu formations (Tedeschi et al., 2017; Pietzsch et al., 2020) summarised in Figure 6.1. In addition, the Barremian-Aptian ages for the first diagenetic event and related temperatures obtained in fluid inclusions suggests that the Macabu Formation was at some level of burial when submitted to the diagenesis. From this observation, this unit could not have been deposited during the Aptian.

Tectonic inversion of normal faults were identified in fault segments located within the branches of Guriri Fault System (GFS) and is interpreted to have started during the deposition of the post-rift II sequence (Figure 4.13). The inversion reactivated selected segments of normal rift faults, leading to localised reverse displacements and formation of fault-propagation-folds. In addition, towards the north along the strike of GFSN, the inversion was more intense, leading to a widespread uplift that involved both hanging and footwall blocks (Figures 4.4a & 4.14b). Hence, it worked as a bulkhead during the down to the basin (eastward) salt gliding, resulting in a relict pod of salt preserved in the hanging wall of the GFSN branch (Figure 4.6a). Therefore, it is suggested that inversion remained

active during the deposition of shallow marine carbonates of Quissamã Formation and the onset of salt tectonics (Figure 6.1).

6.2.3 Diagenetic history (Early Cretaceous to Recent)

According to the U-Pb geochronologic data, three tectono-diagenetic events were identified. The ages were compared with the homogenisation temperatures from fluid inclusions in carbonates, which are in turn compared to the predicted temperature of the host rock read from the subsidence curve (Figures 5.13, 5.14). From that, the diagenetic environments of each diagenetic phase were established based on the classification of Machel (1999) and Machel and Lonnee (2002), based on the burial depth and the temperature contrast between the host rock and the diagenetic fluid during the diagenesis. The first diagenetic event affected the presalt sequence during or just after the deposition of the post-rift II sequence (Figure 5.13). The ages for the vein filling, saddle and replacive dolomites ranges between 125-117 Ma and the temperature of homogenisation (T_h) ranges between 100-146ºC. This event is called Barremian-Aptian Diagenetic Event (BADE) and affected the basement and the syn-rift sediments at shallow to intermediate burial conditions under strong hydrothermal conditions (Figure 5.17). Although apparently restricted to deeper geologic units, the ages of this event could suggest the occurrence of near-surface hydrothermal venting along segments of the Guriri Fault System (GFS) during the deposition of the post-rift II (PRII) sequence (upper Macabu formation). This could explain the PRII mounds stacked onto the up-dip projection of some rift fault segments (Figure 4.14b).

Another characteristic of the BADE-related cements is the richness in Fe in dolomites along with the occurrence of pyrite, chalcopyrite and sphalerite in both basement and

carbonatic rocks (Figure 5.18). Fe-enrichment of basinal brines is commonly observed when they percolate through crystalline basement, basalts and arkoses (Everett et al., 1999; Dewit et al., 2014). However, based on petrographic description, it was not possible to determine whether the sulfides of basement and sediments are the result of the same diagenetic event.

The hydrothermal diagenesis in the North Campos Basin has been attributed to Paleocene magmatism that enhanced the thermal gradient of the basin under deep-burial conditions (Herlinger Jr. et al., 2017; Lima et al., 2020). However, geochronologic and fluid inclusion data have shown that hydrothermal diagenesis affected the presalt sequence not only much earlier than usually interpreted but also repeatedly (Figure 5.17). In addition, diagenetic events display a strong temporal correlation with tectonic events not to magmatism. Although magmatism often leads to an increase in the thermal gradient, conditions to fluid movement could only be reached through hydraulic fracturing (e.g. Cosgrove, 2001). Therefore, if a tectonic event leads to fault reactivation and fracturing, the fault-valve system (c.f. Sibson, 1981) could connect hot, deep-seated fluids to the sedimentary section regardless of additional heat flow promoted by magmatism.

Towards the end of the Albian Stage, the presalt sequence was subjected to a second diagenetic event, denominated Albo-Cenomanian Diagenetic Event (ACDE), with quoted ages ranging 103-98 Ma obtained in calcite veins (Figure 5.13). This event occurred under intermediate- to deep-burial conditions (~ 2 km). The contrast between T_h and ambient temperature is also indicative of hydrothermal diagenesis, although showing a lower value when compared to the BADE event (Figure 5.17). Another difference with BADE event is the constitution of the diagenetic cements being dominated by vug- and vein-filling calcite instead of dolomite (Figure 5.13). A tectonic event of similar age was described in the post-

salt sequence in the Central Campos Basin through section balancing (Fetter, 2009). Hence, is again observed that ACDE is in phase with basement reactivations that disturb the salt tectonics thus increasing strain-rates in the post-salt column.

The ACDE is followed by a period of tectonic quiescence in which temperature rises as full deep burial conditions are reached. However, during the Campanian, U-Pb ages in vug- and vein-filling calcites and dolomites yields quoted ages ranging 83-70 M. These clustered U-Pb ages correspond to the Campanian-Maastrichtian Diagenetic Event (CMDE, Figure 5.13). The constitution of the related cements is very similar to the ACDE event and, interestingly, ages corresponding to both events were obtained in calcite veins in the same sample (Figure 5.11h). T_h obtained in CMDE crystals are also similar with values from ACDE event. However, considering the increasing burial conditions, temperature contrast is low to absent, therefore the CMDE event is interpreted as having occurred under (geothermal) deep-burial conditions (Figure 5.17).

Another characteristic of the CMDE event in common with the previous ones is the coincidence with a tectonic event in the post-salt sequence (Fetter, 2009) (Figure 5.13). Hence, the close relationship between basement reactivation and diagenetic events has become even clearer. Our interpretation is that the deformation related to basement reactivation enhances fracturing and thus fluid flow, creating transient permeability that allows fluid movement, leading to recrystallisation and vug plus vein-filling by calcite and dolomite. However, the close similarity between cement and vein composition is suggestive of active mineral diffusion instead of widespread fluid circulation (Pingitore, 1982). Nevertheless, the occurrence of hydrothermal flow during the CMDE event should not be ruled out because there is a chance that our sampling was not representative of the entire diagenetic evolution.

Last but not least, the early Campanian magmatic event described in the Campos Basin is coeval with the onset of the CMDE (Winter et al., 2007) (Figure 5.13). Despite the fact that several episodes of magmatism have been described in the basin, this is the only one to be coeval with a diagenetic event marked by the geochronologic data here obtained. In addition, CMDE is characterised by the lack of a diagenesis that is clearly hydrothermal (Figure 5.17). This observation differs strongly with previous interpretations that correlated the hydrothermal diagenesis in the North Campos Basin with magmatic events (Herlinger Jr. et al., 2017; Lima & De Ros, 2019; Lima et al., 2020). Therefore, it is the contention of this thesis that, in the North Campos Basin, diagenesis is not a continuous process resulting from continuous burial where temperature increases were enhanced by magmatism, but instead occurred in pulses that are contemporary to and mechanically dependent on episodes of basement reactivation.

Correlation between tectonic events and carbonate cementation, crack-fill veins and formation of MVT deposits have been observed and constrained by geochronology in recent publications. Such correlation was observed in different geological situations, from foreland to rift basins, that is, regardless the tectonic regime responsible for the deformation (Roberts & Walker, 2016; Hall et al., 2021; Pan et al., 2021; Burisch et al., 2022). Corrêa et al. (2022) used macro and micro-tectonic observations constrained by geochronology in an outcropping fault zone in the Provence (France) to evidence that episodes of fault reactivation lead to transient, dynamic permeability, here interpreted as resembling the fault-valve mechanism of Sibson (1981). However, these authors also shown that late-tectonic cementation is a common process that follows transient permeability, preferentially cementing the damage zone, the fault core, or both, depending on the tectonic event.

From the Palaeocene to present day, no evidence of new-formed diagenetic cements are found despite the fact that three magmatic pulses and at least one more tectonic event having been described in previous studies (Winter et al., 2007; Fetter, 2009) (Figure 5.13). However, U-Pb geochronology in carbonate cements in Santos and Namibe basins also yielded Paleocene ages (Rochelle-Bates et al., 2021; Rochelle-Bates et al., 2022). Therefore, there is a possibility that our sampling strategy was not sufficiently representative to characterise all the diagenetic cements. The other relevant geologic event in the Campos Basin is the onset of hydrocarbon generation in the depocentres of the presalt sequence, believed to have occurred during the Miocene (Lima et al., 2020).

6.3 Implications and Some Reflections

The results of this thesis came from a multidisciplinary effort towards a holistic approach on studies of hydrocarbons reservoir rocks. Such an approach came from 15 years-experience of the author in the fields of reservoir characterisation and modelling for the oil industry, which show me that integration was (and is) a major issue for the management of oil and gas production/development projects. I have seen over the years that oil companies are very good in producing high quality data and interpretation. However, I suspect that there is a lack of personnel in both technical and management sides that own a broader, multidisciplinary comprehension of applied geosciences for reservoir management and production development. From conversations with other R&R geologists, this is a common problem within oil companies despite differences in organizational structures.

Reservoir characterisation and modelling are made as building blocks, representing the different specialities (petrography, seismic interpretation, stratigraphy, and so on). For a

reference workflow and broader definitions of all the disciplines involved in reservoir studies (see Cosentino, 2001). Regardless the quality of the studies on each discipline, these building blocks were often misplaced or poorly assembled because 1) lack of an integrated data management, and 2) mismatch of project deadlines and time necessary to digest and include the multidisciplinary dataset in the daily-basis routine and update of 3D geologic models. This could lead to, for example, a project on which the petrophysical modelling uses the latest processing methodology is being scaled-up to a 3D geologic model of which the external geometry is based on a five-year old seismic interpretation. There is no doubt that managing and integrating big datasets in oil companies is challenging and must keep the pace with project maturation and execution. Perhaps, for each asset or development module, a multidisciplinary and fully dedicated team of specialists could be responsible for not only preventing delays in the integration of upcoming information to the geologic and flow simulation models, but also to build-up a parallel integrated workflow of seismic interpretation, geological modelling and flow simulation that is not susceptible to the pressure of the daily-basins routine of reservoir management. Hence, I invite the reader to think about this and feel free to contact me for any feedback, thought or successful case-study on that matter.

Even though my experience within the academia is much shorter than in the industry, I noticed something similar with the reflections on the previous paragraph. In resume, it seems that that most of research are highly specialised but only a handful of researchers are capable to integrate different solutions into applied processes and knowledge. The lack of people with integration skills could be a consequence of the current zeitgeist, which is often also used to blame the lack of political leaders around the world, of whom a holistic view and approach is more than an expected quality, but a necessity.

After this long shot, I think that the holistic and integrated nature of this research is an obvious characteristic. Therefore, its deliverables are quite broad, from regional geology and implications to the study of the opening of the South Atlantic Ocean to geologic modelling and process-based simulations for diagenetic and deformational process.

To begin with, the sampling strategy was different than the adopted in the previous publications (Herlinger Jr. et al., 2017; Lima & De Ros, 2019; Lima et al., 2020). In this research the focus was on a wider lateral distribution, deeper geological units and most diagenetically altered samples. Such approach should be considered complementary to the continuous vertical sampling in fewer wells used not only by these authors but also in most publications on reservoir characterisation in the South Atlantic margins (e.g. Muniz & Bosence, 2015; Teboul et al., 2019; Olivito & Souza, 2020). The combination of these two approaches could be useful while all the samples available for a given accumulation are yet to be analysed during the course of reservoir characterisation workflow.

The first implication of this thesis is to show the importance of an integrated study not only during the exploration but also during the development of an accumulation. Although studying the rocks underneath the reservoir may appear to be supplementary, they could provide vital information for reservoir characterization, fluid-flow simulation, and future exploration campaigns. For example, aquifer dimensions and properties are often over simplified in geologic and flow simulation models. Also, only samples from the basement and syn-rift I units provided data showing the first diagenetic event of Barremian-Aptian age and its particular diagenetic phases in terms of composition. Furthermore, data from basement and earlier syn-rift units are certainly useful for a better understanding of the entire Campos Basin, thus supporting future exploration campaigns. Unfortunately, this

data feedback to exploration team is seldom seen and demands, for example, integration seminars and workshops.

Regarding the geological evolution of the Campos Basin, Chapters 3 and 4 provided significant data and interpretations to 1) constraint the basement units with the onshore geology, and 2) provide further evidence to the new age constraints for the age of presalt deposition (Tedeschi et al., 2017; Pietzsch et al., 2018; Tedeschi et al., 2019; Pietzsch et al., 2020; Sanjinés et al., 2022). Moreover, it is proposed in Chapter 4 that the onset of rifting occurred during the Berriasian instead of the Valanginian and the rift phase is not a single event, but is instead made of two rift phases with distinct fault geometries and syn-rift lithologies. Such an evolutionary trajectory is important for a wider understanding of the rifting of the South Atlantic because it evidences the changes in strain during the evolution. Finally, besides the significant revision of the dating proposed in this thesis for the onset of rifting, the life-span of the rift plus post-rift stages does not differ from the classic stratigraphic scheme of Winter et al. (2007) if the new age constraints for the deposition of the Pre-Salt reservoirs are considered.

Another implication is that the 3D seismic interpretation and the gross structural and stratigraphic framework generated during this project was made available to the reservoir management team during the course of seismic interpretation. Although it has no major difference with the existing model for the Pre-Salt reservoir, the new interpretation provided better constraints for the aquifer and, more fundamentally, for the fault geometry and linkage between fault segments. Despite the fact that faults does not represent, in most cases, barriers for present day fluid flow, it was shown in Chapter 5 that faults could represent an important controlling factor on the intensity of diagenesis and consequently the occurrence of secondary porosity. The incorporation of the geochronologic-based

diagenetic model here proposed is the next task regarding the geologic and petrophysical modelling of the accumulation here studied.

LA-ICP-MS U-Pb geochronology in carbonates (c.f. Roberts et al., 2020) is becoming a key technique to investigate both diagenetic and geologic evolution. It was able to resolve different phases of calcite formation that would be impossible to observe under conventional petrographic and geochemical techniques. In addition, it reveals that both replacive and crack-fill veins of carbonate are not filled instantaneously but took few million years to form, in accordance with the observations in Lander and Laubach (2015); and Laubach et al. (2019). However, it is important to notice the wider implications of the U-Pb ages here obtained were only possible after a multidisciplinary preparatory workflow, consisted of detailed petrographic description and supporting techniques, such as QEMSCAN mapping, C-O stable isotopes study and fluid inclusion microthermometric analyses.

Future work on modelling the strain distribution in the Pre-Salt reservoirs should now be undertaken since the whole presalt sedimentary section and the basement heterogeneities have been recognised, mapped and represented in a 3D geologic model. A distribution of mechanical proprieties based on the gross distribution of clay content based on depositional models can be made based on Chapter 4, Lima and De Ros (2019); and Olivito and Souza (2020). A methodological recap and updated methodologies for forward fracture modelling are discussed in Welch et al. (2020). In addition, it was highlighted in Chapter 5 that there is a close relationship between diagenetic and tectonic events and the paleostresses related to the post-salt tectonic events as described in Fetter (2009). Once the ages, style and paleostress of the tectonic events are known and the gross structural framework is mapped in 3D, some of the parameters that are amongst the most difficult to obtain for fracture

modelling are now available. In addition, though perhaps counter intuitive, the close relationship between cementation and diagenetic events observed in some samples point towards to fracture modelling that may well show that the loci of fracturing represent the more cemented regions, especially for calcite. Finally, geomechanical modelling must consider the contrasting mechanical proprieties between silicified and carbonate layers and, if possible, consider the mechanical variations with time. As observed in Chapter 5, silicified layers often constitute fractured reservoirs due to contrasting mechanical properties with carbonates.

Another way to use the results of U-Pb geochronology for future modelling is to temporally constrain Reactive Transport Models (RTM). RTM have been used to predict the behaviour of dolomitising fluids in replacing limestones, thus enhancing porosity (Whitaker et al., 2004; Corbella et al., 2014; Gomez-Rivas et al., 2014; Consonni et al., 2018; Abarca et al., 2019; Benjakul et al., 2020). As for geomechanical modelling, age constraints are usually difficult to obtain so having this issue solved is a step forward towards the use of RTM in the study area. However, resolving the diagenetic silicification through RTM models are seldom tried because massive and pervasive replacement of carbonate by silica is difficult to model: common parameter space for simultaneous calcite dissolution and silica precipitation is narrow (Garcia-Fresca et al., 2019). Finally, if both geomechanical and RTM modelling works in the Pre-Salt reservoirs in the North Campos Basin, we should investigate within the academia and service companies if coupled simulators are available. This would certainly improve the prediction of variations in porosity and permeability.

The final implication of this research is a qualitative model for the behaviour of hydrothermal silicification with respect to the structural framework and primary porosity.

Despite the abundance of background information on the composition, paleo temperatures and age of the diagenetic events, I recognise that the available well data could not provide further constraints for the distribution of hydrothermal diagenesis except hydrothermal silicification. The abundance of silicon in the lithogeochemical wireline logs is a decent evidence for hydrothermal diagenesis but does not explain all the impacts of diagenesis on the abundance of calcium and magnesium. It is therefore necessary to deploy more sophisticated multivariant analyses integrating well-logs and sample data, which is a theme vast enough to set up another research project.

6.4 Future Work

The multidisciplinary approach of this research has led to not only to conclusions of satisfactory impact, but also to further questions whose answers were far from the time and scope of this thesis. Therefore, in addition to the recommendations above, there are still other themes for future work that could improve the geologic understanding of the North Campos Basin.

1) Investigate radiogenic $^{87}Sr/^{86}Sr$ isotopes in the basement and syn-rift I sequence, complementary to the studies in Pietzsch et al. (2018); and Lima et al. (2020).
2) Investigate $\delta^{18}O$ isotopes in quartz cements, similar to the approach of Teboul et al. (2019) in the Western African margin.
3) Extend the U-Pb geochronology study to the post-rift sequence and compare with the results presented in this research.
4) Seek other well-log constraints for the distribution of calcite cementation and dolostones.

5) Obtain further geochronological data from the basement and basalt rocks to better constrain the age of the onset of rifting. In addition, perform provenance analysis and date the abundant zircons in the arkoses and hybrid deposits on the syn-rift and rift transition deposits.
6) Consider the use of Re-Os geochronology in the sulfides of basement, clay-rich lithologies and carbonates, according to the methodology presented and applied in Creaser et al. (2002); Hnatyshin (2018); and Hnatyshin et al. (2020).

Chapter 7

Conclusions

The main findings of this thesis are listed below. This list aims to summarise the conclusions of chapters 3, 4 and 5, presenting chronologically, unveiling the complex geological history of the presalt succession in the Northern Campos Basin.

- The basement comprises metamorphic rocks of granitic composition that are more heterogeneous, and highly foliated, to the east, but more massive to the west. The structure is oriented NE-SW, defined by shear zones and metamorphic foliation. U-Pb geochronology on zircons yields a Cambrian age (533 ± 15 Ma) for the latest metamorphic event. The nature, structure and age of the basement is comparable with the onshore Cabo Frio Tectonic Domain (c.f. Schmitt et al., 2004);
- Rift tectonics exploited basement structure, resulting in a widespread brittle reactivation of these structures. Contrasting basement heterogeneity between the East and West Domains controlled the strain distribution during rift-related faulting.

- Rift tectonics probably started in the Berriasian and peaked from the Hauterivian to the Early Barremian. A rift transition and post-rift stages follow, of which thermal subsidence is mainly predominant. Evaporite deposition during the Early Aptian set the end of the post-rift stage. Selective inversion of rift faults through tectonic shortening is a remarkable feature of this stage.
- Rift structures are the result of two episodes of extensional tectonics, called rift phases 1 and 2 (RP1 and RP2). RP1 is characterised by isolated grabens trending NNE-SSW filled with volcaniclastics, conglomerates and arkoses of the syn-rift I (SRI) sequence.
- The subsequent syn-rift II and III (SRII and SRIII) sequences are carbonate-rich and were deposited in elongated NE-SW half grabens and onto a horst bounded by high-strain fault branches. This horst is part of a regional fault system in the Campos Basin, here referred to as the Guriri Fault System.
- The strong lithological contrast, together with the angular unconformity between SRI and SRII+III units and the fact that faults related to RP1 and RP2 were initiated under different extensional directions (WNW-ESE and NW-SE) identify the two rift phases.
- The syn-rift III sequence is followed by a rift transition sequence, characterised by prograding wedges of bioclastic rudstones and punctuated by syn-depositional faults. This transition phase marks the onset of thermal subsidence, which is initially asymmetric.
- The post-rift stage is subdivided in two units (I and II) and shows no thickness control by the Guriri Fault Zone. However, in addition to the thermal subsidence, a transverse NNW-SSE structure was also active and defined compartments of contrasting thickness.
- Tectonic inversion leads to selective reactivation of rift faults from the post-rift II stage throughout evaporite deposition. Fault-propagation folds and reverse displacements are

amongst the diagnostic features of these structures. Erosion of some of these folds suggests subaerial exposure prior to the onset of evaporite deposition.

- U-Pb ages of carbonate cements recorded three tectono-diagenetic events. They are: the Barremian-Aptian Diagenetic Event (BADE, 125-117 Ma), the Albo-Cenomanian Diagenetic Event (ACDE, 103-98 Ma), and the Campanian-Maastrichtian Diagenetic Event (CMDE, 83-70 Ma). The diagenetic setting of each event is described below and follows the scheme of Machel (1999) and Machel & Lonnee (2002).
- The BADE event occurred in a shallow- to intermediate-burial conditions (~ 1km) hydrothermal setting (T_h 55-70ºC higher than T_{host}), where T_h is the homogenisation temperature from fluid inclusions in dated carbonate phases and T_{host} is the ambient temperature predicted from subsidence curve. Saddle, vein-filling and replacive Fe-dolomite are the typical diagenetic products and yielded ages from 124.6 ± 1.75 to 117.62 ± 4.99 Ma.
- The ACDE event took place at intermediate- to deep-burial conditions (~ 2km) under hydrothermal conditions (T_h 15-35ºC higher than T_{host}). Replacive, vug- and vein-filling calcite are the dated mineral phase, yielding U-Pb ages ranging from 103.34 ± 2.82 to 97.71 ± 0.37 Ma.
- Finally, the CMDE event occurred in deep-burial conditions (> 3km) with little or no temperature contrast between T_h and T_{host}. Replacive, vug- and vein-filling calcite and floating dolomite rhombs in calcite veins were dated - calcites yielded ages of 82.62 ± 0.89 to 69.96 ± 0.69 Ma, whereas dolomite yielded 70.11 ± 1.21 Ma.

- The three tectono-diagenetic events are coeval with tectonic events that affected the basement and the presalt sequence. These events promoted fracturing and fault

reactivation that enhanced transient fluid flow that created secondary porosity and mineral recrystallization. However, only the CMDE tectono-diagenetic event has a magmatic pulse contemporaneous to it. Therefore, tectonism is deemed the trigger for the three diagenetic events in the North Campos Basin. This is contrary to the current interpretation that consider magmatic events and related fluid flow as the primary cause of hydrothermal diagenesis.

- $\delta^{18}O$ data exhibit depleted values for vein filling carbonates (~ -8 ‰) compared to vug-filling (~ -4 ‰) and replacive (~ -2 ‰) phases. Such $\delta^{18}O$ depletion is suggestive of pulses of fluid flow during diagenesis.
- The correlation between diagenetic and tectonic events suggests processes related to structural diagenesis (c.f. Laubach et al., 2010). In addition, two sets of calcite veins formed during successive diagenetic events, and the correlation between vein and host rock compositions suggests that diffusion was also an important process during diagenesis.
- Hydrothermal silicification occurs preferentially in the vicinity of the high-strain branches of the rift-related Guriri Fault System. Silicified layers are preferentially fractured, creating secondary porosity and forming horizontal corridors of high permeability.

- The ages of BADE event reinforces the new age constraints for the Coqueiros Formation (Pietzsch et al., 2020), which must have been pre-Aptian in order to have been subjected to shallow- to intermediate-burial diagenesis; and
- The ages of ACDE and CMDE diagenetic events reported here are novel for the Campos Basin though being documented elsewhere in the South Atlantic basins. Therefore, they are potentially related to tectonic events of wider dimension, reflecting large plate tectonic motions and processes.

Appendix A

Supporting Information for "Basement Geology and its Controls on the Nucleation and Growth of Rift Faults in the Northern Campos Basin, Offshore Brazil".

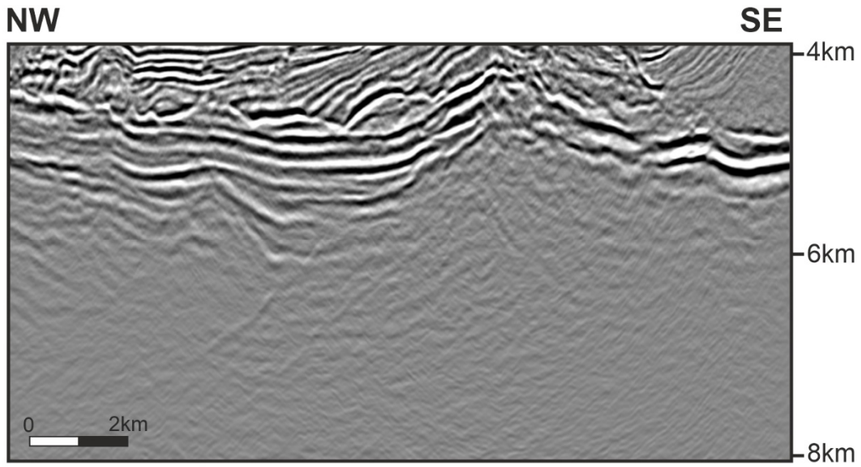


Figure 3.7d - seismic section

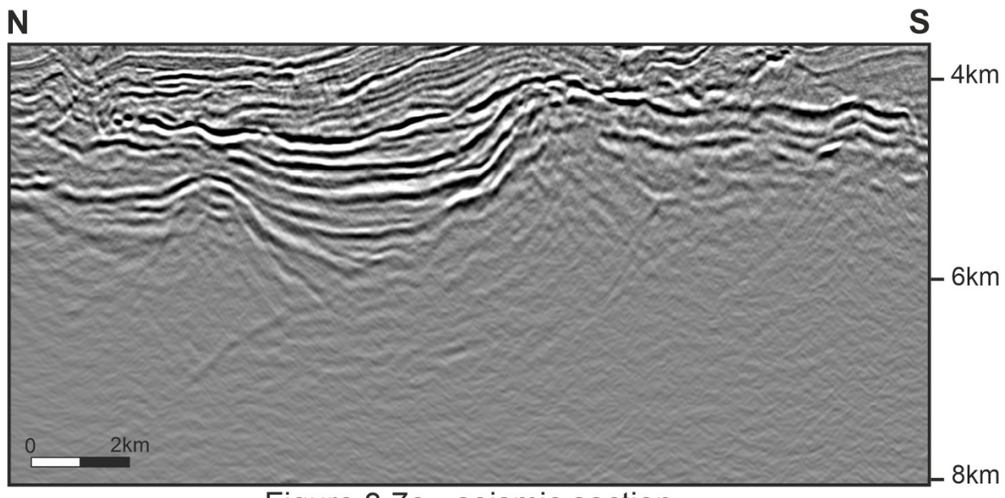


Figure 3.7e - seismic section

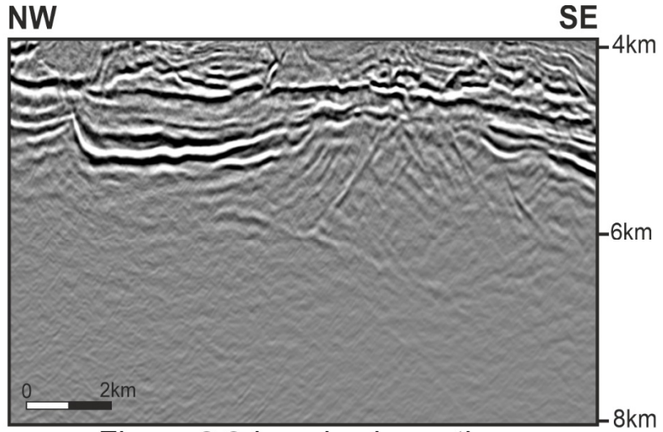


Figure 3.9d - seismic section

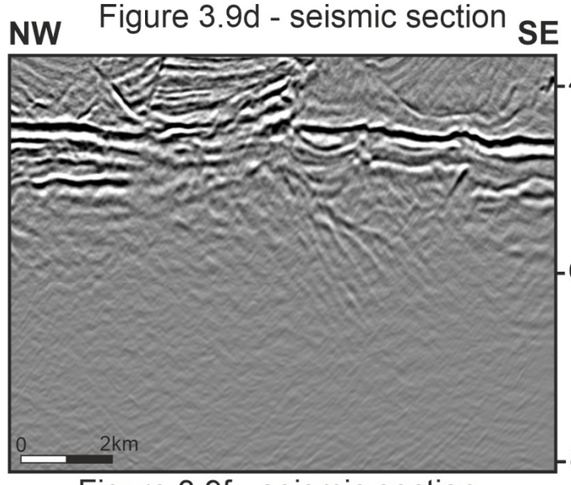


Figure 3.9f - seismic section

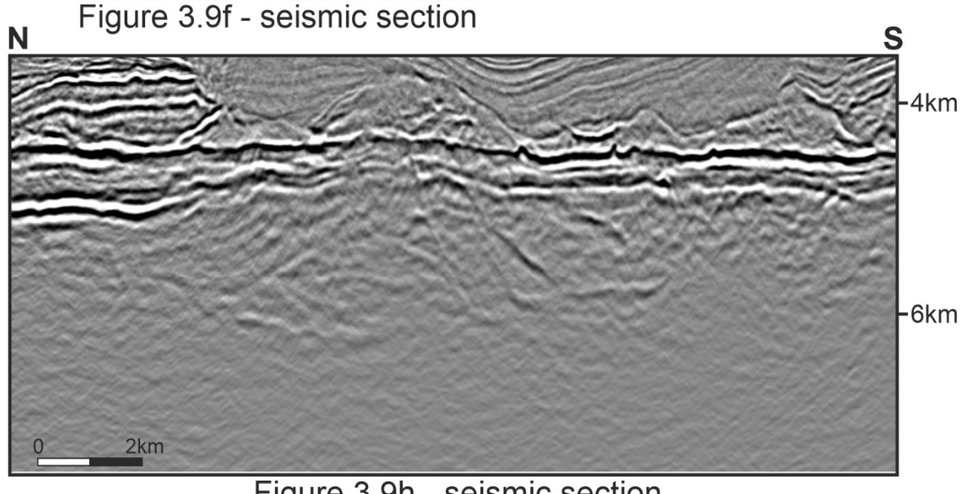


Figure 3.9h - seismic section

Figure A1: Uninterpreted seismic section of Figures 3.7d,e and 3.9d,f,h

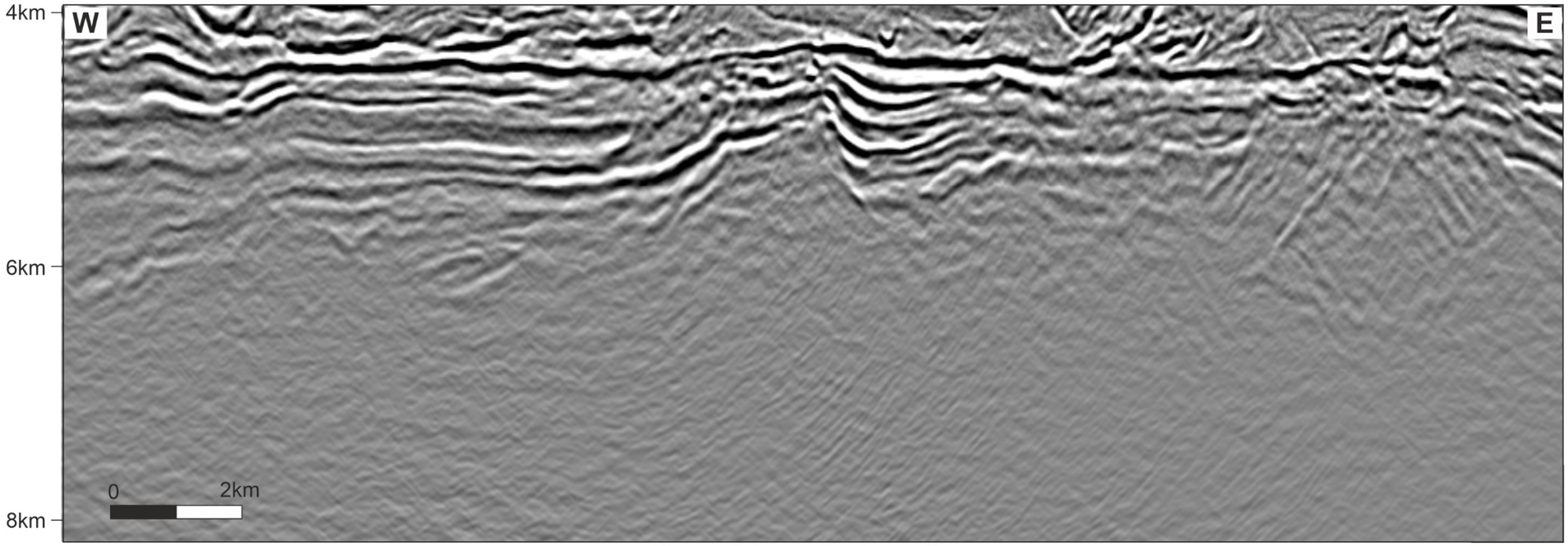


Figure 3.6a - seismic section

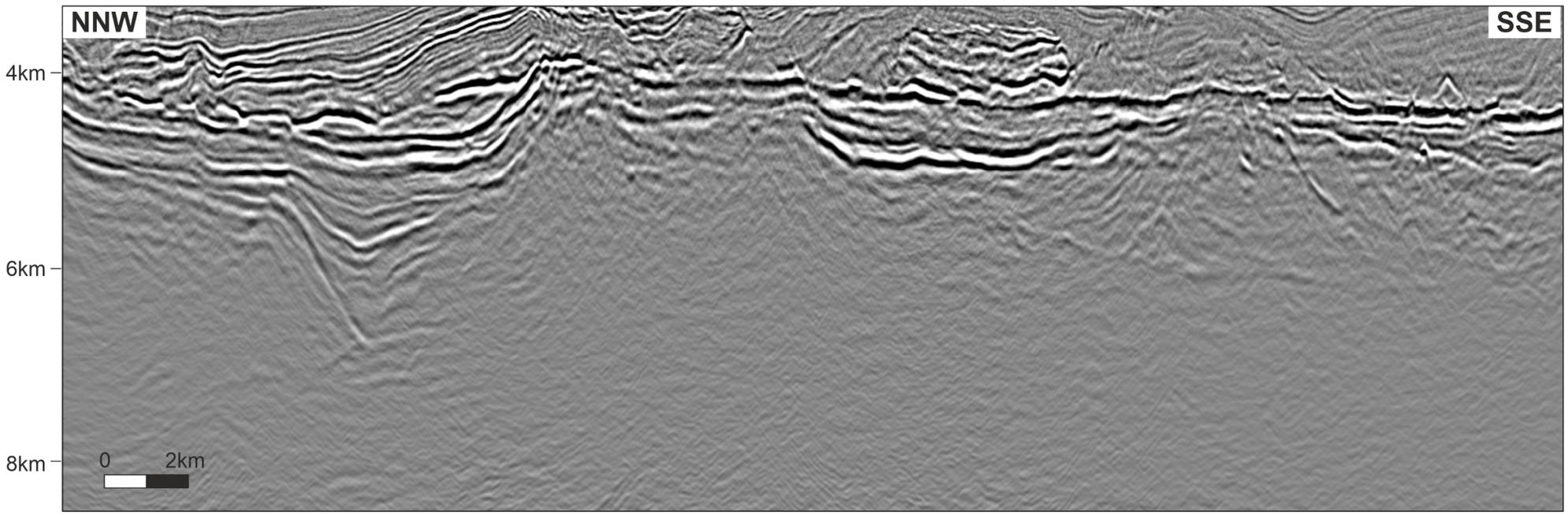


Figure 3.11b - seismic section

Figure A2: Uninterpreted seismic section of Figures 3.6a and 3.11b.

Appendix B

Supporting Information for "Tectono-Stratigraphic Evolution of the Rift and Post-Rift Systems in the Northern Campos Basin, Offshore Brazil".

This material can also be found online in the Wiley Repository address in the following website: https://onlinelibrary.wiley.com/action/downloadSupplement?doi=10.1111%2Fbre.12674&file=BRE12674-sup-0006-supinfo.docx.

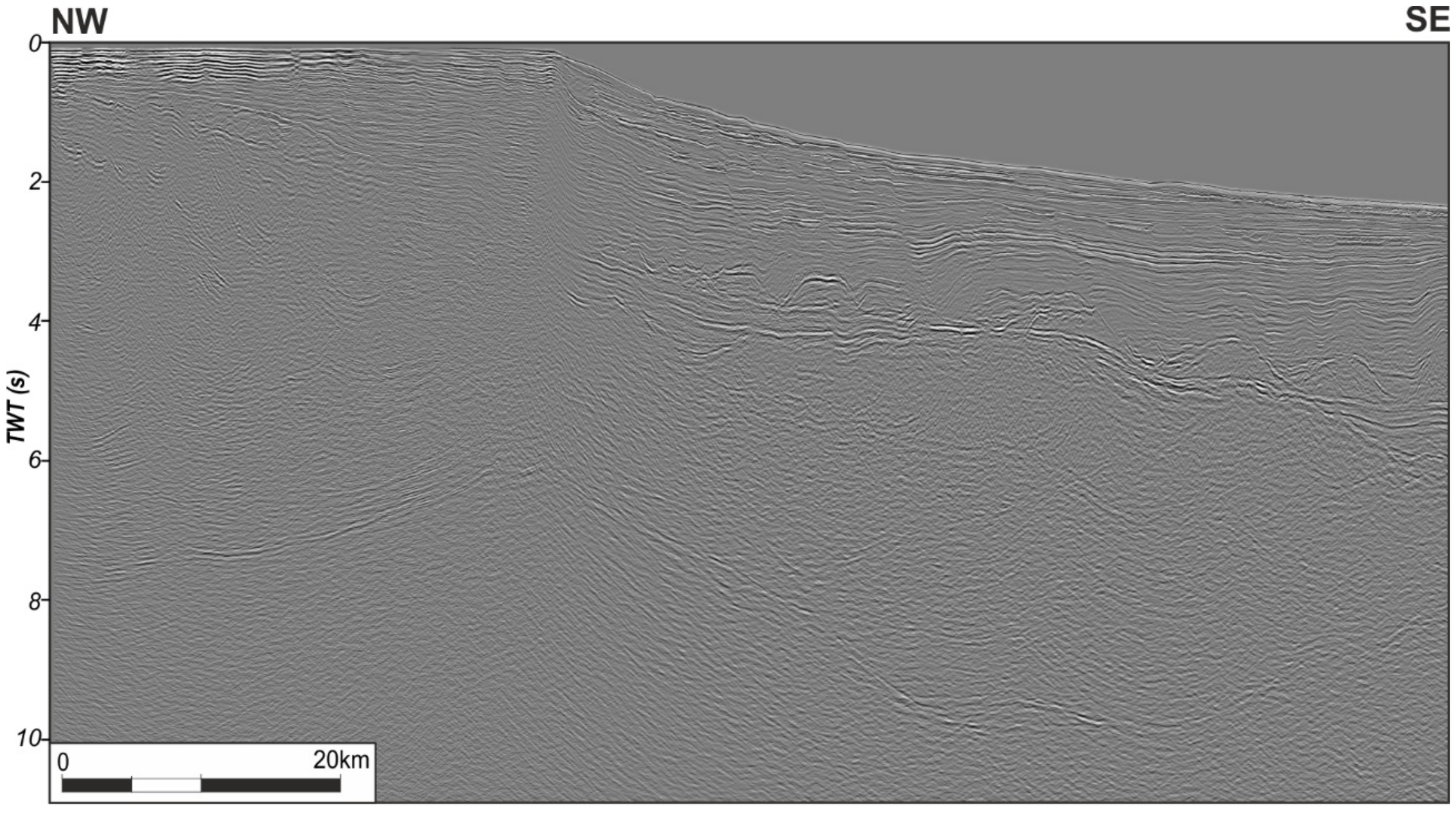


Figure B1: Uninterpreted seismic section of Figure 4.4.

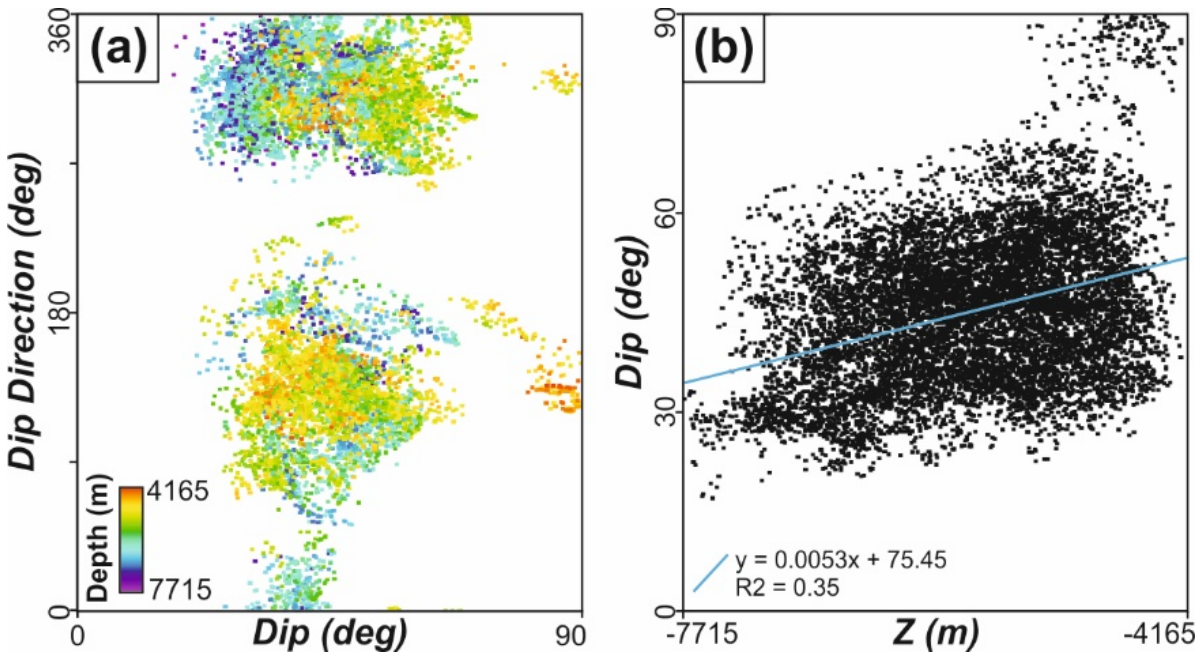
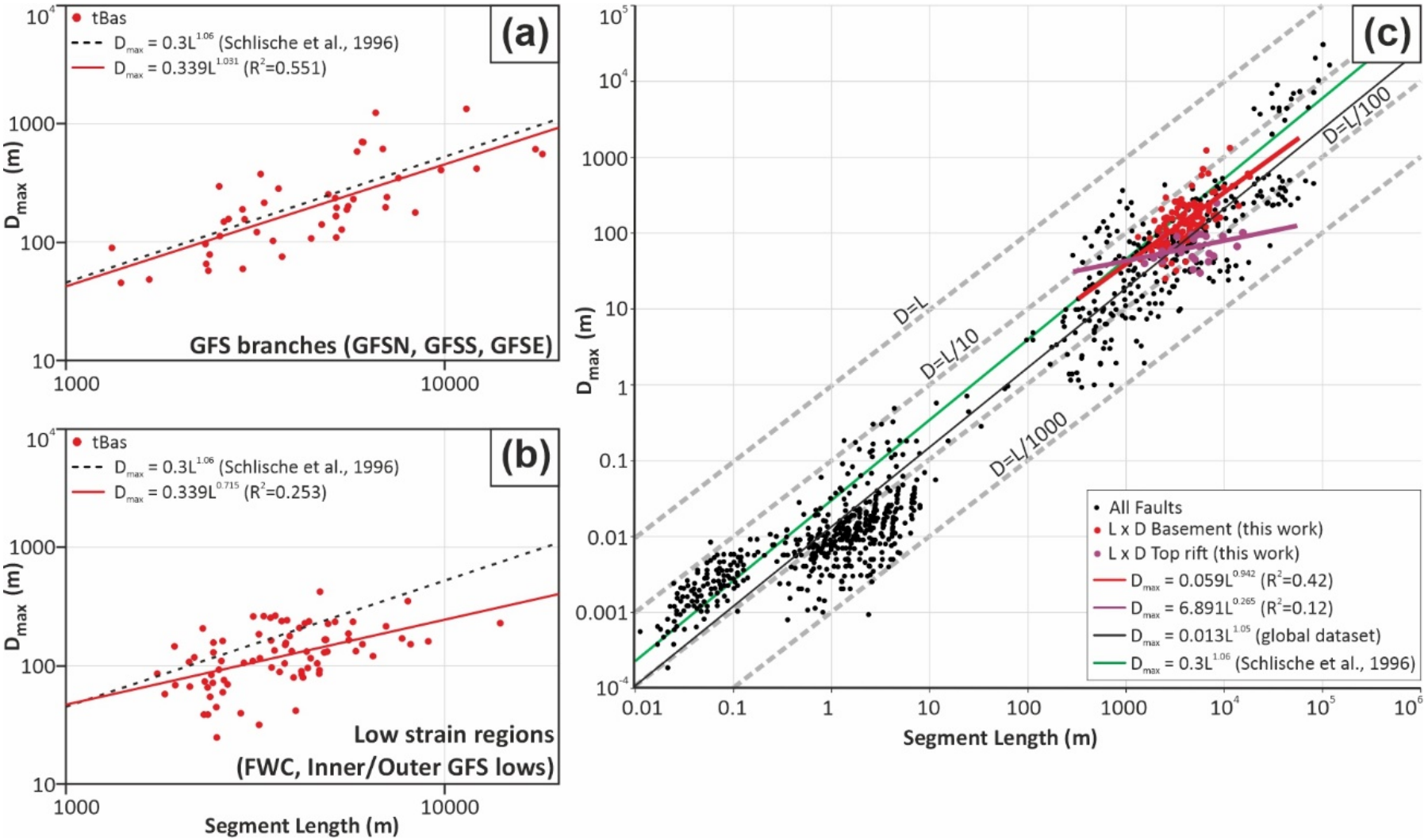


Figure B2: Cross plots showing the distribution of the nodes of the fault planes. a) dip *vs* dip direction, where the colours represent the depth. Notice the two main clusters defining a geometric conjugate set of NE-SW striking faults, a secondary pair of clusters defining a N-S-striking geometric conjugate set of faults. b) depth *vs* dip angle with the respective linear regression. The trend line shows a clearly negative correlation between depth and dip angle.



(Figure B3 - caption on next page)

Figure B3: Length-maximum displacement (L-D_{max}) data at tBas horizon plotted in log-log space for (a) fault segments within the GFS branches (b) fault segments elsewhere (FWC, Inner and Outer GFS Lows). (c) L-D_{max} data and trend lines at tBas horizon (red) and at tRift (purple) in comparison with the global dataset for normal faults (Schlische *et al.*, 1996; Kim & Sanderson, 2005)and references therein, Schlagenhauf *et al.*, 2008; Schultz *et al.*, 2008 and references therein, Morley, 2017). L-D_{max} *log-log* trend line for tRfit horizon (in purple) is also superposed to the global dataset graph. The comparison between 'a' and 'b' suggests that faults are mature and underdisplaced or immature, respectively (c.f. McLeod *et al.*, 2000). Similar behavior is observed in 'c' for tBas and tRift trend lines, which could be explained by the constant-length model for normal fault growth (Cowie, 1998) recently updated to a hybrid growth pattern (Rotevatn *et al.*, 2019). Still in 'c', the LxD_{max} points for tBas fit well in the trend line of Schlische *et al.* (1996). Such adjustment is even better for the faults within the GFS branches (a).

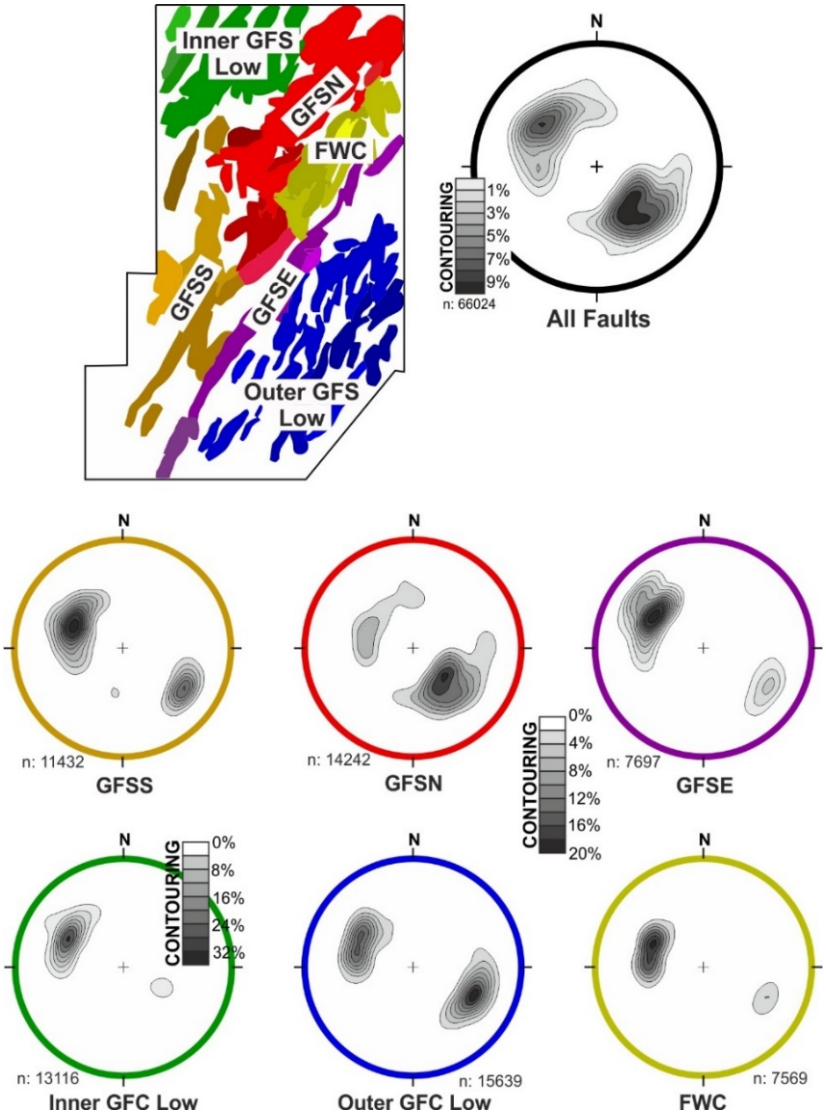


Figure B4: Map view of the structural compartments on which the faults are coloured accordingly to the respective stereographic projections. The stereographic projection for all the faults is also shown. Notice that the fault segments of the GFS branches are NE-SW oriented, while the faults elsewhere, in the low strain compartments, are predominantly NNE-SSW oriented.

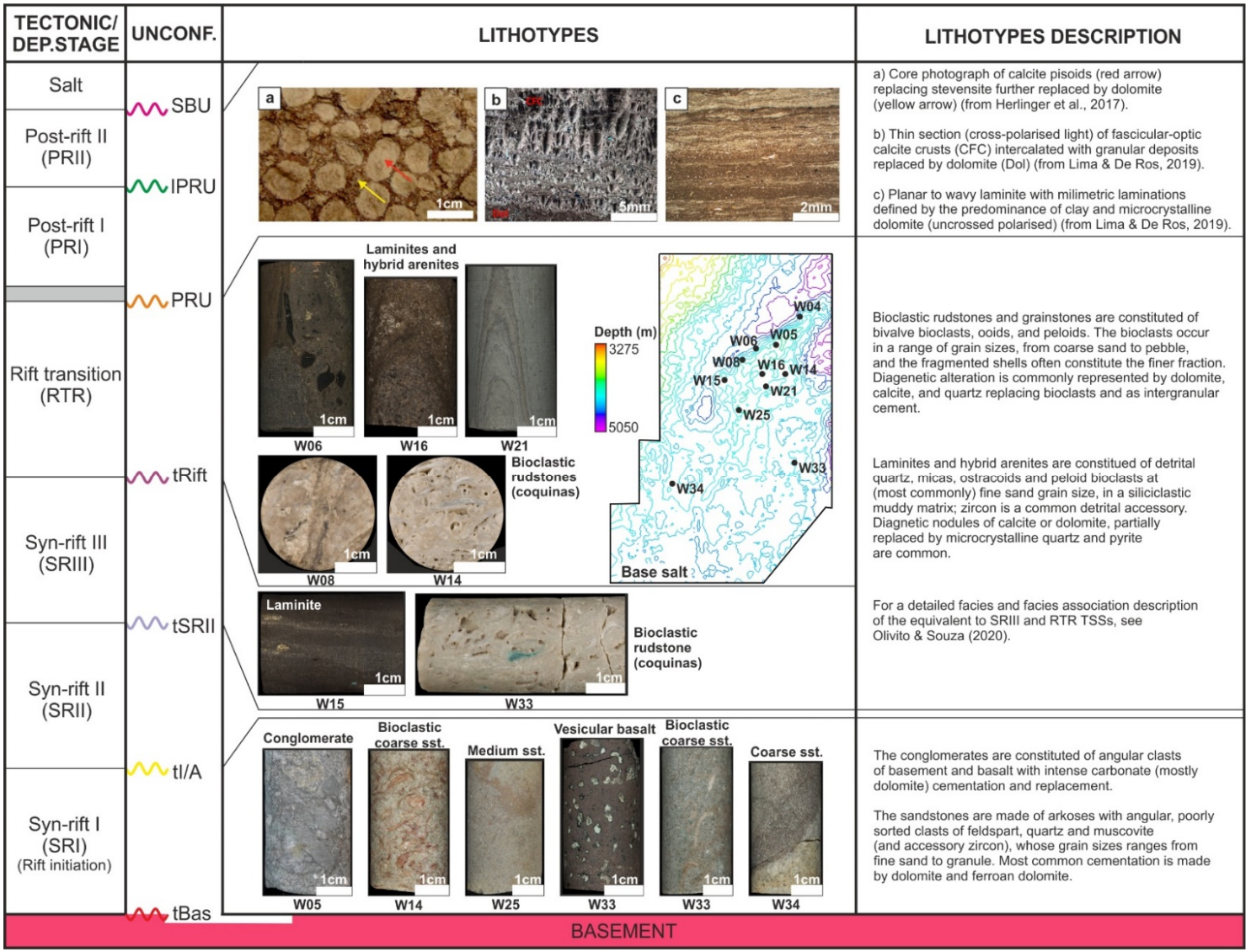
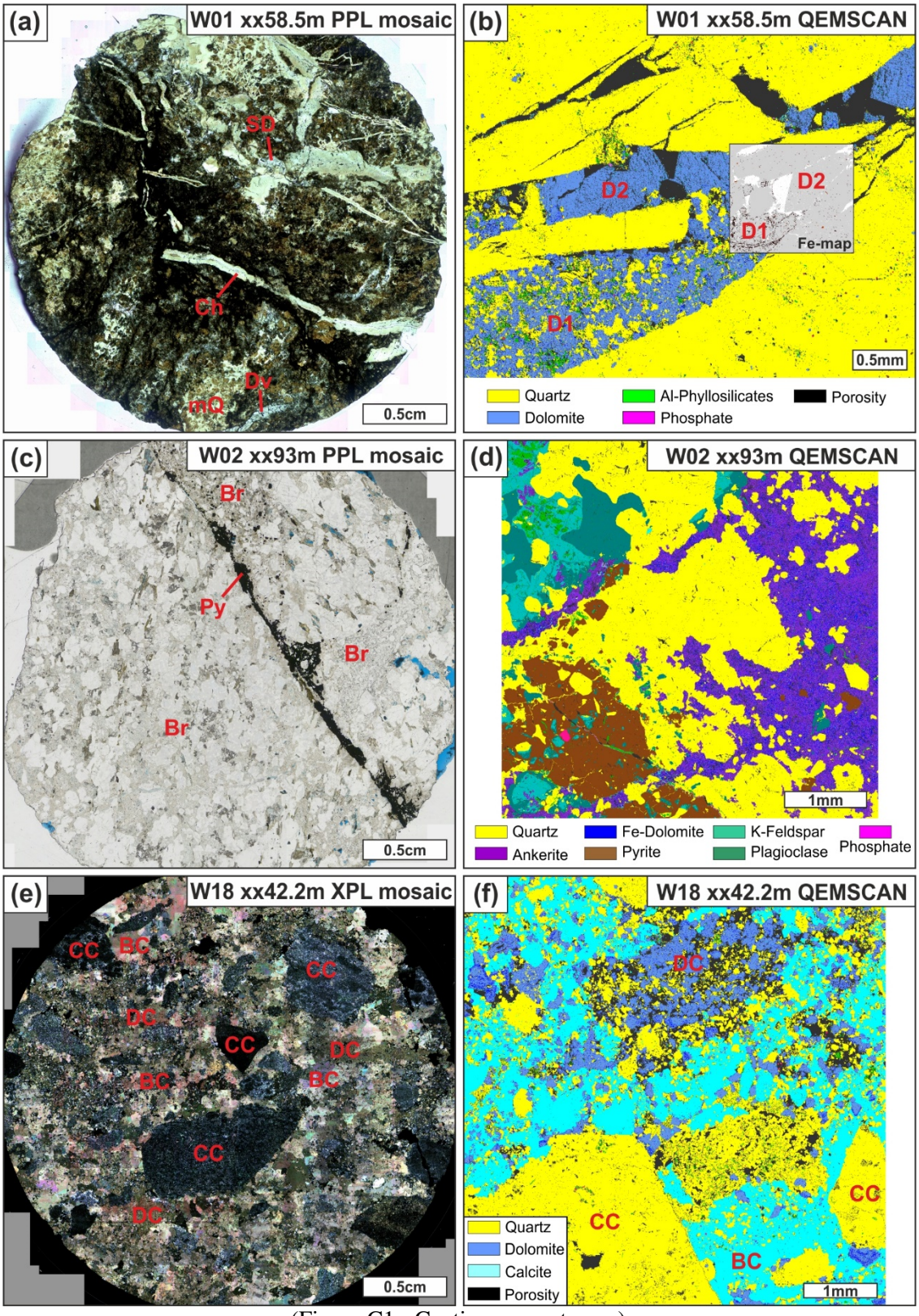


Figure B5: Side-wall cores and thin sections representing the main lithofacies for each of the TSS (see text for description). There is no wellbore data for the SRII. A structural map of the bSalt horizon with the location of the wells from whose samples are described is also shown.

Appendix C

Supporting information for Chapter 5

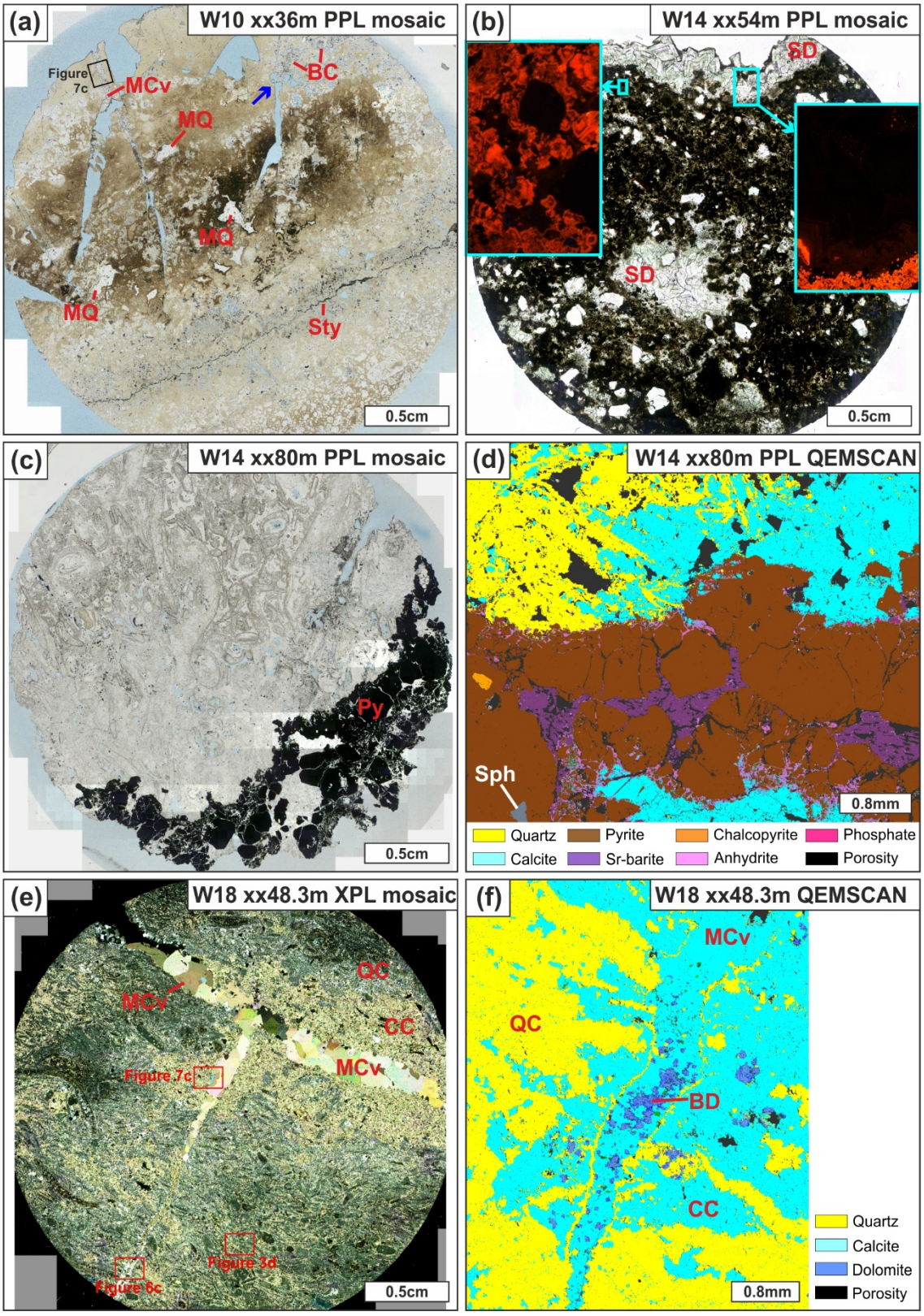
C1 Supporting Optical and QEMSCAN Imagery



(Figure C1 - Caption on next page)

Figure C1: Supplementary material that aims to present broader images of some samples of breccia, helping understanding the context on which the mineral phases occur. QEMSCAN imagery were obtained from samples in resin pods not from the thin sections shown. A) Quartz-rich breccia with fractures and vugs filled with chalcedony (Ch) with microporosity and saddle dolomite (SD). Matrix is constituted of quartz and chalcedony at several grain sizes. B) Partial QEMSCAN imagery of sample shown in "A" showing two generations of fracture-fill dolomites (D1 and D2) that are distinguished by either blocky vs saddle shape and Fe counting on the elemental map derived from QEMSCAN shown as inset overlaid on the image. C) Sample from the crystalline basement evidencing a shear zone filled with pyrite (Py). Wall rocks are brecciated, especially on the right side, and cemented by quartz, pyrite, and carbonate (see figures 3c, 5b). The constituency of both host rock and cement is constrained by the QEMSCAN image shown on "D". This image evidences the brecciated texture and that it involves the pyrite, which suggests a later event of deformation. Notice the blocky, non-zoned Fe-dolomite/ankerite cement lined up along parallel fractures that crosscut pyrite nodules. Separation criteria for dolomite/Fe-dolomite/ankerite is dolomite – $CaMg(CO_3)_2$, Fe-dolomite – $CaMg_{0.75}Fe_{0.25}(CO_3)_2$, ankerite – $CaFe_{0.6}Mg_{0.3}Mn_{0.1}(CO_3)_2$.. E) Photomosaic acquired under crossed polarizers showing the overall texture of the breccia of W18. Notice the cement-supported (BC) aspect and the abundance of chert clasts (CC), followed by dolostone clasts (DC). QEMSCAN image (F) helps distinguishing the constitution of the cement as being blocky macrocrystalline calcite (BC) engulfing dolomite rhombs. It also shows one DC that have abundant quartz cement and pore-space. It is also noticeable that pore space is more abundant in chert clasts with dolomite, in contrast with the major clast on the bottom left.

Figure C2 (next page): Supplementary material that aims to present broader images of some of the samples that contains veins with different filling, helping understanding the context on which the mineral phases occur. QEMSCAN imagery were obtained from samples in resin pods not from the thin sections shown. A) Photomosaic of a highly silicified bioclastic pack to wakestone that exhibits a system of "conjugate" fractures partially filled with macrocrystalline calcite (MCv). Apparently the fractures occur in the most silicified, less porous region, evidenced by the occurrence of vugs of macrocrystalline quartz (MQ). Otherwise, secondary porosity is significant and particularly high in the vicinity of stylolite feature (Sty). There is also some blocky calcite (BC) partially filling some vugs. Notice the connection between open fractures and vugs (blue arrow). B) PPL photomosaic (thick section) of an arkose showing saddle dolomite (SD) occurring as vein and vug filling. Two insets of cathodoluminescence (CL) imagery are also shown. On the left ankerite cement showing well developed zoning and quartz grains with dull response (cement composition constrained from Figure 3c). On the right, despite the well-developed zonation, CL signal is pale to dull, while the host rock contains ankerite cement that appears with bright red-orange colour. C) Bioclastic rudstone with massive pyrite (Py) vein. QEMSCAN data reveals the composition of both vein and host rock (D). Notice the differential relative abundance of quartz and calcite cements in the host rock, with no effect in the porosity. In the vein, notice the chalcopyrite and spharelite (Sph) nuclei within dominating pyrite, and the fractures in pyrite filled by Sr-barite and anhydrite. E) XPL photomosaic of a bioclastic rudstone showing two orthogonal veins of macrocrystalline calcite (MCv). The abundance of calcite (CC) and quartz (QC) has apparently no correlation with the veins. There is an increasing in the quartz filling towards the bottom (see Figure 6c). QEMSCAN image (F) shows blocky dolomite (BD) floating in the MCv and in the matrix, and quartz lined onto the vein walls.



(Figure C2 - Caption on previous page)

C2 Supplementary Table

Table C1: bulk composition of selected areas of samples shown in Table 5.1 obtained through Qemscan 4µm imagery. Notice that some samples have more than one image.

Depth	Well	TSS	Calcite	Dolomite	Fe-Dolomite	Ankerite	Quartz	K-Feldspar	Plagioclase	Al-Phyllosilicates/Illite/Smectite	Anatase	Phosphate	Pyrite	Barite/Sr-Barite	Other Phases	Porosity
XX58.5 m	W01	RTR	0.23	12.97	0.64	0.00	73.40	0.01	0.01	1.25	0.02	0.08	0.32	0.00	0.18	10.88
XX58.5 m	W01	RTR	0.22	9.43	0.59	0.00	72.71	0.02	0.04	1.84	0.01	0.11	0.10	0.00	0.30	14.61
XX90 m	W01	BAS	0.52	25.71	11.67	2.37	11.93	25.43	9.46	5.36	0.04	0.07	0.08	0.00	0.62	6.72
XX93 m	W02	BAS	0.15	1.65	3.85	16.51	44.26	8.30	5.22	1.90	0.02	0.06	11.15	0.00	0.28	6.64
XX93 m	W02	BAS	0.33	1.84	6.54	15.33	27.19	20.03	14.99	6.27	0.07	0.05	1.43	0.00	0.26	5.66
XX60 m	W08	RTR	6.59	50.81	1.93	0.00	22.52	0.00	0.01	0.00	0.00	0.09	0.01	0.00	0.14	17.90
XX60 m	W08	RTR	4.98	28.86	0.74	0.00	47.59	0.00	0.01	0.00	0.00	0.14	0.04	0.00	0.13	17.51
XX11 m	W10	RTR	87.36	0.01	0.00	0.00	2.25	0.02	0.00	1.93	0.10	2.45	0.42	0.00	0.05	5.31
XX11 m	W10	RTR	80.77	0.02	0.00	0.00	2.60	0.03	0.01	4.48	0.06	5.67	0.37	1.85	0.23	3.88
XX80 m	W14	SRIII	26.00	0.01	0.00	0.00	22.05	0.00	0.00	0.00	0.00	0.03	34.74	3.08	2.48	11.69
XX42.2 m	W18	RTR	30.78	12.01	1.52	0.00	42.71	0.01	0.00	1.24	0.00	0.47	0.03	0.00	0.07	11.15
XX48.5 m	W18	RTR	47.92	1.49	0.33	0.00	46.75	0.00	0.00	0.22	0.00	0.02	0.02	0.00	0.07	3.16
XX48.5 m	W18	RTR	80.11	0.96	0.16	0.00	14.08	0.00	0.00	0.43	0.00	0.04	0.02	0.00	0.12	4.07
XX48.5 m	W18	RTR	75.77	0.91	0.18	0.00	17.75	0.00	0.00	0.48	0.00	0.03	0.03	0.00	0.08	4.76
XX75 m	W20	RTR	27.20	0.35	0.01	0.00	71.22	0.00	0.00	0.14	0.00	0.04	0.03	0.00	0.02	0.97
XX75 m	W20	RTR	41.25	3.32	0.10	0.00	51.47	0.02	0.01	1.37	0.03	0.28	0.09	0.00	0.13	1.93
XX75 m	W20	RTR	17.93	0.03	0.00	0.00	81.42	0.00	0.00	0.03	0.00	0.00	0.01	0.00	0.01	0.56
XX40 m	W21	RTR	0.94	18.81	1.06	0.00	33.69	0.49	0.01	25.18	0.31	6.72	1.40	0.00	1.17	10.21
XX40 m	W21	RTR	3.09	4.06	0.21	0.00	74.93	0.21	0.01	10.30	0.12	1.86	0.61	0.00	0.49	4.12
XX40 m	W21	RTR	5.49	7.61	0.40	0.00	64.35	0.18	0.01	12.56	0.10	2.41	0.51	0.00	0.36	6.01
XX48 m	W21	RTR	12.21	0.00	0.00	0.00	79.64	0.00	0.01	0.11	0.00	0.12	0.02	0.40	0.07	7.42
XX75 m	W25	SRI	0.07	7.31	4.37	10.84	21.06	27.74	0.15	21.51	0.68	0.16	1.21	0.00	0.31	4.59
XX08 m	W33	RTR	81.60	0.03	0.00	0.00	2.29	0.00	0.00	0.02	0.01	0.87	0.22	0.00	0.12	14.77

C3 Description of Fluid Inclusion Microthermometry in Each Sample

W01 XX58.5m: this sample of brecciated chert contains vug-filling SD that hosts very abundant petroleum FIs (no aqueous inclusions were resolvable). The FIs exhibit blueish fluorescence in UV. Homogenisation data were collected from one FIA and reveal an average value around 127.5 ^{o}C.

W02 XX93m: FIs from 14 FIAs were analysed. These inclusions occur in older, turbid blocky Fe-dolomites (D1, four FIAs), newer, less turbid saddle dolomites (D2, four FIAs), and prismatic quartz (PQ/MQ, six FIAs) within two distinct growth zones of the same crystal (Figure 5.5b). Average values for T_h (^{o}C) and salinity (wt% NaCl eq.) are, for D1 and D2 phases, 110-115 and 100-115, and 23-24 and 16-17, respectively. For the quartz phase, inner and outer PQ reveals T_h and salinity of, respectively, 115-120 and 105-115, and 20-22 and 23-24. These data show that T_h decrease with time during crystal formation

for both dolomite and quartz, while salinity decreases for the dolomite but increase for quartz.

W10 XX11m: one chip containing five FIAs in BC to MC phases that occur as vug filling crystals within bioclasts. These cements contain a mixture of monophase (liquid only) and two-phase inclusions that show a broad range of T_h with a distinct peak in the frequency distribution at around 90-105ºC. Salinities are very high (mostly between 20-25wt% NaCl eq.). Despite the observation of growth rims in some calcite crystals, FIs across them do not exhibit changes in T_h values.

W10 XX36m: this sample has abundant FIs in macrocrystalline calcite vein filling (MCv), resulting in the identification of 11 FIAs in a single rock chip. The host rock is a chert with some drusiform MQ, on which a single FI was identified, returning a relatively anomalous T_h (157 ºC) and high salinity (23-24 wt% NaCl eq). The FIs in the MCv crystals reveals an average T_h of 115-120 ºC and high salinities (22-23wt% NaCl eq. First melt temperatures suggest the presence of mixed NaCl-$CaCl_2$ brines and temperatures of hydrohalite melting (T_{hyd}) that provide 17-19 wt% NaCl+$CaCl_2$ eq salinities and NaCl/NaCl+$CaCl_2$ calculated ratios around 0.8 (Naden, 1996).

W13 XX68m: drusiform MQ was the mineral phase investigated in a single chip that contains six FIAs. The average values for T_h (ºC) and salinity (wt% NaCl eq.) are 115-125 and 23-24, respectively. T_h are similar with the inner PQ of sample W02 but has higher salinity. However, the small inclusion size limited the number of T_{ice} determinations.

W18 XX42.2m: this sample has a rather complex aqueous FIs settings due to the complex diagenetic evolution of this in-situ breccia. A single FIA on BD that precedes the calcite phases have average values for T_h and salinity of 100-110 oC and 23-24 wt% (NaCl eq.), respectively. Abundant FIs in replacive BC crystals were observed in nine FIAs and

revealed consistent values of T_h, with temperatures concentrated around 90-100 ºC and high salinity, with average of 23-24 wt% (NaCl eq).

W18 XX48.5m: FIs from prismatic and macrocrystalline quartz (MQ) and calcite as vein filling (MCv). One chip with six FIAs were collected from MCv vein shown in Figure 5.7b. Another chip targeted the prismatic quartz rim (PQ) that bounds the calcite vein (Figure 5.6c), resulting in seven FIAs. Results of FIs in MCv have average within the 95-105ºC range for T_h and 21-23 wt% (NaCl eq) for salinity. Average T_h for MCv is the lowest amongst the hydrothermal mineral phases while salinity is the higher (Figure 5.10). On the other hand, the average T_h for PQ/MQ rims (115-125ºC) are amongst the highest between the three samples with FIs in quartz, with average of 19-21 wt% (NaCl eq) for salinity. The PQ rims also revealed petroleum FIs with pretty erratic T_h results, where the two values are 57 and 111ºC.

C4 Methodology for U-Pb Geochronology Through LA-ICP-MS

Selected samples were cut and a thick (>100 μm) polished sections were mounted on glass and described using conventional transmitted light to access the mineralogical phases. Ideally, conventional thin sections and QEMSCAN imagery of the same sample should be used to ease the mineral identification and recognition of chemical variations.

The targets where chosen based on mineral identification and paragenetic evolution. Conventional and SEM-based QEMSCAN imagery are helpful to identify compositional changes within the same mineral and same crystals. However, most of LA-ICP-MS geochronology on carbonates are preceded by cathodoluminescence imaging. These images will guide the laser spots throughout the analytical routine (Figure B9.3).

In this study, the cold cathode cathodoluminescence (CC-CL) analysis was performed using a NewTec Scientific Cathodyne® system in the Petrography Department of the British Geological Survey (Nottingham, UK). The system is hosted on an adapted Leica 2700 optical microscope with x5 and x10 objectives used for CC-CL imaging and an additional x2.5 objective also available for plain polarised white light (WL) imaging. Whole section and selected large area image mosaics were collected frame by frame using a low light adapted 6Mpixel digital RGB camera system controlled by Cathodyne® software (version 2022.02.03). Stitching of the mosaics was performed using the imageJ plug-in and methodology of Preibisch et al. (2009).

Instrument conditions used during CC-CL analysis were as follows: accelerating voltage 12 kV, beam current 50-70 µA, image exposure time 0.4-2.0 s, gain 1-7.2. Gain is an image processing procedure that increases contrast (1 is a minimum which represents no processing applied); this also increases signal noise so a balance is required between image capture time and gain to provide the best balance of output.

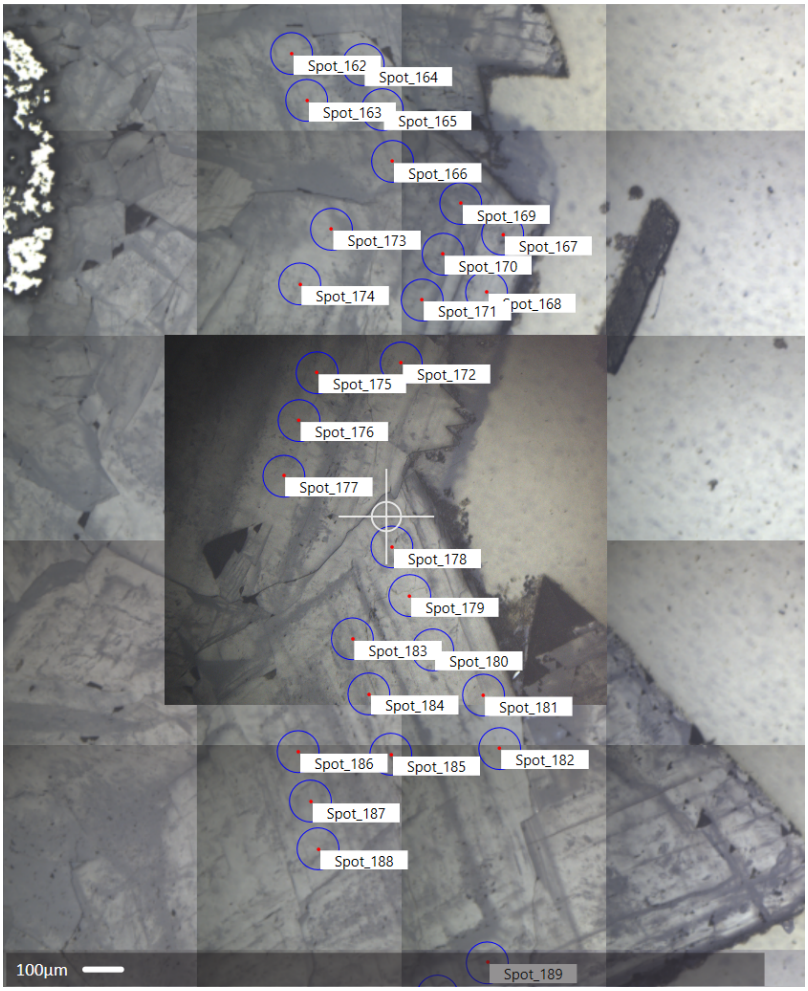


Figure C3. Spots for LA-ICP-MS were chosen based on the SEM imagery built-in the laser ablation cell analysed along with the CL imagery. Notice that spots were positioned within growth rims. In this sample (W14 XX54m) the mineral analysed in saddle ankerite.

U-Pb geochronology via the in-situ Laser Ablation Inductively Coupled Mass Spectrometer (LA-ICP-MS) method was conducted at the Geochronology & Tracers Facility, British Geological Survey (Nottingham, UK). The method utilises an Elemental Scientific Lasers 193nm ImageGeo excimer laser ablation system, fitted with a TV3 cell, coupled to a Nu Instruments Attom single-collector sector-field ICP-MS. The method has been documented in detail by Roberts and Walker (2016) and Roberts et al. (2017). The laser parameters used are 60 to 100 µm static spots (depending on the size of the target phase), at 12 Hz, with a ~3-4 j.cm^2 fluence, for 25 seconds of ablation. Spot sizes were

kept constant between samples and reference materials for each analytical session. Standard sample bracketing uses NIST 614 glass for normalization of $^{207}Pb/^{206}Pb$ ratios (Woodhead & Hergt, 2001), and a carbonate reference material developed in-house for $^{206}Pb/^{238}U$ ratios (WC-1; Roberts et al., 2017). Data are reduced using the time-resolved-analysis function in the Nu Attolab software, and an in-house excel spreadsheet. Normalisation is based on the measured/accepted ratio derived from the session-based drift-corrected (using linear interpolation) mean of the primary WC-1 reference material. No downhole correction is made – the downhole $^{206}Pb/^{238}U$ ratios are flat and linear. No common lead correction is made; ages are determined from lower intercepts on a Tera-Wasserburg plot using IsoplotR (Vermeesch, 2018), using unanchored free regression. Clear outliers in Tera-Wasserburg plots, i.e. statistical outliers, are rejected from the age regressions, and are likely a consequence of analyzing inclusions, different or mixed phases. Resulting ages provided in the summary table have uncertainties quoted as age ± α/β, where α is without systematic uncertainties and β is with these propagated (see Horstwood et al., 2016). The reproducibility of the primary WC-1 reference material is around 1 to 1.5% per session. An estimate of the session reproducibility is propagated (as excess variance) onto the sample data. Additional systematic uncertainties include the decay constant uncertainty and the uncertainty on the reference material age of ~2.5%. Two additional carbonate materials with reported isotope dilution ages in the literature, 'DuffBrown' and 'ASH15' (Figure B9.4), were measured to provide a control on accuracy and precision. An isotope dilution age for DuffBrown of 64.04 ± 0.67 Ma is provided by Hill et al. (2016), the pooled data from these sessions yield an age of 64.01 ± 1.07 Ma (2σ without systematic uncertainties propagated). ASH15D has been measured by several

studies, and Nuriel et al. (2021) provide a recommended age 2.965 ± 0.011 Ma; the pooled data from these sessions provides an age of 2.821 ± 0.129 Ma.

The method uses a calcite reference material to analyse dolomite in addition to calcite; there may be a small bias in the resulting age due to the use of a different matrix (see Guillong et al., 2020). At present, we do not understand how big this bias is, but we expect it to be on the order of a few percent at maximum. This is largely within the uncertainty of the final age data after propagation of systematic uncertainties.

Laboratory & Sample Preparation	
Laboratory name	Geochronology and Tracers Facility
Sample type/mineral	Calcite, Dolomite, Ankerite
Sample preparation	In-situ in polished sections
Imaging	Petrographic and cold-stage CL
Laser Ablation System	
Make, Model & type	ESI 193nm ImageGeo
Ablation cell & volume	TV3
Laser wavelength (nm)	193nm
Pulse width (ns)	3-4ns
Fluence ($J.cm^{-2}$)	~4 $J.cm^{-2}$
Repetition rate (Hz)	12 Hz
Ablation duration (secs)	25 secs
Ablation pit depth / ablation rate	~35 µm pit depth estimated
Spot size (µm)	60, 70, 80 or 100 µm
Sampling mode / pattern	Static spot ablation
Carrier gas	100% He, Ar make-up gas combined ca. 50% along sample line
Cell carrier gas flow (l/min)	0.5 l/min

ICP-MS Instrument	
Make, Model & type	Nu Instruments Attom SC-SF-ICP-MS
Sample introduction	Free air aspiration of desolvator
RF power (W)	1300W
Make-up gas flow (l/min)	0.8 l/min Ar
Detection system	Discrete dynode MassCom ion counter
Masses measured	206, 207, 208, 232, 238
Integration time per peak	200 μs (208, 232), 600 μs (206), 1000 μs (207, 238) 100 sweeps per integration
Total integration time per reading (secs)	~0.3 seconds
Sensitivity / Efficiency (%, element)	~0.2 % for Uranium
IC Dead time (ns)	11 ns
Data Processing	
Gas blank	60 second on-peak zero subtracted
Calibration strategy	NIST614 for Pb-Pb, WC-1 for Pb-U
Reference Material info	Primary: WC-1 254 +/- 6 Ma (2σ) - Roberts et al., 2017 Secondary: Duff Brown 64.04 +/- 0.67 Ma (2σ) - Hill et al., 2016 ASH15D 2.965 ± 0.011 Ma (2σ) - Nuriel et al., 2021
Data processing package used Correction for LIEF	Nu Instruments TRA acquisition software, in-house spreadsheet data processing
Mass discrimination	$^{207}Pb/^{206}Pb$, $^{206}Pb/^{238}U$ normalised to reference materials
Common-Pb correction, composition and uncertainty	Unanchored (model 1) regressions in Tera-Wasserburg (Semi Total-Pb) plots IsoplotR for calculation
Uncertainty level & propagation	Ages in the summary data table are quoted at 2σ absolute and include systematic uncertainties, propagation is by quadratic addition
Quality control / Validation	Duff Brown over the course of the sample analytical sessions gave 64.01 ± 1.07 Ma (2σ), n=8-, MSWD = 3.9 (without propagation of systematic uncertainties). ASH15D gave 2.821 ± 0.129 Ma (2σ) n=62, MSWD = 2.2.

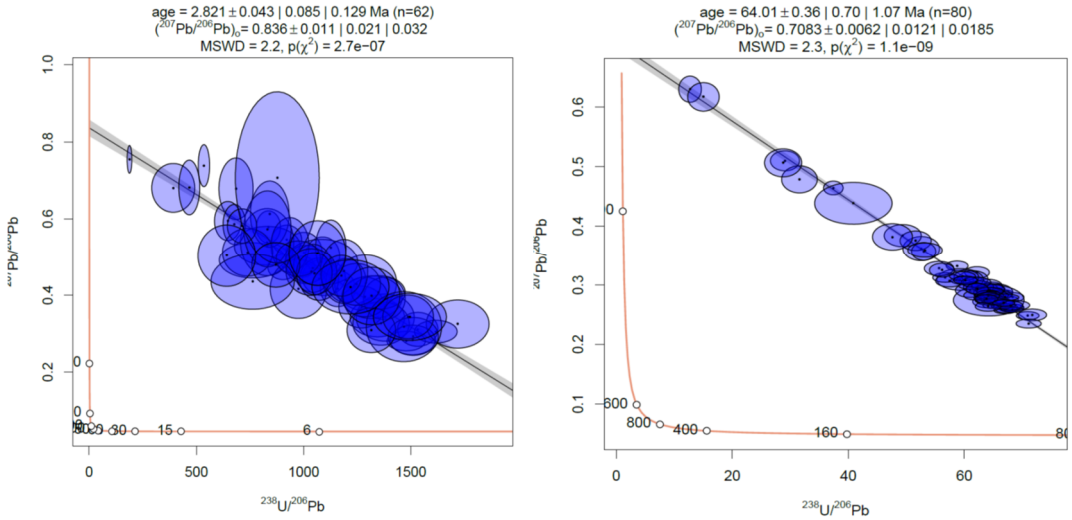


Figure C4: Tera-Wasserburg plot for secondary reference material ASH15 (left) and DuffBrown (right) and data combined from the analytical sessions. Error ellipses are shown at 2σ. Results do not include propagation of systematic uncertainties.

References

Abarca, E., Idiart, A., Grandia, F., Rodríguez-Morillas, N., Pellan, C., Zen, M., Aït-Ettajer, T. & Fontanelli, L. (2019) 3d Reactive Transport Modeling of Porosity Evolution in a Carbonate Reservoir through Dolomitization. *Chemical Geology*, **513,** 184-199.

Alkmim, F.F., Marshak, S., Pedrosa-Soares, A.C., Peres, G.G., Cruz, S.C.P. & Whittington, A. (2006) Kinematic Evolution of the Araçuaí-West Congo Orogen in Brazil and Africa: Nutcracker Tectonics During the Neoproterozoic Assembly of Gondwana. *Precambrian Research*, **149,** 43-64.

Almeida, F.F.M., Hasui, Y., Brito Neves, B.B. & Fuck, R.A. (1981) Brazilian Structural Provinces: An Introduction. *Earth-Science Reviews*, **17,** 1-29.

Almeida, J., Tupinambá, M., Heilbron, M. & Trouw, R.A.J. (1998). *Geometric and Kinematic Analysis at the Central Tectonic Boundary of the Ribeira Belt, Southeastern Brazil*. Congresso Brasileiro de Geologia, 40, Belo Horizonte, Sociedade Brasileira de Geologia.

Almeida, J., Dios, F., Mohriak, W.U., Valeriano, C.D.M., Heilbron, M., Eirado, L.G. & Tomazzoli, E. (2013) Pre-Rift Tectonic Scenario of the Eo-Cretaceous Gondwana Break-up Along Se Brazil–Sw Africa: Insights from Tholeiitic Mafic Dyke Swarms. *Geological Society, London, Special Publications*, **369,** 11-40.

Almeida, J., Heilbron, M., Guedes, E., Neubauer, F., Manfred, B., Klausen, M.B., de Morisson Valeriano, C., Bruno, H., Giro, J.P. & McMaster, M. (2021) Pre-to-Syn-Rift Tholeiitic Magmatism in a Transtensive Hyperextended Continental Margin: Onshore

and Offshore Magmatism of the Campos Basin, Se Brazil. *Journal of South American Earth Sciences*, **108,** 103218.

Alvarenga, R., Iacopini, D., Kuchle, J., Scherer, C. & Goldberg, K. (2016) Seismic Characteristics and Distribution of Hydrothermal Vent Complexes in the Cretaceous Offshore Rift Section of the Campos Basin, Offshore Brazil. *Marine and Petroleum Geology*, **74,** 12-25.

Alvarenga, R., Kuchle, J., Iacopini, D., Goldberg, K., Scherer, C., Pantopoulos, G. & Ene, P.L. (2021) Tectonic and Stratigraphic Evolution Based on Seismic Sequence Stratigraphy: Central Rift Section of the Campos Basin, Offshore Brazil. *Geosciences*, **11,** 338.

Alvarez, P., Araüjo, A., Stanton, N., Oliveira, J., Ferro, R., Iemma, M., Nascimento, I. & Borghi, L. (2021). *Crustal Features and Transfer Zone of Campos Basin: A Review and Evaluation*. Second EAGE Conference on Pre-Salt Reservoir, European Association of Geoscientists & Engineers.

Alves, T., Fetter, M., Lima, C., Cartwright, J.A., Cosgrove, J., Gangá, A., Queiroz, C.L. & Strugale, M. (2017) An Incomplete Correlation between Pre-Salt Topography, Top Reservoir Erosion, and Salt Deformation in Deep-Water Santos Basin (Se Brazil). *Marine and Petroleum Geology*, **79,** 300-320.

Alves, T., Fetter, M., Busby, C., Gontijo, R., Cunha, T.A. & Mattos, N.H. (2020) A Tectono-Stratigraphic Review of Continental Breakup on Intraplate Continental Margins and Its Impact on Resultant Hydrocarbon Systems. *Marine and Petroleum Geology*, **117,** 104341.

Araujo, M.N., Perez-Gussinye, M. & Mushaldev, I. (2022) Oceanward Rift Migration During Formation of Santos-Benguela Ultra-Wide Rifted Margin. *Geological Society, London, Special Publications*, **524**.

Armelenti, G., Goldberg, K., Kuchle, J. & De Ros, L. (2016) Deposition, Diagenesis and Reservoir Potential of Non-Carbonate Sedimentary Rocks from the Rift Section of Campos Basin, Brazil. *Petroleum Geoscience*, **22,** 223-239.

Artyushkov, E. (1973) Stresses in the Lithosphere Caused by Crustal Thickness Inhomogeneities. *Journal of Geophysical Research*, **78,** 7675-7708.

Aslanian, D., Moulin, M., Olivet, J.-L., Unternehr, P., Matias, L., Bache, F., Rabineau, M., Nouzé, H., Klingelheofer, F., Contrucci, I. & Labails, C. (2009) Brazilian and African

Passive Margins of the Central Segment of the South Atlantic Ocean: Kinematic Constraints. *Tectonophysics*, **468,** 98-112.

Assumpcao, M. (1992) The Regional Intraplate Stress Field in South America. *Journal of Geophysical Research: Solid Earth*, **97,** 11889-11903.

Barnett, A.J., Fu, L., Rapasi, T., Scotellaro, C., Guha, J., Cabolova, A. & Domingues, A.L. (2021) Seismic Characterization and Origin of Clinoforms in Lacustrine Depositional Environments: A Case Study from the Cretaceous of the South Atlantic. *Geological Society, London, Special Publications*, **509,** 127-145.

Baumgarten, C.S., Dultra, A.J.C., Scuta, M.d.S., Figueiredo, M.V.L. & Sequeira, M.F.P.B. (1988) Coquinas Da Formação Lagoa Feia, Bacia De Campos: Evolução Da Geologia De Desenvolvimento. *Boletim de Geociências da Petrobras*, **2,** 27-36.

Benjakul, R., Hollis, C., Robertson, H.A., Sonnenthal, E.L. & Whitaker, F.F. (2020) Understanding Controls on Hydrothermal Dolomitisation: Insights from 3d Reactive Transport Modelling of Geothermal Convection. *Solid Earth*, **11,** 2439-2461.

Bertani, R.T. & Carozzi, A.V. (1985a) Lagoa Feia Formation (Lower Cretaceous) Campos Basin, Offshore Brazil: Rift Valley Type Lacustrine Carbonate Reservoirs—Ii. *Journal of Petroleum Geology*, **8,** 199-220.

Bertani, R.T. & Carozzi, A.V. (1985b) Lagoa Feia Formation (Lower Cretaceous) Campos Basin, Offshore Brazil: Rift Valley Type Lacustrine Carbonate Reservoirs - I. *Journal of Petroleum Geology*, **8,** 37-58.

Bezerra, F.H., do Nascimento, A.F., Ferreira, J.M., Nogueira, F.C., Fuck, R.A., Neves, B.B.B. & Sousa, M.O. (2011) Review of Active Faults in the Borborema Province, Intraplate South America—Integration of Seismological and Paleoseismological Data. *Tectonophysics*, **510,** 269-290.

Bezerra, F.H., Balsamo, F., Corsi, G., Legrand, J.M., Sousa, M.O., Nogueira, F.C., Salvioli-Mariani, E. & Menezes, C.P. (2021) Hydrothermal Silicification in the Intraplate Samambaia Seismogenic Fault, Brazil: Implications for Fault Loss of Cohesion and Healing in Rifted Crust. *Tectonophysics*, **815,** 229002.

Bird, P.C., Cartwright, J.A. & Davies, T.L. (2014) Basement Reactivation in the Development of Rift Basins: An Example of Reactivated Caledonide Structures in the West Orkney Basin. *Journal of the Geological Society*, **172,** 77-85.

Bischoff, J.L., Stine, S., Rosenbauer, R.J., Fitzpatrick, J.A. & Stafford Jr, T.W. (1993) Ikaite Precipitation by Mixing of Shoreline Springs and Lake Water, Mono Lake, California, USA. *Geochimica et cosmochimica acta*, **57,** 3855-3865.

Bjørlykke, K. (1999) An Overview of Factors Controlling Rates of Compaction, Fluid Generation and Flow in Sedimentary Basins. In: *Growth, Dissolution Pattern Formation in Geosystems* (Ed. by J. B. & M. P.), 381-404. Springer Dordrecht.

Bosworth, W. (1994) A Model for the Three-Dimensional Evolution of Continental Rift Basins, North-East Africa. *J Geologische Rundschau*, **83,** 671-688.

Brito Neves, B.B., Campos Neto, M.C. & Fuck, R.A. (1999) From Rodinia to Western Gondwana: An Approach to the Brasiliano-Pan African Cycle and Orogenic Collage. *Episodes*, **22,** 155-166.

Bruhn, C.H. & Walker, R.G. (1995) High-Resolution Stratigraphy and Sedimentary Evolution of Coarse-Grained Canyon-Filling Turbidites from the Upper Cretaceous Transgressive Megasequence, Campos Basin, Offshore Brazil. *Journal of Sedimentary Research*, **65,** 426-442.

Bühn, B., Pimentel, M.M., Matteini, M. & Dantas, E.L. (2009) High Spatial Resolution Analysis of Pb and U Isotopes for Geochronology by Laser Ablation Multi-Collector Inductively Coupled Plasma Mass Spectrometry (La-Mc-Icp-Ms). *Anais da Academia Brasileira de Ciências*, **81,** 99-114.

Burisch, M., Markl, G. & Gutzmer, J. (2022). Breakup with benefits-hydrothermal mineral systems related to the disintegration of a supercontinent. *Earth and Planetary Science Letters*, **580,** 117373.

Bustillo, M.Á. (2010) Silicification of Continental Carbonates. *Developments in Sedimentology*, **62,** 153-178.

Cainelli, C. & Mohriak, W.U. (1999) Some Remarks on the Evolution of Sedimentary Basins Along the Eastern Brazilian Continental Margin. *Episodes*, **22,** 206-216.

Calegari, S.S., Neves, M.A., Guadagnin, F., França, G.S. & Vincentelli, M.G.C. (2016) The Alegre Lineament and Its Role over the Tectonic Evolution of the Campos Basin and Adjacent Continental Margin, Southeastern Brazil. *Journal of South American Earth Sciences*, **69,** 226-242.

Cantrell, D., Swart, P. & Hagerty, R. (2004) Genesis and Characterization of Dolomite, Arab-D Reservoir, Ghawar Field, Saudi Arabia. *GeoArabia*, **9,** 11-36.

Carminatti, M., Wolff, B. & Gamboa, L. (2008). *New Exploratory Frontiers in Brazil*. 19th World Petroleum Congress, Madrid, Spain, Society of Petroleum Engineers.

Carmo, I., Schmitt, R., Araújo, M. & Romeiro, M. (2017). *Evidence for the Paleoproterozoic/Cambrian Angolan Belt in the Brazilian Margins–New Data from Offshore Basement Drill Core*. 5th Conjugate Margins Conference, Porto de Galinhas - Brazil.

Cartwright, J. (1991) The Kinematic Evolution of the Coffee Soil Fault. *Geological Society, London, Special Publications*, **56,** 29-40.

Cartwright, J., Bouroullec, R., James, D. & Johnson, H. (1998) Polycyclic Motion History of Some Gulf Coast Growth Faults from High-Resolution Displacement Analysis. *Geology*, **26,** 819-822.

Carvalho, A.S.G. & De Ros, L.F. (2015) Diagenesis of Aptian Sandstones and Conglomerates of the Campos Basin. *Journal of Petroleum Science and Engineering*, **125,** 189-200.

Catuneanu, O. (2006) *Principles of Sequence Stratigraphy*. Elsevier.

Cavalcante, C., Fossen, H., Almeida, R.P.d., Hollanda, M.H.B.M. & Egydio-Silva, M. (2019) Reviewing the Puzzling Intracontinental Termination of the Araçuaí-West Congo Orogenic Belt and Its Implications for Orogenic Development. *Precambrian Research*, **322,** 85-98.

Ceraldi, T.S. & Green, D. (2017) Evolution of the South Atlantic Lacustrine Deposits in Response to Early Cretaceous Rifting, Subsidence and Lake Hydrology. *Geological Society, London, Special Publications*, **438,** 77-98.

Chang, H.K., Kowsmann, R.O., Figueiredo, A.M.F. & Bender, A.A. (1992) Tectonics and Stratigraphy of the East Brazil Rift System: An Overview. *Tectonophysics*, **213,** 97-138.

Childs, C., Manzocchi, T., Walsh, J.J., Bonson, C.G., Nicol, A. & Schöpfer, M.P. (2009) A Geometric Model of Fault Zone and Fault Rock Thickness Variations. *Journal of Structural Geology*, **31,** 117-127.

Choquette, P. & James, N. (1987) Diagenesis in Limestones: The Deep Burial Environment. *Geoscience Canada*, **14,** 3-35.

Clendenin, C. & Duane, M. (1990) Focused Fluid Flow and Ozark Mississippi Valley-Type Deposits. *Geology*, **18,** 116-119.

Clerc, C., Ringenbach, J.-C., Jolivet, L. & Ballard, J.-F. (2018) Rifted Margins: Ductile Deformation, Boudinage, Continentward-Dipping Normal Faults and the Role of the Weak Lower Crust. *Gondwana Research*, **53,** 20-40.

Cobbold, P.R. & Szatmari, P. (1991) Radial Gravitational Gliding on Passive Margins. *Tectonophysics*, **188,** 249-289.

Cobbold, P.R., Meisling, K.E. & Mount, V.S. (2001) Reactivation of an Obliquely Rifted Margin, Campos and Santos Basins, Southeastern Brazil. *AAPG Bulletin*, **85,** 1925-1944.

Cobbold, P.R., Rossello, E.A., Roperch, P., Arriagada, C., Gómez, L.A. & Lima, C. (2007) Distribution, Timing, and Causes of Andean Deformation across South America. *Geological Society, London, Special Publications*, **272,** 321-343.

Collanega, L., Siuda, K., Jackson, C.A.-L., Bell, R.E., Coleman, A.J., Lenhart, A., Magee, C. & Breda, A. (2019) Normal Fault Growth Influenced by Basement Fabrics: The Importance of Preferential Nucleation from Pre-Existing Structures. *Basin Research*, **31,** 659-687.

Consonni, A., Frixa, A. & Maragliulo, C. (2018) Hydrothermal Dolomitization: Simulation by Reaction Transport Modelling. *Geological Society, London, Special Publications*, **435,** 235-244.

Corbella, M., Ayora, C. & Cardellach, E. (2004) Hydrothermal Mixing, Carbonate Dissolution and Sulfide Precipitation in Mississippi Valley-Type Deposits. *Mineralium Deposita*, **39,** 344-357.

Corbella, M., Gomez-Rivas, E., Martín-Martín, J.D., Stafford, S.L., Teixell, A., Griera, A., Travé, A., Cardellach, E. & Salas, R. (2014) Insights to Controls on Dolomitization by Means of Reactive Transport Models Applied to the Benicàssim Case Study (Maestrat Basin, Eastern Spain). *Petroleum Geoscience*, **20,** 41-54.

Corrêa, R.S., Ukar, E., Laubach, S.E., Aubert, I., Lamarche, J., Wang, Q., Stockli, D., Stockli, L. & Larson, T. (2022). Episodic reactivation of carbonate fault zones with implications for permeability–An example from Provence, Southeast France. *Marine and Petroleum Geology***,** 105905.

Cosentino, L. (2001) *Integrated Reservoir Studies*. Editions Technip.

Cosgrove, J.W. (2001) Hydraulic Fracturing During the Formation and Deformation of a Basin: A Factor in the Dewatering of Low-Permeability Sediments. *AAPG Bulletin*, **85,** 737-748.

Creaser, R.A., Sannigrahi, P., Chacko, T. & Selby, D. (2002) Further Evaluation of the Re-Os Geochronometer in Organic-Rich Sedimentary Rocks: A Test of Hydrocarbon Maturation Effects in the Exshaw Formation, Western Canada Sedimentary Basin. *Geochimica et cosmochimica acta*, **66,** 3441-3452.

Cross, N.E. & Burchette, T.P. (2022). *Discrete Zones of Elevated Permeability (Dzep) in Middle Eastern Carbonate Reservoirs – Causes and Consequences*. Development and Production Geology of Carbonate Reservoirs, London, The Geological Society - London.

Daly, M.C., Chorowicz, J. & Fairhead, J.D. (1989) Rift Basin Evolution in Africa: The Influence of Reactivated Steep Basement Shear Zones. *Geological Society, London, Special Publications*, **44,** 309-334.

Davies, G.R. & Smith Jr, L.B. (2006) Structurally Controlled Hydrothermal Dolomite Reservoir Facies: An Overview. *AAPG Bulletin*, **90,** 1641-1690.

Davison, I. (2007) Geology and Tectonics of the South Atlantic Brazilian Salt Basins. *Geological Society, London, Special Publications*, **272,** 345-359.

Dehler, N.M., Magnavita, L.P., Gomes, L.C., Rigoti, C.A., de Oliveira, J.A.B., Sant'Anna, M.V. & Costa, F.G.D. (2016) The 'Helmut' geophysical Anomaly: A Regional Left-Lateral Transtensional Shear Zone System Connecting Santos and Campos Basins, Southeastern Brazil. *Marine and Petroleum Geology*, **72,** 412-422.

Dekov, V., Egueh, N., Kamenov, G., Bayon, G., Lalonde, S.V., Schmidt, M., Liebetrau, V., Munnik, F., Fouquet, Y. & Tanimizu, M. (2014) Hydrothermal Carbonate Chimneys from a Continental Rift (Afar Rift): Mineralogy, Geochemistry, and Mode of Formation. *Chemical Geology*, **387,** 87-100.

Deng, C., Gawthorpe, R.L., Fossen, H. & Finch, E. (2018) How Does the Orientation of a Preexisting Basement Weakness Influence Fault Development During Renewed Rifting? Insights from Three-Dimensional Discrete Element Modeling. *Tectonics*, **37,** 2221-2242.

Dewit, J., Foubert, A., El Desouky, H., Muchez, P., Hunt, D., Vanhaecke, F. & Swennen, R. (2014) Characteristics, Genesis and Parameters Controlling the Development of a Large Stratabound Htd Body at Matienzo (Ramales Platform, Basque–Cantabrian Basin, Northern Spain). *Marine and Petroleum Geology*, **55,** 6-25.

Dias, J.L., Oliveira, J.Q. & Vieira, J.C. (1988) Sedimentological and Stratigraphic Analysis of the Lagoa Feia Formation, Rift Phase of Campos Basin, Offshore Brazil. *Brazilian Journal of Geology*, **18,** 252-260.

Dickson, J.A.D. (1965) A Modified Staining Technique for Carbonates in Thin Section. *Nature*, **205,** 587-587.

Duffy, O.B., Bell, R.E., Jackson, C.A.-L., Gawthorpe, R.L. & Whipp, P.S. (2015) Fault Growth and Interactions in a Multiphase Rift Fault Network: Horda Platform, Norwegian North Sea. *Journal of Structural Geology*, **80,** 99-119.

Ebert, H.D. & Hasui, Y. (1998) Transpressional Tectonics and Strain Partitioning During Oblique Collision between Three Plates in the Precambrian of Southeast Brazil. *Geological Society, London, Special Publications*, **135,** 231-252.

Egydio-Silva, M., Vauchez, A., Fossen, H., Cavalcante, G.C.G. & Xavier, B.C. (2018) Connecting the Araçuaí and Ribeira Belts (Se–Brazil): Progressive Transition from Contractional to Transpressive Strain Regime During the Brasiliano Orogeny. *Journal of South American Earth Sciences*, **86,** 127-139.

Eichhubl, P. & Boles, J.R. (2000) Rates of Fluid Flow in Fault Systems; Evidence for Episodic Rapid Fluid Flow in the Miocene Monterey Formation, Coastal California. *American Journal of Science*, **300,** 571-600.

Eldrett, J.S., Bergman, S.C., Heine, Edwards, C.P., Jakeman, M., Miles, N., Bastian, H., Bohaty, S.M., Wilding, M.R. (2023) Integrated bio-and chemo-stratigraphy for Early Cretaceous strata offshore Gabon: Additional constraints on the timing of salt deposition and rifting of the South Atlantic. *Marine and Petroleum Geology*, **148**.

Everett, C., Wilkinson, J. & Rye, D. (1999) Fracture-Controlled Fluid Flow in the Lower Palaeozoic Basement Rocks of Ireland: Implications for the Genesis of Irish-Type Zn-Pb Deposits. *Geological Society, London, Special Publications*, **155,** 247-276.

Farias, F., Szatmari, P., Bahniuk, A. & Franca, A.B. (2019) Evaporitic Carbonates in the Pre-Salt of Santos Basin–Genesis and Tectonic Implications. *Marine and Petroleum Geology*, **105,** 251-272.

Fazlikhani, H., Fossen, H., Gawthorpe, R.L., Faleide, J.I. & Bell, R.E. (2017) Basement Structure and Its Influence on the Structural Configuration of the Northern North Sea Rift. *Tectonics*, **36,** 1151-1177.

Fetter, M. (2009) The Role of Basement Tectonic Reactivation on the Structural Evolution of Campos Basin, Offshore Brazil: Evidence from 3d Seismic Analysis and Section Restoration. *Marine and Petroleum Geology*, **26,** 873-886.

Fetter, M., Penteado, H., Madrucci, V. & Spadini, A. (2018). *The Paleogeography of the Lacustrine Rift System of the Pre-Salt in Santos Basin, Offshore Brazil*. Annual Convention and Exhibition, AAPG.

Fossen, H. & Rørnes, A. (1996) Properties of Fault Populations in the Gullfaks Field, Northern North Sea. *Journal of Structural Geology*, **18,** 179-190.

Fossen, H., Khani, H.F., Faleide, J.I., Ksienzyk, A.K. & Dunlap, W.J. (2017) Post-Caledonian Extension in the West Norway–Northern North Sea Region: The Role of Structural Inheritance. *Geological Society, London, Special Publications*, **439,** 465-486.

França, R.L., Del Rey, A.C., Tagliari, C.V., Brandão, J.R. & Fontanelli, P.d.R. (2007) Bacia Do Espírito Santo. *Boletim de Geociências da Petrobras*, **15,** 501-509.

Gamboa, L.A.P. & Rabinowitz, P.D. (1981) The Rio Grande Fracture Zone in the Western South Atlantic and Its Tectonic Implications. *Earth and Planetary Science Letters*, **52,** 410-418.

Ganade, C.E., Cioffi, C.R., Machado, J.P., Miranda, T., Lopes, L.B., Weinberg, R.F., Celestino, M.A., Carvalho, B., Guillong, M. & Roberts, N.M.W. (2022) Recurrent Tectonic Activity in Northeastern Brazil During Pangea Breakup: Constraints from U-Pb Carbonate Dating. *Geology*, **50,** 969-974.

Garcia-Fresca, B., Gabellone, T. & Whitake, F. (2019). *Reactive Transport Modeling Approach to Studying Silicification of Carbonates*. AAPG Annual Convention and Exhibition, San Antonio, TX, USA.

Garven, G., Ge, S., Person, M. & Sverjensky, D. (1993) Genesis of Stratabound Ore Deposits in the Midcontinent Basins of North America; 1, the Role of Regional Groundwater Flow. *American Journal of Science*, **293,** 497-568.

Gawthorpe, R.L. & Leeder, M.R. (2008) Tectono-Sedimentary Evolution of Active Extensional Basins. *Basin Research*, **12,** 195-218.

Goldberg, K., Kuchle, J., Scherer, C., Alvarenga, R., Ene, P.L., Armelenti, G. & De Ros, L.F. (2017) Re-Sedimented Deposits in the Rift Section of the Campos Basin. *Marine and Petroleum Geology*, **80,** 412-431.

Goldstein, R.H. & Reynolds, T.J. (1994) Systematics of Fluid Inclusions in Diagenetic Minerals. *SEPM Short Course*, **31**.

Gomes, A.S. & Vasconcelos, P.M. (2021) Geochronology of the Paraná-Etendeka Large Igneous Province. *Earth Science Reviews*, **220,** 103716.

Gomes, J.P., Bunevich, R., Tedeschi, L., Tucker, M. & Whitaker, F. (2020) Facies Classification and Patterns of Lacustrine Carbonate Deposition of the Barra Velha Formation, Santos Basin, Brazilian Pre-Salt. *Marine and Petroleum Geology*, **113,** 104176.

Gomez-Rivas, E., Corbella, M., Martín-Martín, J., Stafford, S., Teixell, A., Bons, P., Griera, A. & Cardellach, E. (2014) Reactivity of Dolomitizing Fluids and Mg Source Evaluation of Fault-Controlled Dolomitization at the Benicassim Outcrop Analogue (Maestrat Basin, E Spain). *Marine and Petroleum Geology*, **55,** 26-42.

Guardado, L.R., Gamboa, L.A.P. & Lucchesi, C.F. (1989a) Petroleum Geology of the Campos Basin, Brazil, a Model for a Producing Atlantic Type Basin: Part 2. In: *Memoir 48* (Ed. by J. D. Edwards & P. A. Santogrossi), **48**, 37-79. AAPG, Tulsa.

Guardado, L.R., Gamboa, L.A.P. & Lucchesi, C.F. (1989b) Petroleum Geology of the Campos Basin, Brazil, a Model for a Producing Atlantic Type Basin: Part 1. In: *Memoir 48* (Ed. by J. D. Edwards & P. A. Santogrossi), **48**, 3-36. AAPG, Tulsa.

Guardado, L.R., Spadini, A., Brandão, J. & Mello, M.R. (2000) Petroleum System of the Campos Basin, Brazil. In: *Memoir 73* (Ed. by M. R. Mello & B. J. Katz), **48**, 317-324. AAPG, Tulsa.

Gupta, S., Cowie, P.A., Dawers, N.H. & Underhill, J.R. (1998) A Mechanism to Explain Rift-Basin Subsidence and Stratigraphic Patterns through Fault-Array Evolution. *Geology*, **26,** 595-598.

Hall, W.S., Stein, H.J., Kylander-Clark, A.R.C., Hitzman, M.W., Kuiper, Y.D., Knight, C. & Enders, M.S. (2021). Diagenetic and Epigenetic Mineralizing Events in the Kalahari Copperbelt, Botswana: Evidence from Re-Os Sulfide Dating and U-Th-Pb Xenotime Geochronology. *Economic Geology*, **116,** 863-881

Heilbron, M., Valeriano, C.M., Tassinari, C.C.G., Almeida, J., Tupinambá, M., Siga, O. & Trouw, R. (2008) Correlation of Neoproterozoic Terranes between the Ribeira Belt, Se Brazil and Its African Counterpart: Comparative Tectonic Evolution and Open Questions. *Geological Society, London, Special Publications*, **294,** 211-237.

Heine, C., Zoethout, J. & Müller, R.D. (2013) Kinematics of the South Atlantic Rift. *Solid Earth*, **4,** 215-253.

Herlinger Jr., R., Zambonato, E.E. & De Ros, L.F. (2017) Influence of Diagenesis on the Quality of Lower Cretaceous Pre-Salt Lacustrine Carbonate Reservoirs from Northern Campos Basin, Offshore Brazil. *Journal of Sedimentary Research*, **87,** 1285-1313.

Hesse, R. (1989) Silica Diagenesis: Origin of Inorganic and Replacement Cherts. **26,** 253-284.

Hesthammer, J. & Fossen, H. (1999) Evolution and Geometries of Gravitational Collapse Structures with Examples from the Statfjord Field, Northern North Sea. *Marine and Petroleum Geology*, **16,** 259-281.

Hirani, J., Bastesen, E., Boyce, A., Corlett, H., Gawthorpe, R., Hollis, C., John, C.M., Robertson, H., Rotevatn, A. & Whitaker, F. (2018) Controls on the Formation of Stratabound Dolostone Bodies, Hammam Faraun Fault Block, Gulf of Suez. *Sedimentology*, **65,** 1973-2002.

Hitzman, M.W. & Beaty, D.W. (1996) The Irish Zn-Pb-(Ba) Orefield. In: *Carbonate-Hosted Lead-Zinc Deposits: 75th Anniversary Volume* (Ed. by Society of Economic Geologists.

Hitzman, M.W., Redmond, P.B. & Beaty, D.W. (2002) The Carbonate-Hosted Lisheen Zn-Pb-Ag Deposit, County Tipperary, Ireland. *Economic Geology*, **97,** 1627-1655.

Hnatyshin, D. (2018) Development and Application of the Re-Os Isotope System to Sediment-Hosted Zn-Pb Ores and Sedimentary Pore Waters, University of Alberta.

Hnatyshin, D., Creaser, R.A., Meffre, S., Stern, R.A., Wilkinson, J.J. & Turner, E.C. (2020) Understanding the Microscale Spatial Distribution and Mineralogical Residency of Re in Pyrite: Examples from Carbonate-Hosted Zn-Pb Ores and Implications for Pyrite Re-Os Geochronology. *Chemical Geology*, **533,** 119427.

Hoefs, J. (1997) *Stable Isotope Geochemistry*, 8th edn. Springer.

Hollanda, M.H.B.M., Archanjo, C.J., Macedo Filho, A.A., Fossen, H., Ernst, R.E., de Castro, D.L., Melo, A.C., and Oliveira, A.L., 2019, The Mesozoic Equatorial Atlantic Magmatic Province (EQUAMP): A new large igneous province in South America, In Srivastava, R.K., et al., eds., *Dyke Swarms of the World: A Modern Perspective*. Singapore, Springer, p. 87–110.

Hollis, C., Bastesen, E., Boyce, A., Corlett, H., Gawthorpe, R., Hirani, J., Rotevatn, A. & Whitaker, F. (2017) Fault-Controlled Dolomitization in a Rift Basin. *Geology*, **45,** 219-222.

Immenhauser, A. (2022) On the Delimitation of the Carbonate Burial Realm. *The Depositional Record*, **8,** 524-574.

Kallweit, R. & Wood, L. (1982) The Limits of Resolution of Zero-Phase Wavelets. *Geophysics*, **47,** 1035-1046.

Karner, G.D. & Gambôa, L.A.P. (2007) Timing and Origin of the South Atlantic Pre-Salt Sag Basins and Their Capping Evaporites. *Geological Society, London, Special Publications*, **285,** 15-35.

Kelly, P., Peacock, D., Sanderson, D. & McGurk, A. (1999) Selective Reverse-Reactivation of Normal Faults, and Deformation around Reverse-Reactivated Faults in the Mesozoic of the Somerset Coast. *Journal of Structural Geology*, **21,** 493-509.

Klimchouk, A.B. (2009) Morphogenesis of Hypogenic Caves. *Geomorphology*, **106,** 100-117.

Klimchouk, A.B. (2012) Hypogene Speleogenesis. In: *Encyclopedia of Caves* (Ed. by W. B. White & D. C. Colver), 945. Elsevier Science & Technology, Amsterdam.

Klimchouk, A.B. (2015) The Karst Paradigm: Changes, Trends and Perspectives. *Acta Carsologica*, **44**.

Konstantinovskaya, E.A., Harris, L.B., Poulin, J. & Ivanov, G.M. (2007) Transfer Zones and Fault Reactivation in Inverted Rift Basins: Insights from Physical Modelling. *Tectonophysics*, **441,** 1-26.

Kuchle, J., dos Santos Scherer, C.M., Born, C.C., dos Santos Alvarenga, R. & Adegas, F. (2011) A Contribution to Regional Stratigraphic Correlations of the Afro-Brazilian Depression–the Dom João Stage (Brotas Group and Equivalent Units–Late Jurassic) in Northeastern Brazilian Sedimentary Basins. *Journal of South American Earth Sciences*, **31,** 358-371.

Kukla, P.A., Strozyk, F. & Mohriak, W.U. (2018) South Atlantic Salt Basins–Witnesses of Complex Passive Margin Evolution. *Gondwana Research*, **53,** 41-57.

Kyne, R., Torremans, K., Güven, J., Doyle, R. & Walsh, J. (2019) 3-D Modeling of the Lisheen and Silvermines Deposits, County Tipperary, Ireland:Insights into Structural Controls on the Formation of Irish Zn-Pb Deposits. *Economic Geology*, **114,** 93-116.

Lambiase, J.J. (1990) A Model for Tectonic Control of Lacustrine Stratigraphic Sequences in Continental Rift Basins. *AAPG Memoir*, **50,** 11.

Lander, R. & Laubach, S. (2015) Insights into Rates of Fracture Growth and Sealing from a Model for Quartz Cementation in Fractured Sandstones. *Geological Society of America Bulletin*, **127,** 516-538.

Laubach, S.E., Eichhubl, P., Hilgers, C. & Lander, R. (2010) Structural Diagenesis. *Journal of Structural Geology*, **32,** 1866-1872.

Laubach, S.E., Lander, R., Criscenti, L.J., Anovitz, L.M., Urai, J., Pollyea, R.M., Hooker, J.N., Narr, W., Evans, M.A. & Kerisit, S.N. (2019) The Role of Chemistry in Fracture Pattern Development and Opportunities to Advance Interpretations of Geological Materials. *Reviews of Geophysics*, **57,** 1065-1111.

Lavier, L.L. & Manatschal, G. (2006) A Mechanism to Thin the Continental Lithosphere at Magma-Poor Margins. *Nature*, **440,** 324-328.

Lawson, M., Sitgreaves, J., Rasbury, T., Wooton, K., Esch, W., Marcon, V., Henares, S., Konstantinou, A., Kneller, E. & Gombosi, D. (2022) New Age and Lake Chemistry Constraints on the Aptian Pre-Salt Carbonates of the Central South Atlantic. *GSA Bulletin*.

Leach, D.L., Bradley, D., Lewchuk, M.T., Symons, D.T., de Marsily, G. & Brannon, J. (2001) Mississippi Valley-Type Lead–Zinc Deposits through Geological Time: Implications from Recent Age-Dating Research. **36,** 711-740.

Leach, D.L., Sangster, D.F., Kelley, K.D., Large, R.R., Garven, G., Allen, C.R., Gutzmer, J., Walters, S., Hedenquist, J.W., Thompson, J.F.H., Goldfarb, R.J. & Richards, J.P. (2005) Sediment-Hosted Lead-Zinc Deposits: A Global Perspective. *Economic Geology*, **100,** 561-607.

Lenhart, A., Jackson, C.A.-L., Bell, R.E., Duffy, O.B., Gawthorpe, R.L. & Fossen, H. (2019) Structural Architecture and Composition of Crystalline Basement Offshore West Norway. *Lithosphere*, **11,** 273-293.

Lepley, S., Piccoli, L., Chitale, V., Kelley, I. & Quest, M. (2017). *The Importance of Understanding Diagenesis for the Development of Pre-Salt Lacustrine Carbonates*. AAPG Annual Convention and Exhibition.

Letouzey, J., Werner, P. & Marty, A. (1990) Fault Reactivation and Structural Inversion. Backarc and Intraplate Compressive Deformations. Example of the Eastern Sunda Shelf (Indonesia). *Tectonophysics*, **183,** 341-362.

Lima, B.E.M. & De Ros, L.F. (2019) Deposition, Diagenetic and Hydrothermal Processes in the Aptian Pre-Salt Lacustrine Carbonate Reservoirs of the Northern Campos Basin, Offshore Brazil. *Sedimentary Geology*, **383,** 55-81.

Lima, B.E.M., Tedeschi, L.R., Pestilho, A.L.S., Santos, R.V., Vazquez, J.C., Guzzo, J.V.P. & De Ros, L.F. (2020) Deep-Burial Hydrothermal Alteration of the Pre-Salt Carbonate Reservoirs from Northern Campos Basin, Offshore Brazil: Evidence from Petrography, Fluid Inclusions, Sr, C and O Isotopes. *Marine and Petroleum Geology*, **113,** 104-143.

Lima, F., Sanjinés, A., Maizatto, J., Ferreira, E., Ng, C., Costa, D., Zerfass, G., Alves, C., Strohschoen Jr, O. & Viviers, M. (2018). *Aptian Marine Post-Salt Rocks in Santos, Campos and Espírito Santo Basins, Brazil: A Biochronostratigraphical Approach*. 49th Congresso Brasileiro de Geologia, Rio de Janeiro, SBG.

López-Horgue, M., Iriarte, E., Schröder, S., Fernández-Mendiola, P., Caline, B., Corneyllie, H., Frémont, J., Sudrie, M. & Zerti, S. (2010) Structurally Controlled Hydrothermal Dolomites in Albian Carbonates of the Asón Valley, Basque Cantabrian Basin, Northern Spain. *Marine and Petroleum Geology*, **27,** 1069-1092.

Loucks, R.G. (1999) Paleocave Carbonate Reservoirs: Origins, Burial-Depth Modifications, Spatial Complexity, and Reservoir Implications. *AAPG Bulletin*, **83,** 1795-1834.

Loucks, R.G., Mescher, P.K. & McMechan, G.A. (2004) Three-Dimensional Architecture of a Coalesced, Collapsed-Paleocave System in the Lower Ordovician Ellenburger Group, Central Texas. *AAPG Bulletin*, **88,** 545-564.

Lourenço, F.S., Alkmim, F.F.d., Araújo, M.N.C., Romeiro, M.A.T., Matos, G.C. & Crósta, A.P. (2016) The Piúma Lineament, Southern Espirito Santo: Structural Expression and Tectonic Significance. *Brazilian Journal of Geology*, **46,** 531-546.

Lovecchio, J.P., Rohais, S., Joseph, P., Bolatti, N.D., Kress, P.R., Gerster, R. & Ramos, V.A. (2018) Multistage Rifting Evolution of the Colorado Basin (Offshore Argentina): Evidence for Extensional Settings Prior to the South Atlantic Opening. *Terra Nova*, **30,** 359-368.

Ludwig, K.R. (2003) User's Manual for Isoplot 3.00, a Geochronlogical Toolkit for Microsoft Excel. *Berkeley Geochronl. Cent. Spec. Publ.*, **4,** 25-32.

Machel, H.G. (1999) Effects of Groundwater Flow on Mineral Diagenesis, with Emphasis on Carbonate Aquifers. *Hydrogeology Journal*, **7,** 94-107.

Machel, H.G. (2001) Bacterial and Thermochemical Sulfate Reduction in Diagenetic Settings—Old and New Insights. *Sedimentary Geology*, **140,** 143-175.

Machel, H.G. & Lonnee, J. (2002) Hydrothermal Dolomite—a Product of Poor Definition and Imagination. *Sedimentary Geology*, **152,** 163-171.

Machel, H.G. (2004) Concepts and Models of Dolomitization: A Critical Reappraisal. *Geological Society, London, Special Publications*, **235,** 7-63.

Martín-Martín, J., Gomez-Rivas, E., Gómez-Gras, D., Travé, A., Ameneiro, R., Koehn, D. & Bons, P. (2018) Activation of Stylolites as Conduits for Overpressured Fluid Flow in Dolomitized Platform Carbonates. *Geological Society, London, Special Publications*, **459,** 157-176.

Martins-Neto, M. & Catuneanu, O. (2010) Rift Sequence Stratigraphy. *Marine and Petroleum Geology*, **27,** 247-253.

Martins, G., Mendes, J.C., da Silva Schmitt, R. & Armstrong, R. (2021) Unravelling Source and Tectonic Environment of an Ediacaran Magmatic Province from Southeast Brazil: Insights from Geochemistry and Isotopic Investigation. *Lithos*, **404,** 106428.

Matos, R.M.D. (2021) Magmatism and Hotspot Trails During and after Continental Break-up in the South Atlantic. *Marine and Petroleum Geology*, **129,** 105077.

Matos, R.M.D., Krueger, A., Norton, I. & Casey, K. (2021) The Fundamental Role of the Borborema and Benin–Nigeria Provinces of Ne Brazil and Nw Africa During the Development of the South Atlantic Cretaceous Rift System. *Marine and Petroleum Geology*, **127,** 104872.

McHargue, T.R., Heidrick, T.L. & Livingston, J.E. (1992) Tectonostratigraphic Development of the Interior Sudan Rifts, Central Africa. *Tectonophysics*, **213,** 187-202.

McLeod, A.E., Dawers, N.H. & Underhill, J.R. (2000) The Propagation and Linkage of Normal Faults: Insights from the Strathspey–Brent–Statfjord Fault Array, Northern North Sea. *Basin Research*, **12,** 263-284.

Meisling, K.E., Cobbold, P.R. & Mount, V.S. (2001) Segmentation of an Obliquely Rifted Margin, Campos and Santos Basins, Southeastern Brazil. *AAPG Bulletin*, **85,** 1903-1924.

Menezes, C.P., Bezerra, F.H., Balsamo, F., Mozafari, M., Vieira, M.M., Srivastava, N.K. & de Castro, D.L. (2019) Hydrothermal Silicification Along Faults Affecting Carbonate-Sandstone Units and Its Impact on Reservoir Quality, Potiguar Basin, Brazil. *Marine and Petroleum Geology*, **110,** 198-217.

Milani, E.J. & Davison, I. (1988) Basement Control and Transfer Tectonics in the Recôncavo-Tucano-Jatobá Rift, Northeast Brazil. *Tectonophysics*, **154,** 41-70.

Milani, E.J. & De Wit, M. (2008) Correlations between the Classic Paraná and Cape–Karoo Sequences of South America and Southern Africa and Their Basin Infills Flanking the Gondwanides: Du Toit Revisited. *Geological Society, London, Special Publications*, **294,** 319-342.

Mitchum Jr, R.M., Vail, P.R. & Thompson III, S. (1977) Seismic Stratigraphy and Global Changes of Sea Level: Part 2. The Depositional Sequence as a Basic Unit for Stratigraphic Analysis: Section 2. Application of Seismic Reflection Configuration to Stratigraphic Interpretation. *AAPG Memoir*, **26,** 53-62.

Mizuno, T.A., Mizusaki, A.M.P. & Lykawka, R. (2018) Facies and Paleoenvironments of the Coqueiros Formation (Lower Cretaceous, Campos Basin): A High Frequency Stratigraphic Model to Support Pre-Salt "Coquinas" Reservoir Development in the Brazilian Continental Margin. *Journal of South American Earth Sciences*, **88,** 107-117.

Mizusaki, A.M.P., Petrini, R., Bellieni, P., Comin-Chiaramonti, P., Dias, J., De Min, A. & Piccirillo, E.M. (1992) Basalt Magmatism Along the Passive Continental Margin of Se Brazil (Campos Basin). *Contributions to Mineralogy and Petrology*, **111,** 143-160.

Mohriak, W., Mello, M., Dewey, J. & Maxwell, J. (1990) Petroleum Geology of the Campos Basin, Offshore Brazil. *Geological Society, London, Special Publications*, **50,** 119-141.

Mohriak, W., Nemčok, M. & Enciso, G. (2008) South Atlantic Divergent Margin Evolution: Rift-Border Uplift and Salt Tectonics in the Basins of Se Brazil. *Geological Society, London, Special Publications*, **294,** 365-398.

Monié, P., Bosch, D., Bruguier, O., Vauchez, A., Rolland, Y., Nsungani, P. & Buta Neto, A. (2012) The Late Neoproterozoic/Early Palaeozoic Evolution of the West Congo Belt of Nw Angola: Geochronological (U-Pb and Ar-Ar) and Petrostructural Constraints. *Terra Nova*, **24,** 238-247.

Morad, S., Ketzer, J. & De Ros, L.F. (2000) Spatial and Temporal Distribution of Diagenetic Alterations in Siliciclastic Rocks: Implications for Mass Transfer in Sedimentary Basins. *Sedimentology*, **47,** 95-120.

Moreira, J.L.P., Madeira, C.V., Gil, J.A. & Machado, M.A.P. (2007) Bacia De Santos. *Boletim de Geociências da Petrobras*, **15,** 531-549.

Morgan, J.P., Taramón, J.M., Araujo, M., Hasenclever, J. & Perez-Gussinye, M. (2020) Causes and Consequences of Asymmetric Lateral Plume Flow During South Atlantic Rifting. *Proceedings of the National Academy of Sciences*, **117,** 27877-27883.

Morley, C.K. (2002) Evolution of Large Normal Faults: Evidence from Seismic Reflection Data. *AAPG Bulletin*, **86,** 961-978.

Morley, C.K., Haranya, C., Phoosongsee, W., Pongwapee, S., Kornsawan, A. & Wonganan, N. (2004) Activation of Rift Oblique and Rift Parallel Pre-Existing Fabrics During Extension and Their Effect on Deformation Style: Examples from the Rifts of Thailand. *Journal of Structural Geology*, **26,** 1803-1829.

Morley, C.K., Ionnikoff, Y., Pinyochon, N. & Seusutthiya, K. (2007) Degradation of a Footwall Fault Block with Hanging-Wall Fault Propagation in a Continental-Lacustrine Setting: How a New Structural Model Impacted Field Development Plans, the Sirikit Field, Thailand. *AAPG Bulletin*, **91,** 1637-1661.

Morley, C.K. (2014) The Widespread Occurrence of Low-Angle Normal Faults in a Rift Setting: Review of Examples from Thailand, and Implications for Their Origin and Evolution. *Earth Science Reviews*, **133,** 18-42.

Morley, C.K. (2017) The Impact of Multiple Extension Events, Stress Rotation and Inherited Fabrics on Normal Fault Geometries and Evolution in the Cenozoic Rift Basins of Thailand. *Geological Society, London, Special Publications*, **439,** 413-445.

Moulin, M., Aslanian, D. & Unternehr, P. (2010) A New Starting Point for the South and Equatorial Atlantic Ocean. *Earth-Science Reviews*, **98,** 1-37.

Muniz, M.C. & Bosence, D.W.J. (2015) Pre-Salt Microbialites from the Campos Basin (Offshore Brazil): Image Log Facies, Facies Model and Cyclicity in Lacustrine Carbonates. *Geological Society, London, Special Publications*, **418,** 221-242.

Muniz, M.C. & Bosence, D.W.J. (2018) Lacustrine Carbonate Platforms: Facies, Cycles, and Tectonosedimentary Models for the Presalt Lagoa Feia Group (Lower Cretaceous), Campos Basin, Brazil. *AAPG Bulletin*, **102,** 2569-2597.

Naden, J. (1996). *Calcicbrine: A Microsoft Excel 5.0 Add-in for Calculating Salinities from Microthermometric Data in the System Nacl–Cacl2–H2o*. PACROFI VI, Madison, WI, University of Wisconsin.

Neilson, J. & Oxtoby, N. (2008) The Relationship between Petroleum, Exotic Cements and Reservoir Quality in Carbonates–a Review. *Marine and Petroleum Geology*, **25,** 778-790.

Oakes, C.S., Bodnar, R.J. & Simonson, J.M. (1990) The System Nacl-Cacl2-H2o: I. The Ice Liquidus at 1 Atm Total Pressure. *Geochimica et Cosmochimica Acta*, **54,** 603-610.

Oliveira, V.C.B.d., de Assis Silva, C.M., Borghi, L.F. & de Souza Carvalho, I. (2019) Lacustrine Coquinas and Hybrid Deposits from Rift Phase: Pre-Salt, Lower Cretaceous, Campos Basin, Brazil. *Journal of South American Earth Sciences*, **95,** 102254.

Olivito, J.P.R. & Souza, F.J. (2020) Depositional Model of Early Cretaceous Lacustrine Carbonate Reservoirs of the Coqueiros Formation-Northern Campos Basin, Southeastern Brazil. *Marine and Petroleum Geology*, **111,** 414-439.

Osagiede, E.E., Rotevatn, A., Gawthorpe, R., Kristensen, T.B., Jackson, C.A.-L. & Marsh, N. (2020) Pre-Existing Intra-Basement Shear Zones Influence Growth and Geometry of Non-Colinear Normal Faults, Western Utsira High–Heimdal Terrace, North Sea. *Journal of Structural Geology*, **130**.

Paarlberg, N. & Evans, L. (1977) Geology of the Fletcher Mine, Viburnum Trend, Southeast Missouri. *Economic Geology*, **72,** 391-397.

Packard, J.J., Al-Aasm, I., Samson, I., Berger, Z. & Davies, J. (2001) A Devonian Hydrothermal Chert Reservoir: The 225 Bcf Parkland Field, British Columbia, Canada. *AAPG Bulletin*, **85,** 51-84.

Palmer, A.N. (2011) Distinction between Epigenic and Hypogenic Maze Caves. *Geomorphology*, **134,** 9-22.

Pan, L., Hu, A., Liang, F., Jiang, L., Hao, Y., Feng, Y., Shen, A. & Zhao, J. (2021). Diagenetic conditions and geodynamic setting of the middle Permian hydrothermal dolomites from southwest Sichuan Basin, SW China: insights from in situ U-Pb carbonate geochronology and isotope geochemistry. *Marine and Petroleum Geology*, **129**.

Parise, M., Gabrovsek, F., Kaufmann, G. & Ravbar, N. (2018) Recent Advances in Karst Research: From Theory to Fieldwork and Applications. *Geological Society, London, Special Publications*, **466,** 1-24.

Paula Faria, D.L.d., dos Reis, A.T. & de Souza Jr, O.G. (2017) Three-Dimensional Stratigraphic-Sedimentological Forward Modeling of an Aptian Carbonate Reservoir Deposited During the Sag Stage in the Santos Basin, Brazil. *Marine and Petroleum Geology*, **88,** 676-695.

Peacock, D., Knipe, R. & Sanderson, D. (2000) Glossary of Normal Faults. *Journal of Structural Geology*, **22,** 291-305.

Pessano, P.C., Ganade, C.E., Tupinambá, M. & Teixeira, W. (2021) Updated Map of the Mafic Dike Swarms of Brazil Based on Airborne Geophysical Data. *Journal of South American Earth Sciences*, **107,** 103076.

Phillips, T.B., Jackson, C.A.-L., Bell, R.E., Duffy, O.B. & Fossen, H. (2016) Reactivation of Intrabasement Structures During Rifting: A Case Study from Offshore Southern Norway. *Journal of Structural Geology*, **91,** 54-73.

Phillips, T.B., Fazlikhani, H., Gawthorpe, R.L., Fossen, H., Jackson, C.A.L., Bell, R.E., Faleide, J.I. & Rotevatn, A. (2019) The Influence of Structural Inheritance and Multiphase Extension on Rift Development, the Northern North Sea. *Tectonics*, **38,** 4099-4126.

Pietzsch, R., Oliveira, D.M., Tedeschi, L.R., Neto, J.V.Q., Figueiredo, M.F., Vazquez, J.C. & Souza, R.S. (2018) Palaeohydrology of the Lower Cretaceous Pre-Salt Lacustrine System, from Rift to Post-Rift Phase, Santos Basin, Brazil. *Palaeogeography, Palaeoclimatology, Palaeoecology*, **507,** 60-80.

Pietzsch, R., Tedeschi, L.R., Oliveira, D.M., dos Anjos, C.W.D., Vazquez, J.C. & Figueiredo, M.F. (2020) Environmental Conditions of Deposition of the Lower Cretaceous Lacustrine Carbonates of the Barra Velha Formation, Santos Basin (Brazil), Based on Stable Carbon and Oxygen Isotopes: A Continental Record of Pco2 During the Onset of the Oceanic Anoxic Event 1a (Oae 1a) Interval? *Chemical Geology*, **535**.

Pingitore, N.E. (1982) The Role of Diffusion During Carbonate Diagenesis. *Journal of Sedimentary Research*, **52,** 27-39.

Ponte, F.C. & Asmus, H.E. (1976) The Brazilian Marginal Basins: Current State of Knowledge. *International Symposiumon Continental Margins of Atlantic Type,*, Academia Brasileira de Ciências. São Paulo. **48**.

Poros, Z., Jagniecki, E., Luczaj, J., Kenter, J., Gal, B., Correa, T.S., Ferreira, E., McFadden, K.A., Elifritz, A. & Heumann, M. (2017) Origin of Silica in Pre-Salt Carbonates, Kwanza Basin, Angola. *AAPG Search and Discovery*.

Preibisch, S., Saalfeld, S. & Tomancak, P. (2009) Globally Optimal Stitching of Tiled 3d Microscopic Image Acquisitions. *Bioinformatics*, **25,** 1463-1465.

Prosser, S. (1993) Rift-Related Linked Depositional Systems and Their Seismic Expression. *Geological Society, London, Special Publications*, **71,** 35-66.

Rabinowitz, P.D. & LaBrecque, J. (1979) The Mesozoic South Atlantic Ocean and Evolution of Its Continental Margins. *Journal of Geophysical Research*, **84,** 5973-6002.

Reeve, M.T., Bell, R.E. & Jackson, C.A.-L. (2014) Origin and Significance of Intra-Basement Seismic Reflections Offshore Western Norway. *Journal of the Geological Society*, **171,** 1-4.

Reeve, M.T., Bell, R.E., Duffy, O.B., Jackson, C.A.-L. & Sansom, E. (2015) The Growth of Non-Colinear Normal Fault Systems; What Can We Learn from 3d Seismic Reflection Data? *Journal of Structural Geology*, **70,** 141-155.

Reston, T. (2020) On the Rotation and Frictional Lock-up of Normal Faults: Explaining the Dip Distribution of Normal Fault Earthquakes and Resolving the Low-Angle Normal Fault Paradox. *Tectonophysics*, **790**.

Riccomini, C. (1989) O Rift Continental do Sudeste do Brasi, Universidade de São Paulo, São Paulo (SP). PhD Thesis. 256p.

Roberts, N.M.W. & Walker, R.J. (2016) U-Pb Geochronology of Calcite-Mineralized Faults: Absolute Timing of Rift-Related Fault Events on the Northeast Atlantic Margin. *Geology*, **44,** 531-534.

Roberts, N.M.W., Rasbury, E.T., Parrish, R.R., Smith, C.J., Horstwood, M.S.A. & Condon, D.J. (2017) A Calcite Reference Material for La-Icp-Ms U-Pb Geochronology. *Geochem., Geophys. Geosys.*, **18,** 2807-2814.

Roberts, N.M.W., Drost, K., Horstwood, M.S.A., Condon, D.J., Chew, D., Drake, H., Milodowski, A.E., McLean, N.M., Smye, A.J., Walker, R.J., Haslam, R., Hodson, K., Imber, J., Beaudoin, N. & Lee, J.K. (2020) Laser Ablation Inductively Coupled Plasma Mass Spectrometry (La-Icp-Ms) U–Pb Carbonate Geochronology: Strategies, Progress, and Limitations. *Geochronology*, **2,** 33-61.

Rocha, B.C., Davies, J.H.F.L., Janasi, V.A., Schaltegger, U., Nardy, A.J.R., Greber, N.D., Lucchetti, A.C.F., and Polo, L.A., 2020, Rapid eruption of silicic magmas from the Paraná magmatic province (Brazil) did not trigger the Valanginian event: *Geology*, **48**, 1174–1178,

Rochelle-Bates, N., Roberts, N., Sharp, I., Freitag, U., Verwer, K., Halton, A., Fiordalisi, E., van Dongen, B., Swart, R. & Ferreira, C. (2021) Geochronology of Volcanically Associated Hydrocarbon Charge in the Pre-Salt Carbonates of the Namibe Basin, Angola. *Geology*, **49,** 335-340.

Rochelle-Bates, N., Wood, R., Schröder, S. & Roberts, N.M.W. (2022) In Situ U–Pb Geochronology of Pre-Salt Carbonates Reveals Links between Diagenesis and Regional Tectonics. *Terra Nova*. **34**, 271-277.

Roedder, E. (1984) Fluid Inclusions. *Mineralogical Society of America, Reviews in mineralogy*, **12**.

Saller, A.H., Budd, D.A. & Harris, P.M. (1994) Unconformities and Porosity Development in Carbonate Strata: Ideas from a Hedberg Conference. *AAPG Bulletin*, **78,** 857-872.

Sanjinés, A.E.S., Viviers, M.C., Costa, D.S., dos Anjos Zerfass, G.d.S., Beurlen, G. & Strohschoen Jr, O. (2022) Planktonic Foraminifera from the Aptian Section of the Southeastern Brazilian Atlantic Margin. *Cretaceous Research*, **134,** 105-141.

Santiago, R., de Andrade Caxito, F., Neves, M.A., Dantas, E.L., de Medeiros Júnior, E.B. & Queiroga, G.N. (2020) Two Generations of Mafic Dyke Swarms in the Southeastern Brazilian Coast: Reactivation of Structural Lineaments During the Gravitational Collapse of the Araçuaí-Ribeira Orogen (500 Ma) and West Gondwana Breakup (140 Ma). *Precambrian Research*, **340**.

Savastano, V.L.M., Schmitt, R.S., Araújo, M.N.C. & Inocêncio, L.C. (2017) Rift Brittle Deformation of Se-Brazilian Continental Margin: Kinematic Analysis of Onshore Structures Relative to the Transfer and Accommodation Zones of Southern Campos Basin. *Journal of Structural Geology*, **94,** 136-153.

Schaller, H. (1973). *Estratigrafia Da Bacia De Campos*. Anais do XXVII Congresso Brasileiro de Geologia.

Schlische, R.W. (1995) Geometry and Origin of Fault-Related Folds in Extensional Settings. *AAPG Bulletin*, **79,** 1661-1678.

Schmitt, R.S., Trouw, R.A.J., Van Schmus, W.R. & Pimentel, M.M. (2004) Late Amalgamation in the Central Part of West Gondwana: New Geochronological Data and the Characterization of a Cambrian Collisional Orogeny in the Ribeira Belt (Se Brazil). *Precambrian Research*, **133,** 29-61.

Schmitt, R.S., Trouw, R.A.J., Van Schmus, W.R. & Passchier, C.W. (2008) Cambrian Orogeny in the Ribeira Belt (Se Brazil) and Correlations within West Gondwana: Ties That Bind Underwater. *Geological Society, London, Special Publications*, **294,** 279-296.

Schmitt, R.S., Trouw, R., Van Schmus, W.R., Armstrong, R. & Stanton, N.S.G. (2016) The Tectonic Significance of the Cabo Frio Tectonic Domain in the Se Brazilian Margin: A Paleoproterozoic through Cretaceous Saga of a Reworked Continental Margin. *Brazilian Journal of Geology*, **46,** 37-66.

Schmitt, R.S., Fragoso, R.A. & Collins, A.S. (2018) Suturing Gondwana in the Cambrian: The Orogenic Events of the Final Amalgamation. In: *Geology of Southwest Gondwana* (Ed. by S. Siegesmund, M. A. S. Basei, P. Oyhantçabal & S. Oriolo), 411-432. Springer International Publishing, Cham.

Sharp, I., Gillespie, P., Morsalnezhad, D., Taberner, C., Karpuz, R., Vergés, J., Horbury, A., Pickard, N., Garland, J. & Hunt, D. (2010) Stratigraphic Architecture and Fracture-Controlled Dolomitization of the Cretaceous Khami and Bangestan Groups: An Outcrop Case Study, Zagros Mountains, Iran. *Geological Society, London, Special Publications*, **329,** 343-396.

Sibson, R.H. (1981) Fluid Flow Accompanying Faulting: Field Evidence and Models. In: *Earthquake Prediction: An International Review* (Ed. by P. G. R. D.W. Simpson), **4**, 593-603. American Geophysical Union.

Sibson, R.H. (1992) Fault-Valve Behavior and the Hydrostatic-Lithostatic Fluid Pressure Interface. *Earth Science Reviews*, **32,** 141-144.

Silva, M.A., Camozzato, E., Paes, V.J.C., Junqueira, P.A. & Ramgrab, G.E. (2004) Carta Geológica Do Brasil Ao Milionésimo, Folha Sf. 24-Vitoria, CPRM. Brasília.

Souza, R.S., Arienti, L.M., Viana, S.M., Falcão, L.C., Cuglieri, M.A., Silva Filho, R.P., Leite, C.O., Oliveira, V.C., Oliveira, D.M. & Anjos, C. (2018). *Petrology of the Hydrothermal and Evaporitic Continental Cretaceous (Aptian) Pre-Salt Carbonates and Associated Rocks, South Atlantic Santos Basin, Offshore Brazil*. AAPG ACE 2018.

Souza, V.H., Bezerra, F.H., Vieira, L.C., Cazarin, C.L. & Brod, J.A. (2021) Hydrothermal Silicification Confined to Stratigraphic Layers: Implications for Carbonate Reservoirs. *Marine and Petroleum Geology*, **124,** 104818.

Stanton, N., Schmitt, R.S., Galdeano, A., Maia, M. & Mane, M. (2010) Crustal Structure of the Southeastern Brazilian Margin, Campos Basin, from Aeromagnetic Data: New Kinematic Constraints. *Tectonophysics*, **490,** 15-27.

Stanton, N., Kusznir, N., Gordon, A. & Schmitt, R.S. (2019) Architecture and Tectono-Magmatic Evolution of the Campos Rifted Margin: Control of Oct Structure by Basement Inheritance. *Marine and Petroleum Geology*, **100,** 43-59.

Strugale, M., Schmitt, R.S. & Cartwright, J. (2021) Basement Geology and Its Controls on the Nucleation and Growth of Rift Faults in the Northern Campos Basin, Offshore Brazil. *Basin Research*, **33,** 1906-1933.

Strugale, M. & Cartwright, J.A. (2022) Tectono-Stratigraphic Evolution of the Rift and Post-Rift Systems in the Northern Campos Basin, Offshore Brazil. *Basin Research*, **34,** 1655-1687.

Swennen, R., Dewit, J., Fierens, E., Muchez, P., Shah, M., Nader, F. & Hunt, D. (2012) Multiple Dolomitization Events Along the Pozalagua Fault (Pozalagua Quarry, Basque–Cantabrian Basin, Northern Spain). *Sedimentology*, **59,** 1345-1374.

Szatmari, P. & Milani, E.J. (2016) Tectonic Control of the Oil-Rich Large Igneous-Carbonate-Salt Province of the South Atlantic Rift. *Marine and Petroleum Geology*, **77,** 567-596.

Szatmari, P., de Lima, C.M., Fontaneta, G., de Melo Lima, N., Zambonato, E., Menezes, M.R., Bahniuk, J., Coelho, S.L., Figueiredo, M. & Florencio, C.P. (2021) Petrography, Geochemistry and Origin of South Atlantic Evaporites: The Brazilian Side. *Marine and Petroleum Geology*, **127,** 104805.

Tack, L., Wingate, M.T.D., Liégeois, J.-P., Fernandez-Alonso, M. & Deblond, A. (2001) Early Neoproterozoic Magmatism (1000–910 Ma) of the Zadinian and Mayumbian Groups (Bas-Congo): Onset of Rodinia Rifting at the Western Edge of the Congo Craton. *Precambrian Research*, **110,** 277-306.

Teboul, P.-A., Kluska, J.-M., Marty, N.C., Debure, M., Durlet, C., Virgone, A. & Gaucher, E.C. (2017) Volcanic Rock Alterations of the Kwanza Basin, Offshore Angola-Insights from an Integrated Petrological, Geochemical and Numerical Approach. *Marine and Petroleum Geology*, **80,** 394-411.

Teboul, P.-A., Durlet, C., Girard, J.-P., Dubois, L., San Miguel, G., Virgone, A., Gaucher, E.C. & Camoin, G. (2019) Diversity and Origin of Quartz Cements in Continental Carbonates: Example from the Lower Cretaceous Rift Deposits of the South Atlantic Margin. *Applied Geochemistry*, **100,** 22-41.

Tedeschi, L.R., Jenkyns, H.C., Robinson, S.A., Sanjinés, A.E.S., Viviers, M.C., Quintaes, C.M.S.P. & Vazquez, J.C. (2017) New Age Constraints on Aptian Evaporites and Carbonates from the South Atlantic: Implications for Oceanic Anoxic Event 1a. *Geology*, **45,** 543-546.

Tedeschi, L.R., Jenkyns, H.C., Robinson, S.A., Lana, C.C., Menezes Santos, M.R.F. & Tognoli, F.M.W. (2019) Aptian Carbon-Isotope Record from the Sergipe-Alagoas Basin: New Insights into Oceanic Anoxic Event 1a and the Timing of Seawater Entry into the South Atlantic. *Newsletters on Stratigraphy*, **53,** 333-364.

Thomas Filho, A., Mizusaki, A.M.P., Milani, E.J. & Cesero, P. (2000) Rifting and Magmatism Associated with the South America and Africa Break Up. *Brazilian Journal of Geology*, **30,** 017-019.

Thompson, D.L., Stilwell, J.D. & Hall, M. (2015) Lacustrine Carbonate Reservoirs from Early Cretaceous Rift Lakes of Western Gondwana: Pre-Salt Coquinas of Brazil and West Africa. *Gondwana Research*, **28,** 26-51.

Torremans, K., Kyne, R., Doyle, R., Güven, J.F. & Walsh, J.J. (2018) Controls on Metal Distributions at the Lisheen and Silvermines Deposits: Insights into Fluid Flow Pathways in Irish-Type Zn-Pb Deposits. *Economic Geology*, **113,** 1455-1477.

Torsvik, T.H., Rousse, S., Labails, C. & Smethurst, M.A. (2009) A New Scheme for the Opening of the South Atlantic Ocean and the Dissection of an Aptian Salt Basin. *Geophysical Journal International*, **177,** 1315-1333.

Tosca, N.J. & Wright, V.P. (2015) Diagenetic Pathways Linked to Labile Mg-Clays in Lacustrine Carbonate Reservoirs: A Model for the Origin of Secondary Porosity in the Cretaceous Pre-Salt Barra Velha Formation, Offshore Brazil. *Geological Society, London, Special Publications*, **435,** 33-46.

Tritlla, J., Loma, R., Esteban, M., Sanders, C., Sánchez, V., Benito, V., Carrasco, A., Peña, J.L., Herra, A. & Gerona, M. (2018). *Pre-Salt Lacustrine Carbonates, Diagenetic Silicification and Hydrothermal Overprinting in Kwanza Basin (Offshore Angola): A Tale of Two Silicas*. AAPG ACE 2018, Salt Lake City.

Trouw, R.A., Peternel, R., Ribeiro, A., Heilbron, M., Vinagre, R., Duffles, P., Trouw, C.C., Fontainha, M. & Kussama, H.H. (2013) A New Interpretation for the Interference Zone between the Southern Brasília Belt and the Central Ribeira Belt, Se Brazil. *Journal of South American Earth Sciences*, **48,** 43-57.

Turner, J.P. & Williams, G.A. (2004) Sedimentary Basin Inversion and Intra-Plate Shortening. *Earth Science Reviews*, **65,** 277-304.

Turner, S., Regelous, M., Kelley, S., Hawkesworth, C. & Mantovani, M. (1994) Magmatism and Continental Break-up in the South Atlantic: High Precision40ar-39ar Geochronology. *Earth and Planetary Science Letters*, **121,** 333-348.

Valente, S.d.C., Corval, A., Duarte, B.P., Ellam, R.M., Fallick, A.E., Meighan, I.G. & Dutra, T. (2007) Tectonic Boundaries, Crustal Weakness Zones and Plume-Subcontinental Lithospheric Mantle Interactions in the Serra Do Mar Dyke Swarm, Se Brazil. *Brazilian Journal of Geology*, **37**.

Vandeginste, V., Swennen, R., Gleeson, S.A., Ellam, R.M., Osadetz, K. & Roure, F. (2005) Zebra Dolomitization as a Result of Focused Fluid Flow in the Rocky Mountains Fold and Thrust Belt, Canada. *Sedimentology*, **52,** 1067-1095.

Vandeginste, V., John, C.M., van de Flierdt, T. & Cosgrove, J.W. (2013) Linking Process, Dimension, Texture, and Geochemistry in Dolomite Geobodies: A Case Study from Wadi Mistal (Northern Oman) Linking Process, Dimension, Texture, and Geochemistry in Dolomite Geobodies. *AAPG Bulletin*, **97,** 1181-1207.

Vasconcelos, D.L., Bezerra, F.H., Medeiros, W.E., de Castro, D.L., Clausen, O.R., Vital, H. & Oliveira, R.G. (2019) Basement Fabric Controls Rift Nucleation and Postrift Basin Inversion in the Continental Margin of Ne Brazil. *Tectonophysics*, **751,** 23-40.

Vieira de Luca, P.H., Matias, H., Carballo, J., Sineva, D., Pimentel, G.A., Tritlla, J., Esteban, M., Loma, R., Alonso, J.L.A. & Jiménez, R.P. (2017) Breaking Barriers and Paradigms in Presalt Exploration: The Pão De Açúcar Discovery (Offshore Brazil). *AAPG Memoir*, **113**.

Walsh, J.J. & Watterson, J. (1988) Analysis of the Relationship between Displacements and Dimensions of Faults. *Journal of Structural Geology*, **10,** 239-247.

Walsh, J.J., Watterson, J. & Yielding, G. (1991) The Importance of Small-Scale Faulting in Regional Extension. *Nature*, **351,** 391-393.

Walsh, J.J., Torremans, K., Güven, J., Kyne, R., Conneally, J. & Bonson, C. (2018) Fault-Controlled Fluid Flow within Extensional Basins and Its Implications for Sedimentary Rock-Hosted Mineral Deposits. In: *Metals, Minerals, and Society* (Ed. by A. M. Arribas R & J. L. Mauk), **21**, 0. Society of Economic Geologists (SEG).

Warren, J. (2000) Dolomite: Occurrence, Evolution and Economically Important Associations. *Earth Science Reviews*, **52,** 1-81.

Welch, M.J., Lüthje, M. & Oldfield, S.J. (2020) *Modelling the Evolution of Natural Fracture Networks*. Springer.

Wennberg, O., McQueen, G., de Luca, P.V., Lapponi, F., Hunt, D., Chandler, A., Waldum, A., Camargo, G.N., Castro, E. & Loures, L. (2021) Open Fractures in Pre-Salt Silicified Carbonate Reservoirs in Block Bm-C-33, the Outer Campos Basin, Offshore Brazil. *Petroleum Geoscience*, **27,** petgeo2020-2125.

Whitaker, F.F., Smart, P.L. & Jones, G.D. (2004) Dolomitization: From Conceptual to Numerical Models. *Geological Society, London, Special Publications*, **235,** 99-139.

White, D.E. (1957) Thermal Waters of Volcanic Origin. *GSA Bulletin*, **68,** 1637-1658.

Wilkinson, J.J., Eyre, S.L. & Boyce, A.J. (2005) Ore-Forming Processes in Irish-Type Carbonate-Hosted Zn-Pb Deposits: Evidence from Mineralogy, Chemistry, and Isotopic Composition of Sulfides at the Lisheen Mine. *Economic Geology*, **100,** 63-86.

Winter, W.R., Jahnert, R.J. & França, A.B. (2007) Bacia De Campos. *Boletim de Geociências da Petrobras*, **15,** 511-529.

Wiprut, D. & Zoback, M.D. (2000) Fault Reactivation and Fluid Flow Along a Previously Dormant Normal Fault in the Northern North Sea. *Geology*, **28,** 595-598.

Withjack, M.O., Schlische, R.W. & Olsen, P.E. (1998) Diachronous Rifting, Drifting, and Inversion on the Passive Margin of Central Eastern North America: An Analog for Other Passive Margins. *AAPG Bulletin*, **82,** 817-835.

Withjack, M.O., Schlische, R.W. & Olsen, P.E. (2002) Rift-Basin Structure and Its Influence on Sedimentary Systems. *SEPM Special Publication*, **73**.

Woodcock, N.H. (2004) Life Span and Fate of Basins. *Geology*, **32,** 685-688.

Worthington, S., Ford, D. & Beddows, P.A. (2000) Porosity and Permeability Enhancement in Unconfined Carbonate Aquifers as a Result of Solution. In: *Speleogenesis: Evolution of Karst Aquifers* (Ed. by, 463-471.

Wright, V.P. & Barnett, A.J. (2015) An Abiotic Model for the Development of Textures in Some South Atlantic Early Cretaceous Lacustrine Carbonates. *Geological Society, London, Special Publications*, **418,** 209-219.

Wright, V.P. & Tosca, N.J. (2016) A Geochemical Model for the Formation of the Pre-Salt Reservoirs, Santos Basin, Brazil: Implications for Understanding Reservoir Distribution. *Search and discovery article #51304. Adapted from oral presentation given at AAPG Annual Conference & Exhibition, Calgary, Alberta, Canada, June 19-22, 2016*, AAPG.

Zhao, J., Chen, H., Yin, L. & Li, N. (2017) Mineral Inversion for Element Capture Spectroscopy Logging Based on Optimization Theory. *Journal of Geophysics and Engineering*, **14,** 1430-1436.